PACIFIC EARTHQUAKE ENGINEERING
RESEARCH CENTER

The Use of Base Isolation Systems to Achieve Complex Seismic Performance Objectives

Troy A. Morgan
Center for Urban Earthquake Engineering
Tokyo Institute of Technology

Stephen A. Mahin
Department of Civil and Environmental Engineering
University of California, Berkeley

PEER 2011/06
JULY 2011

The Use of Base Isolation Systems to Achieve Complex Seismic Performance Objectives

Troy A. Morgan
Center for Urban Earthquake Engineering
Tokyo Institute of Technology

Stephen A. Mahin
Department of Civil and Environmental Engineering
University of California, Berkeley

PEER Report 2011/06
Pacific Earthquake Engineering Research Center
College of Engineering
University of California, Berkeley

July 2011

ABSTRACT

One concern in the design of base isolated structures is the selection of isolation system properties so that optimal performance is achieved over a range of seismic levels and performance metrics. To withstand very rare ground motions, isolation bearings are frequently designed with significant strength or damping, and as a result such devices provide reduced isolation effect for more frequent seismic events. To investigate possible improvements to the design of isolated structures, an extensive research program is conducted. Analytical and experimental investigations are presented to characterize multi-stage spherical sliding isolation bearings capable of progressively exhibiting different hysteretic properties at different stages of response. Shaking table tests are conducted on a 1/4-scale seismically isolated steel braced frame on multi-stage bearings, including harmonic characterizations tests and earthquake simulations. These tests included various input intensities, multi-component excitation, bearing uplift, and superstructure response. A newly developed analytical model is implemented as part of a parametric study of single- and multi-story buildings incorporating a wide class of isolation systems. Behavior of the new triple pendulum bearing is compared with that of linear isolation systems with both nonlinear viscous and bilinear hysteretic energy dissipation mechanisms. The results of parametric analyses are used to develop a design framework based on targeting a multi-objective Seismic Performance Classification (SPC). This SPC is introduced to describe satisfaction of a complex seismic performance objective, defined as aggregate damage state limitation over multiple levels of seismic hazard. The probability of satisfying specific SPCs is computed for three- and nine-story buildings on all classes of isolators investigated.

ACKNOWLEDGMENTS

The authors greatly appreciate the financial and other support provided by many individuals and organizations. Partial financial support of the analytical and theoretical portions of the research was provided by the National Science Foundation under Grant No. CMMI-0724208. Significant financial support for the overall effort was provided by Earthquake Protection Systems, Inc., and the intellectual contributions of Victor Zayas, Anoop Mokha, and Stanley Low were vital to the research described in this dissertation. Additionally, financial support for the first author through the 2005–2006 EERI/FEMA NEHRP Graduate Fellowship in Earthquake Hazard Reduction is greatly appreciated. The support of the Pacific Earthquake Engineering Research Center in publishing and disseminating this report is gratefully acknowledged. Any opinions, findings, and conclusions expressed here are those of the authors and do not necessarily reflect the views of the National Science Foundation, Earthquake Protection Systems or the Earthquake Engineering Research Institute.

The authors were assisted in completion of the experimental work described in this dissertation by graduate students Chui-Hsin Chen, Yuli Huang, Sanaz Rezaeian, and Eric Okstad. The invaluable assistance and support of the EERC laboratory staff, including Wesley Neighbors, David MacLam, and Jose Robles is also greatly appreciated.

CONTENTS

LIST OF FIGURES

LIST OF TABLES

1 Introduction

One of the most significant developments in structural engineering in the past twenty years has undoubtedly been the emergence of performance-based design as a means of selecting, proportioning, and building structural systems to resist seismic excitations. This methodology is an ideal framework for design due to its flexibility with respect to the selection of performance objectives, characterization and simulation of both demand and resistance, and the overarching treatment of uncertainty. A great strength of the methodology is that performance objectives may be defined in terms of structural performance, architectural function, socio-economic considerations, and environmental sustainability. This framework has the attractive feature of providing a metric of performance that can be implemented by a wide variety of infrastructure stakeholders, including architects, building owners, contractors, insurance providers, capital investment proprietors, and public officials. As civil engineers train their focus on broadly defined solutions to the challenges posed by maintaining and improving civilization, performance-based design will increasingly play a central role. This design approach requires the use of innovative structural systems to achieve the complex and potentially multi-objective performance goals that the various stakeholders are likely to envision. Given the uncertainty that is unavoidably present in any earthquake resistant design framework, innovative systems must not only be capable of predictable response to deterministic input, but also be sufficiently robust to respond reliably to a broad range of potential input.

1.1 GOALS OF PERFORMANCE-BASED SEISMIC DESIGN

Performance-based seismic design of structures is currently undergoing significant development in response to consequences experienced in recent earthquakes. Not only has

there been substantial loss of human life as a result of damage caused by major earthquakes, the economic toll resulting from direct losses (repair of infrastructure, replacement of damaged contents) and indirect losses (business disruptions, relocations expenses, supply chain interruption) has also been significant [Brookshire et al., 1997]. As a result of the significant socio-economic turmoil due to the occurrence of earthquakes worldwide, major research efforts have been aimed at identifying the sources of losses, and the correlation of specific damage states to these losses to identify strategies for mitigation.

A description of earthquake engineering has been proposed by Bertero and Bozorgnia [2004] that embodies the modern approach to seismic hazard mitigation:

> *Earthquake engineering encompasses multidisciplinary efforts from various branches of science and engineering with the goal of controlling the seismic risks to socio-economically acceptable levels.*

This description is appropriate because the objective of earthquake-resistant design is intentionally left open to interpretation. What may be an appropriate seismic design philosophy for critical facilities such as hospitals, mass data storage centers, or public utility buildings may be inappropriate and/or excessively costly for conventional facilities whose functionality or damage state following a major earthquake is not critical to either the public welfare or the financial solvency of an organization.

A philosophical framework for Performance–Based Seismic Design (PBSD) was recently proposed by Bertero and Bertero [2002], who suggest the following:

> *To satisfy the objectives of a reliable PBSD philosophy and procedure it is necessary to start with a multi-level seismic design criteria, to consider a probabilistic design approach, to consider local structural and non-structural damage and therefore design spectra for buildings (*n *degrees of freedom), to take into account the cumulative damage, and to control not only displacements but also ductility (minimum strength) to limit damage. Finally, it is concluded that a transparent and conceptual comprehensive preliminary design approach is necessary.*

It is within this framework of multi-level seismic design criteria that appropriate decisions regarding seismic design may be made. Moreover, the reliability of achieving a targeted seismic performance objective must by quantifiable. Only with a measurable reliability in place can strategies for improving this reliability be implemented. Reliability in this context can be thought of as limiting the probability of failure to some level deemed

acceptable given the consequences of failure. Once the significance of a probabilistic, multi-level design criteria is realized, the need is clear for innovative seismic systems whose response is both robust and optimized to minimize damage in accordance with the defined performance objectives.

1.2 ENHANCED SEISMIC PERFORMANCE THROUGH BASE ISOLATION

In the past 20 years, seismic isolation and other response modification technologies have seen a variety of applications in the design of structures to mitigate seismic risk. A summary of specific devices for isolating structures and prior implementation is summarized in Chapter 2 of this report. While such technologies provide a means of controlling the demands imposed by earthquakes, very few new seismic isolated buildings have been constructed in the U.S., compared to other countries with significant seismic hazards, such as Japan, China, and Taiwan. While a number of reasons for this have been identified, one is the lack of a transparent design method for choosing isolator properties that can minimize damage to the structure from various sources, while achieving isolator designs and displacement demands that are practical. The introduction of new technologies, such as supplemental energy dissipation devices and new types of isolator devices, has only compounded this problem.

As such, performance-based seismic design provides a useful framework for developing an understanding of the relationships among the characteristics of the ground motion, superstructure and isolation system, and to evaluate the ability of various design approaches and isolator system properties to reliably achieve targeted performance goals. While significant effort has been devoted to these areas by organizations devoted to collaborative research, less attention has been given to the role of innovative seismic isolation devices and systems in achieving the goals of a performance-based design framework described above. These types of devices are ideally suited for implementation within a performance-based framework because (a) robust characterization of their behavior can be made through experimentation; (b) the uncertainty associated with their behavior is generally low relative to conventional structural elements; and (c) it can be challenging, or even impossible, to *reliably* achieve an enhanced performance objective without their use. These benefits, combined with the fact that the implementation of innovative systems in practice is often met with resistance from building officials, owners, contractors, and even

design professionals, make future research critical to the continued evolution of performance-based design. Such structural systems have been developed and investigated by both the research and practicing communities for decades, but implementation has been slow, and mainstream application has yet to emerge. As a result, there is a need for strategies and techniques that broaden the use of innovative structural systems, and it is in the context of performance-based design that an effective methodology may be developed.

1.3 OBJECTIVES OF RESEARCH

The research described in this report focuses on

(a) the improvement of techniques used to both quantify and qualify descriptors and parameters used in performance-based design of base isolated buildings;
(b) the application of innovative base isolation technologies in achieving multiple-objective performance classifications; and
(c) the distillation and packaging of results such that their advantages can be realized within a probabilistic framework.

A major component of this research is the investigation of the cyclic behavior of a new class of multi-stage friction pendulum bearings. These isolation devices are characterized by parameters that can be selected such that the bearing exhibits cyclic performance that evolves with the amplitude of displacement demand. Characterization of the behavior of these devices and validation of the derived model though extensive experimentation provides a basis for further parametric analytical studies and performance assessment.

The analytical research described in this report investigates the potential for innovative isolation systems to reliably target multiple, independent performance objectives corresponding to different seismic hazard levels (i.e., functional after a frequent seismic event; immediately habitable after a rare seismic event; or near collapse, but structurally stable, following a very rare seismic event). Isolation systems studied include linear isolators with nonlinear viscous and bilinear hysteretic damping, and a new triple pendulum sliding isolator. Current design practice (for both conventional and isolated buildings) restricts the designer to target a *particular* level of performance at a *particular* level of seismic hazard.

Characteristics of isolation systems are investigated with respect to which parameters lead to the satisfaction of generally defined complex performance objectives.

1.4 ORGANIZATION OF REPORT

This report is organized into eight chapters. Chapter 2 summarizes the current status of seismic isolation as both an applied technology and a subject of continued research. Chapter 3 introduces a class of innovative spherical sliding isolators exhibiting multi-stage force-deformation behavior. A monotonic relationship is developed from fundamental mechanics, which is then extended to a cyclic model that responds to general displacement input and is therefore appropriate for nonlinear response history analysis. Chapter 4 summarizes the experimental specimen and test program conducted to investigate the behavior of two types of multi-stage sliding bearings under both harmonic and earthquake excitation. Chapter 5 presents the results of the experimental program, including comparisons of the newly developed cyclic model with observed behavior of the specimen, and experimental assessment of superstructure behavior under seismic excitation.

Chapter 6 summarizes a comprehensive series of parametric analytical studies carried out using the validated numerical isolator model on the newly introduced multi-stage spherical sliding system. For comparative purposes, these parametric studies are also conducted for nonlinear viscous and bilinear hysteretic isolation systems. Studies are first conducted on a canonical two-degree-of-freedom isolated model considering incremental dynamic analysis under single realization of ground acceleration. These results are supported by further studies on three- and nine-story isolated models considering the same three classes of isolation systems, subjected to an ensemble of ground motions developed for three levels of seismic hazard. Chapter 7 summarizes a probabilistic performance assessment methodology within which a wide variety of isolation systems may be compared and optimized to reliably target complex seismic performance objectives. These objectives are termed “complex” because they are defined by the satisfaction of prescribed deformation- and acceleration-sensitive damage states that are potentially distinct for multiple levels of seismic hazard.

Chapter 8 summarizes the key results of this report, makes recommendations for practical applications of seismic isolation as well as directions for further research. A list of references immediately follows Chapter 8.

2 Review of Seismic Isolation

2.1 THE CONCEPT OF SEISMIC ISOLATION

Seismic isolation has its roots in the need to control structural response due to harmonic vibrations. This need stems from a) the discomfort caused to occupants as a result of oscillatory motion of floor-supported equipment and b) the potential for damage to sensitive equipment caused by vibrations of the supporting structure [Clough and Penzien, 1993]. The sources of such vibrations have traditionally been rotating machinery, ambient traffic conditions, and walker induced floor vibrations. A common method of reducing the accelerations due to harmonic excitation is to provide a compliant base (either from steel springs or elastomeric pads) that adjusts the natural frequency of the supported equipment such that it is unable to reach resonance under the operating frequency of the excitation [Rivin, 2003]. This idea is behind the concept of "transmissibility," or the ratio of the response amplitude to the input amplitude. For example, in vibration isolation, one can define the transmissibility as $TR = \ddot{u}_{tot} / \ddot{u}_s$ where $\ddot{u}_{tot}$ is the peak total acceleration of the equipment and $\ddot{u}_s$ is the peak input acceleration of the support. TR is generally a function of the forcing frequency, the natural frequency of the supporting hardware, and the amount and type of damping present. Whereas the forcing frequency may be a function of the operating speed and weight (and therefore a fixed quantity independent of the support), the natural frequency and damping of the supporting hardware may be adjusted to limit the total acceleration due to harmonic excitation.

The reduction of transmissibility is also the goal of seismic isolation. Unlike traditional equipment isolation, however, the excitation is due to ground shaking, and cannot be characterized by harmonic input. Ground shaking resulting from a seismic event is stochastic in nature, and this excitation may contain a rich array of frequency content. Data

collected from numerous historical seismic events has demonstrated that the predominant frequency of seismic excitation is generally above 1 Hz, and hence systems having a lower natural frequency than this will experience a reduction in transmissibility of acceleration from the ground into the structure. The reduction of natural frequency (or elongation of natural period) provides the so-called "decoupling" of the motion of the structure with that of the ground. This reduction in natural frequency has the undesirable consequence of increasing deformation demand under the input excitation. These undesirable deformations can be mitigated to some extent through the addition of damping, typically through a combination of velocity-dependent (termed viscous damping) and deformation-dependent (termed hysteretic damping) energy dissipation mechanisms. As a result, a properly designed isolation system will have the appropriate combination of stiffness and damping such that substantial dynamic decoupling is achieved without detrimental deformation demands in the isolation hardware.

Period elongation is not, however, the only necessary component to a seismic isolation system. Indeed, if adding flexibility were sufficient to reduce seismic response, then an effective design strategy would be to use the most flexible members possible given the consideration of stability under gravity. An equally important aspect of isolation is the change in fundamental mode shape. The introduction of a layer that is compliant relative to the supported structure introduces a key modification to the free vibration characteristics of the structure. The more similar the fundamental mode shape is to rigid-body behavior, the less mass participation is present in higher modes. Such rigid-body behavior is associated with the relative compliance of the isolation layer. Hence, as the natural period of the isolation system increases relative to the natural period of the supported structure, the participation of higher modes becomes closer to zero and the seismic deformation is concentrated at the isolation layer and not in the superstructure. A mathematically rigorous treatment of the dynamics of base isolated structures is presented in Chapter 7 of this report.

2.2 CURRENT STATUS OF SEISMIC ISOLATION

The concept of seismic isolation has been documented since the early 1900s, and its development surely extended prior to that. Naeim and Kelly [1999] recount the infancy of seismic isolation for civil construction, where the concept was simply to detach a structure at

its foundation, and provide some interstitial joint with a low-friction interface. This method of isolating a structure from the ground represents a simple, if not indelicate, way of reducing transmission of horizontal ground movement into the supported structure. Obviously, if some zero-friction interface is introduced (akin to the structure suspended in mid-air), any ground movement will excite zero movement of the structure relative to its original position. However, these methods of isolation have proved impractical, and more sophisticated methods of decoupling the motion of a structure and the ground was sought. Modern seismic isolation found its origins in the mid-1960s with the New Zealand Department of Scientific and Industrial Research [Skinner et al., 1993]. Many researchers contributed to the development of reliable devices to achieve the requisite flexible layer for successful isolation while retaining sufficient vertical stiffness to resist service loading. These isolation bearings exploited the beneficial properties of natural rubber to provide flexibility. A brief description of modern isolation devices can be found in Section 2.3 of this Chapter. Since the development of reliable seismic isolation hardware in the mid-1970s there has been significant adoption of isolation as a design strategy for seismic hazard mitigation.

Naeim and Kelly [1999] provide a detailed description of substantial isolation projects undertaken in various parts of the world. Higashino and Okamoto [2006] summarize the worldwide adoption of seismic isolation and describe the current state of the practice, including specific applications and regulatory environments, in the following countries: China, Italy, Japan, Korea, New Zealand, Taiwan, and the United States. They also include detailed design and construction information for many specific projects. Below is a brief summary of notable practical achievements in seismic isolation of buildings.

The first modern building to incorporate base isolation was the Pestalozzi School in Skopje, Macedonia, constructed in 1969. This project used rubber blocks in the basement to provide flexibility between the structure and foundation. The first building to be seismically isolated in the United States, and the first in the world to incorporate high-damping rubber bearings, was the Foothill Community Law and Justice Center in Rancho Cucamonga, California. The first rehabilitation of an existing structure with seismic isolation was in 1986 with the City and County Building in Salt Lake City, Utah. This project pioneered many construction methods of jacking and post-installation of bearings that are still used today. The existing United States Court of Appeals Building in San Francisco, California, was renovated in 1994, and was the first building (new or existing) to be isolated with friction

pendulum bearings. The first seismic isolated hospital in the world was the USC University Hospital in Los Angeles, California, constructed in 1991.

A number of isolated buildings have been subjected to strong ground motion in both the United States and Japan, and recorded data are available for many. In all post-earthquake observations and analysis of recorded data, the performance and behavior of isolated buildings has been consistent with expectations, and very little damage has been reported. For descriptions of observed behavior of isolated buildings in past earthquakes, see Clark et al. [1994], Nagarajaiah and Sun [2000], and Higashino et al. [2006].

2.2.1 Evolution of Code Provisions for Seismically Isolated Buildings

The first document describing prescriptive design requirements for seismic isolated buildings was published by the Structural Engineers Association of Northern California in 1986 [SEAONC, 1986]. This was informally referred to as the "Yellow Book," ostensibly to avoid confusion with the existing *Blue Book* that described lateral force requirements for conventional structures. This document was created in response to the design and construction of isolated buildings and bridges that had already taken place. A need was identified for some minimum standard to assure the safety of the general public who may occupy isolated facilities. These early provisions sought to provide a margin of safety comparable to that of conventional structures. To this effect, the 1986 Yellow Book states:

> *[These] limits on isolation system and superstructure response are intended to ensure that seismically isolated buildings will be at least as safe as conventional buildings during extreme events considering the uncertainties in the new and developing technology of seismic isolation.*

In these recommended provisions, a clear process for selecting and proportioning the isolation system and the supported structure is provided. This process mimics that for conventional structures in an effort to maintain consistence between the design methodologies. Several key distinctions for the design requirements were introduced, including the following:

1. The design base shear for the isolated superstructure is intended to limit ductility demand in the design basis earthquake relative to that expected for the conventional fixed-base structure in the same level of earthquake.

2. A review of the isolation concept and design is required, as established by the governing regulatory agency. Significantly, no prescriptive requirements for the scope of this review are established in recognition of the diverse nature of potential projects and the agencies charged with permit issuance.
3. Testing requirements for isolation devices are required as part of the plan approval process.

Since the publication of the 1986 Yellow Book, these requirements were included as an Appendix to the 1991 UBC. The isolation provisions remained as an Appendix through each edition of the UBC, although revisions were made alongside those for conventional structures. Subsequent to the final version of the UBC in 1997, provisions for isolated structures have been contained in the International Building Code, the current version of which [ICC, 2002] directly references provisions contained in ASCE 7 [ASCE, 2002]. A carefully detailed summary of the progression of code provisions through this development process is given by Aiken and Whittaker, summarized in Higashino and Okamoto [2006].

Shenton and Lin [1993] report a study on the relative performance of a 1991 UBC-conforming fixed-base and base isolated frames using response-history analysis. This research concluded that a base isolated concrete moment frame building could be designed to 25% to 50% of the base shear for a fixed-base building, and the two designs would perform comparably when based on superstructure ductility, roof displacement, and interstory drift. For shear wall buildings, the isolated building designed to the same fraction of the equivalent fixed-base building performed superior in all above categories. An interesting discussion is presented regarding the philosophical differences in code-based design of isolated buildings. The authors conclude that provisions requiring isolated buildings to be designed for lower ductility-based reduction factors inherently penalize the isolated superstructure and lead to unnecessarily high costs for the superstructure. A recommendation is put forth that future code provisions include optional performance requirements for conventional isolated buildings, where the design forces are reduced substantially compared to the fixed-base counterpart, while the expected performance is at least equivalent between the two. This is one of several discussions of the impediments to the implementation of seismic isolation in the context of the current code. Other discussions on impediments are provided in Naeim and Kelly [1999], Naaseh et al. [2001], and Mayes [2002].

2.3 CATEGORIES OF ISOLATION DEVICES

A critical ingredient of seismic isolation is the introduction of a specially designed stratum between the structure and the foundation that is both horizontally flexible and vertically stiff. A stratum with these properties is generally achieved through a series of manufactured isolation bearings, whose required performance is specified on a set of contract documents, and acceptance is verified through prototype (quality assurance) and production (quality control) testing.

Manufactured bearings primarily fall into two categories: elastomeric-based or sliding-based. Elastomeric-based bearings take advantage of the flexible properties of rubber to achieve isolation, while sliding-based bearings rely on the inherently low stiffness of a structure resting on its foundation with no connection other than friction at the interface.

Devices that are designed and manufactured to effectively achieve the goals of seismic isolation possess three general characteristics:

1. High axial stiffness to resist gravity and other vertical loads (both sustained and transient) without excessive deformation that would compromise the serviceability of a structure.
2. Sufficiently low horizontal stiffness such that the fundamental frequency of the isolated structure is substantially lower than the predominant frequency content of the expected ground motions, and adequate separation is provided between the natural frequency of the superstructure and that of the isolated structure.
3. An effective mechanism for energy dissipation [1] to mitigate excessive lateral deformations for practical reasons or to avoid instability of the isolation devices and connected structural elements due to combined horizontal and vertical forces.

Categories of devices currently manufactured to exhibit these characteristics are discussed in this section.

2.3.1 Elastomeric Bearings

A broad category of seismic isolation devices is elastomeric bearings. Such bearings rely on the flexible properties of natural and synthetic elastomeric compounds to achieve the desired characteristics of an isolation system. Elastomeric bearings can be divided into three sub-

[1] Energy dissipation is not a requisite property to achieve the advantages of seismic isolation; however, this quality is typically seen as favorable by designers.

categories: lead rubber (LR), high-damping rubber (HDR) and natural rubber (NR). Any elastomeric isolation bearing is constructed of alternating layers of rubber pads and steel shims, bonded together with a robust, non-degrading adhesive. The steel shims prevent the rubber pads from excessive bulging at their perimeter, and hence enhance the vertical stiffness of the device. The layers of rubber pads in natural rubber bearings are compounded with an unfilled rubber that exhibits very little inherent damping. In contrast, the rubber layers in high-damping rubber bearings are specially compounded with a blend of synthetic elastomers and fillers, such as carbon black, which enhances the internal energy dissipation capability of the rubber matrix. Lead rubber bearings generally consist of natural rubber bearings with a lead core press-fit into the central mandrel hole. This mandrel hole is required of any elastomeric bearing type since the vulcanization process requires heating from both the center and the exterior surface of the bearings. Sections showing natural and high-damping rubber bearings are shown below in Figure 2.1(a) and a lead-rubber bearing is shown in Figure 2.1(b). A detailed treatment of the mechanical characteristics of elastomeric isolation bearings is provided by Kelly [1996].

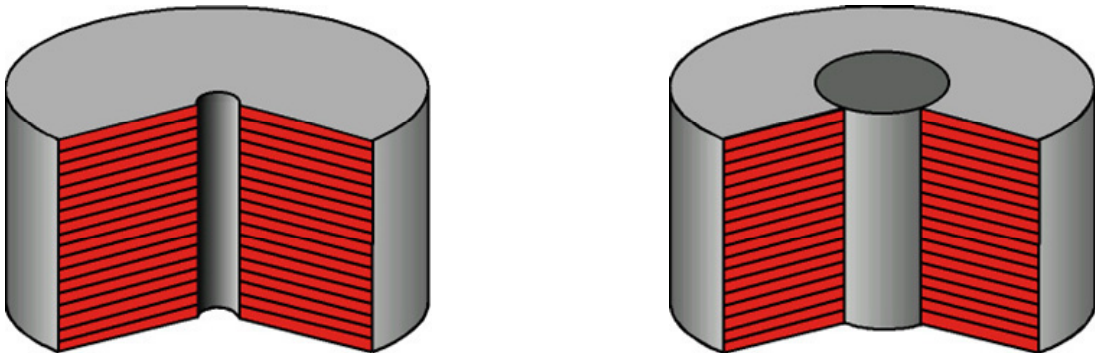

(a) NR/HDR (b) LR

Figure 2.1: Sections depicting two common types of elastomeric bearings (a) natural rubber (NR) bearing or high-damping rubber (HDR) bearings and (b) lead rubber (LR) bearing

2.3.2 Sliding Bearings

Another class of isolation devices is the "sliding bearing," in which the action of sliding is the basis for achieving low horizontal stiffness. Energy dissipation is achieved at the sliding interface through Coulomb (or friction) damping. One such isolation device is the friction

pendulum (FP) bearing, shown below schematically in section in Figure 2.2. In this type of bearing, an articulating slider rests on a spherical stainless steel surface. The lateral restoring force arises from the spherical shape of the sliding surface. Where the lateral displacement is small relative to the radius of curvature of the surface, the force-displacement relationship is linear and defined completely by the spherical radius. A detailed treatment of this and similar classes of sliding isolation bearings is given in Chapter 3 of this report.

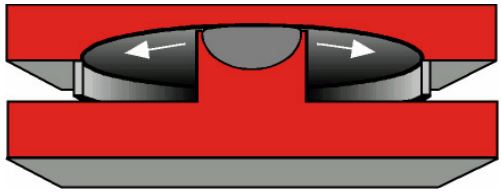

Figure 2.2: Section depicting a single concave friction pendulum (FP) bearing

2.4 SUPPLEMENTAL DAMPERS TO CONTROL ISOLATOR DEFORMATION

Although typical isolation hardware is manufactured with an inherent energy dissipation mechanism to control peak isolation system displacement, specific applications exist where supplementary energy dissipation mechanisms are required. Such applications include: sites located in close proximity to a controlling seismic source, sites underlain by soft and/or weak soil strata, isolation devices that are susceptible to instability under large lateral deformation, architectural considerations that limit the allowable seismic separation (isolation moat), and practical limits on the ability of flexible utility lines to accommodate displacement across the isolation interface.

Figure 2.3: Supplemental viscous damper at isolation plane to control displacement (New de Young Museum, San Francisco, CA, courtesy of Rutherford & Chekene)

2.5 PREVIOUS RESEARCH ON SEISMIC ISOLATION

2.5.1 Elastomeric Isolation Systems

The pioneering work in modern seismic isolation was undertaken at the New Zealand Department of Scientific and Industrial Research, and this work is reported in Skinner, Kelly, and Heine [1975] and Skinner, Beck, and Bycroft [1975]. The focus of this research was the development of reliable mechanical devices for seismic isolation and energy dissipation with applications to civil structures. Energy dissipation devices studied were metallic yielding elements in either flexure or torsion. The need to develop substantial movement to obtain damping from these devices motivated the study of isolation systems. Here, isolation was identified as a reliable method to protect against both structural and nonstructural damage. Not only did this research present a theoretical framework for seismic isolation systems, but an in-depth discussion is included on a variety of practical implementation topics.

The mechanical behavior of laminated elastomeric bearings typical of modern practice is described by Kelly [1996]. This behavior includes force deformation in shear, axial compression, and bending; instability of bearings; and methods of design to achieve target properties. Clark et al. [1997] summarized a series of earthquake simulator tests on a three-story isolated model subjected to severe seismic excitation. These tests identified the behavior of high-damping elastomeric bearings under large cyclic deformation and provided important limit states for both the bearings and the supported structure.

2.5.2 Sliding Isolation Systems

Among the earliest contributions to sliding isolation systems is the seminal work on steady-state harmonic forced vibration of a linear oscillator with Coulomb friction damping, an exact solution to which is due to Den Hartog [1947]. The result of this solution is a response spectrum for harmonic input that demonstrates the benefit of reduced transmissibility resulting from a reduction in natural frequency below that of the excitation, even with the presence of dry friction as a damping mechanism.

Early studies of multi-story buildings isolated with systems incorporating sliding elements are reported by Kelly and Beucke [1983] and Constantinou and Tadjbakhsh [1984]. In this work, the effect of friction on an otherwise linear isolation system is investigated, and found to mitigate large isolation system displacements while retaining the benefits of decoupling due to the linear elastomeric bearings.

The first analytical and experimental studies on friction pendulum (FP) isolation bearings was conducted by Zayas et al. [1987]. This research program identified the potential to achieve reliable base isolation through the introduction of a spherical sliding surface, thereby simulating pendulum behavior. Substantial experimental characterization of FP bearings and development of nonlinear analytical models was reported by Zayas et al. [1989], Mokha et al. [1990, 1991, 1993], Nagarajaiah et al. [1992], and Constantinou et al. [1993]. Almazán and De la Llera [1998, 2002] summarized bidirectional modeling considering first- and second-order displacement and velocity effects in computing the deformation response and base shear of structures isolated on FP bearings. Experimental characterizations of FP under multi-component excitation and validation of nonlinear models to describe such behavior was reported by Anderson [2003] and Mosqueda et al. [2004]. Roussis and Constantinou [2006] conducted analytical and experimental investigations on the behavior of FP bearings with the ability to resist tensile forces.

Recently, multi-stage friction pendulum bearings have been introduced and applied on projects worldwide. Tsai et al. [2008] proposed a multiple friction pendulum system (MFPS) consisting of multiple sliding interfaces and an articulating slider. Such bearings exhibit large displacement capacity relative to bearings consisting of only a single spherical surface. Fenz and Constantinou [2006] presented further work on friction pendulum (FP) bearings with two spherical surfaces and distinct friction coefficients on each sliding interface,

leading to sliding behavior that exhibits multi-stage hysteretic response. The analytical behavior of triple pendulum (TP) bearings, including suitable cyclic models with experimental verification, has been reported by Fenz and Constantinou [2008a,b] and Becker and Mahin [2010]. These types of bearings are described further in Chapter 3 of this report.

2.5.3 Behavior of Secondary Systems

It has long been recognized that damage to secondary systems (elements not part of the primary structure) is a major source of earthquake-induced losses. Secondary systems include both a) nonstructural components, such as interior partitions, cladding, glazing, piping, and ceilings; and b) contents, such as mechanical and electrical equipment, stored inventory, cabinetry, and assorted freestanding objects. Many studies have been conducted summarizing the overall potential for damage to both nonstructural components and contents, and the effect of base isolation on the mitigation of damage to these. Some of the relevant research in these areas is summarized in this section.

2.5.3.1 Nonstructural Component and Content Damage

One of the earliest attempts to quantify damage to nonstructural components through experimental evaluation is summarized by Bouwkamp and Meehan [1960]. They describe a research program to investigate the behavior of glazing systems under in-plane shear demands. Subsequent to this research, many experimental programs have sought to quantify damage to nonstructural elements as a function of demand parameters that can be estimated by analysis.

An early study on the performance of secondary structural elements under seismic loading was conducted by Sakamoto [1978]. In this work, both interstory deformations and inertial forces due to absolute acceleration were identified as major contributors to nonstructural damage. A damageability index was introduced for assessment relative to some established criteria. Also, observed nonstructural damage was summarized for the following earthquakes: 1964 Niigata, 1968 Tokachi-oki, 1971 San Fernando, and 1972 Managua.

As part of the PEER research program, Filiatrault et al. [2002] summarized previous analytical and experimental investigations on the seismic response of nonstructural components, including building contents, service equipment, interior and exterior

architectural systems, and performance in past earthquakes. Taghavi and Miranda [2003] describe the development of a database for organization, storage, and retrieval of information related to seismic performance on nonstructural components and contents. This database is designed for simple implementation within a performance-based design framework, including item-specific cost functions describing losses or repair costs given a damage state.

2.5.3.2 Protection of Secondary Systems through Seismic Isolation

Significant initial research on secondary system response for isolated structures was conducted by Kelly and his collaborators. Early studies (Kelly [1981]; Kelly and Tsai [1985]) indicated that natural rubber isolation devices were expected to provide the best protection to equipment and contents, given the state of knowledge at that time. Earthquake simulator experiments on a five-story isolated model were conducted, and observed results were presented and substantiated by analytical studies. These studies identified the effect of the presence of lead and its effect on higher-mode response. Fan and Ahmadi [1990] reported extensive floor response spectra analysis for various base isolation systems and ground motions. The potential drawback of friction as an energy dissipation mechanism is identified with respect to the inducement of high-frequency floor acceleration response. Juhn et al. [1992] presented experimental results of a five-story building on a sliding isolation system and reported observed acceleration in the superstructure and the corresponding floor response spectra. Skinner et al. [1993] also summarized the effect of supplemental hysteretic damping on the excitation of higher-mode acceleration response in an isolated superstructure.

Hernried and Lei [1993] investigated the response of equipment in structures isolated with a hybrid friction-elastomeric bearing. These bearings, originally described by Mostaghel [1986], incorporate a central elastomeric core to provide restoring force, and a series of stacked PTFE plates to dissipate energy thorough friction. Conclusions drawn as part of this study include the relative reduction in equipment demands are greatest for strong ground shaking, and the lower friction coefficients lead to more substantial reductions in equipment response.

Dolce and Cardone [2003] conducted earthquake simulator tests on isolated building specimens to examine various isolation systems effect on damage to equipment and contents. Although the study focused on a newly developed shape-memory alloy isolation device, results from high-damping rubber and hysteretic systems were also investigated. Their results

indicate that not only do highly nonlinear isolation systems (such as those where damping is dominated by metallic yielding) excite high-frequency vibrations, but available analytical methods capture the frequency content of the acceleration response with fidelity.

Wolff and Constantinou [2004] summarized analytical and experimental investigations on the response of secondary systems in isolated structures. A six-story building model on both LR and FP bearings was tested on an earthquake simulator platform. It was concluded that increased energy dissipation through either hysteretic or nonlinear viscous damping results in decreased isolator displacement at the expense of increased primary and secondary system response. However, no definitive relationship was drawn between the nonlinearity of the isolation system and the amplitude of high-frequency floor spectral accelerations.

A study by Pavlou [2005] examined the sensitivity of nonstructural response parameters to the properties of isolated buildings. Two moment-frame buildings, each having distinct natural periods, were subjected to earthquake records having various source characteristics and soil types. The isolation systems considered were bilinear with a variation of characteristic strength and elastic period. The results of this research verified that all considered isolation systems showed favorable nonstructural response compared to the equivalent conventional structure. However, analyses were carried out with reported numerical instabilities that likely affect high-frequency acceleration response in the isolated structure. In addition, the effect of property modification factors for long-term changes in isolator properties were accounted for, as was the presence of vertical acceleration. These last two effects were concluded to be of minor consideration in the estimation of secondary system response.

3 Multi-stage Friction Pendulum Bearings

In this chapter, common types of friction pendulum (FP) bearings currently available in the United States are summarized, including mechanical characteristics, analytical models, and important considerations for design. Multi-stage FP bearings are defined as those characterized by more than one pendulum mechanism. Emphasis is placed herein on multi-stage FP bearings since there is scant documentation on these devices in the available literature, and investigations into their modeling and behavior serve as the basis for several of the studies contained in this report.

3.1 SINGLE-PENDULUM BEARINGS

The single concave friction pendulum bearing is the original Friction Pendulum System described by Zayas et al. [1987] and represents the first manufactured sliding-bearing to make use of the pendulum concept. This bearing consists of an articulated slider resting on a concave spherical surface. The slider is coated with a woven PTFE (polytetrafluoroethylene) composite liner, and the spherical surface is overlain by polished stainless steel. A picture showing an FP bearing and a cross-section is shown in Figure 3.1, indicating the above-described components.

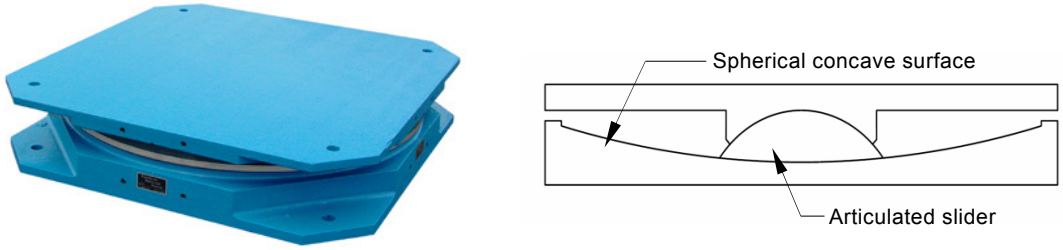

Figure 3.1: Photo (left) and section (right) of a typical FP bearing

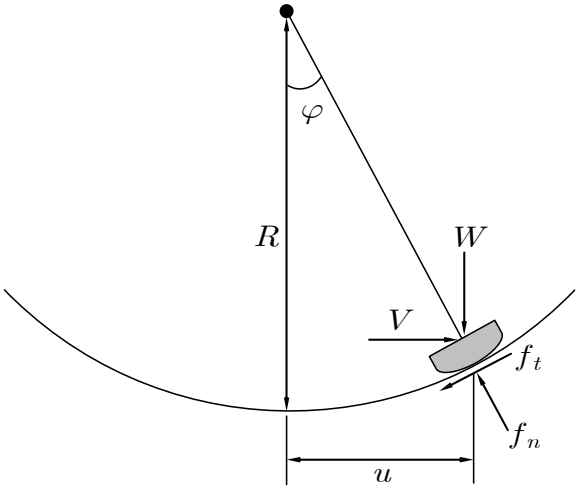

Figure 3.2: Idealized equilibrium of slider in displaced configuration

Although there is an abundance of published work on the cyclic behavior of FP bearings (e.g., Zayas et al. [1987], Constantinou et al. [1990], Alamzán et al. [1998], Mosqueda et al. [2004]), it is useful to recapitulate the essential aspects of their behavior since the modeling of multi-stage FP bearings is an extension of the single-concave case. To develop a mathematical model of the force-displacement relationship of an FP bearing, the geometry of the device must be fully understood. In the formulations that follow, only the horizontal degree of freedom is considered, and both vertical deformation and rotation are ignored. This is appropriate given the applications to isolated structures considered in this report include only horizontally flexible bearings between flexurally rigid elements, and the vertical stiffness of FP bearings is very high compared to the stiffness of elements to which the bearing is typically attached.

First, we can write the equilibrium equations of the bearing in its displaced condition (as seen above in Figure 3.2), summing forces along the horizontal and vertical axes, and obtaining

$$\begin{aligned} V - f_t \cos\varphi + f_n \sin\varphi = 0 \\ W + f_t \sin\varphi - f_n \cos\varphi = 0 \end{aligned} \tag{3.1}$$

Or, in matrix form, the mapping from local tractions to global external forces is through a simple linear coordinate transformation, shown below.

$$\begin{pmatrix} V \\ W \end{pmatrix} = \begin{bmatrix} \cos\varphi & \sin\varphi \\ -\sin\varphi & \cos\varphi \end{bmatrix} \begin{pmatrix} f_t \\ f_n \end{pmatrix} \tag{3.2}$$

From geometry, it is clear that $\sin\varphi = u / R$ and $\cos\varphi = \sqrt{R^2 - u^2} / R$, hence Equation (3.2) can be written as

$$\begin{pmatrix} V \\ W \end{pmatrix} = \frac{1}{R} \begin{bmatrix} \sqrt{R^2 - u^2} & u \\ -u & \sqrt{R^2 - u^2} \end{bmatrix} \begin{pmatrix} f_t \\ f_n \end{pmatrix} \tag{3.3}$$

Assuming the tangential traction f_t is related to the normal traction f_n through Coulomb friction by the equation $f_t = \mu f_n$ (where μ is the coefficient of friction), and defining a normalized shear force $\tilde{V} = V / W$, Equation (3.3) reduces to

$$\tilde{V} = \frac{\mu\sqrt{R^2 - u^2} + u}{\sqrt{R^2 - u^2} - \mu u} \tag{3.4}$$

Equation (3.4) returns a normalized shear force in the bearing given an imposed displacement *u*, and is nonlinear in *u*. While in some cases it may be important to consider the large displacement formulation of the normalized restoring force $\tilde{V}$, a common simplifying assumption here is useful. For virtually all FP bearings, the effective radius of curvature is much greater than the maximum expected displacement. The consequence of this assumption can be seen by expanding $g(u) = \sqrt{R^2 - u^2}$ in a Taylor series about the point *u* = 0. Carrying out this expansion yields the following series

$$\sqrt{R^2 - u^2} = R - \frac{1}{2} R \left(\frac{u}{R}\right)^2 - \frac{1}{8} R \left(\frac{u}{R}\right)^4 - \cdots \tag{3.5}$$

From this series, it is clear that for $R \gg u$, $\sqrt{R^2 - u^2} \approx R$. Substituting this approximation into Equation (3.4) and simplifying, the actual restoring force is

$$V = \mu W \operatorname{sgn}(\dot{u}) + \frac{W}{R} u \tag{3.6}$$

This is the well-known force-deformation relationship for a single-concave FP bearing at a particular sliding displacement and velocity u and $\dot{u}$, respectively. The function $\operatorname{sgn}(\cdot)$ is the *signum* function, and returns 1 (or -1) if the argument is positive (or negative). The inclusion of the *signum* function is necessary since the direction of the friction force always opposes that of the sliding velocity. A normalized force-deformation plot of a single-concave FP bearing under one complete cycle of loading, based on Equation (3.6) is shown below in Figure 3.3.

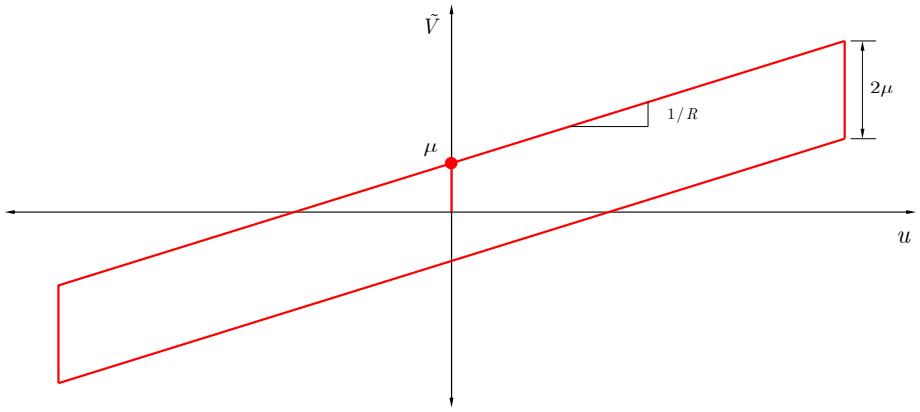

Figure 3.3: Idealized hysteresis loop of single-concave FP bearing based on Equation (3.6)

An implication of Equation (3.6) is that the frequency characteristics of a rigid structure isolated on FP bearings are independent of its mass. This can seen by writing the equation of motion for an undamped single-degree-of-freedom oscillator with an FP bearing as the restoring force (where m is the supported mass, hence $W = mg$). Neglecting friction, the natural frequency is seen as

$$m\ddot{u} + \frac{mg}{R} u = 0 \quad \Rightarrow \quad \omega_n = \sqrt{\frac{g}{R}} \tag{3.7}$$

The above derivations of the force-displacement behavior of the FP bearing will form the basis for extension to multi-stage FP bearings, discussed below.

3.2 DOUBLE PENDULUM BEARINGS

Recent developments in the design and manufacturing of FP bearings have centered on the use of multiple pendulum mechanisms. Whereas the single-concave FP bearing has two key parameters that characterize cyclic behavior (R and μ), a multi-stage FP bearing has greater design flexibility because the pendulum length and friction coefficient are specific for each independent pendulum mechanism. In the case of a double-concave FP bearing, shown below in Figure 3., the parameters characterizing the cyclic behavior are (R_1, $\mu 1$) for one concave sliding interface, (R_2, $\mu 2$) for the other, and (h_1, h_2) for the kinematic relation between the position of the two sliding surfaces. The behavior of the double pendulum (DP) bearing has been described by Fenz and Constantinou [2006].

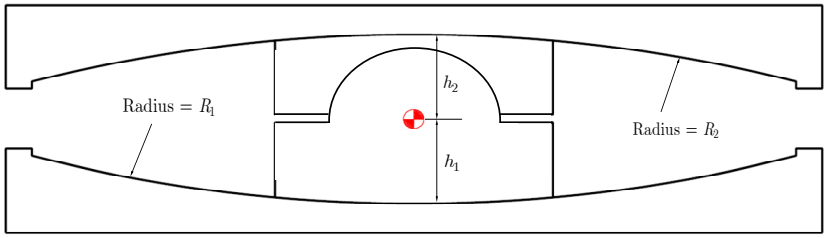

Figure 3.4: Section through a typical DP bearing

Since each sliding surface must resist the same force, the hysteretic model for the bearing can be derived by considering single-pendulum bearings in *series*. To develop this relationship, a general model of n single-pendulum bearings in series is first considered, then specialized to the double-concave case. From Equation (3.6) let

$$V_i = \mu_i W \operatorname{sgn}(\dot{u}_i) + \frac{W}{L_i} u_i \quad , \quad i = 1, \ldots, n \tag{3.8}$$

represent the shear force in the i^{th} FP element in a series system of n FP elements. In this equation, the *effective pendulum length* L_i is defined as $L_i = R_i - h_i$, as the slider height reduces the radius along which the restoring force acts. Regardless of the configuration, each of the n FP elements resists the same vertical force W, and therefore the subscript is omitted. Here, we reintroduce the normalized shear $\tilde{V}_i = V_i / W$ to simplify notation and non-

dimensionalize the equilibrium equations. Substituting this normalization into Equation (3.8) and writing the system of uncoupled equilibrium equations in matrix form, we obtain

$$\begin{pmatrix} \tilde{V}_1 \\ \vdots \\ \tilde{V}_n \end{pmatrix} = \begin{bmatrix} \mu_1 \operatorname{sgn}(\dot{u}_1) & & 0 \\ & \ddots & \\ 0 & & \mu_n \operatorname{sgn}(\dot{u}_n) \end{bmatrix} + \begin{bmatrix} L_1 & & 0 \\ & \ddots & \\ 0 & & L_n \end{bmatrix}^{-1} \begin{pmatrix} u_1 \\ \vdots \\ u_n \end{pmatrix} \tag{3.9}$$

or in compact notation

$$\tilde{\mathbf{V}} = \mathbf{M} \operatorname{sgn}(\dot{\mathbf{u}}) + \mathbf{L}^{-1}\mathbf{u} \tag{3.10}$$

Equation (3.10) can be rearranged to solve for the displacement in each bearing in the series

$$\mathbf{u} = \mathbf{L}\left[\tilde{\mathbf{V}} - \mathbf{M} \operatorname{sgn}(\dot{\mathbf{u}})\right] \tag{3.11}$$

Implicit in the above relationship is that each of the n FP elements is sliding, or that $\tilde{V}_k - \mu_k \geq 0$ for all k. Indeed, this may not be the case, so a slight modification is necessary. If we define the Heaviside operator as

$$H(x) = \begin{cases} x & x \geq 0 \\ 0 & x < 0 \end{cases} \tag{3.12}$$

and assume no reversal of displacement, then Equation (3.11) may be more generally written as

$$\mathbf{u} = \mathbf{L}H\left[\tilde{\mathbf{V}} - \mathbf{M}\mathbf{1}_{n\times 1}\right] \tag{3.13}$$

where $\mathbf{1}_{n\times 1}$ is an n-dimensional vector of ones. The desired result, however, is a scalar displacement in the bearing in terms of a scalar force, since the internal mechanics of the multi-stage bearing are insignificant in determining global system response. Let V_b be the force in the bearing, and u_b the displacement. Since the bearing is a series system, each $V_k = V_b$ for all k, and $u_b = \Sigma_{i=1}^{n} u_i$. Extending the matrix notation defined above and rearranging slightly, the bearing displacement is

$$u_b = \mathbf{1}_{n\times 1}^{T}\, \mathbf{L}H\left(\tilde{V}_b \mathbf{I}_{n\times n} - \mathbf{M}\right)\mathbf{1}_{n\times 1} \tag{3.14}$$

Applying Equation (3.14), a bearing shear can be mapped to a bearing displacement knowing the effective length matrix **L** and the friction matrix **M** of the n-component multi-stage FP

bearing. Recall that **L** is simply a function of the concave radii and slider heights, and therefore the entries are geometric quantities.

If we consider the DP bearing, and assume sliding occurs on both surfaces (i.e., $\tilde{V}_b - \mu_k \geq 0$, $k = 1, 2$) Equation (3.14) becomes

$$u_b = \mathbf{1}_{2\times1}^T \mathbf{L}\left(\tilde{V}_b \mathbf{I}_{2\times2} - \mathbf{M}\right)\mathbf{1}_{2\times1} \tag{3.15}$$

$$u_b = \begin{pmatrix} 1 & 1 \end{pmatrix}\begin{bmatrix} L_1 & 0 \\ 0 & L_2 \end{bmatrix}\begin{bmatrix} \tilde{V}_b - \mu_1 & 0 \\ 0 & \tilde{V}_b - \mu_2 \end{bmatrix}\begin{pmatrix} 1 \\ 1 \end{pmatrix} \tag{3.16}$$

$$u_b = \tilde{V}_b\left(L_1 + L_2\right) - L_1\mu_1 - L_2\mu_2 \tag{3.17}$$

Rearranging to express the force in terms of the displacement, replacing the normalized shear with the actual shear, and substituting $L_i = R_i - h_i$, Equation (3.17) becomes

$$V_b = \left(\frac{W}{R_1 + R_2 - h_1 - h_2}\right)u_b + \frac{W\mu_1\left(R_1 - h_1\right) + W\mu_2\left(R_2 - h_2\right)}{R_1 + R_2 - h_1 - h_2} \tag{3.18}$$

This expression for the force-displacement relationship for the entire bearing is identical to that developed for the DP bearing by Fenz and Constantinou [2006]. A force-displacement relationship for a DP bearing under one complete cycle of loading is shown below in Figure 3.5.

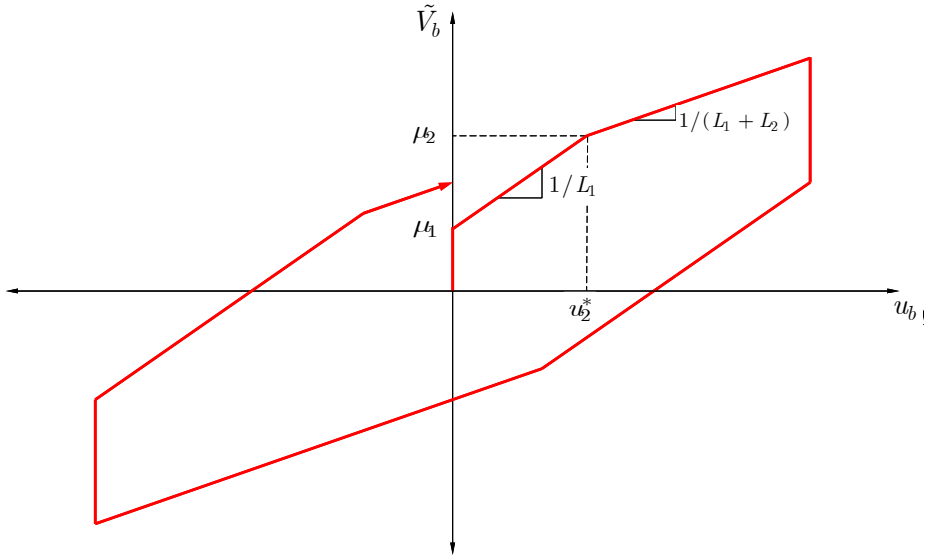

Figure 3.5: Idealized hysteresis loop of DP bearing based on Equation (2.18)

In the above hysteresis plot, the transition displacement at which sliding on both surfaces occurs, u_2^*, can be determined by dividing the difference between μ_2 and μ_1 by the slope. Doing so, and substituting for L_1, yields

$$u_2^* = \Delta\tilde{V}\, L_1 = \left(\mu_2 - \mu_1\right)\left(R_1 - h_1\right) \tag{3.19}$$

The key improvements of the DP bearing over the FP bearing are as follows:

1. The lateral deformation is divided between the top and bottom concave surfaces; consequently the required plan diameter of each concave dish is significantly less than the equivalent single-concave FP bearing.
2. Equilibrium in the displaced condition shows that the internal moments are distributed to the top and bottom plates in proportion to their displacement from the centerline of the undeformed condition.
3. The radii and friction coefficients of the two pendulum mechanisms may be independently selected to achieve a particular tri-linear force-displacement relationship.
4. By making the radii and friction coefficients the same (that is, $R_1 = R_2 = R$, $\mu_1 = \mu_2 = \mu$), a bilinear relation such as that shown in Figure 3.3 can be achieved, in which the effective friction and radii are represented by $\mu^* = \mu$ and $R^* = 2R - h_1 - h_2$.

3.3 TRIPLE PENDULUM BEARINGS

The triple pendulum bearing introduced by EPS, Inc., consists of four concave surfaces and three independent pendulum mechanisms. The outer slider consists of concave surfaces on either side of a cylindrical inner slider with a low-friction interface on both ends. This forms one pendulum mechanism, and defines the properties of the isolation system under low levels of excitation. The outer slider also consists of sliding interfaces between top and bottom outer sliders and the major spherical surfaces of the bearing. The bottom sliding surface is in contact with a spherical surface of a particular radius of curvature, forming the second pendulum mechanism. This mechanism defines the primary properties of the isolation system under moderate levels of excitation. The upper sliding surface is in contact with another spherical surface of a particular radius of curvature, forming the third pendulum mechanism. The friction coefficient of this third sliding interface is sufficiently large to prevent sliding until an extreme level of excitation occurs. The mode of behavior described represents one likely to be selected by a designer; however, other types of behavior could be achieved through variation of the frictional characteristics. The properties of these three pendulum mechanisms may be selected to optimize the performance of the seismic isolated structure considering multiple levels of seismic hazard. A section through the TP bearing is shown below in Figure 3.6. An identification of all components of the TP bearing is shown in Figure 3.7, including geometric parameters and friction coefficients. For derivations involving the radius of curvature, it will be assumed that this is the *effective* pendulum length, which is the nominal radius minus the slider height. That is, the following relationships will be assumed:

$$L_1 = R_1 - h_1 \, , \, L_2 = R_2 - h_2 \, , \, L_3 = R_3 - h_3 \tag{3.20}$$

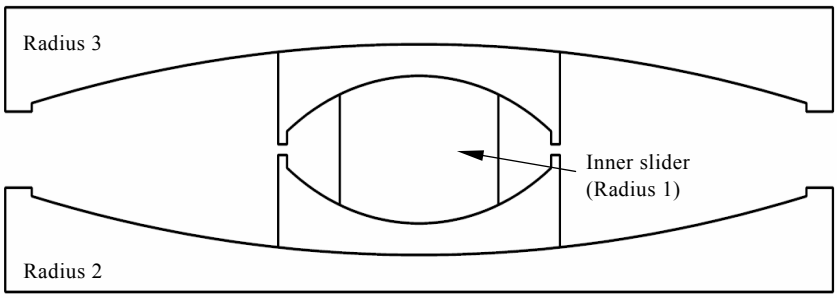

Figure 3.6: Section through a typical TP bearing

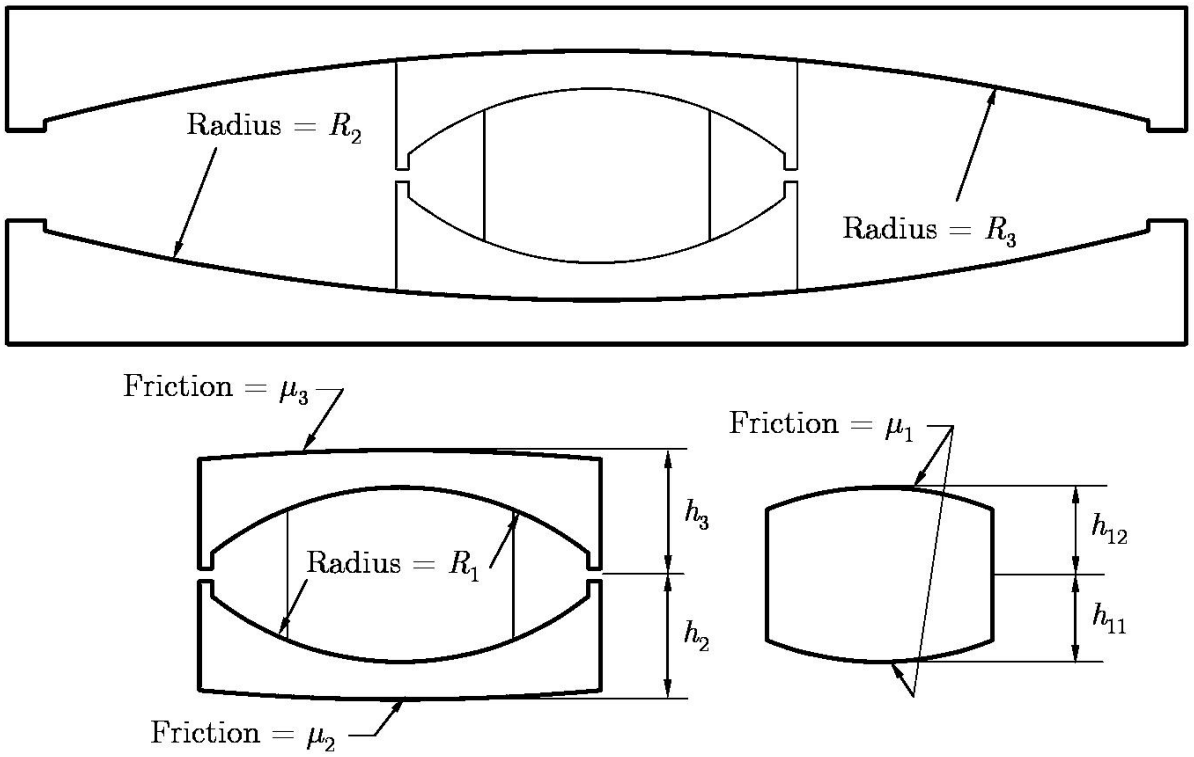

Figure 3.7: Parameters characterizing each component of the TP bearing

A schematic description of each sliding mechanism as the TP bearing is subjected to increasing displacement demand in shown below in Figure 3.8. In this figure, the friction coefficient on the lower major spherical surface is less than the friction coefficient on the upper major spherical surface. A photograph of a full-scale TP bearing depicting all sliding components is shown in Figure 3..

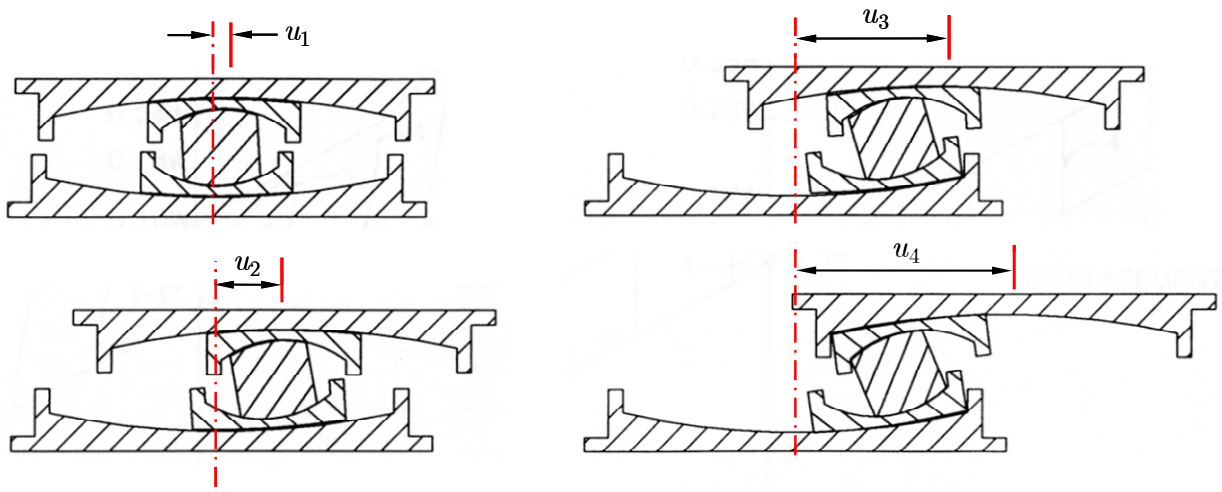

Figure 3.8: Schematic description of sliding mechanisms for TP bearing, where $u_1 < u_2 < u_3 < u_4$ (adapted from figure courtesy of EPS, Inc.)

Figure 3.9: Photograph showing components of full-scale TP bearing (courtesy of EPS, Inc.)

Given the geometry and properties of the TP bearing, the force-displacement relationship for the element can be derived by taking equilibrium in the deformed configuration, similar to the DP case. However, the TP bearing cannot be treated simply as a series of three single-pendulum elements, as shown below. As a result, the general formulation developed for the DP bearing cannot be simply extended to the TP bearing. This would ignore the relative rotation of the inner slider relative to the outer concave surfaces. In the subsequent section, the displacement of the bearing given the applied external forces is derived for each stage of sliding.

3.3.1 Stages of Lateral Displacement

3.3.1.1 Deformation of Inner Slider

Consider a free-body diagram of the inner slider in the deformed condition indicated by Figure 3.. It is assumed that the top and bottom outer surfaces are restrained against rotation. This is a valid assumption if sliding is restricted to the inner slider only.

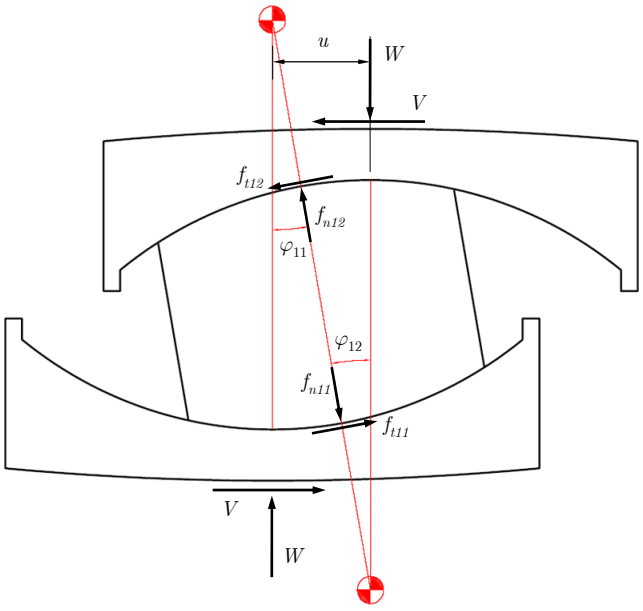

Figure 3.10: Free-body diagram of inner slider in deformed condition

In the deformed condition, equilibrium of the inner slider yields the coordinate transformation below

$$\begin{pmatrix} V \\ W \end{pmatrix} = \begin{bmatrix} \cos\varphi_{11} & \sin\varphi_{11} \\ -\sin\varphi_{11} & \cos\varphi_{11} \end{bmatrix} \begin{pmatrix} f_{t11} \\ f_{n11} \end{pmatrix} = \begin{bmatrix} \cos\varphi_{12} & \sin\varphi_{12} \\ -\sin\varphi_{12} & \cos\varphi_{12} \end{bmatrix} \begin{pmatrix} f_{t12} \\ f_{n12} \end{pmatrix} \tag{3.21}$$

Recognizing the coupling of the tangential and normal forces through friction, we let $f_{t11} = \mu_1 f_{n11}$ and $f_{t12} = \mu_1 f_{n12}$. Furthermore, the normalized shear force on the bearing is defined as $\tilde{V} = V / W$. Equation (3.21) becomes

$$\tilde{V} = \frac{\sin\varphi_{11} + \mu_1 \cos\varphi_{11}}{\cos\varphi_{11} - \mu_1 \sin\varphi_{11}} = \frac{\sin\varphi_{12} + \mu_1 \cos\varphi_{12}}{\cos\varphi_{12} - \mu_1 \sin\varphi_{12}} \tag{3.22}$$

Assuming small angles, or $\sin\varphi \approx \varphi$ and $\cos\varphi \approx 1$, and rearranging to solve for the unknown rotation angles φ_{11} and φ_{12}

$$\varphi_{11} = \varphi_{12} = \frac{\tilde{V} - \mu_1}{1 - \mu_1 \tilde{V}} \tag{3.23}$$

Generally, it can be assumed that $1 - \mu_1 \tilde{V} \approx 1$ because (a) the friction coefficient is a number typically less than 0.05; and (b) the normalized isolator shear is roughly equal to the pseudo-spectral acceleration demand (in units of *g*) which, for isolated structures, rarely exceeds 0.4. Therefore, it is expected that $\mu_1 \tilde{V} \leq 0.02$, and the rotations of the inner slider can be approximated as $\varphi_{11} = \varphi_{12} = \tilde{V} - \mu_1$. Recognizing that, from geometry, $u = L_1\varphi_{11} + L_1\varphi_{12}$, the total lateral displacement under this stage of loading can be described as

$$u = 2L_1\left(\tilde{V} - \mu_1\right), \quad \mu_1 \leq \tilde{V} < \mu_2 \tag{3.24}$$

3.3.1.2 Deformation of Inner Slider and Sliding on Lower Surface

The second stage of movement is that of the inner slider and bottom surface. This stage initiates when the normalized shear force exceeds the friction coefficient of the lower slider, that is, $\tilde{V} > \mu_2$. As before, we begin by solving the equilibrium equations on the deformed configuration, shown graphically in Figure 3. (bearing is shown separated for clarity).

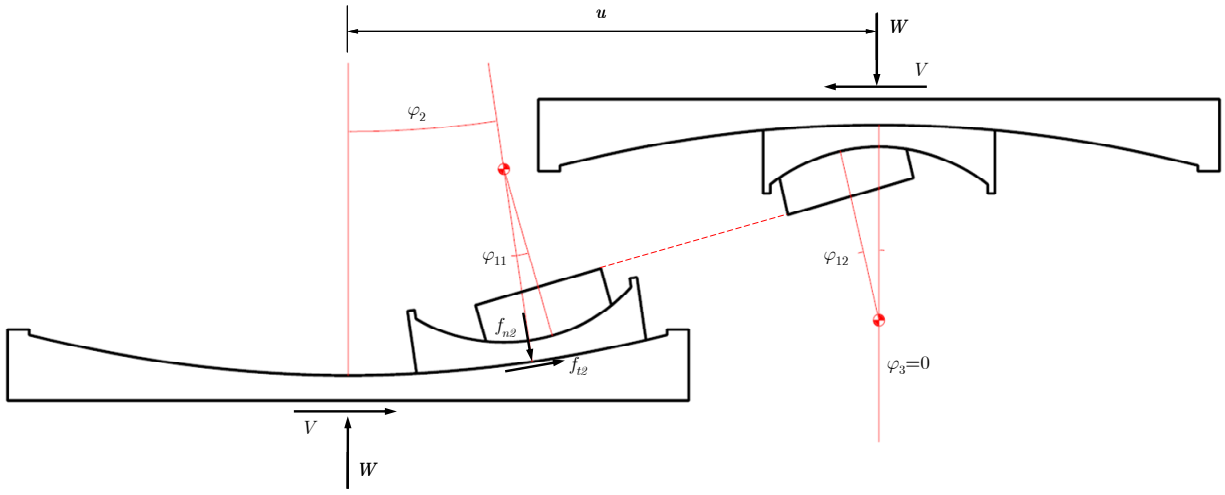

Figure 3.11: Free-body diagram of TP bearing in deformed condition when sliding occurs on the bottom dish but not the top dish

Similar to the derivation above for the inner slider, the basic coordinate transformation of the forces on the bottom slider is given by

$$\begin{pmatrix} V \\ W \end{pmatrix} = \begin{bmatrix} \cos\varphi_2 & \sin\varphi_2 \\ -\sin\varphi_2 & \cos\varphi_2 \end{bmatrix} \begin{pmatrix} f_{t2} \\ f_{n2} \end{pmatrix} \tag{3.25}$$

After performing the same operations as Equations (3.22) and (3.23), the rotation of the bottom slider can be expressed as

$$\varphi_2 = \tilde{V} - \mu_2 \tag{3.26}$$

Isolating a free-body diagram of the inner slider, whose rotation relative to a vertical datum is $\varphi_{12} = \varphi_{11} + \varphi_2$, yields the following expression of equilibrium:

$$\tilde{V} = \varphi_{11} + \varphi_2 + \mu_1 = \varphi_{12} + \mu_1 \tag{3.27}$$

And after substituting Equation (3.26) and rearranging terms, the following two expressions are obtained for the rotations of the inner slider relative to the lower and upper concave dishes, respectively:

$$\begin{aligned} \varphi_{11} &= \mu_2 - \mu_1 \\ \varphi_{12} &= \tilde{V} - \mu_1 \end{aligned} \tag{3.28}$$

An important consequence of these two expressions is that, where sliding is prevented on the upper concave surface (i.e., $\tilde{V} \le \mu_3$) but permitted on the bottom dish, the inner slider does

not rotate relative to the bottom dish, but *does* rotate relative to the vertical datum (and hence the top dish). The implications of this will become clear in the final derivation of the force-displacement relationship for the bearing.

From geometry, the lateral displacement u can be obtained from the slider rotations as $u = L_1\varphi_{11} + L_1\varphi_{12} + L_2\varphi_2$. After substituting Equations (3.26) and (3.28), the total bearing displacement can be expressed as

$$u = \underbrace{L_1\left(\mu_2 - \mu_1\right) + L_1\left(\tilde{V} - \mu_1\right)}_{u_1} + \underbrace{L_2\left(\tilde{V} - \mu_2\right)}_{u_2}, \quad \mu_2 \le \tilde{V} < \mu_3 \tag{3.29}$$

It should be noted that this expression differs slightly from that from the series-formulation presented from the FP-DC bearing. Specifically, from Equation (3.17) above, the displacement for a two-component series FP bearing would be

$$u = \underbrace{L_1\left(\tilde{V} - \mu_1\right)}_{u_1} + \underbrace{L_2\left(\tilde{V} - \mu_2\right)}_{u_2} \tag{3.30}$$

which is less than the displacement computed from Equation (3.29) by the quantity $L_1\left(\mu_2 - \mu_1\right)$. If the inner slider were designed to have a friction coefficient greater than the bottom dish ($\mu_1 \ge \mu_2$), the additional term would vanish and the bearing behave like a two-component series model. This indeed follows intuition, as for $\mu_1 \ge \mu_2$, the inner slider is essentially rigid, which is the case for the DP bearing.

3.3.1.3 Simultaneous Sliding on Lower and Upper Surfaces

The third stage of movement is that of all three pendulum mechanisms deforming simultaneously. This stage initiates when the normalized shear force exceeds the friction coefficient of the upper slider; that is, when $\tilde{V} > \mu_3$. This condition is shown graphically in Figure 3. below.

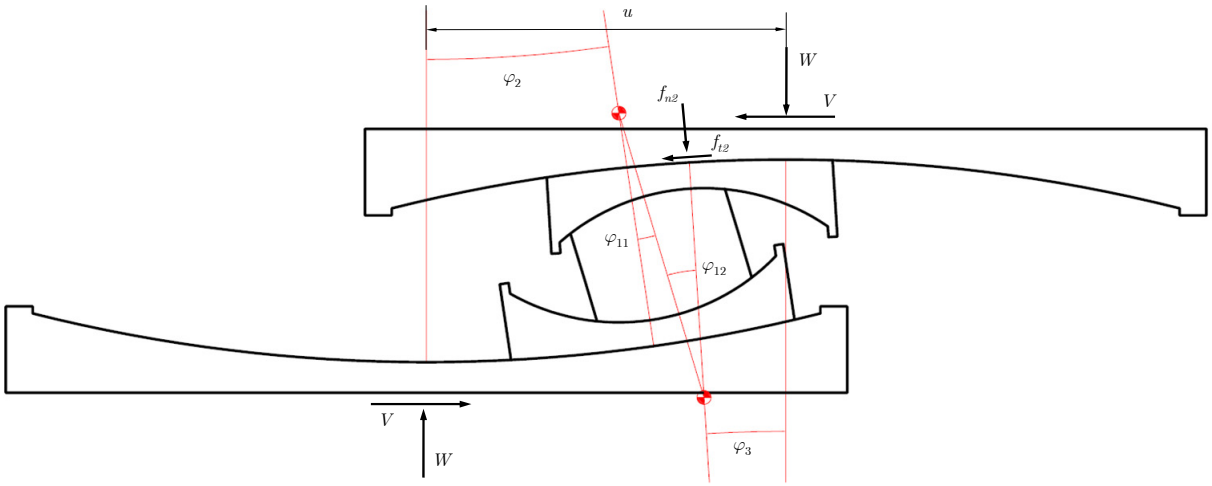

Figure 3.12: Free-body diagram of TP bearing in deformed condition when sliding occurs on all three pendulum mechanisms

Equilibrium of the deformed slider is found by the coordinate transformation

$$\begin{pmatrix} V \\ W \end{pmatrix} = \begin{bmatrix} \cos(\varphi_2 + \varphi_{11} - \varphi_{12}) & \sin(\varphi_2 + \varphi_{11} - \varphi_{12}) \\ -\sin(\varphi_2 + \varphi_{11} - \varphi_{12}) & \cos(\varphi_2 + \varphi_{11} - \varphi_{12}) \end{bmatrix} \begin{pmatrix} f_{t3} \\ f_{n3} \end{pmatrix} \tag{3.31}$$

This expression is sufficient to develop an expression for the bearing displacement, u, as a function of the normalized shear force, $\tilde{V}$. Using the same small angle approximation as before, and substituting the normalized shear, Equation (3.31) becomes

$$\varphi_2 + \varphi_{11} - \varphi_{12} = \tilde{V} - \mu_3 \tag{3.32}$$

Substituting (3.26) and (3.28a) above for the known rotation angles φ_{11} and φ_2, and solving gives

$$\varphi_{12} = \mu_3 - \mu_1 \tag{3.33}$$

In this stage of deformation, the rotation of the inner slider is now constant as neither φ_{11} nor φ_{12} depends on the applied forces. The constraint that there is no relative rotation of the top of the bearing relative to the bottom is defined by the following equality:

$$\varphi_2 + \varphi_{11} - \varphi_{12} - \varphi_3 = 0 \tag{3.34}$$

Substituting (3.32) into (3.33) yields

$$\varphi_3 = \tilde{V} - \mu_3 \tag{3.35}$$

With all slider rotations known, the familiar expression for bearing displacement, $u = L_1\varphi_{11} + L_1\varphi_{12} + L_2\varphi_2 + L_3\varphi_3$, gives a total displacement

$$u = \underbrace{L_1\left(\mu_2 + \mu_3 - 2\mu_1\right)}_{u_1} + \underbrace{L_2\left(\tilde{V} - \mu_2\right)}_{u_2} + \underbrace{L_3\left(\tilde{V} - \mu_3\right)}_{u_3}, \quad \tilde{V} \geq \mu_3 \tag{3.36}$$

where the contributions to the total displacement for each of the three pendulum mechanisms are denoted u_1, u_2, and u_3. Of interest in the above equation is by how much the displacement at a particular level of shear differs from the three-component series model derived above in Section 3.2. We let the difference in displacement be defined as $\Delta u = u_s - u_{tp}$ where u_s is the displacement of the series model as described by Equation (3.14) and u_{tp} is the displacement of the TP bearing described by Equation (3.36) above. Computing this difference gives

$$\begin{aligned}
\Delta u &= \left(\tilde{V} - \mu_1\right)2L_1 + \left(\tilde{V} - \mu_2\right)L_2 + \left(\tilde{V} - \mu_3\right)L_3 \\
&\quad - \left(\mu_2 + \mu_3 - 2\mu_1\right)L_1 + \left(\tilde{V} - \mu_2\right)L_2 + \left(\tilde{V} - \mu_3\right)L_3 \\
&= \left(\tilde{V} - \mu_2\right)L_1 + \left(\tilde{V} - \mu_3\right)L_1 \\
&= u_2\frac{L_1}{L_2} + u_3\frac{L_1}{L_3}
\end{aligned} \tag{3.37}$$

where u_2 and u_3 are the contributions to the total displacement from the second and third concave surfaces, respectively. Therefore, the pure series model yields a higher bearing displacement for a given shear force, and this difference is proportional to the overall bearing shear.

3.3.1.4 Deformation of Inner Slider and Sliding on Upper Surface

The sliding stage described in Section 3.3.1.3 continues until the bottom slider reaches its displacement capacity, defined as $\bar{u}_2$. This displacement is a function of the plan diameters of the bottom plate and the slider, and is therefore a geometric quantity. From geometry, the displacement capacity of the bottom concave surface is defined as

$$\bar{u}_2 = \frac{L_2}{R_2}\frac{\left(D_2 - d_2\right)}{2} \tag{3.38}$$

where D_2 is the plan diameter of the bottom concave surface and d_2 is the plan diameter of the inner slider. At the initiation of this sliding stage, the rotation of the bottom slider can be

expressed as $\varphi_2 = \bar{u}_2 / L_2$, and remains constant under increased deformation. The same reasoning leads to the conclusion that the rotation of the bottom inner slider does not change when the top surface does not slide also applies when the bottom surface does not slide, but instead is applicable to the top inner slider. As a result, any additional displacement must be due to rotation of the bottom of the inner slider, denoted above as φ_{l1}.

3.3.1.5 Deformation of Inner Slider Only (final stage)

The final sliding stage is when displacement capacity of the upper slider has been reached. This displacement is a function of the diameter of the top plate and the diameter of the top slider. From geometry, the displacement capacity of the top concave surface is defined as

$$\bar{u}_3 = \frac{L_3}{R_3}\frac{\left(D_3 - d_3\right)}{2} \tag{3.39}$$

where D_3 is the plan diameter of the top concave surface and d_3 is the plan diameter of the inner slider. At the initiation of this sliding stage, the rotation of the top slider, which can be expressed as $\varphi_3 = \bar{u}_3 / L_3$, may not increase. Any additional displacement must occur through deformation of the inner slider only. This sliding stage persists until the displacement capacity of the inner slider, $\bar{u}_1$, has been reached, at which point the bearing lateral deformation capacity has been reached, and behaves as laterally rigid under excess lateral demand. The displacement capacity of the inner slider is defined as

$$\bar{u}_1 = \frac{L_1}{R_1}\frac{\left(D_1 - d_1\right)}{2} \tag{3.40}$$

3.3.2 Construction of a Force-Displacement Relation

To develop a force-displacement relation, the key transition points must be accurately identified. These transition points are described above in Sections 3.3.1.1 through 3.3.1.5.

First, the displacement at which sliding initiates on the lower surface must be identified. This is done by substituting $\tilde{V} = \mu_2$ into Equation (3.29), and denoting this displacement u_2^*. This substitution yields

$$u_2^* = 2L_1\left(\mu_2 - \mu_1\right) \tag{3.41}$$

The displacement at which sliding initiates on the upper surface can also be identified in the same fashion, that is, substitute $\tilde{V} = \mu_3$ into Equation (3.25), thereby obtaining

$$u_3^* = L_1\left(\mu_2 + \mu_3 - 2\mu_1\right) + L_2\left(\mu_3 - \mu_2\right) \tag{3.42}$$

The displacement at which sliding ceases on the bottom surface is defined by its displacement capacity $\bar{u}_2$. By computing the additional displacement between u_3^* and the limiting displacement of the bottom surface, we determine

$$u_4^* = u_3^* + \left(\frac{\bar{u}_2}{L_2} + \mu_2 - \mu_3\right)\left(L_2 + L_3\right) \tag{3.43}$$

We also compute the lateral displacement at which both top and bottom surfaces have reached their displacement limits. The incremental displacement beyond u_4^* (described above) is due to rotation of the top of the inner slider and the top slider on the upper concave surface. Therefore, the transition displacement can be described as

$$u_5^* = u_4^* + \left(\frac{\bar{u}_3}{L_3} + \mu_3 - \frac{\bar{u}_2}{L_2} - \mu_2\right)\left(L_1 + L_3\right) \tag{3.44}$$

Finally, it is useful to derive the equivalent pendulum lengths for each stage of sliding. This is done by determining the slope of the force-displacement relation, and setting this to the reciprocal of some *effective* length. For each portion of the curve, the following is then used to solve for the effective pendulum radius:

$$L_{eff} = \frac{\Delta u}{\Delta \tilde{V}} \tag{3.45}$$

For initial movement, defined in Section 3.3.1.1 above, the effective radius is

$$L_{eff}^{I} = \frac{u_2^*}{\mu_2 - \mu_1} = \frac{2L_1\left(\mu_2 - \mu_1\right)}{\mu_2 - \mu_1} = 2L_1 \tag{3.46}$$

Similarly, the expressions for the effective radii for sliding stages II and III are:

$$\begin{aligned} L_{eff}^{II} &= \frac{u_3^* - u_2^*}{\mu_3 - \mu_2} = \frac{L_1\left(\mu_2 + \mu_3 - 2\mu_1\right) - L_2\left(\mu_3 - \mu_2\right) - 2L_1\left(\mu_2 - \mu_1\right)}{\mu_3 - \mu_2} \\ &= L_1 + L_2 \end{aligned} \tag{3.47}$$

$$
\begin{aligned}
L_{eff}^{III} &= \frac{u - u_3^*}{\tilde{V} - \mu_3} \\
&= \frac{L_1\left(\mu_2 + \mu_3 - 2\mu_1\right) + L_2\left(\tilde{V} - \mu_2\right) + L_3\left(\tilde{V} - \mu_3\right)}{\tilde{V} - \mu_3} \\
&\quad - \frac{L_1\left(\mu_2 + \mu_3 - 2\mu_1\right) - L_2\left(\mu_3 - \mu_2\right)}{\tilde{V} - \mu_3} \\
&= L_2 + L_3
\end{aligned}
\tag{3.48}
$$

The expressions for the effective pendulum length for sliding Stage IV can be directly computed from Equation (3.43) as

$$
\begin{aligned}
L_{eff}^{IV} &= \frac{u_5^* - u_4^*}{\frac{\overline{u}_3}{L_3} + \mu_3 - \frac{\overline{u}_2}{L_2} - \mu_2 - \mu_3} \\
&= L_1 + L_3
\end{aligned}
\tag{3.49}
$$

The effective pendulum length for sliding Stage V is the same as that for Stage I, or

$$
L_{eff}^{V} = L_{eff}^{I} = 2L_1 \tag{3.50}
$$

This is shown graphically on a force-displacement plot in Figure 3.3.

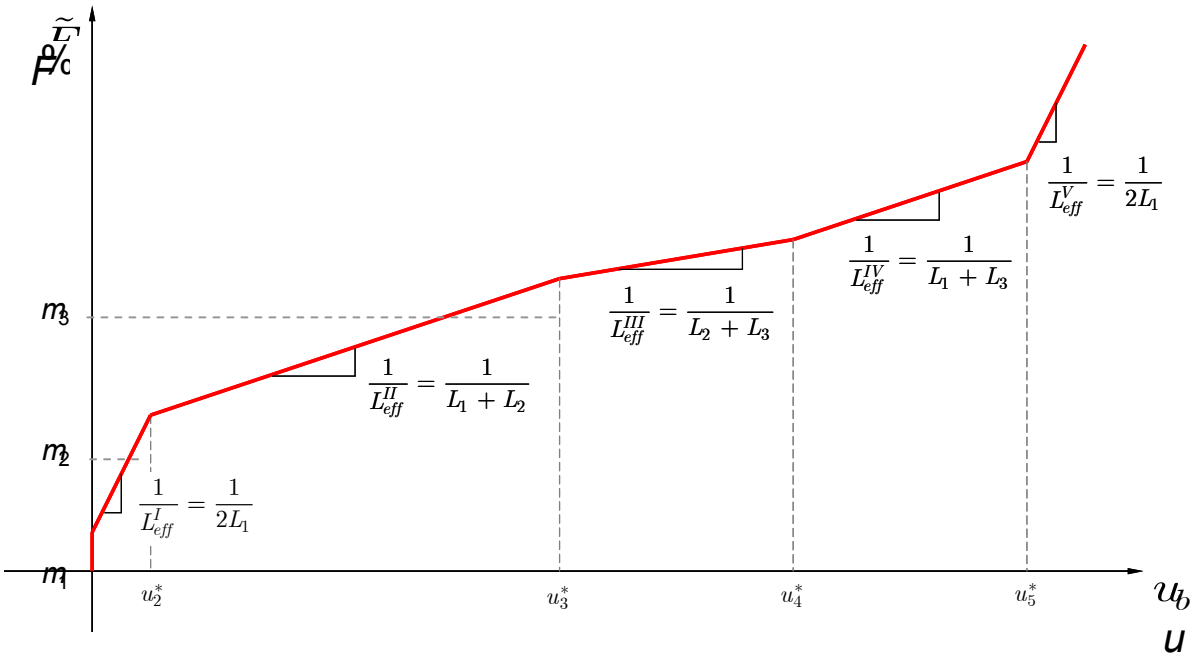

Figure 3.3: Idealized monotonic force-displacement relationship for TP bearing

Another way of interpreting the behavior of the TP bearing is to compare the individual displacements of each sliding component at a particular normalized shear force. This is effective because each element is subject to the same shear, and this shear yields a unique displacement in each sliding mechanism. The total displacement at a given shear is simply taken as the sum of the individual displacements. The normalized force-displacement relationships for each sliding mechanism are shown below in Figure 3.4.

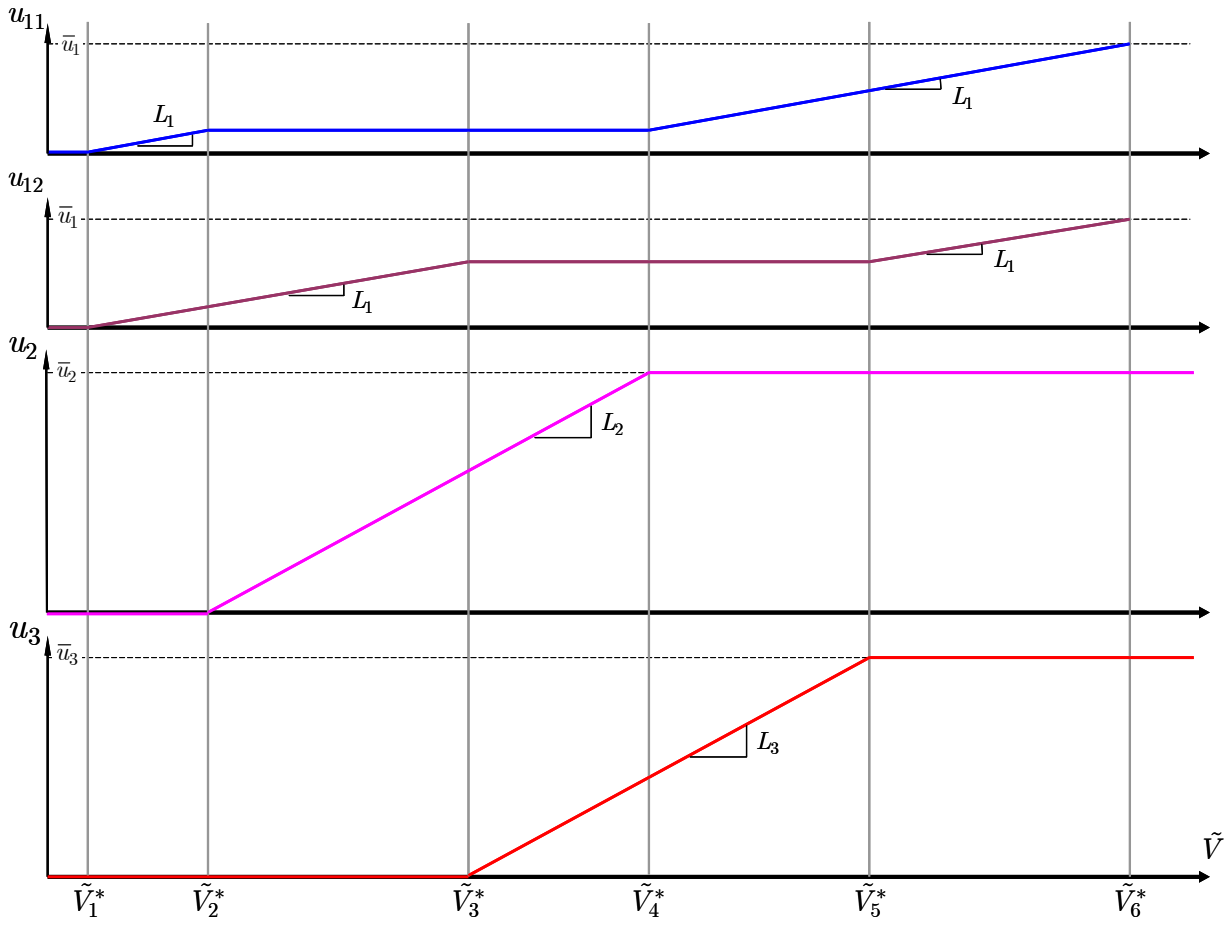

Figure 3.4: Normalized force-displacement relationship for each sliding mechanism of the TP bearing

The definition of each transition shear, denoted above in Figure 3.11 by a superscript asterisk, can be readily computed from the transition displacements described in Equations (3.40)–(3.43). These transition shears are defined as follows:

$$\begin{aligned} \tilde{V}_1^* &= \mu_1 & \tilde{V}_4^* &= \frac{\bar{u}_2}{L_2} + \mu_2 \\ \tilde{V}_2^* &= \mu_2 & \tilde{V}_5^* &= \frac{\bar{u}_3}{L_3} + \mu_3 \\ \tilde{V}_3^* &= \mu_3 & \tilde{V}_6^* &= \frac{\bar{u}_3}{L_3} + \frac{\bar{u}_1}{L_1} + \mu_1 \end{aligned} \tag{3.51}$$

3.3.3 The Suitability of Small-Deformation Theory

One question that may arise is whether a small angle approximation is appropriate for an inner slider with an effective radius that is small with respect to the lateral displacement. To

investigate this issue, a reasonable example is considered. Following the notation of the 1997 Uniform Building Code, suppose a site has a 1-sec spectral acceleration of C_v (in units of g) for a 72-year return period seismic event. A typical value of this C_v for a far-field site in the Los Angeles metropolitan area is approximately 0.4. If we are to restrict sliding to the inner slider for this level of earthquake, we can make a reasonable estimate of the expected lateral displacement. If we write the spectral displacement as

$$S_d = S_a \omega^{-2} = \frac{C_v g}{T} \frac{T^2}{4\pi^2} = \frac{C_v g}{4\pi^2} T \tag{3.52}$$

where T is the natural period of the building sliding only on the inner slider. Substituting $T = 2\pi\sqrt{2L_1 / g}$, and letting the isolator displacement equal the spectral displacement, equation (3.52) becomes

$$u = \left(\frac{C_v \sqrt{g}}{2\pi} \right) \sqrt{2L_1} \tag{3.53}$$

which gives the ratio of displacement to radius as

$$\frac{u}{2L_1} = \frac{C_v}{2\pi} \sqrt{\frac{g}{2L_1}} \tag{3.54}$$

Rewriting Equation (3.4) above assuming zero friction, and making use of the second-order Taylor expansion in Equation (3.5), the normalized restoring force for the inner slider is

$$\tilde{V} = \frac{u}{L_1}\left[1 + \varepsilon\right], \quad \varepsilon = \frac{1}{2}\left(\frac{u}{L_1} \right)^2 \tag{3.55}$$

where ε is the approximation error. By substituting Equation (3.53), the error can be written as

$$\varepsilon = \frac{C_v^2 g}{8\pi^2} \frac{1}{L_1} \tag{3.56}$$

Therefore, the error in the first-order approximation is proportional to the square of the spectral demand at the site, and inversely proportional to the effective radius of curvature of the dish (and hence the square root of the natural period). Figure 3.5 below shows the

magnitude of this error for various inner slider natural periods and 1-sec spectral accelerations (C_v).

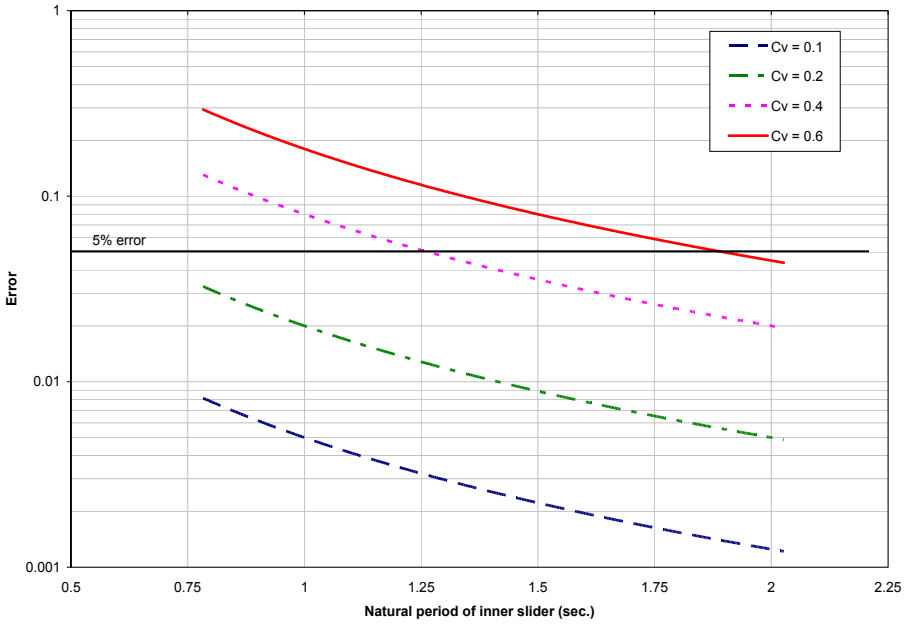

Figure 3.5: Variation of first-order approximation error for inner slider

3.3.4 Development of Cyclic Model

To extend the monotonic force-displacement model for the multi-stage FP bearing to generalized loading, it is important to recognize the path-dependent behavior of each component of the FP bearing. The cyclic behavior of each FP element is hysteretic because of the force reversals due to the friction force being proportional to the sign of the velocity. Therefore, given a generalized displacement signal, the analytical model must be able to follow the individual deformations of each FP element, recognizing that the force in each is equal to the external force, and the imposed displacement is the sum of the deformations of each FP element.

One major difficulty in developing a model for the multi-stage FP bearing that responds to displacement control is that, at a particular imposed displacement, there are n unknown element deformations (where n is the number of pendulum mechanisms). The condition that defines these individual deformations is the constraint that all element forces must be equal to each other. Because of this unique set of constraints, a force-based approach

must be taken to generate the global force output of the bearing at an imposed total displacement. This formulation is developed in this section.

3.3.4.1 Model Components

Here we consider an *n*-component FP bearing, which can be specialized to the two- or three-component bearing as necessary. In the case of the TP bearing, care must be taken in defining each pendulum mechanism since it is not strictly a series system, but can still be formulated as one with careful definition of each element.

Here we define U as the lateral displacement of the bearing, and P as the resultant shear at this displacement. These represent external deformations and forces, and correspond to those imposed by adjacent elements in a finite element analysis. Similarly, we define the vector $\mathbf{v} \in \mathbb{R}^n$ as the local lateral deformations of each of the *n*-pendulum mechanisms. The local shear forces are defined by the vector $\mathbf{s} \in \mathbb{R}^n$.

3.3.4.2 Equilibrium Conditions

The equations of equilibrium can be expressed by relating the internal element force vector $\mathbf{s}$ to the scalar external force P through the relation

$$\mathbf{s} = P \begin{pmatrix} 1 \\ \vdots \\ 1 \end{pmatrix}_{n\times 1} = \mathbf{B}P \tag{3.57}$$

This relation is a consequence of each element shear being identical to the external force. Because of this, the equilibrium map $\mathbf{B} : P \mapsto \mathbf{s}$ is simply an *n*-dimensional column of ones.

3.3.4.3 Compatibility Conditions

The compatibility equations may be obtained through the principle of virtual forces, also known as the *principle of complementary virtual work*. This principle expresses the compatibility between external (global) and internal (local) deformations for any arbitrary force field that is in equilibrium.

We let $\bar{P}$ and $\bar{\mathbf{s}}$ be a pair of virtual external and internal forces, respectively. These forces are assumed to be in equilibrium. We also let U and $\mathbf{v}$ be real external and internal deformations, respectively. The external work on this system is the virtual force $\bar{P}$ acting

through the real displacement U, and the internal work is the sum of each virtual force $\bar{s}_k$ acting through its corresponding real deformation v_k. Therefore, the complementary external work is expressed by $\bar{W}^*_{ext} = \bar{P}U$, and complementary internal work by $\bar{W}^*_{\text{int}} = \sum_k \bar{s}_k v_k = \bar{\mathbf{s}}^T \mathbf{v}$. Since these two expressions must be equal, we obtain

$$\bar{P}U = \bar{\mathbf{s}}^T \mathbf{v} \tag{3.58}$$

However, since $\bar{P}$ and $\bar{\mathbf{s}}$ are assumed to be in equilibrium, Equation (3.57) holds, giving the following

$$\bar{P}U = \left(\mathbf{B}\bar{P}\right)^T \mathbf{v} = \bar{P}\,\mathbf{B}^T \mathbf{v} \tag{3.59}$$

Or, rearranging to one side

$$\bar{P}\left(\mathbf{B}^T \mathbf{v} - U\right) = 0 \tag{3.60}$$

As Equation (3.60) must hold for any arbitrary virtual force $\bar{P} \in \mathbb{R}$, it must be true that

$$U = \mathbf{B}^T \mathbf{v} = \left(1 \cdots 1\right) \begin{pmatrix} v_1 \\ \vdots \\ v_n \end{pmatrix} \tag{3.61}$$

This establishes the well-known contragradience relationship between the equilibrium mapping (Eq. 3.57) and the compatibility mapping (Eq. 3.61). Therefore, the compatibility map $\mathbf{B}^T : \mathbf{v} \mapsto U$ is simply an n-dimensional row of ones. Expanding Equation (3.61) gives $U = \sum_k v_k$, or the external displacement is the sum of the local deformations. Indeed, this is true for any series system, and could have been stated outright; however, the application of virtual work is a more general method of developing equations of compatibility from imposed equilibrium.

3.3.4.4 Constitutive Relations

With the equilibrium and compatibility equations for the n-component FP element defined, a relationship between element forces and element deformations is necessary to formulate the behavior of the system. Here, we define the constitutive relation for each element as $v_k = f_k\left(s_k\right)$ where $f_k(\cdot)$ is the flexibility relation for the kth element, and may be generally nonlinear. In the formulation developed here, the flexibility relation is assumed to be bilinear

hysteretic. Given the parameters μ_k, L_k, and d_k, (friction coefficient, pendulum length, yield displacement) for the kth element, the bilinear model is described completely. This model is shown graphically below in Figure 3.6, including the path-dependent behavior under load reversal.

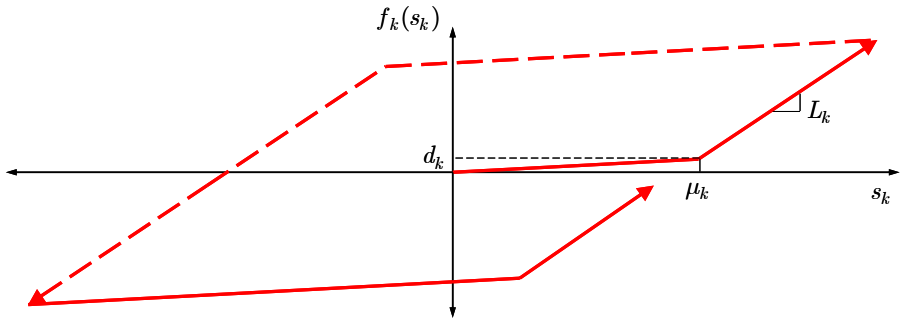

Figure 3.6: Idealized bilinear hysteretic flexibility relation, with parameters indicated (dashed lines indicate negative incremental change in force)

The yield displacement d_k may be taken either arbitrarily small, or may be estimated from experimental data. Based on the work of Constantinou, et al. [1999], it is assumed to be 0.01 inches or nearly rigid prior to slip. With the parameters of each element defined, the assembly of a model for the entire bearing may proceed.

3.3.4.5 Force-Based Hysteretic Model

The model being developed is designed to take a displacement input, and return a force output. This displacement input must be a displacement history because of the path-dependency of each element. This is a desirable form of a hysteretic model since the numerical integrations algorithms of finite element software are generally set up to predict a displacement at a particular time step, and iterate to find force equilibrium.

Let U_i be the imposed displacement at a load step i. This can be considered the ith entry in a vector of displacements as part of an input displacement signal. Given this displacement U_i, we assume an initial force field that is in equilibrium with an external force P_i^0 (the superscript indicates the $j = 0$ iteration). This is an initial guess of the external force resulting from U_i. Applying Equation (3.57), the initial guess of basic element forces is

$$\mathbf{s}_i^0 = \mathbf{B}P_i^0 \tag{3.62}$$

Applying the simple bilinear hysteretic constitutive model defined in Section 3.3.4.4, the element deformations are

$$\mathbf{v}_i^0 = \begin{pmatrix} f_1(s_i^0) \\ \vdots \\ f_n(s_i^0) \end{pmatrix} \tag{3.63}$$

Given this iteration of element deformations, the tangent flexibility is

$$F_T = \mathbf{B}^T \mathbf{f}\left(\mathbf{s}_i^0\right)\mathbf{B} \tag{3.64}$$

where $\mathbf{f}\left(\mathbf{s}_i^0\right)$ is a diagonal element flexibility matrix whose *k*th diagonal entry is $f_k\left(s_k\right)$. This tangent flexibility is used to iterate to a solution, as will be seen shortly. From the element deformations, the external displacement is computed using the compatibility relation of Equation (4.5), and is

$$U_i^0 = \mathbf{B}^T \mathbf{v}_i^0 \tag{3.65}$$

To assess the adequacy of this external displacement with respect to the imposed displacement, a residual displacement $U_r = U_i - U_i^0$ is defined. If this residual is not suitably close to zero, the imposed displacement is not compatible with the internal deformations, and a new trial external force must be assumed. This new trial force is $P_i^1 = P_i^0 + \Delta P$ where $\Delta P = F_T^{-1} U_r$. This method of iteration is the well-known Newton-Raphson procedure, and is commonly used to find solutions to a variety of nonlinear problems. This iteration continues, whereby

$$P_i^j \rightarrow \mathbf{s}_i^j \xrightarrow{f} \mathbf{v}_i^j \rightarrow U_i^j \tag{3.66}$$

then continues until $U_i^j \approx U_i$, at which point P_i^j is recorded as a converged external force, and the next global displacement U_{i+1} is imposed and the process repeats for all *U*. Sample hysteretic curves and element deformation histories resulting from two types of displacement input are shown below in Figure 3.7 and Figure 3.8.

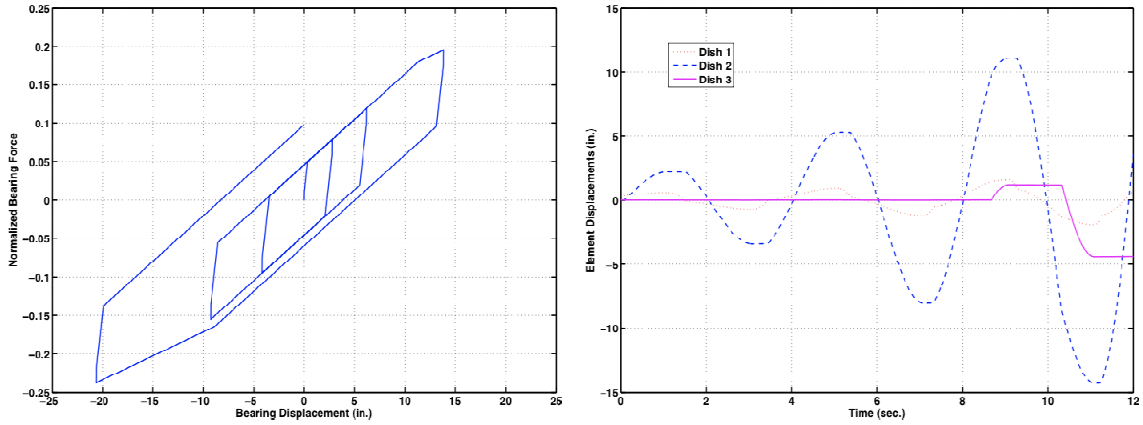

Figure 3.7: Model hysteresis (left) and individual slider deformation histories (right) for exponentially growing displacement input

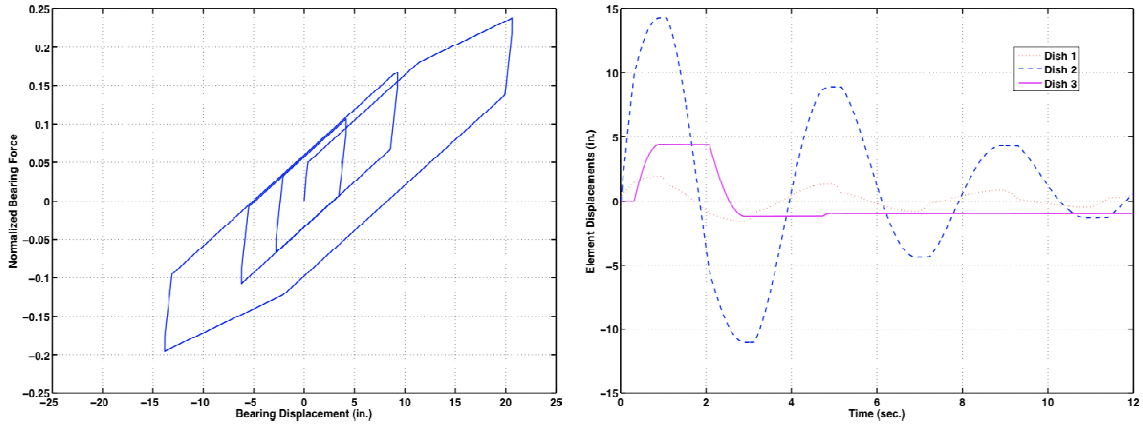

Figure 3.8: Model hysteresis (left) and individual slider deformation histories (right) for exponentially decaying displacement input

3.3.4.6 Selection of Cyclic Series Model Parameters

The cyclic series model (CSM) described above behaves under the assumption that, once sliding commences on a pendulum mechanism, deformation is linearly accumulated in that spring over the entire global displacement excursion. However, Section 3.3 above describes the behavior of each spherical surface, and it is clear that the inner slider does not accumulate displacement consistently, thereby violating the assumption of the series model. Despite this, it is possible to construct a CSM with parameters tuned to exhibit exactly the force-deformation characteristics described in Section 3.3. This formulation is particularly

attractive since each element is based on simple nonlinear elements, each of which can be implemented in widely used commercial analysis software packages.

Consider the available parameters for a particular element of the CSM. Each bilinear element is completely characterized by an initial stiffness (k_1), yield force (f_y), and a secondary stiffness (k_2). To model the deformation capacity of each dish, a gap and hook element may be implemented with gap (or hook) distance G (or H) and gap (or hook) stiffness k_G (or k_H). The objective is to select the value for each of these parameters, for each of the three elements in the series, given (a) the geometric properties of the bearing (dish radii, slider heights, and dish diameter); and (b) the three friction coefficients. For the remainder of this section, all parameters are assumed to be normalized with respect to the supported weight W.

We first consider the properties of each of the three bilinear elements. Since each element behaves nearly as a Coulomb friction element, the initial stiffness k_1 is large, and can be computed knowing a yield force and yield displacement. The yield force of the jth element is taken as the friction coefficient, or $f_{y,j} = \mu_j$, since this is the force level at which movement along the secondary slope occurs. From a previous discussion, the yield displacement of the frictional slider may be assumed to be $u_{y,j} = 0.01"$. The magnitude of this yield displacement, however, is not significant so long as it is arbitrarily small with respect to the displacement demand across the spring. Based on the yield displacement, the initial stiffness of the jth element is computed as $k_{1,j} = f_{y,j} / u_{y,j} = 100\mu_j$.

The second stiffness k_2 of each spring is based on the effective pendulum length, subject to a slight modification. Consider a displacement that induces Stage I sliding. Under this level of displacement, only Spring 1 accumulates deformation, since Springs 2 and 3 have yet to reach their respective yield forces. Hence, the second stiffness must be equal to the reciprocal of the effective pendulum length for Stage I, or $k_{2,1} = 1/2L_1$. Once the force across the series reaches $f_{y,2} = \mu_2$, sliding commences on both Spring 1 and Spring 2. The aggregate flexibility must equal that for Stage II sliding, or $L_1 + L_2$. Recalling that, for springs in series, the total flexibility is the sum of individual flexibilities, the flexibility of Spring 2 must be equal to $L_2 - L_1$. Therefore, we compute the second stiffness of Spring 2 as the reciprocal of the required flexibility, or $k_{2,2} = 1/(L_2 - L_1)$. Similarly, under Stage III

sliding, all three springs accumulate deformation, and the aggregate flexibility must be equal to $L_2 + L_3$. This implies a required flexibility of Spring 3 equal to $L_3 - L_1$, or $k_{2,3} = 1/(L_3 - L_1)$. Given the above computed secondary stiffness parameters, the total element stiffness matches exactly that derived for Stages I, II, and III in Section 3.3.

To properly characterize the stiffening of the TP bearing in Stages IV and V due to the displacement capacity of each dish, it is necessary to calibrate gap and hook elements for each of the three elements. As previously discussed, the major shortcoming of a series model versus the actual behavior of the TP bearing is the difference in accumulation of deformation on each sliding mechanism during lateral displacement. Whereas the physical displacement limits of each mechanism would typically define the gap dimension in the model, the CSM exhibits deformation accumulation across *all* pendulum mechanisms. In contrast, Figure 3.4 indicates a nonlinear flexibility of the inner slider over a linear increase in shear force. Therefore, at a particular normalized shear force $\tilde{v}$, the deformation of each pendulum mechanism in the CSM formulation generally varies from the true deformation. Therefore, a correction must be made to the gap sizes, G_1, G_2, and G_3, corresponding respectively to pendulum mechanisms 1, 2, and 3.

Figure 3.9 below is a convenient representation of the pendulum flexibility relationship over a monotonically increasing normalized shear force. This plot indicates the behavior of each pendulum in the actual TP bearing (shown dashed, based on Figure 3.4 above) and the CSM model. The corrected CSM model exhibits a sliding stage at a shear force equal to the actual TP bearing. Each transition shear is shown, as are the actual displacement limits of each pendulum, $\bar{u}_1, \bar{u}_2, \bar{u}_3$. In this figure, the second and third pendulums have the same displacement limit, but the derivations of corrected gap sizes that follow assume arbitrary and potentially distinct displacement limits.

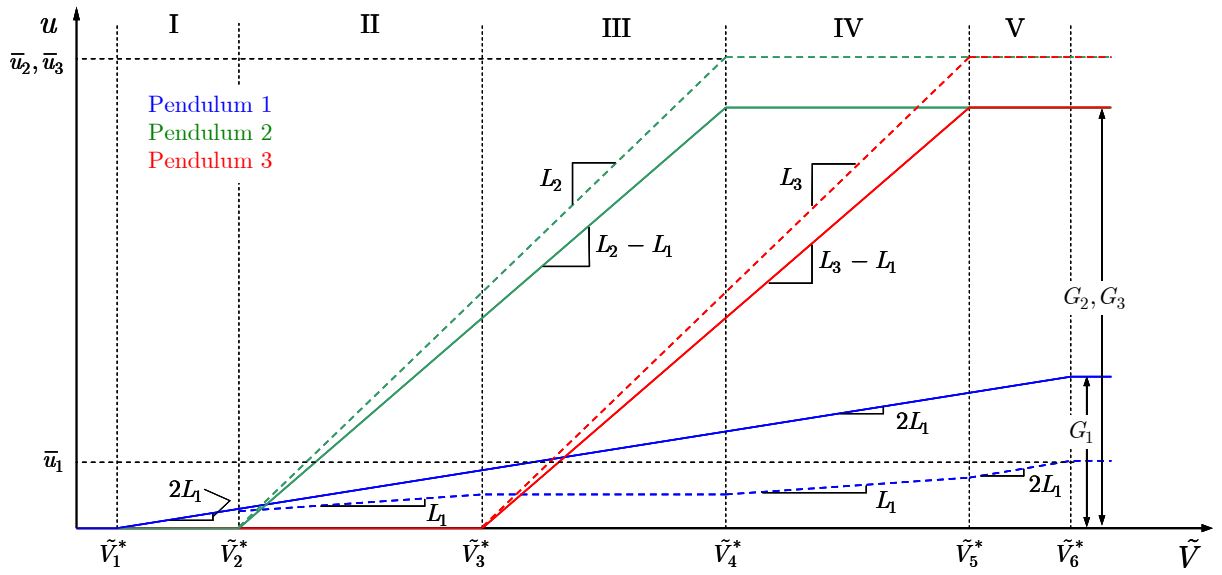

Figure 3.9: Stages of sliding for each pendulum mechanism in the actual TP bearing (shown dashed) and the CSM formulation (shown solid)

The calculation of the gap size for the first pendulum mechanism is clear from Figure 3.9 above. Since, in general, $\Delta u_j = L_j \Delta \tilde{V}$ for pendulum j, it follows that

$$\begin{aligned} G_1 &= 2L_1\left(V_6^* - V_1^*\right) \\ &= 2L_1\left(\frac{\bar{u}_3}{L_3} + \frac{\bar{u}_1}{L_1} + \mu_1 - \mu_1\right) \\ &= 2\left(\frac{L_1}{L_3}\bar{u}_3 + \bar{u}_1\right) \end{aligned} \tag{3.67}$$

Similarly, for the second pendulum mechanism, the gap size is

$$\begin{aligned} G_2 &= \left(L_2 - L_1\right)\left(V_4^* - V_2^*\right) \\ &= \left(L_2 - L_1\right)\left(\frac{\bar{u}_2}{L_2} + \mu_2 - \mu_2\right) \\ &= \bar{u}_2\left(1 - \frac{L_1}{L_2}\right) \end{aligned} \tag{3.68}$$

Finally, for the third pendulum mechanism, the gap size is

$$\begin{aligned} G_3 &= \left(L_3 - L_1\right)\left(V_5^* - V_3^*\right) \\ &= \left(L_3 - L_1\right)\left(\frac{\overline{u}_3}{L_3} + \mu_3 - \mu_3\right) \\ &= \overline{u}_3\left(1 - \frac{L_1}{L_3}\right) \end{aligned} \tag{3.69}$$

Each parameter of the CSM has been calibrated to exhibit precisely the force-displacement behavior derived above in Section 3.3. As a summary, the following matrix is useful for assigning parameters to the CSM given a set of bearing geometric properties and target friction coefficients.

Table 3.1: Parameters of calibrated CSM elements

Element	1	2	3
k_1	$100\mu_1$	$100\mu_2$	$100\mu_3$
f_y	μ_1	μ_2	μ_3
k_2	$1/\ 2L_1$	$1/(L_2 - L_1)$	$1/(L_3 - L_1)$
G	$2\left(\frac{L_1}{L_3}\overline{u}_3 + \overline{u}_1\right)$	$\overline{u}_2\left(1 - \frac{L_1}{L_2}\right)$	$\overline{u}_3\left(1 - \frac{L_1}{L_3}\right)$

Chapter 4 of this report describes an experimental program to characterize DP and TP bearings subject to harmonic and earthquake input. Chapter 5 describes the results of this experimental program, and includes a comparison of the experimental force-displacement relations with those resulting from the above-described cyclic series model.

4 Experimental Program

A series of experiments was designed and conducted to examine the behavior of actual double pendulum (DP) and triple pendulum (TP) bearings under a variety of conditions. This chapter outlines the purpose of the experiments, describes the facilities and test apparatus, and details the specimen, its instrumentation, and each class of excitation, and the nature of the data collected. The purposes of this experimental program are the following:

1. Characterize the cyclic behavior of multi-stage FP bearings at multiple levels of displacement, sliding velocity, and axial pressure.
2. Identify the parameters necessary for the development of a robust analytical model for double- and triple pendulum bearings that captures observed cyclic characteristics.
3. Record structural response quantities of interest (interstory drifts, floor accelerations, base shear) and compare these observations with response quantities computed from nonlinear response history analysis.
4. Examine behavior as bearings approach displacement and force limits.

The objectives of the studies described here center on the verification of anticipated seismic behavior of multi-stage isolation bearings, in particular double- and triple pendulum bearings, and the investigation of the ability of nonlinear analytical models and solution algorithms employed by commercially available structural analysis software to predict response quantities of interest. In particular, while the estimation of deformations in both the isolation system and superstructure appear quite robust from past response history analyses, the amplitude and frequency content of floor acceleration histories appear to be quite sensitive to both the nonlinear model used for the bearing and the selected time integration method.

In this chapter, a complete description of the experimental program is given, including the details of the specimen, bearing types, instrumentation, cyclic characterization tests, and earthquake excitation tests.

4.1 DESCRIPTION OF TEST FACILITY

The facility used for large-scale dynamic testing at the Earthquake Engineering Research Center (EERC) in Richmond, CA, is the Earthquake Simulator Laboratory (or shaking table). The supporting platform of this simulator is 20' 0" square in plan, and consists of a 12" thick reinforced and post-tensioned concrete slab with a two-way girder system. The combined self-weight of the table and the specimen is supported by pneumatically pressurized chamber beneath the platform. Eight horizontal actuators and four vertical actuators drive the platform, providing three translational and three rotational degrees of freedom. Key performance parameters characterizing the earthquake simulator are described below in Table 4-1.

The table is perforated by 2.25" diameter through-holes at 36" on center, each way. These holes provide a means of post-tensioning a specimen to the table using high-strength rods to prevent unintended sliding or overturning during testing.

The actuators are driven by command signals sent from the digital control system. This control system imposes and monitors two components of horizontal displacement (X and Y), a vertical displacement (Z), rotation about the principle in-plane directions (pitch θ_X and roll θ_Y), and rotation about the axis normal to the table (twist θ_Z). The command signal can be any digitized displacement/rotation history subject to the performance limitations indicated in Table 4.1. Also reported in this table are the scale limits, that is, the limits expressed for an assumed length scale factor. These experiments were designed with a length scale $L = 4$, and time scale $T = 2$, resulting in equal acceleration at both model and prototype scales.

Table 4.1: Performance limits of earthquake simulator

Performance Parameter	Limit	Scale Limit[1]
Horizontal Displacement	±5.0 in.	±20 in
Vertical Displacement	±2.0 in.	±8.0 in
Horizontal Acceleration	1.5 g	1.5 g
Vertical Acceleration	4.0 g	4.0 g
Horizontal Velocity	25 in./sec.	50 in./sec.
Payload	165 kips	2640 kips

[1]Assumes length scale = 4, time scale = 2

4.2 EXPERIMENTAL SPECIMEN

To facilitate collection of response data for both isolation bearings and the supported structure (i.e., superstructure), an experimental specimen was developed. The development of this specimen considered a number of factors:

1. Friction pendulum bearings need adequate axial pressure on the slider such that the observed friction coefficient is consistent and repeatable over numerous tests. Therefore, the total ballast supported by the specimen must be sufficiently large to develop such a face pressure.
2. Variation of axial load due to overturning effects, including possible bearing uplift, is an important parameter of interest. Therefore, the height-to-width aspect ratio of the superstructure must be large enough to induce uplift under the selected table excitations.
3. In characterizing the amplitude and frequency content of story acceleration histories, a multi-story specimen with observable lateral flexibility (but sufficient strength to prevent yielding during repeated testing) is necessary to capture contributions to the response from multiple modes of vibration.
4. The connection of the isolation bearings to the base plate of the superstructure was required to allow bearings to be replaced.

4.2.1 Supported Model Structure

A three-story concentrically braced steel frame was used as the isolated building specimen. A rendering and photograph of the frame are shown in Figure 3-1. This frame has seen extensive prior experimentation. It was originally fabricated as part of a research program to

investigate modeling procedures for predicting seismic response of steel moment-resisting frames. In the original tests, a moderate ballast of approximately eight kips per floor was applied. Details of the design and construction of the test structure can be found in Clough and Tang's report [1975]. The original test specimen was modified through the addition of braced frames in series with Added Damping and Stiffness (ADAS) elements [Whittaker et al., 1987]. This specimen was tested as a small structural system and not a similitude-scaled replica of a full-scale building. However, the ballast at each floor level was increased to approximately 30 kips, for the purpose of developing a realistic relationship between the stiffness and strength of the ADAS elements. A diaphragm bracing system was added for these tests, consisting of wide-flange infill beams and double-angle diagonal bracing to resist the increased inertial forces compared to the original tests. A transverse angle bracing system was also added to compensate for the increased lateral demands. This test specimen was further modified through the addition of Slotted Bolted Connections (SBCs) to the longitudinal bay in a chevron configuration (Grigorian and Popov, 1994). In this series of tests, a ballast of approximately 30 kips per floor was also used to sufficiently activate the SBCs. Because the existing structure tested with SBCs installed was subjected to story shears much larger than those expected for an isolated structure, and because the SBCs were designed to slip at a relatively substantial first-mode spectral acceleration, it was chosen as the test specimen superstructure for this experimental program. Pertinent details of this frame are described below.

The longitudinal bay of this frame is 12' 0" between column centerlines, and the transverse bay is 6' 0". Story heights are 6' 8" for the first floor, and 5' 4" for the upper two floors. Each of the four columns are W5 × 16 rolled sections of ASTM A36 structural steel, and beams are W6 × 12. In the transverse bays, double L2 × 2 × 3/16 angle bracing elements, produced from ASTM A500 Grade B steel, were installed. Longitudinal chevron bracing is structural steel tubing with SBCs at the gussets. The details of the SBCs are described extensively by Grigorian and Popov [1992], although these connections are not intended to slip in any of the tests described herein.

At each of the three levels, there were four concrete blocks, each of which had dimensions 40" × 6" × 48". At the first two levels, there were 36 pallets of lead ingots, each pallet weighing approximately 0.51 kips. At the roof level, there were 12 pallets of lead ingots. Layers of non-shrink grout were set between all concrete-steel and concrete-lead

interfaces for increased resistance to sliding. High-strength threaded-rod (ASTM A193, Grade B7) was used to post-tension the ballast components to the steel frame. In total, the first two levels support approximately 22 kips of ballast, and the roof supports approximately 10 kips of ballast. The total steel weight of the specimen is approximately 6 kips, giving a total test specimen weight of approximately 60 kips. This corresponds to an axial load on each of the four bearings of about 15 kips. A photograph depicting attachment of floor ballast is shown in Figure 4.2.

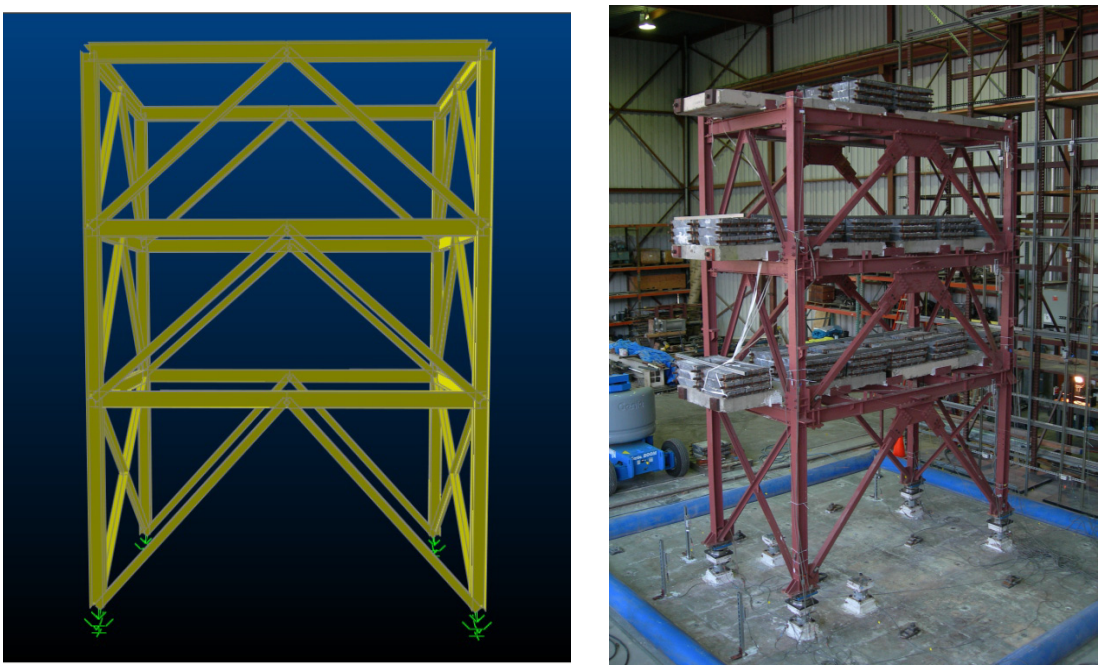

Figure 4.1: Rendered longitudinal elevation (left) and photograph (right) depicting specimen

Figure 4.2: Photograph depicting attachment of floor ballast

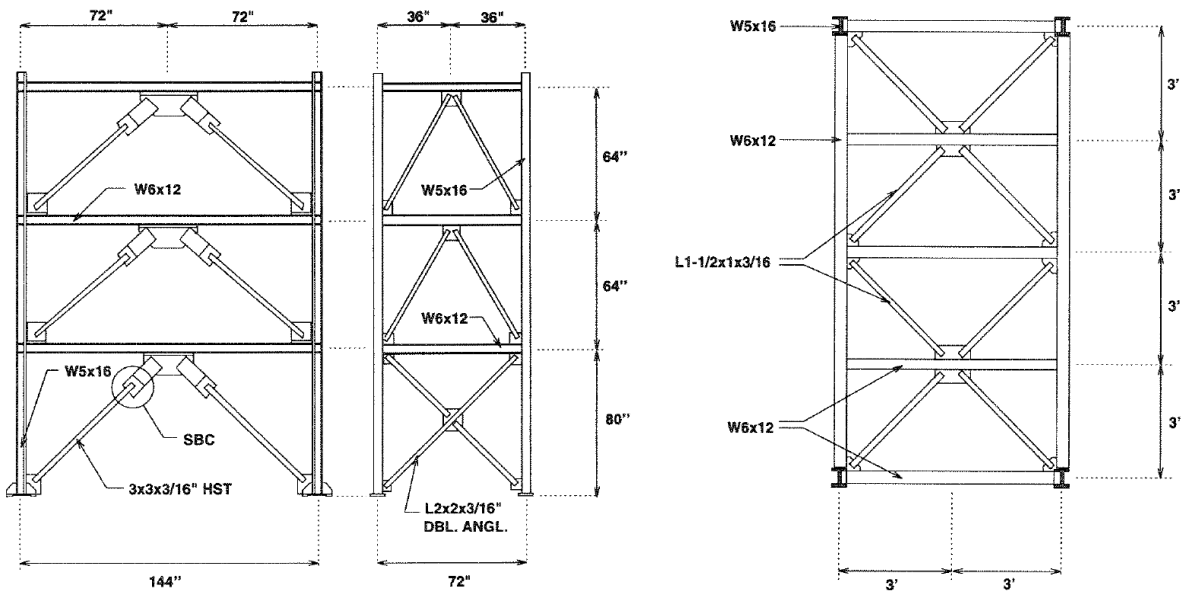

Figure 4.3: Schematic description of specimen showing elevations (left) and typical framing plan (right), reproduced from Grigorian and Popov [1992]

4.2.2 Model Friction Pendulum Bearings

For the purposes of the research described in this report, sets of four double pendulum and four triple pendulum scale-model isolation bearings were manufactured by Earthquake Protection Systems, Inc. (EPS) in Vallejo, CA. This section described each of these isolation systems and their pertinent characteristics.

4.2.3 Double Pendulum Bearings

The first isolation system implemented in the experimental program consists of four double pendulum (DP) bearings. A section through a typical scale DP bearing used for experimentation is shown in Figure 4.3, including all parameters necessary for characterization. A photograph of a typical scale DP bearing, disassembled for clarification of each component, is shown in Figure 4.5. These bearings consist of two concave surfaces and an articulating slider with PTFE sliding surfaces on each end. The mechanics of the DP bearing are discussed in Section 3.2 of this report. Each of the sliding surfaces is designed to have the same friction coefficient, and as a result, the cyclic behavior is exactly like that of a traditional single-pendulum bearing. Given the dish radii of R = 18.64" and a slider height of

h = 2.6", the effective pendulum length is $L = 2\left(R - h/2\right) = 34.68"$. This corresponds to an isolated natural period of $T = 2\pi\sqrt{L/g} = 1.88\,\text{sec}$ in model scale. In prototype scale, this is equivalent to $T = 3.76\,\text{sec}$, which is representative of a typical target period for a full-scale isolated building.

The displacement capacity of the scale bearings in an important parameter since this limits the amplitude of input table motions. It is desirable for most tests that the isolator displacements remain below the displacement capacity to limit unintended damage to either the bearings or the superstructure. From Chapter 3, Equation (3.38), the displacement capacity of the *j*th concave dish is

$$\overline{u}_j = \frac{L_j}{R_j}\frac{\left(D_j - d_j\right)}{2} \tag{4.1}$$

where D_j is the plan diameter of the concave surface and d_j is the diameter of the inner slider. Substituting the values of these parameters for the model DP bearing, the displacement capacity for each dish is

$$\overline{u}_1 = \overline{u}_2 = \frac{17.34"}{18.64"}\frac{\left(9" - 3"\right)}{2} = 2.8" \tag{4.2}$$

Therefore, the total displacement capacity of the bearing is $\overline{u} = \overline{u}_1 + \overline{u}_2 = 5.6"$. This is equivalent to 22.3" in prototype scale, a reasonable displacement limit for an isolated structure located a moderate distance from an active fault.

Given the slider diameter of 3", the axial load on each bearing of 15 kips corresponds to a face pressure on the PTFE composite liner of approximately 2.0 ksi. With overturning from seismic excitation, this axial load was expected to increase to about 30 kips (or a slider face pressure of 4.0 ksi).

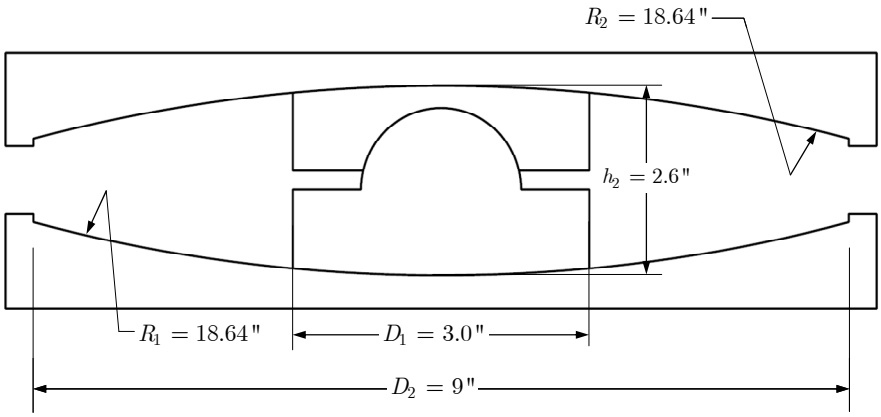

Figure 4.4: Section through a reduced-scale double pendulum bearing

Figure 4.5: Photograph of a scale DP bearing, disassembled for clarification of each component

4.2.4 Triple Pendulum Bearings

The second isolation system investigated as part of this experimental program consists of four triple pendulum (TP) bearings. A section through a typical scale TP bearing used for experimentation is shown in Figure 4.6, including all parameters necessary for characterization. A photograph of a typical scale model inner slider, disassembled for clarification of each component, is shown in Figure 4.7. These bearings consist of two outer concave surfaces and a slider with PTFE sliding surfaces on each end. The slider itself has an

inner pendulum mechanism that behaves essentially as a DP bearing. The mechanics of the TP bearing are discussed in Section 3.3 of this report. Each of the sliding mechanisms is designed to have a distinct friction coefficient, and can be determined experimentally. The inner sliding surface is lubricated to achieve a very low friction coefficient, whereas the major spherical surfaces are not lubricated. From the geometric parameters given in Figure 4-4, the three effective pendulum lengths are

$$\begin{aligned} L_1 &= R_1 - h_1/2 = 3" - 0.9" = 2.1" \\ L_2 &= R_2 - h_2/2 = 18.64" - 1.4" = 17.2" \\ L_3 &= R_3 - h_3/2 = 18.64" - 1.4" = 17.2" \end{aligned} \tag{4.3}$$

Given the above pendulum lengths, the pendulum-based period of the bearing in model scale in each of the first three phases of sliding is

$$\begin{aligned} T_I &= 2\pi\sqrt{2L_1/g} = 0.66 \text{ sec} \\ T_{II} &= 2\pi\sqrt{(L_1+L_2)/g} = 1.4 \text{ sec} \\ T_{III} &= 2\pi\sqrt{(L_2+L_3)/g} = 1.88 \text{ sec} \end{aligned} \tag{4.4}$$

In prototype scale, these correspond to $T_I = 1.32 \text{ sec}$, $T_{II} = 2.8 \text{ sec}$, $T_{III} = 3.76 \text{ sec}$, which represent plausible periods for full-scale base-isolated buildings.

The displacement capacity of the scale bearings is computed in the same manner as for the DP bearing above, using Equation (4.1). Substituting the values of these parameters for the model TP bearing gives the displacement capacity for each outer dish as

$$\bar{u}_2 = \bar{u}_3 = \frac{17.2"}{18.64"}\frac{(9" - 4")}{2} = 2.3" \tag{4.5}$$

The displacement capacity for each inner dish is

$$\bar{u}_{11} = \bar{u}_{12} = \frac{2.1"}{3"}\frac{(3.5" - 2")}{2} = 0.525" \tag{4.6}$$

Therefore, the total displacement capacity of the bearing is

$$\bar{u} = \bar{u}_{11} + \bar{u}_{12} + \bar{u}_2 + \bar{u}_3 = 5.825" \tag{4.7}$$

This is equivalent to 23.3" in prototype scale, or very similar to that computed for the DP bearing.

4.2.5 Attachments

Each bearing is bolted to a 1" thick steel end plate. The top end plate is fillet welded to the column base plate, and the bottom end plate has four tapped holes that accept high-strength bolts through a load-cell connection plate. A photograph of an isolation bearing connection at the base of each column is shown in Figure 4.8. This condition is typical of both DP and TP bearings, at all four column locations.

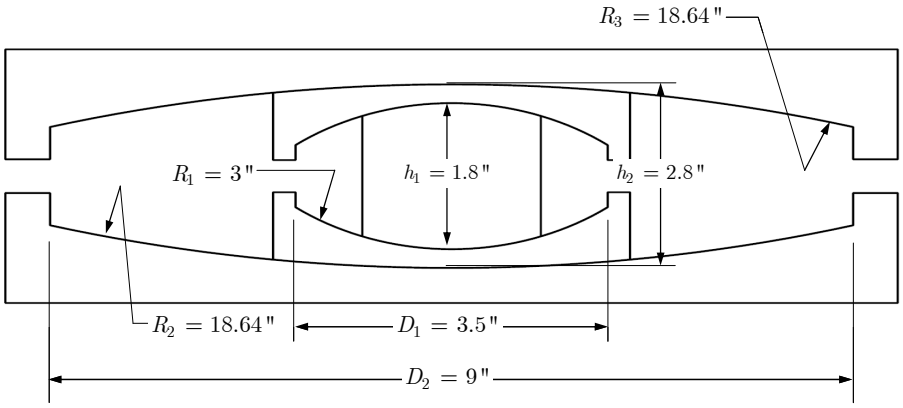

Figure 4.6: Section through a reduced-scale triple pendulum bearing

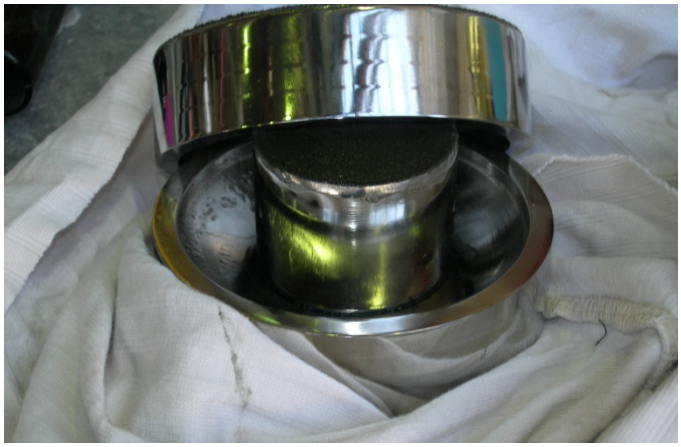

Figure 4.7: Photograph showing TP inner slider, disassembled for clarification of each component

Figure 4.8: Photograph showing bearing connection at base of column, typical for all four columns and both DP and TP bearings

4.3 DATA ACQUISITION AND INSTRUMENTATION

The data acquisition system for the earthquake simulator tests was set up to collect 76 channels of data for each test conducted. The first 16 channels were reserved to record the displacement and acceleration of the simulator platform in each translational direction. Twelve channels were used to record load cell data for each of the four load cells. Each load cell measured axial force, and two orthogonal components of horizontal shear. Twenty channels were used to record displacement as measured from linear potentiometers at each of the four levels of the structure, two in each principal direction of the structure. Twenty channels were used to record acceleration as measured from accelerometers, located identically to the linear potentiometers. Finally, six channels were used to measure interstory deformations from Novatec displacement transducers. These transducers were oriented diagonally between beam-column centerlines, at each story level for both longitudinal frames. A summary of instrumentation is described for each of the above channels at the end of this Chapter in Table 4-10. A plan layout of accelerometers at each floor level is shown below in Figure 4.9, including channel numbers, north orientation, and definition of principal axes *X* (longitudinal) and *Y* (transverse). A plan layout of linear potentiometers is shown in Figure 4.10. A photograph depicting instrumentation for recording bearing and structural response is shown in Figure 4.11.

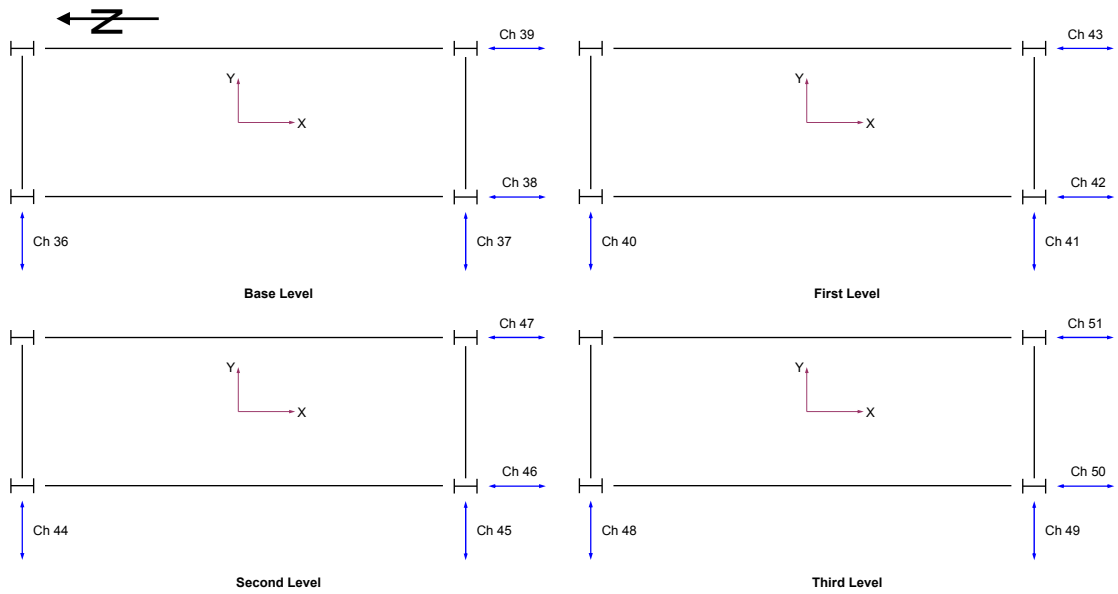

Figure 4.9: Layout of superstructure accelerometers

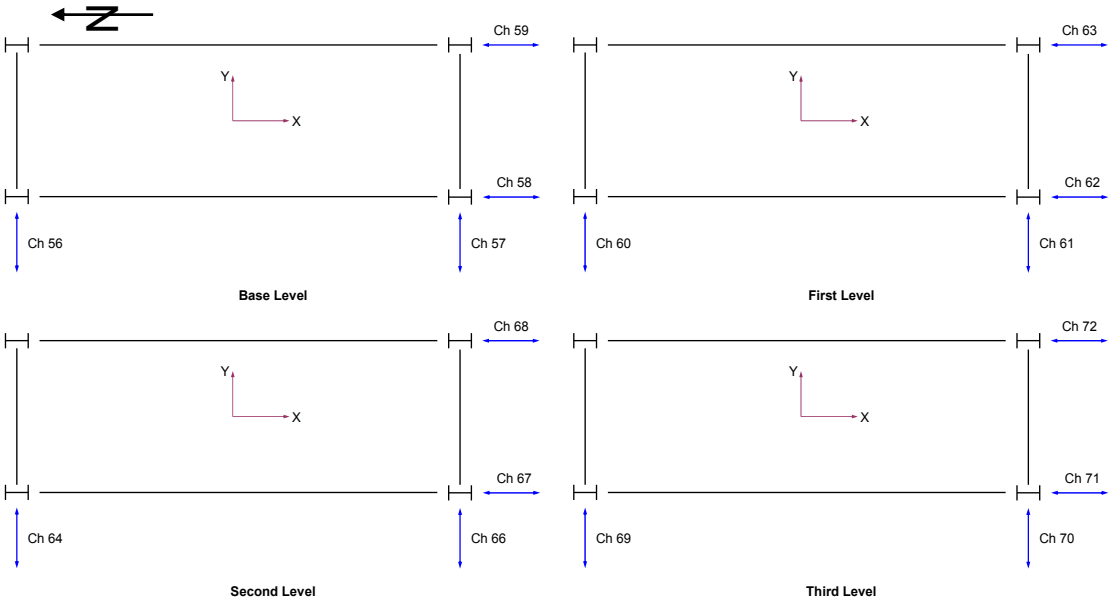

Figure 4.10: Layout of superstructure linear potentiometers

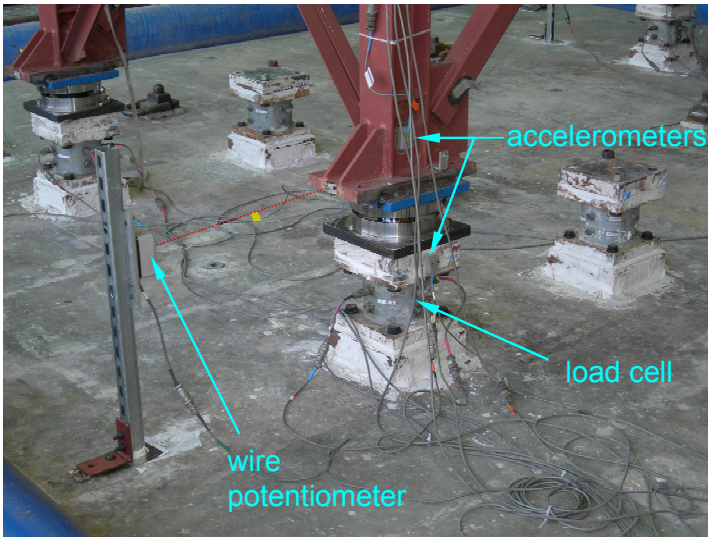

Figure 4.11: Instrumentation to record bearing force, acceleration, and displacement response

4.4 HARMONIC CHARACTERIZATION TESTS

To characterize and validate the cyclic hysteretic behavior of the double and triple pendulum bearings, sinusoidal input excitations consisting of three cycles at an input frequency equal to the natural frequency of the model was used as the table command signal. This led to a wide array of displacement and velocity demands, and thus yielded cyclic data that is suitable for the assessment of both displacement-sensitive and velocity-sensitive parameters.

To generate a displacement command signal that would achieve a sinusoidal excitation while maintaining velocity and displacement of zero at the beginning and end of the excitation, a modification to the typical sine input signal was necessary. If we consider the sinusoidal displacement input as

$$u_s(t) = A \sin \bar{\omega} t \tag{4.8}$$

where A is the amplitude and $\bar{\omega}$ is the excitation frequency; it is clear that the velocity is nonzero at t = 0. This condition causes very high initial accelerations because the table actuators generate a non-zero velocity over a short time-step. To mitigate these high initial accelerations, a third-order polynomial is generated that achieves the desired initial conditions. Consider the general third-order polynomial displacement input $u_p(t) = a_3 t^3 + a_2 t^2 + a_1 t + a_0$, subject to the following constraints:

$$\begin{aligned} u_p(0) &= 0 \\ \dot{u}_p(0) &= 0 \\ u_p(t_f) &= u_s(t_f) \\ \dot{u}_p(t_f) &= \dot{u}_s(t_f) \end{aligned} \tag{4.9}$$

where t_f is the time at which the polynomial displacement transitions to the sinusoidal displacement. This modified displacement input has the advantages of zero initial displacement and velocity, and displacement and velocity equal to that of the sinusoidal signal at the transition time. This well-behaved analytic function mitigates potential unwanted high table acceleration input at the beginning and end of the excitation. The four conditions in (4.8) are sufficient to solve the unknown coefficients $a_0,\ldots,a_3$ and therefore characterize $u_p(t)$. Solving for this transition polynomial displacement yields

$$u_p(t) = \frac{A}{t_f^3}\left[\left(\bar{\omega}t_f \cos\bar{\omega}t_f - 2\sin\bar{\omega}t_f\right)t^3 + \left(3t_f \sin\bar{\omega}t_f - \bar{\omega}t_f^2\cos\bar{\omega}t_f\right)t^2\right] \tag{4.10}$$

Therefore, the displacement command signal can be summarized as

$$u(t) = \begin{cases} u_p(t) & 0 \le t < t_f \\ u_s(t) & t_f \le t < T - t_f \\ -u_p(T-t) & T - t_f \le t < T \end{cases} \tag{4.11}$$

Here, T is the total duration of the excitation signal, and can be defined as $T = n_{cycles}\,2\pi / \bar{\omega}$. The functions $u_s(t)$ and $u_p(t)$ are as defined in Equations (4.8) and (4.10), respectively. For the table displacement signal, zero-padding of two seconds is added to the beginning and end of $u(t)$ in Equation (4.11). A generated harmonic table displacement signal is shown in Figure 4.12, including inset figures showing the transition polynomials. Such a signal may be imposed on the platform in either orthogonal translational direction (X and/or Y).

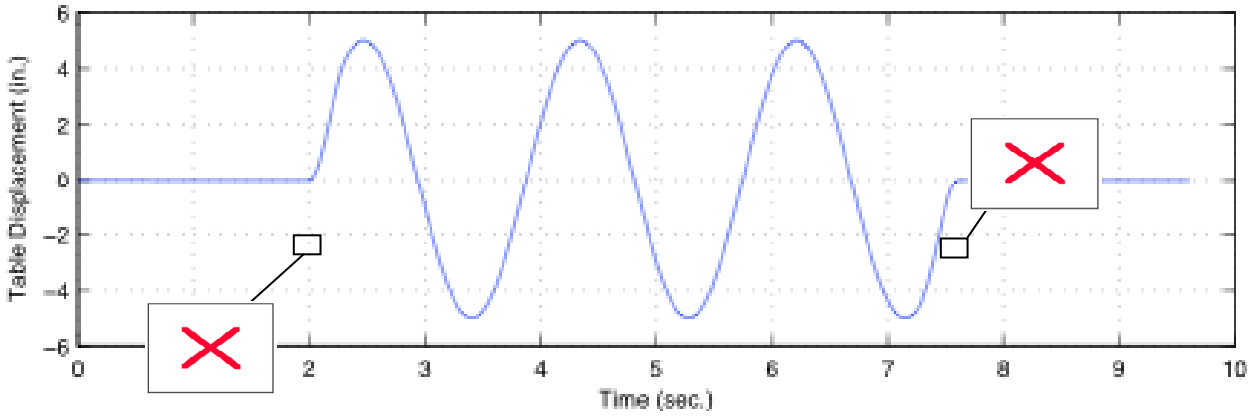

Figure 4.12: Harmonic signal scaled to platform span setting of 1,000 (beginning and end transition polynomials shown inset)

As part of the experimental program, the harmonic displacement signal described above was input to the simulator platform at six levels of amplitude, all at the same excitation frequency. These amplitudes were chosen to excite the isolated model to a range of displacement demands. Table 4.2 summarizes the amplitudes and frequencies of the harmonic characterization signals implemented as part of the experimental program. A platform span setting of 1,000 corresponds to a command displacement equal to the displacement limit of the simulator platform (5 inches). The sequence of harmonic characterization tests for both DC-FP and TC-FP specimens is described below in Section 4.5 of this chapter.

Table 4.2: List of harmonic characterization signals

Test Name	Frequency	Num. cycles	Span[1]	Amplitude[2]
SIN-10.DSP	0.56 Hz	3	63	0.32 in
SIN-25.DSP	0.56 Hz	3	158	0.79 in
SIN-50.DSP	0.56 Hz	3	316	1.58 in
SIN-80.DSP	0.56 Hz	3	500	2.50 in
SIN-95.DSP	0.56 Hz	3	600	3.00 in
SIN-100.DSP	0.56 Hz	3	630	3.15 in

[1]Platform span setting

[2]Displacement amplitude of platform

4.5 EARTHQUAKE SIMULATION TESTS

To assess the behavior of the above-described specimen under seismic excitation, a series of earthquake simulation tests was conducted. These tests are conducted to investigate the behavior of the superstructure and isolation bearings under various types and levels of input. This section describes the details of the ground-motion records run as part of the earthquake simulation tests.

4.5.1 Selection of Ground-Motion Recordings

To facilitate selection of ground-motion recordings, the PEER Strong Motion Database (*http://peer.berkeley.edu/smcat*) was used to search for appropriate acceleration histories. The key factors influencing the selection of input table motions were

(a) the capability of the simulator to replicate the input signal given the performance limitations of the hydraulic actuators (see Table 4.1 above); and

(b) the response of the isolation system to the scaled record, which reflects the expected deformation under a severe level of seismic shaking without exceeding the deformation capacity of the bearings.

After a review of the available strong motion records from the PEER database, subject to the two considerations listed immediately above, the three recordings listed in Table 4.3 were chosen for the earthquake simulation test program.

Table 4.3: Summary of selected ground motion recordings

ID	Event	Recording Station	M[a]	R[b]	Soil[c]
G03	1989 Loma Prieta	Gilroy Array #3	6.9	14.4	C
CHY	1999 Chi-Chi	CHY028	7.6	7.31	C
SYL	1994 Northridge	Sylmar - Olive View Med FF	6.7	6.4	C

[a]Moment magnitude

[b]Distance (in kilometers) closest to fault rupture

[c]USGS soil classification

Each of the above ground motions recordings contains three components of excitation: two horizontal components and one vertical component, all mutually orthogonal.

Important parameters for each acceleration history from the records listed above are listed in Tables 4.4 through 4.6. Among the listed parameters are: HP (high-pass filter frequency), LP (low-pass filter frequency), PGA (peak ground acceleration), PGV (peak ground velocity), and PGD (peak ground displacement). Consideration of these parameters is important in evaluating the capability of the simulator to replicate these records in light of the performance limitations.

Table 4.4: Properties of G03 Earthquake Records

Record/Component	HP (Hz)	LP (Hz)	PGA (g)	PGV (in/s)	PGD (in)
LOMAP/G03-UP	0.1	50	0.338	6.1	2.8
LOMAP/G03000	0.1	33	0.555	14.1	3.2
LOMAP/G03090	0.1	40	0.367	17.6	7.6

Table 4.5: Properties of CHY Earthquake Records

Record/Component	HP (Hz)	LP (Hz)	PGA (g)	PGV (in/s)	PGD (in)
CHICHI/CHY028-V	0.04	50	0.337	14.3	5.3
CHICHI/CHY028-N	0.1	50	0.821	26.4	9.2
CHICHI/CHY028-W	0.12	50	0.653	28.7	5.8

Table 4.6: Properties of SYL Earthquake Records

Record/Component	HP (Hz)	LP (Hz)	PGA (g)	PGV (in/s)	PGD (in)
NORTHR/SYL-UP	0.12	23	0.535	7.5	3.4
NORTHR/SYL090	0.12	23	0.604	30.8	6.3
NORTHR/SYL360	0.12	23	0.843	51.0	12.9

4.5.2 Scaling of Records for Simulation

Implementation of the selected ground motions records as part of a simulation test program required processing of the raw records described in Section 4.5.1. Processing included high-pass and low-pass filtering of acceleration records, and scaling in both time and amplitude.

To improve the performance of the simulator platform actuators in reproducing the command displacement signal, a low-pass/high-pass trapezoidal window filter was applied to each acceleration record. For each record, the parameters of this filter were: low cut = 0.1 Hz, low corner = 0.15 Hz, high corner = 10 Hz, high cut = 15 Hz. These filter parameters resulted in processed records whose spectral parameters (i.e., displacement and pseudo-acceleration) were virtually indistinguishable from the unprocessed records.

For all records, time scaling was necessary to match the similitude requirements of the model. The specimen was developed with equal acceleration at both model and prototype scales, and was achieved using a length scale $L = 4$ and a time scale $T = 2$. To preserve the frequency content of the original acceleration records, a time scale of 2 was applied to the acceleration records. Hence, $dt' = dt / 2$, where dt is the time step of the original record, and dt' is the modified time step used for simulation. The amplitude of each record was modified such that replication by the platform was possible, and that displacement capacity of the isolators was not exceeded. However, amplitude scaling was equal for a given ground motion triplet, thereby preserving the relative intensity of each record in the three orthogonal directions.

An important aspect of the research presented in this report is the response of base isolated structures to multiple levels of seismic hazard. Consequently, the earthquake simulator program was designed to address three distinct levels of seismic hazard, termed: SLE (Service Level Event), DBE (Design Basis Event) and MCE (Maximum Considered Event). Following guidelines such as FEMA 440 [BSSC, 2003], these three levels of hazard correspond to seismic events having respective return periods of 72 years, 475 years, and 2,475 years. An important clarification regarding scaling is that the scaled ground motion input is *not* necessarily representative of the level of seismic hazard being targeted. Rather, the scaling is developed such that the resulting isolator displacement demand is consistent with that expected under the targeted level of seismic hazard. To consider these three levels of hazard in the simulation program, each of the three ground motion records was first scaled such that the resulting isolator displacement would be approaching the displacement limit of the bearings. This scale factor was used for the MCE, since it is under this hazard level that the isolation system must remain stable [BSSC, 2003]. The scale factor for the DBE was taken as 75% of the MCE, and the scale factor for the SLE was taken as 35% of the MCE. These values are by assumption, and do not correspond to any particular site. However, using

the methodology of FEMA 356 [BSSC, 2000], the constant-velocity spectral ratio, $S_{1,SLE} / S_{1,DBE}$, is 0.44 for sites in California, compared with 0.47 under the above assumption. The constant-velocity spectral ratio $S_{1,DBE} / S_{1,MCE}$ is approximately 0.75 for many sites in California, as evidenced by USGS hazard maps [USGS, 2007].

A summary description of the table input signals corresponding to the MCE level of seismic hazard is shown in Figure 4.13 through Figure 4.21. For each signal, the displacement, velocity, and acceleration history is shown, and the Fourier amplitude spectrum of the acceleration. The response spectra for the table input motions, with scale factor of 1.0, are shown in Figure 4.22 through Figure 4.27.

Three recorded ground motions were selected, and these ground motions were simulated at three levels of seismic hazard. Additionally, ground motion was simulated along the three principal axes of the specimen, *X* (transverse), *Y* (longitudinal), and *Z* (vertical). There are a total of 21 earthquake simulation tests for each of the two specimens, and the combinations of ground motion, hazard level, and direction of shaking is summarized in the test matrix shown below in Table 4.7. The effect of vertical acceleration is investigated for all three input motions, and at all three levels of seismic hazard. The tri-directional behavior, and hence the effect of three-dimensional coupling, is investigated for all three records, but only at the DBE hazard level.

Table 4.7: Summary of earthquake simulation program

Hazard Level	Ground Motion: G03	Ground Motion: CHY	Ground Motion: SYL
SLE	X	X	X
	X+Z	X+Z	X+Z
DBE	X	X	X
	X+Z	X+Z	X+Z
	X+Y+Z	X+Y+Z	X+Y+Z
MCE	X	X	X
	X+Z	X+Z	X+Z

4.6 SUMMARY OF SHAKE TABLE TEST SEQUENCE

The complete sequence of shake table tests is summarized, described for the DP and TP specimens, in Table 4.8 and 4.9, respectively. In these tables, the headings are defined as follows:

Test ID: a distinct number assigned to the test by the data acquisition system

Signal: the command signal sent to the table control system. SIN is the sinusoidal signal described above in Section 4.4, and CHY, G03, and SYL are the earthquake inputs, defined above in Section 4.5

Span: the amplitude of motion in X, Y, or Z direction (span setting of 1,000 corresponds to simulator displacement limit)

% of signal: the scale factor applied to input signal

Table 4.8: Complete shake table test sequence for DP specimen

Test ID	Signal	Span Settings X	Y	Z	% of signal	Test ID	Signal	Span Settings X	Y	Z	% of signal
112603	SIN	63	0	0	10%	145554	CHY	329	512	650	65%
112706	SIN	158	0	0	25%	150149	G03	202	0	0	25%
112811	SIN	316	0	0	50%	150249	G03	524	0	0	65%
113601	SIN	316	0	0	50%	150338	G03	645	0	0	80%
115010	SIN	316	0	0	50%	'15054	G03	202	0	250	25%
134223	SIN	0	158	0	25%	150550	G03	524	0	650	65%
134411	SIN	0	316	0	50%	150743	G03	645	0	800	80%
134810	SIN	0	316	0	50%	151024	G03	524	0	650	65%
142803	CHY	127	0	0	25%	151716	SYL	153	0	0	25%
143439	CHY	329	0	0	65%	151806	SYL	397	0	0	65%
143915	CHY	405	0	0	80%	151905	SYL	488	0	0	80%
144255	CHY	127	250	0	25%	152037	SYL	153	0	93	25%
144558	CHY	127	0	250	25%	152150	SYL	397	0	241	65%
144808	CHY	329	0	650	65%	152330	SYL	488	0	297	80%
144942	CHY	405	0	800	80%	152502	SYL	397	0	241	65%

Table 4.9: Complete shake table test sequence for TP specimen

Test ID	Signal	Span Settings X	Y	Z	% of signal	Test ID	Signal	Span Settings X	Y	Z	% of signal
151647	CHY	177	0	0	35%	161459	SYL	192	0	0	35%
151910	CHY	329	0	0	65%	161636	SYL	397	0	0	65%
152532	CHY	430	0	0	85%	161901	SYL	549	0	0	90%
152851	CHY	177	0	350	35%	165220	SYL	397	0	241	65%
153033	CHY	329	0	650	65%	165852	SYL	329	512	650	65%
153252	CHY	430	0	850	85%	170258	SYL	610	0	0	100%
153452	CHY	329	512	650	65%	170355	SYL	610	0	371	100%
153920	G03	282	0	0	35%	170733	SIN	63	0	0	10%
154042	G03	605	0	0	75%	170830	SIN	158	0	0	25%
155005	G03	524	0	0	65%	170912	SIN	316	0	0	50%
155236	G03	282	0	350	35%	171402	SIN	500	0	0	79%
155539	G03	524	0	650	65%	171519	SIN	600	0	0	95%
155744	G03	605	0	750	75%	173337	SIN	660	0	0	104%
155950	G03	524	0	650	65%	173916	SIN	700	0	0	111%
160559	SYL	192	0	0	35%	172230	SIN	0	200	0	32%
160705	SYL	397	0	0	65%	172305	SIN	0	400	0	63%
161130	SYL	549	0	0	90%	172857	SIN	0	600	0	95%

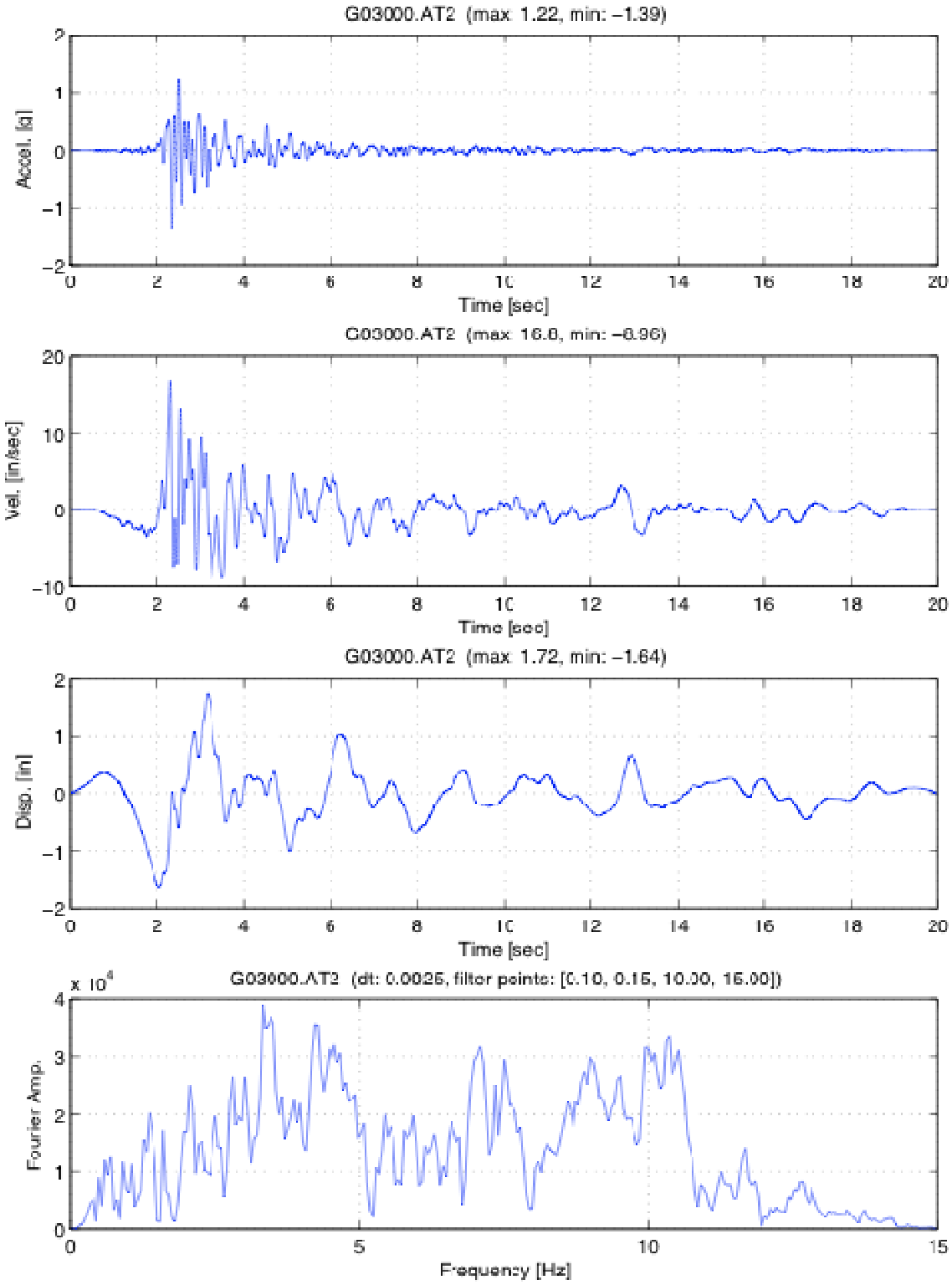

Figure 4.13: Characteristics of scaled G03 input signal, N-S component

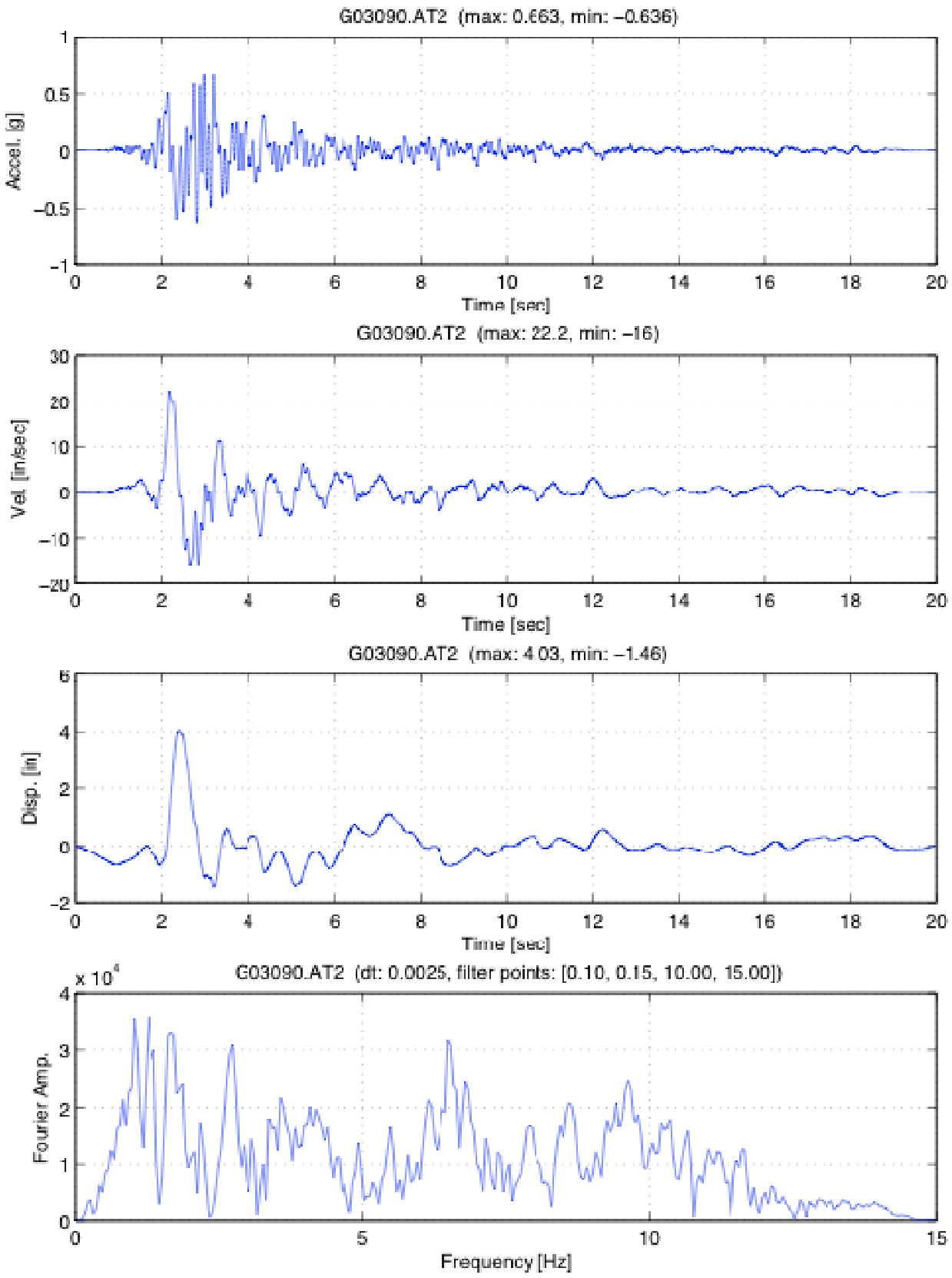

Figure 4.14: Characteristics of scaled G03 input signal, E-W component

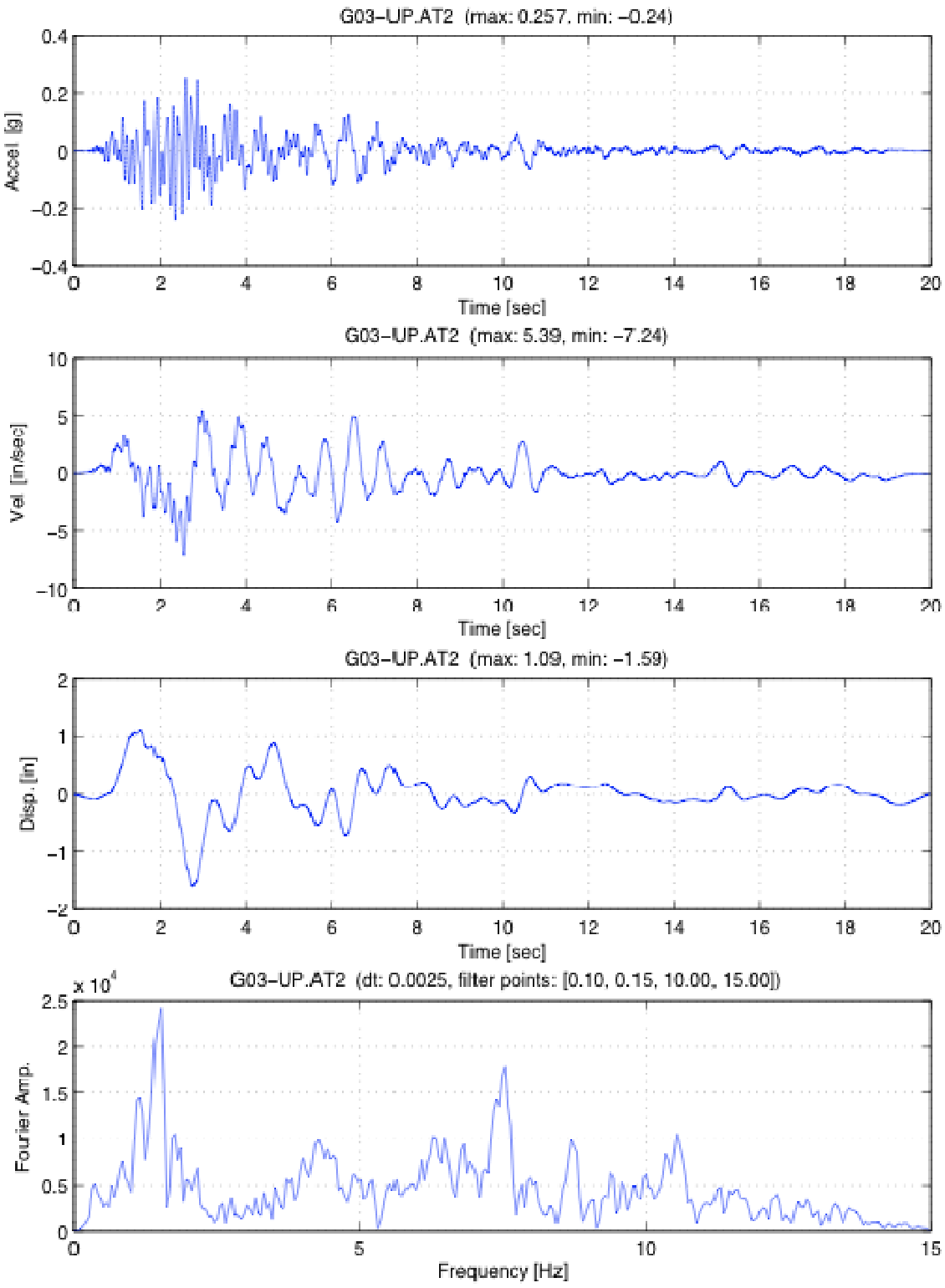

Figure 4.15: Characteristics of scaled G03 input signal, vertical component

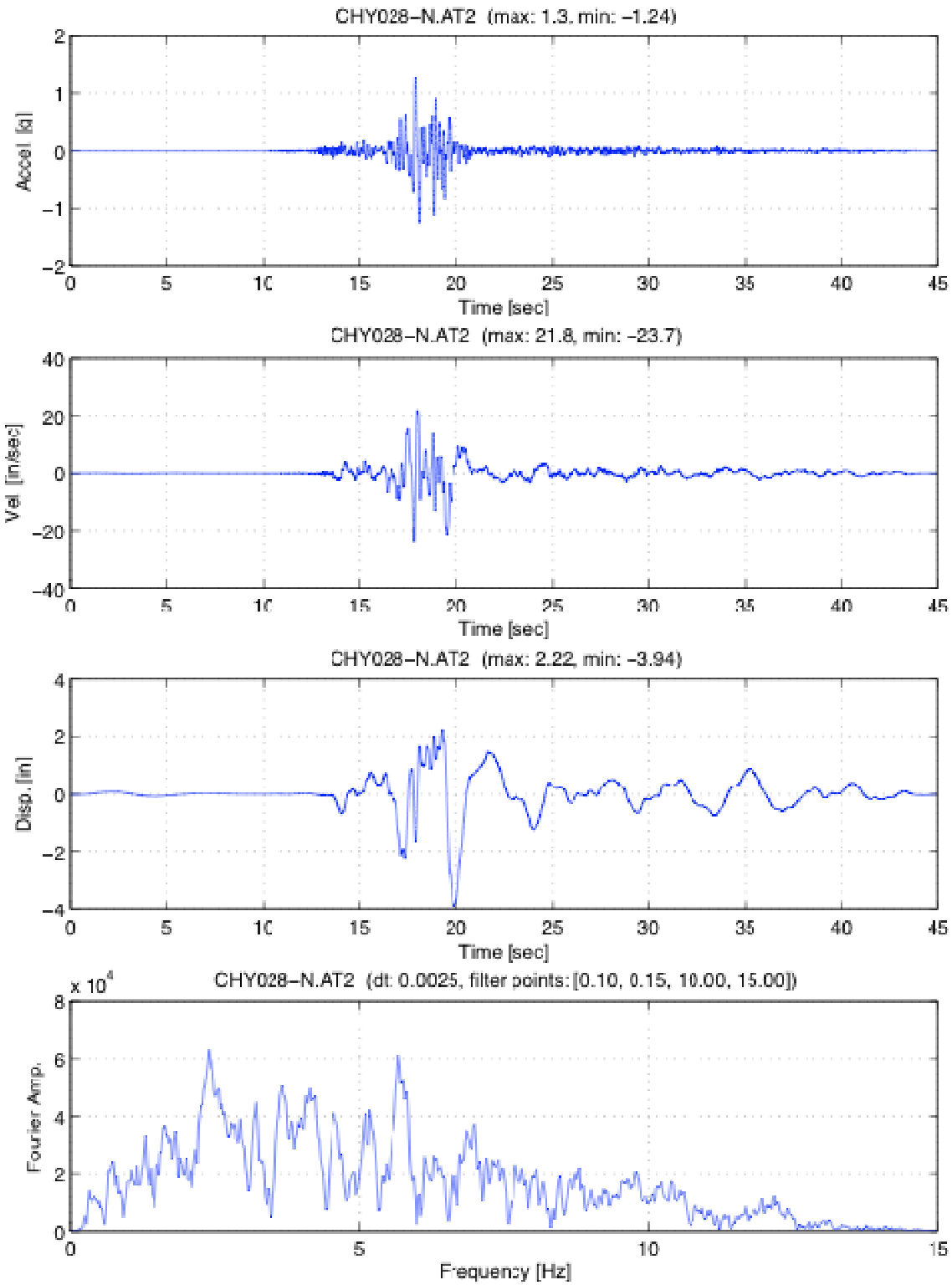

Figure 4.16: Characteristics of scaled CHY input signal, N-S component

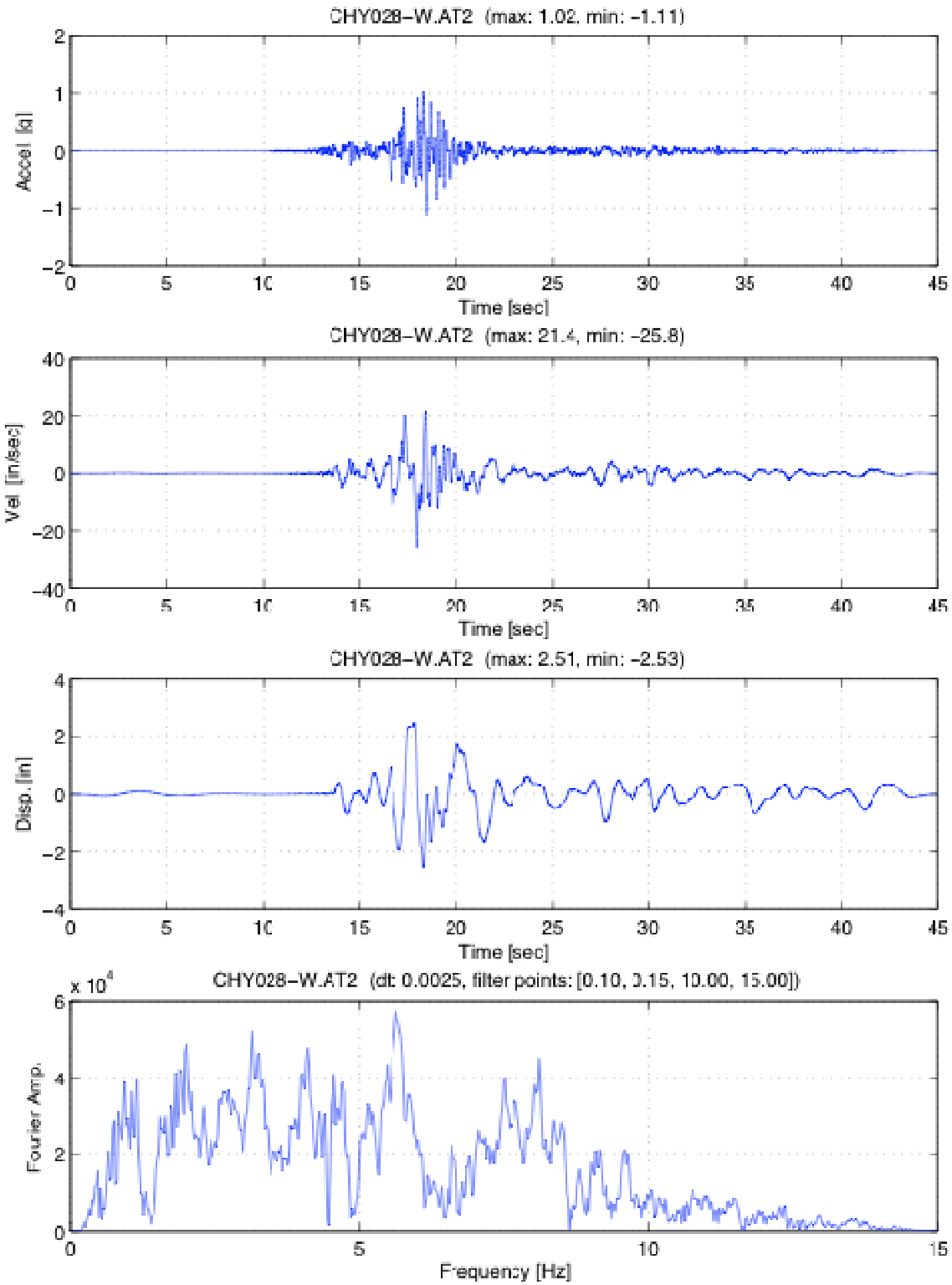

Figure 4.17: Characteristics of scaled CHY input signal, E-W component

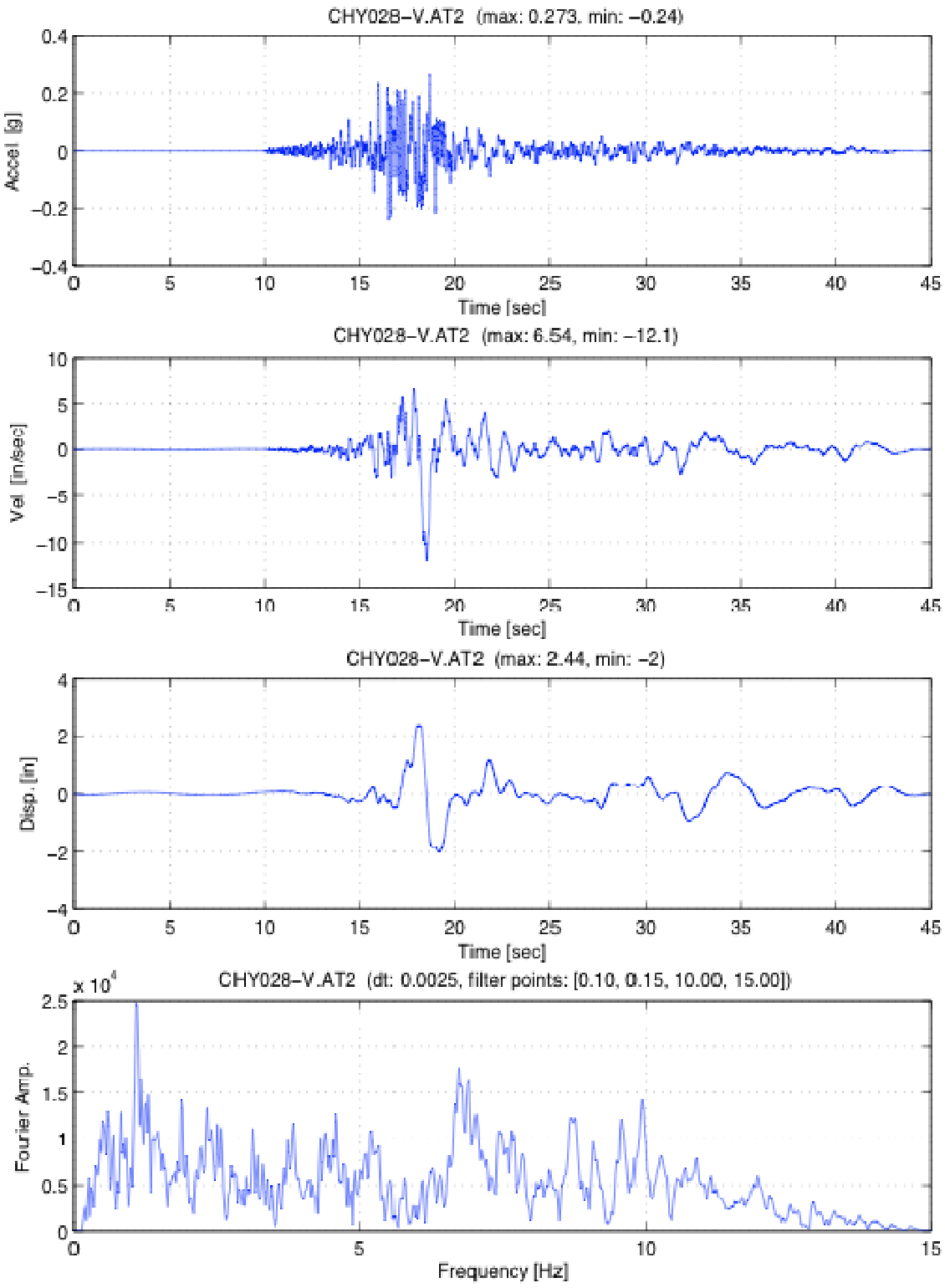

Figure 4.18: Characteristics of scaled CHY input signal, vertical component

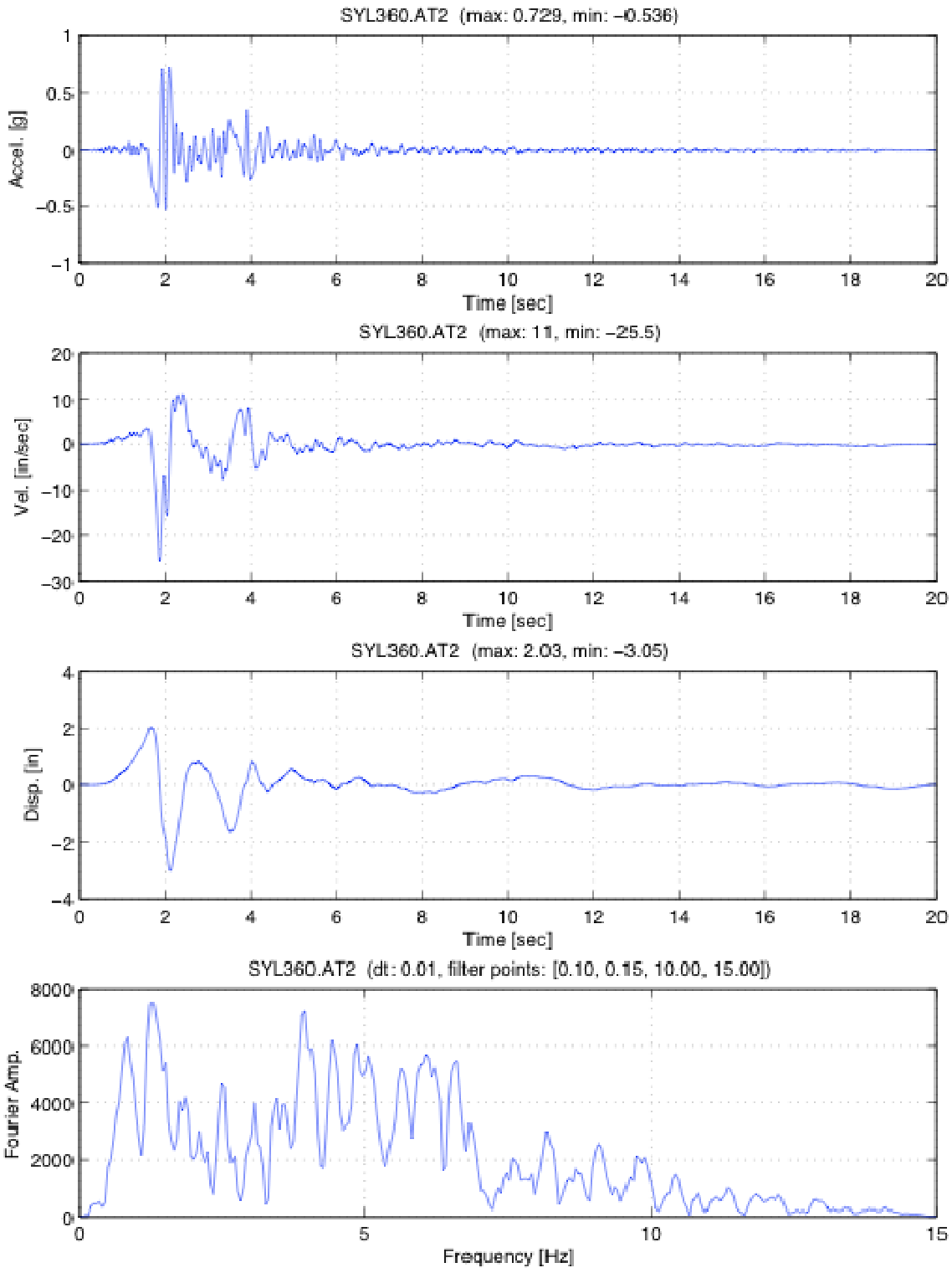

Figure 4.19: Characteristics of scaled SYL input signal, N-S component

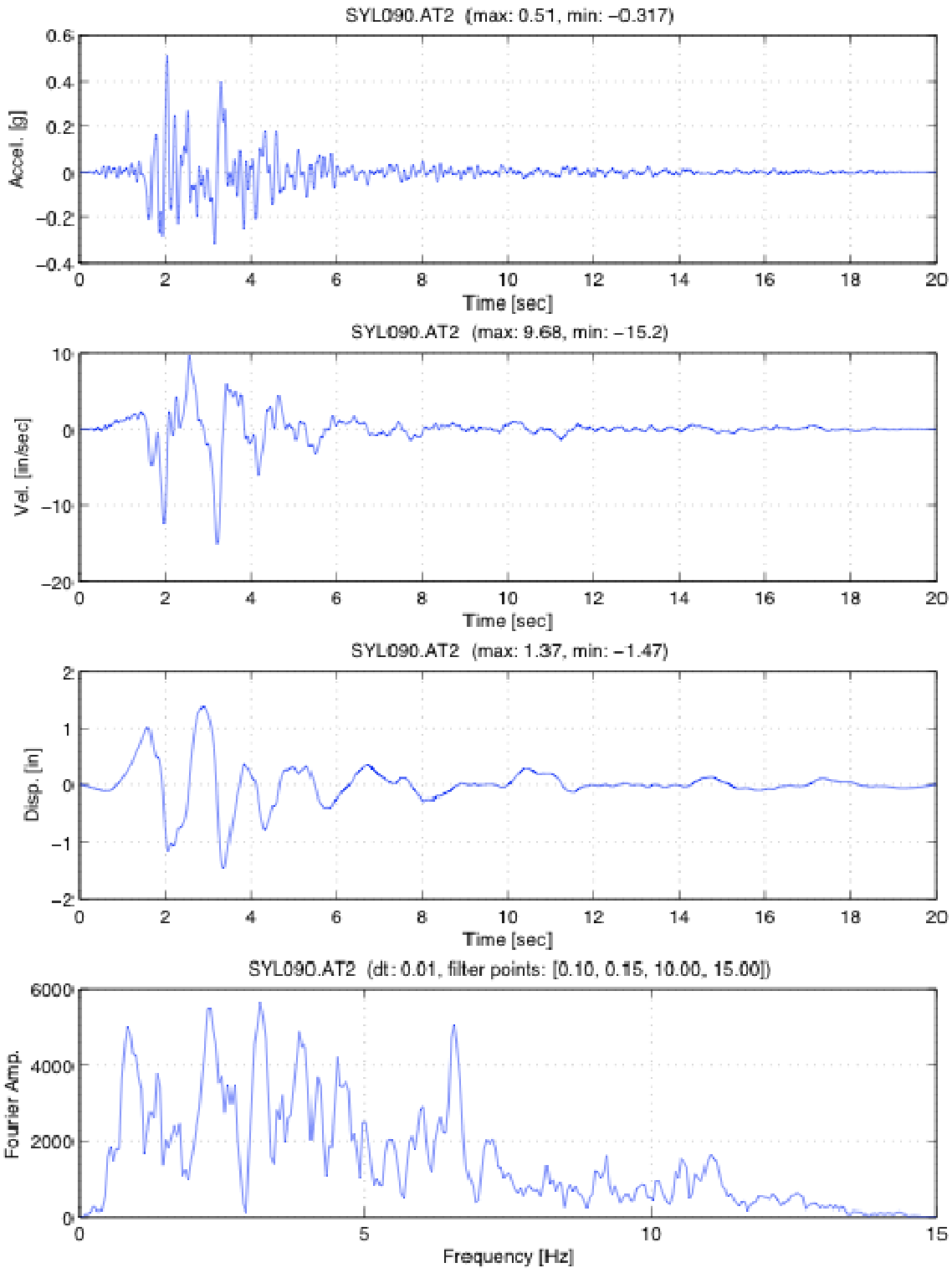

Figure 4.20: Characteristics of scaled SYL input signal, E-W component

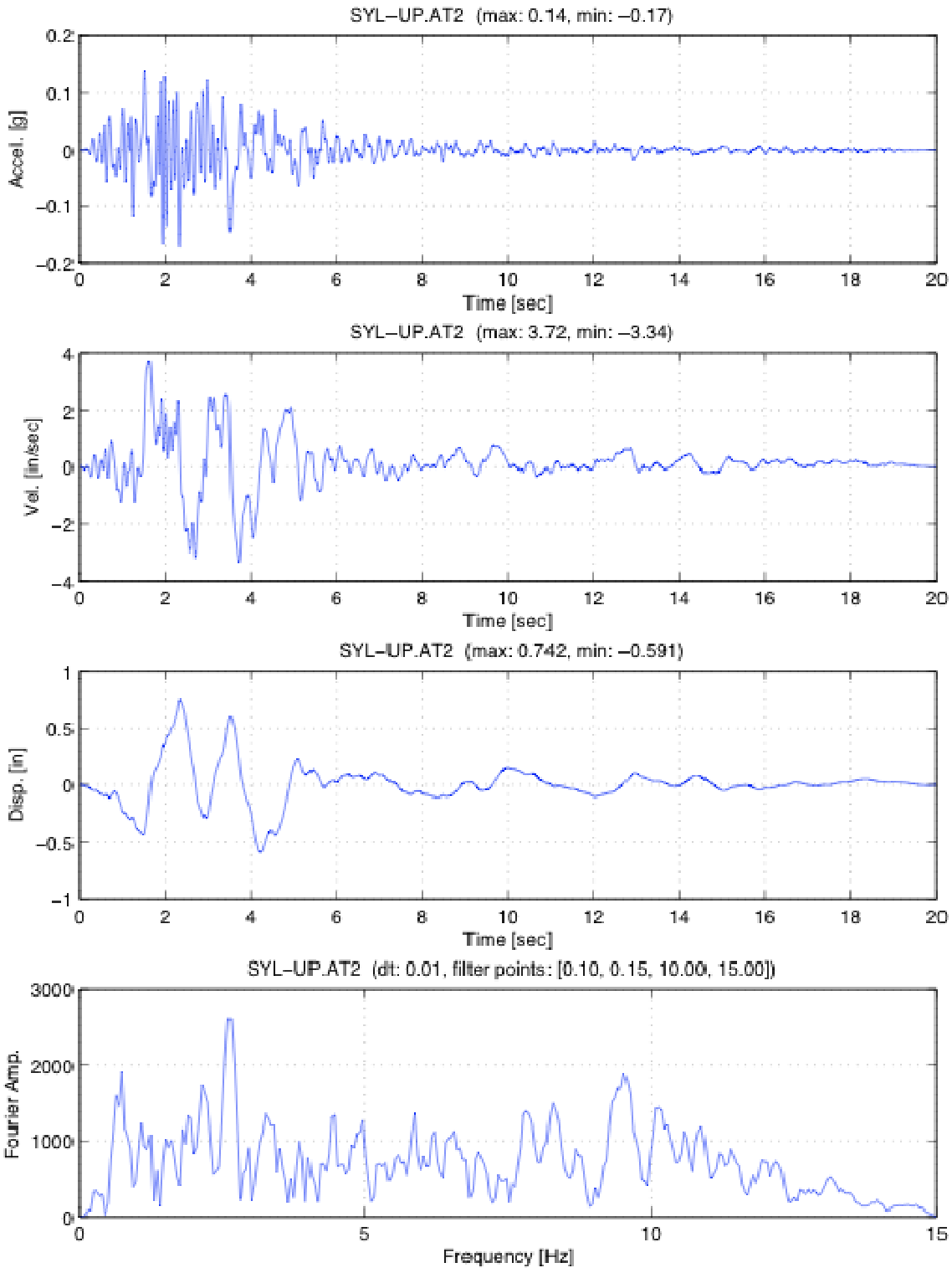

Figure 4.21: Characteristics of scaled SYL input signal, vertical component

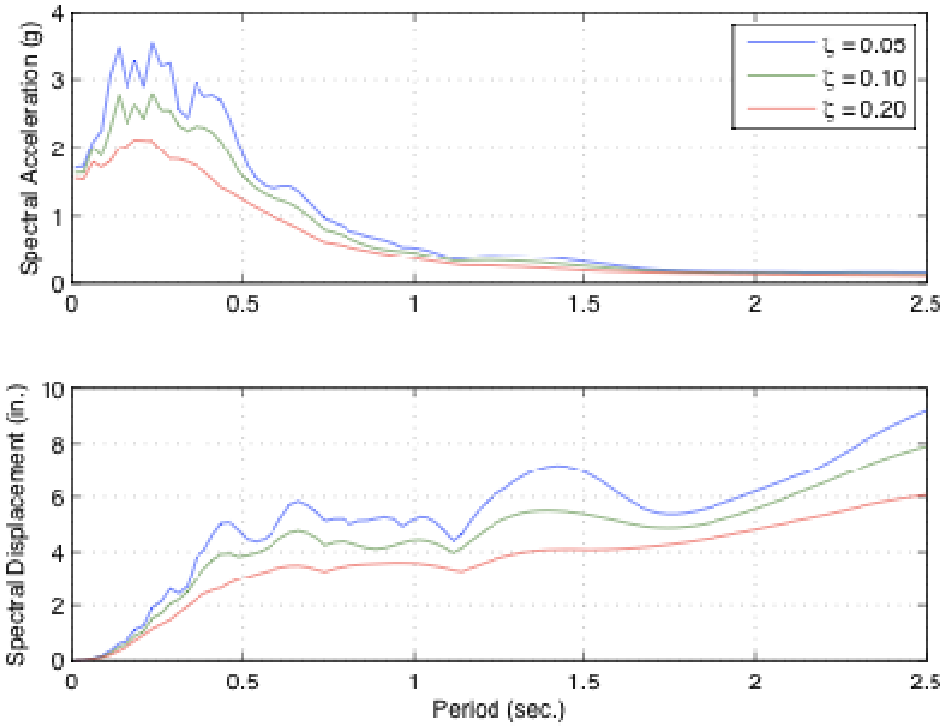

Figure 4.22: Response spectra of scaled CHY input signal, N-S component

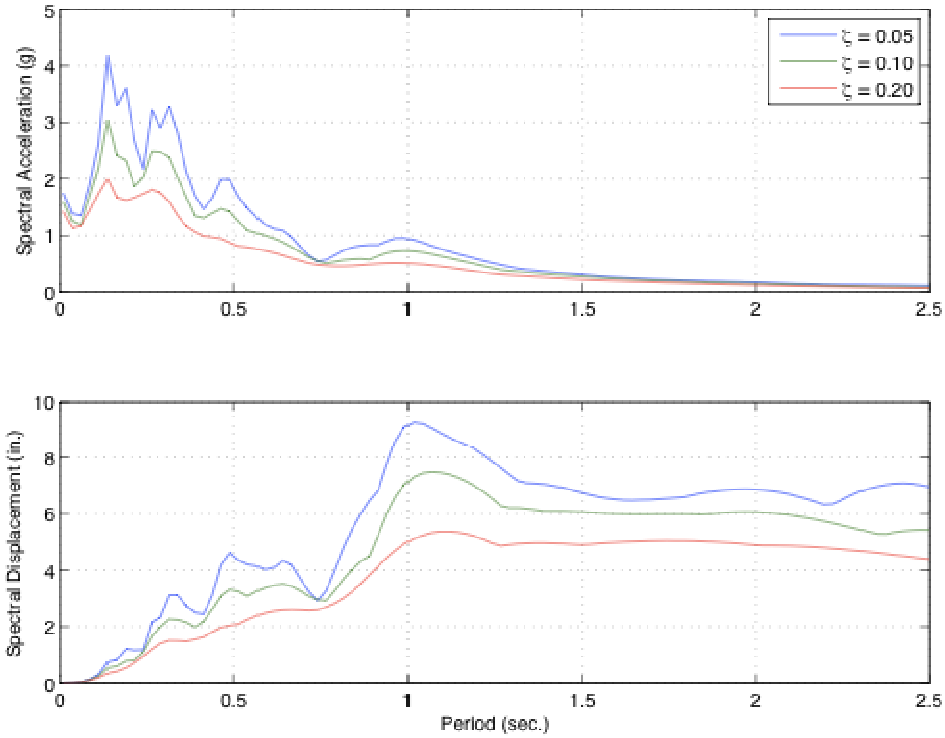

Figure 4.23: Response spectra of scaled CHY input signal, E-W component

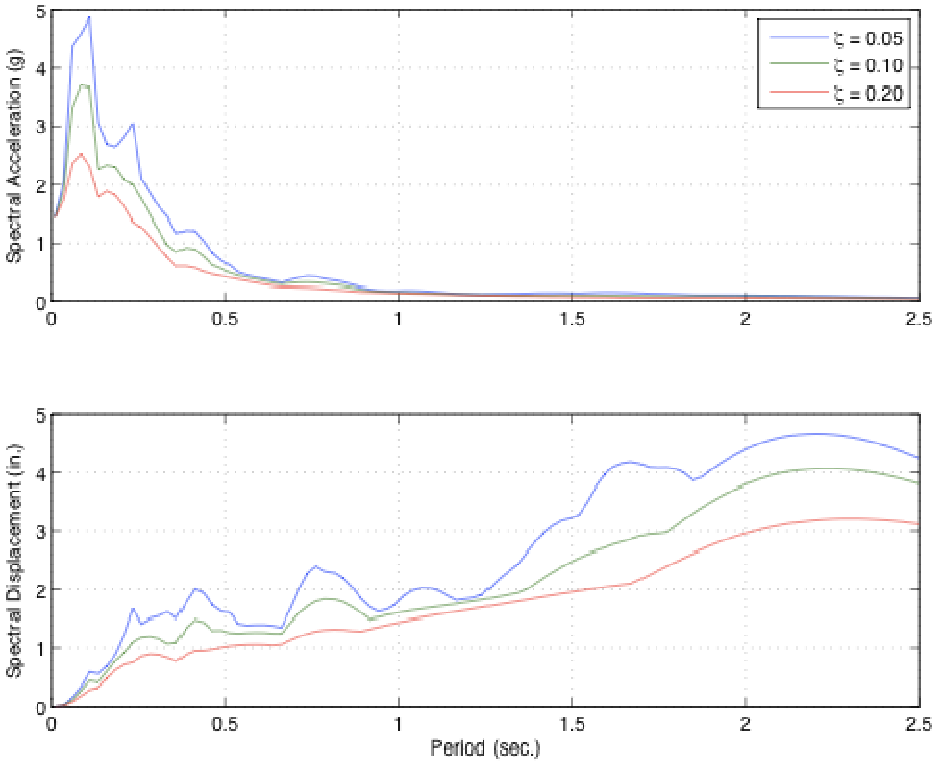

Figure 4.24: Response spectra of scaled G03 input signal, N-S component

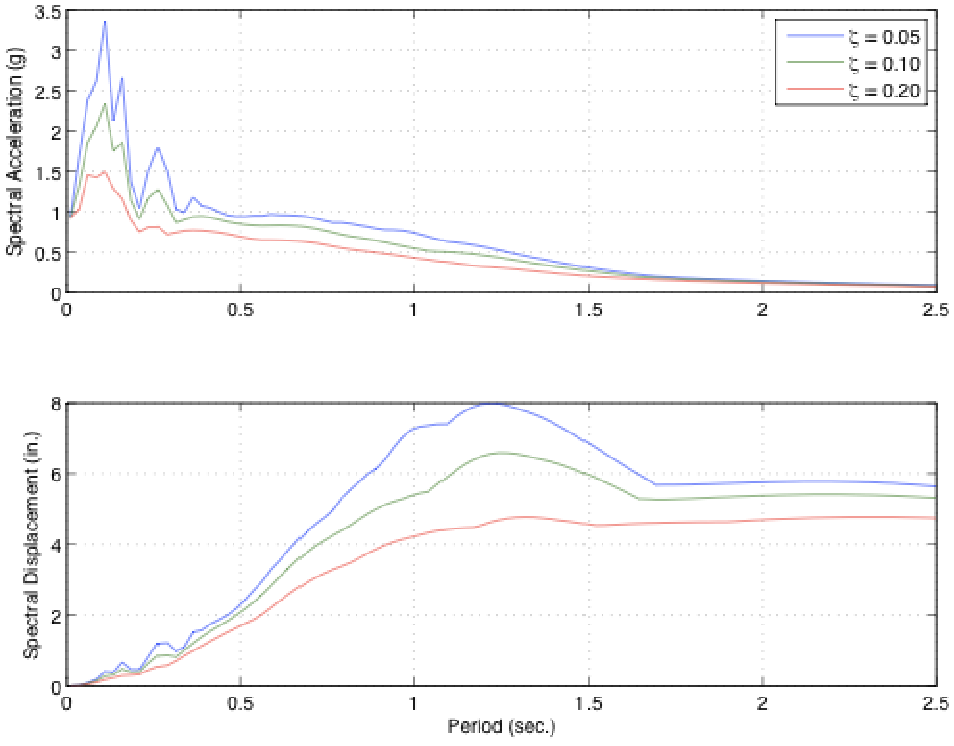

Figure 4.25: Response spectra of scaled G03 input signal, E-W component

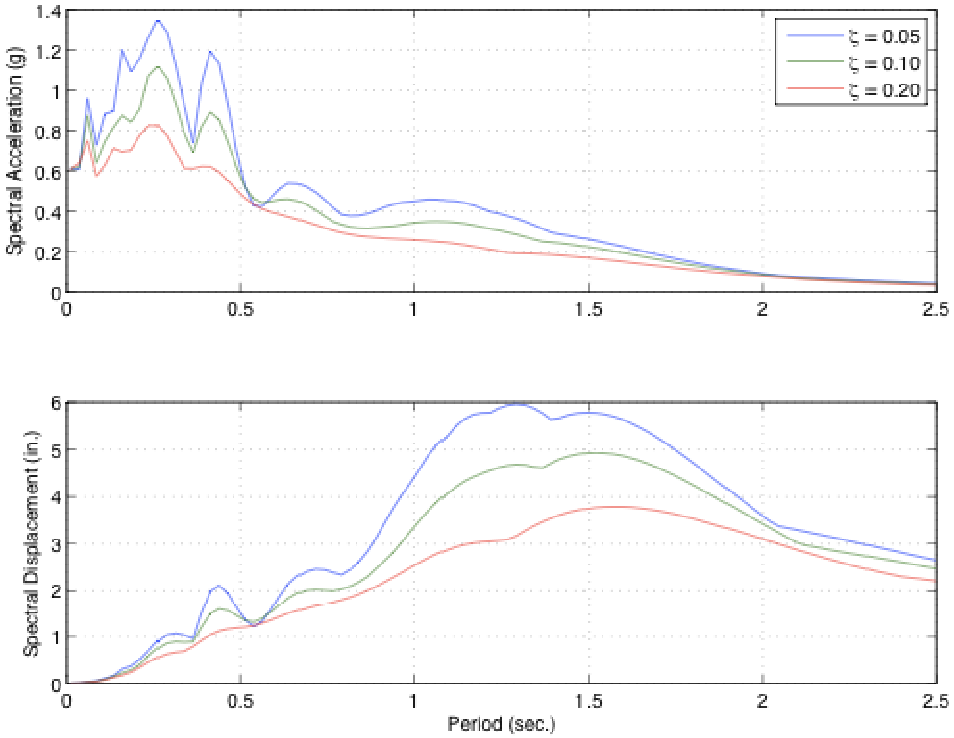

Figure 4.26: Response spectra of scaled SYL input signal, N-S component

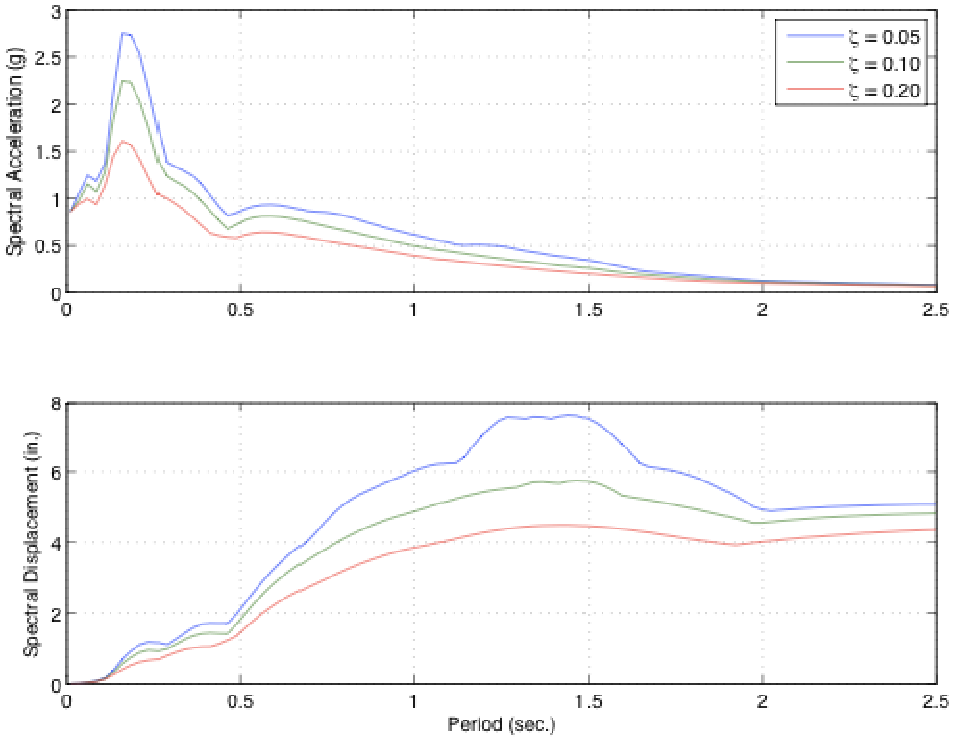

Figure 4.27: Response spectra of scaled SYL input signal, E-W component

Table 4.10: Instrumentation List

Channel	Label	Description	Units
1	H1O	Longitudinal Table Displacement	inches
2	H2O	Transverse Table Displacement	inches
3	H3O	Longitudinal Table Displacement	inches
4	H40	Transverse Table Displacement	inches
5	V10	NW Vertical Table Displacement	inches
6	V20	SW Vertical Table Displacement	inches
7	V30	NE Vertical Table Displacement	inches
8	V40	SE Vertical Table Displacement	inches
9	H1-2	Longitudinal Table Acceleration	g
10	H3-4	Longitudinal Table Acceleration	g
11	H4-1	Transverse Table Acceleration	g
12	H2-3	Transverse Table Acceleration	g
13	V1ACC	NW Vertical Table Acceleration	g
14	V2ACC	SW Vertical Table Acceleration	g
15	V3ACC	NE Vertical Table Acceleration	g
16	V4ACC	SE Vertical Table Acceleration	g
20	LC4S1	NE Load Cell - Shear Y	kips
21	LC4S2	NE Load Cell - Shear X	kips
22	LC4A	NE Load Cell - Axial	kips
23	LC3S1	SE Load Cell - Shear Y	kips
24	LC3S2	SE Load Cell - Shear X	kips
25	LC3A	SE Load Cell - Axial	kips
26	LC7S1	SW Load Cell - Shear Y	kips
27	LC7S2	SW Load Cell - Shear X	kips
28	LC7A	SW Load Cell - Axial	kips
29	LC8S1	NW Load Cell - Shear Y	kips
30	LC8S2	NW Load Cell - Shear X	kips
31	LC8A	NW Load Cell - Axial	kips

Table 4.10: Instrumentation List (Continued)

Channel	Label	Description	Units
32	ACCNYT	NW Accelerometer Y - Table Level	g
33	ACCSYT	SW Accelerometer Y - Table Level	g
34	ACCEXT	SW Accelerometer X - Table Level	g
35	ACCWXT	SE Accelerometer X - Table Level	g
36	ACCNYB	NW Accelerometer Y - Base Level	g
37	ACCSYB	SW Accelerometer Y - Base Level	g
38	ACCEXB	SW Accelerometer X - Base Level	g
39	ACCWXB	SE Accelerometer X - Base Level	g
40	ACCNY1	NW Accelerometer Y - First Level	g
41	ACCSY1	SW Accelerometer Y - First Level	g
42	ACCEX1	SW Accelerometer X - First Level	g
43	ACCWX1	SE Accelerometer X - First Level	g
44	ACCNY2	NW Accelerometer Y - Second Level	g
45	ACCSY2	SW Accelerometer Y - Second Level	g
46	ACCEX2	SW Accelerometer X - Second Level	g
47	ACCWX2	SE Accelerometer X - Second Level	g
48	ACCNYR	NW Accelerometer Y - Roof Level	g
49	ACCSYR	SW Accelerometer Y - Roof Level	g
50	ACCEXR	SW Accelerometer X - Roof Level	g
51	ACCWXR	SE Accelerometer X - Roof Level	g
52	POTNYT	NE Potentiometer Y - Bearing-to-table	inches
53	POTSYT	SE Potentiometer Y - Bearing-to-table	inches
54	POTEXT	NW Potentiometer X - Bearing-to-table	inches
55	POTWXT	NE Potentiometer X - Bearing-to-table	inches
56	POTNYB	NW Potentiometer Y - Base Level	inches
57	POTSYB	SW Potentiometer Y - Base Level	inches
58	POTEXB	SW Potentiometer X - Base Level	inches
59	POTWXB	SE Potentiometer X - Base Level	inches

Table 4.10: Instrumentation List (Continued)

Channel	Label	Description	Units
60	POTNY1	NW Potentiometer Y - First Level	inches
61	POTSY1	SW Potentiometer Y - First Level	inches
62	POTEX1	SW Potentiometer X - First Level	inches
63	POTWX1	SE Potentiometer X - First Level	inches
64	POTNY2	NW Potentiometer Y - Second Level	inches
66	POTSY2	SW Potentiometer Y - Second Level	inches
67	POTEX2	SW Potentiometer X - Second Level	inches
68	POTWX2	SE Potentiometer X - Second Level	inches
69	POTNYR	NW Potentiometer Y - Roof Level	inches
70	POTSYR	SW Potentiometer Y - Roof Level	inches
71	POTEXR	SW Potentiometer X - Roof Level	inches
72	POTWXR	SE Potentiometer X - Roof Level	inches
73	NOVAE1	Level 1 NOVATEC - East Frame	inches
74	NOVAW1	Level 1 NOVATEC - West Frame	inches
75	NOVAE2	Level 2 NOVATEC - East Frame	inches
76	NOVAW2	Level 2 NOVATEC - West Frame	inches
77	NOVAE3	Level 3 NOVATEC - East Frame	inches
78	NOVAW3	Level 3 NOVATEC - West Frame	inches

5 Experimental Results

The previous chapter of this report describes the experimental program developed to characterize the behavior of multi-stage friction pendulum bearings and simulate the response of a multi-story structure isolated using such devices. A description of the significant results of this experimental program is presented in this chapter, including cyclic characterization and earthquake simulation tests for both Double Pendulum (DP) and Triple Pendulum (TP) bearing specimens.

5.1 CYCLIC CHARACTERIZATION OF ISOLATOR BEHAVIOR

The harmonic shaking table tests described in Chapter 4 were conducted to establish the properties of the isolation devices, and to calibrate analytical models for use in subsequent parametric studies. Two classes of friction pendulum bearings were tested on the three-story steel frame described in Section 4.2.1 of this report. This test program was designed such that a range of isolator demands were observed and recorded. The demand parameters targeted for investigation as part of this test program were (a) isolator displacement; (b) isolator velocity; and (c) axial load/uplift.

For each cyclic characterization test, the force-displacement behavior was recorded at each bearing using wire potentiometers between the simulator table and the base plate of the columns, and load cells under each isolator specimen. In general, hysteresis of each bearing is reported as *normalized* shear force vs. displacement, where the normalized shear force at time t_i is the actual shear force at time t_i divided by the normal force at time t_i. This is a convenient representation that can be compared to the theoretical normalized shear vs. displacement relations developed in Chapter 3. Only in cases where uplift occurs in a bearing is this normalization abandoned, since dividing by an axial force of zero yields a singularity.

5.1.1 Double Pendulum Bearings

The DP bearings used for the experimental program are described in Section 4.2.2.1 of this report. The composite liner for each sliding mechanism was designed to provide the same friction coefficient. This results in the initiation of sliding on each surface at the same lateral force, leading to cyclic behavior that is in principle indistinguishable from a single pendulum bearing [Fenz et al., 2006]. This provides a valuable basis of comparison with the results of the triple pendulum experimental program, particularly with respect to isolator demand and floor accelerations.

5.1.1.1 Force-Displacement Behavior

The double pendulum bearing specimens for this test program are not expected to exhibit multi-stage behavior. Therefore, a single, carefully designed test is capable of exciting the structure to a sufficient number and variety of displacement and velocity excursions to completely characterize the parameters of the isolation system. Recall that the DP bearing supporting weight W, with two distinct friction coefficients (μ_1 and μ_2), dish radii (R_1 and R_2), and slider heights (h_1 an h_2) follows the force-displacement relationship

$$V = \left(\frac{W}{R_1 + R_2 - h_1 - h_2} \right) u + \frac{W\mu_1 \left(R_1 - h_1 \right) + W\mu_2 \left(R_2 - h_2 \right)}{R_1 + R_2 - h_1 - h_2} \tag{5.1}$$

For this specimen, $\mu_1 = \mu_2$, $R_1 = R_2$, and $h_1 = h_2$, therefore substituting these values and the normalized shear force $\tilde{V} = V / W$, Equation (5.1) reduces to

$$\tilde{V} = \frac{1}{\underbrace{2(R-h)}_{L}} u + \mu \operatorname{sgn}(\dot{u}) \tag{5.2}$$

Therefore, there are only two physical parameters necessary to completely describe the behavior of the DP bearing specimen, μ and L. The pendulum length L is a geometric quantity, and therefore need not be estimated from experimental data. Based on Section 4.2.2.1 of this report, this pendulum length is $L = 2\left(18.64" - 1.3"\right) = 34.68"$, or a pendulum period of T = 1.88 sec. The friction coefficient, however, is a quantity that must be determined based on experimental results. In general, friction between the composite liner and stainless steel is velocity dependent. A relationship for the friction coefficient μ given the sliding velocity $\dot{u}$ is given by Mokha et al. [1993] as

$$\mu(\dot{u}) = \mu_f - \left(\mu_f - \mu_s\right) e^{-\alpha|\dot{u}|} \tag{5.3}$$

where μ_f and μ_s are the friction coefficients at high velocity and at rest, respectively, and α is a positive number that characterizes the velocity at which the friction becomes essentially rate independent. A suggested value for α in the case of the single-pendulum bearing is 50 sec/m, or 1.28 sec/inch. However, for a particular DP bearing velocity, the sliding velocity on each surface is some fraction of the total velocity, subject to the constraint that $\Sigma_{j=1}^{2}\dot{u}_j = \dot{u}$. If the friction coefficients of each sliding interface are equal, then it is easy to show that

$$\dot{u} = \frac{L_1\dot{u}_1 + L_2\dot{u}_2}{L_1 + L_2} \tag{5.4}$$

Since compatibility dictates that $\dot{u} = \dot{u}_1 + \dot{u}_2$, the sliding velocity on each surface is computed as

$$\dot{u}_1 = \frac{L_1\dot{u}}{L_1 + L_2}, \quad \dot{u}_2 = \frac{L_2\dot{u}}{L_1 + L_2} \tag{5.5}$$

In particular, for a DP bearing of equal friction coefficients and dish radii, each surface slides at a velocity exactly half of the total sliding velocity. This implies that for the parameter α in Equation (5.3) an appropriate value is 0.64 sec/in. Given this parameter, the parameters μ_f and μ_s may be estimated from the experimental data by linear least-squares regression [Stone, 1996]. Here, the response variable is the measured friction force, and the input variable is the sliding velocity. From the harmonic characterization tests, the friction force was measured as the load cell recording at each zero-displacement crossing, neglecting any breakaway friction force. This friction force was normalized by the instantaneous vertical load. Based on least squares estimation, and assuming α = 0.64 sec/in, the following parameters were obtained for Equation (5.3): $\mu_f = 0.0286$, $\mu_s = 0.006$. Figure 5.1 describes the data collected and analyzed to develop these estimates of friction coefficients. Figure 5.2 shows a comparison of cyclic behavior from the experimental results and the model of Equation (5.2) considering the calibrated rate-dependent friction model in Equation (5.3).

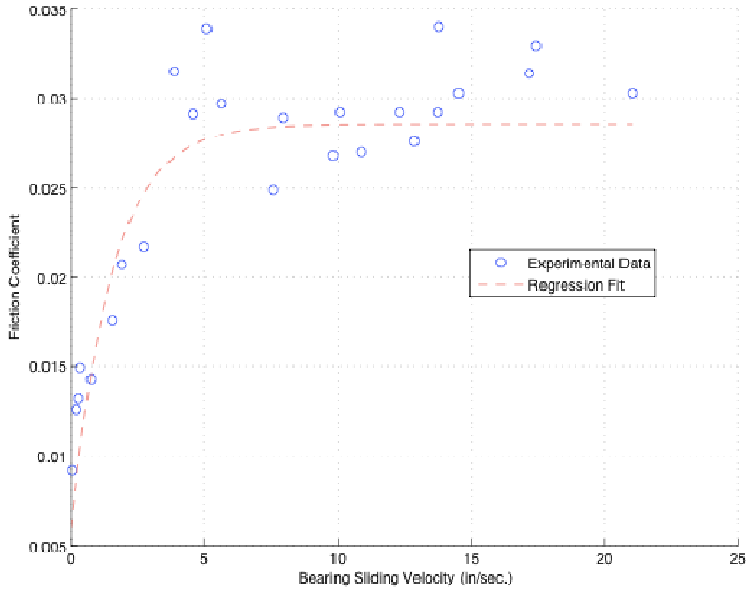

Figure 5.1: Friction coefficient as a function of sliding velocity from sinusoidal experimental data, including least-squares fit of Eq. (5.3)

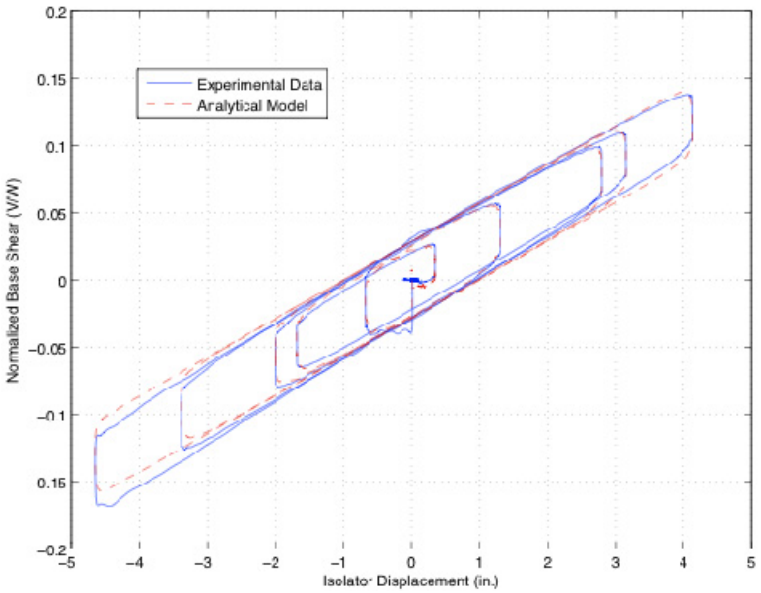

Figure 5.2: Comparison of hysteresis for DP system from experimental results and analytical model considering friction according to Eq. (5.3)

5.1.2 Triple Pendulum Bearing

A complete description of the TP bearings used for the experimental program can be found in Section 4.2.2.2 of this report. This section reports the significant results of the cyclic characterization program described in Section 4.4.

5.1.2.1 Force-Displacement Behavior

Figure 5.3 shows the cyclic behavior of each of the four isolator specimens under low-level harmonic excitation (25% of the full-scale signal, span setting = 158). This level of excitation was sufficiently low such that the shear force in each bearing caused sliding of the inner sliders, but did not overcome the friction coefficient of the lower dish, and hence the upper dish. This corresponds to Stage I sliding, as defined in Section 3.1.1 of this report. It is clear from each of the hysteresis loops (Figure 5.3) for this low-level test that the behavior is identical to the single-pendulum bearing with a coefficient of friction varying between 0.01 and 0.02. It is noteworthy that the face pressure of 2 ksi is much less than the 8 to 10 ksi expected of a full-scale building. It has been noted that such low pressure on the slider can lead to inconsistent estimates of friction coefficients from bearing to bearing. However, the data of Figure 5.3 suggests relative consistency of the inner slider friction coefficient for all four bearings. There is also a noticeable lack of increase in first-cycle force output due to breakaway friction, indicating that the lubricated spherical surface is likely not prone to breakaway frictional effects.

Figure 5.4 shows the cyclic behavior of each bearing under a moderate-level harmonic test (50% of the full-scale signal, span setting = 316). It is evident from the recorded hysteresis for each bearing that this level of excitation induced sufficient shear force to initiate sliding on the lower dish, thus corresponding to Stage II sliding. There is an observable increase in first-cycle force output at the second sliding interface. This effect and its likely source are addressed later in this section.

Figure 5.5 shows the cyclic behavior of each bearing under a high-level harmonic test (79% of the full-scale signal, span setting = 500). From these data, it is clear that the hysteresis shows the expected softening at the largest displacement excursion. This observed multi-linear force displacement indicates that this level of excitation induced sufficient shear force to initiate sliding on the upper dish, thus corresponding to Stage III sliding. The data of Figure 5.6, showing response under a high-level harmonic test (95% of the full-scale signal,

span setting = 600) gives clear indication of Stage III sliding, although there no evidence of stiffening due to the bottom slider reaching the deformation capacity of the lower dish. There is also a noticeable first-cycle increase in friction along the second sliding interface, in both the initial initiation of sliding and on the first instance of velocity reversal, but a lack of this same first-cycle effect along the third sliding interface.

Based on extensive investigations into the cause of the increase in friction in the first cycle of slip along the second sliding interface of the model bearings, the manufacturer has concluded that a number of simultaneous factors contributed to the observed effect. These factors are related to changes in the bonding agent utilized, a result of the scale bearings described in this report as being part of a research and development effort. Further experimentation is expected to verify that the first-cycle force increase effect is peculiar to these tests. In any case, bearings are tested as part of a prototype and production program in actual applications, and specifications limit such first-cycle effects as observed from project-specific tests.

Figure 5.7 describes the cyclic behavior of each bearing under the most extreme harmonic test conducted as part of this characterization program (112% of the full-scale signal, span setting = 710). From these data, there is observable stiffening of each specimen, indicating Stage IV and V sliding. The extreme stiffening beyond a displacement amplitude of 5 in. indicates Stage V sliding, or deformation along the second and third sliding interfaces that has reached the physical limit of both the lower and upper spherical surfaces. It is noteworthy that the north bearings exhibit Stage V sliding on the negative displacement excursion, whereas the south bearings show the same response, but on the positive displacement excursion. This is likely evidence of some permanent internal offset of the slider at the start of the test, since there must have been a difference in the accumulated deformation on the second and third pendulum mechanisms. However, the hysteresis of the combined isolation system, shown in Figure 5.8, indicates symmetric cyclic behavior. It is a general observation that the initial internal deformations of each pendulum mechanism do not affect the global cyclic behavior of the system.

A description of an experimental single-cycle hysteresis loop from each level of displacement demand for the TP isolation system is shown in Figure 5.9. All five sliding stages can be observed from these data. Additionally, Figure 5.10 and Figure 5.11 show a summary of normalized experimental hysteresis and platform displacement, respectively, of

the overall TP system for select sinusoidal characterization tests. The overall DP bearing hysteresis is shown in the lower right for comparison. In the next section, the experimental data are used to estimate the friction coefficient of each sliding interface. These estimates of friction are then used to calibrate the cyclic model described in Section 3.3.4.

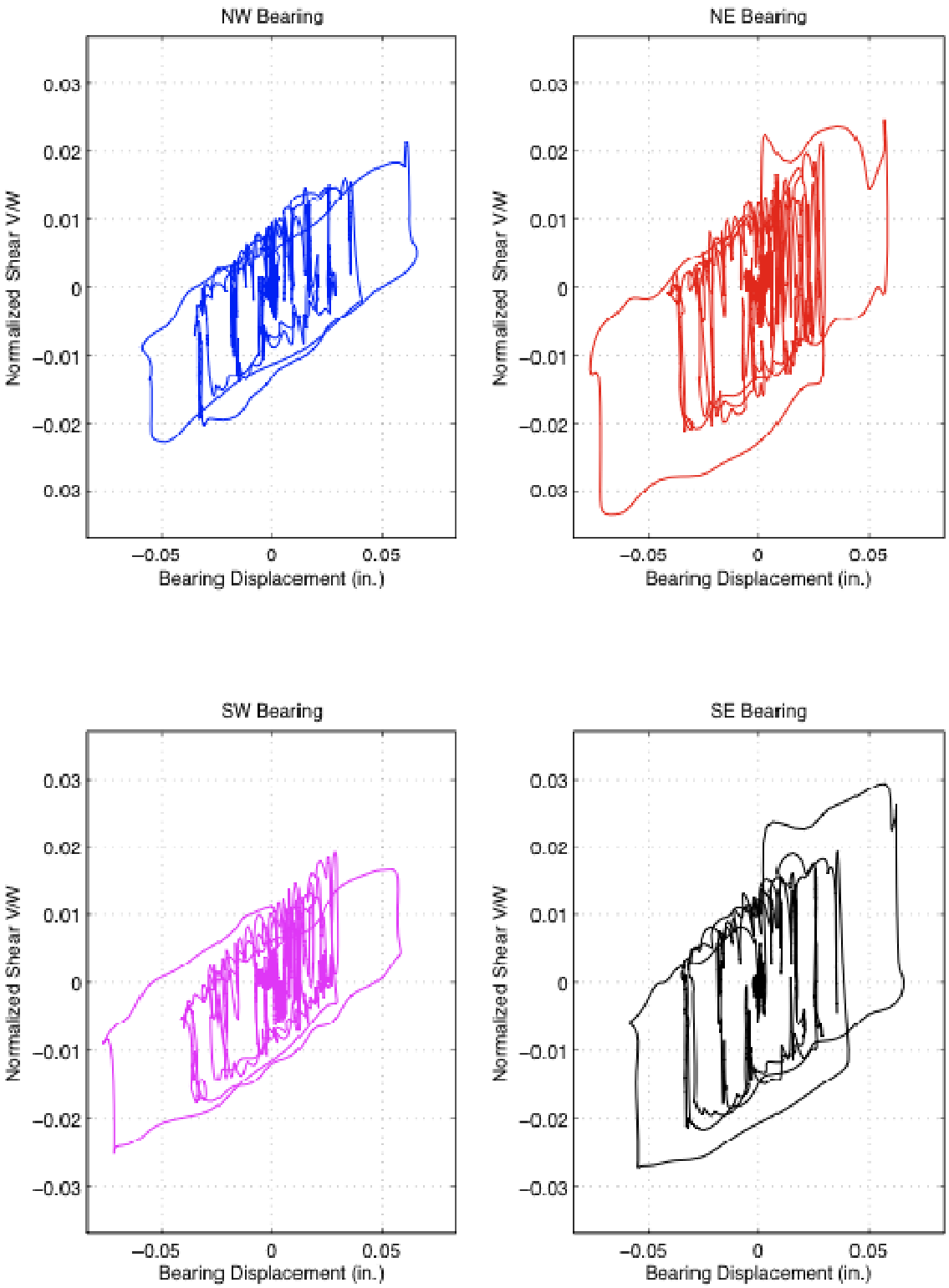

Figure 5.3: Cyclic behavior for all TP bearings in Sine-10 Test (ID 170830)

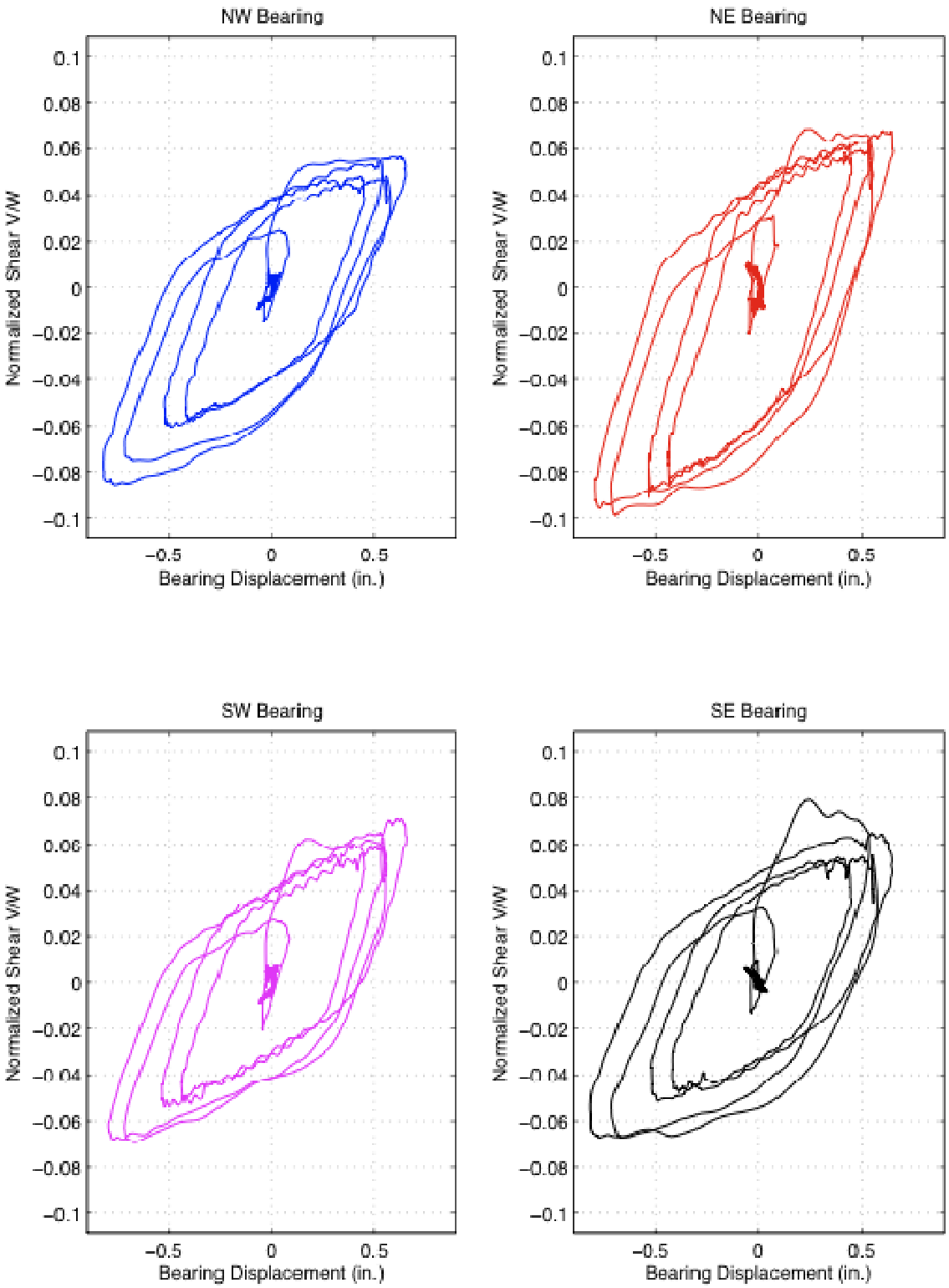

Figure 5.4: Cyclic behavior for all TP bearings in Sine-50 Test (ID 170912)

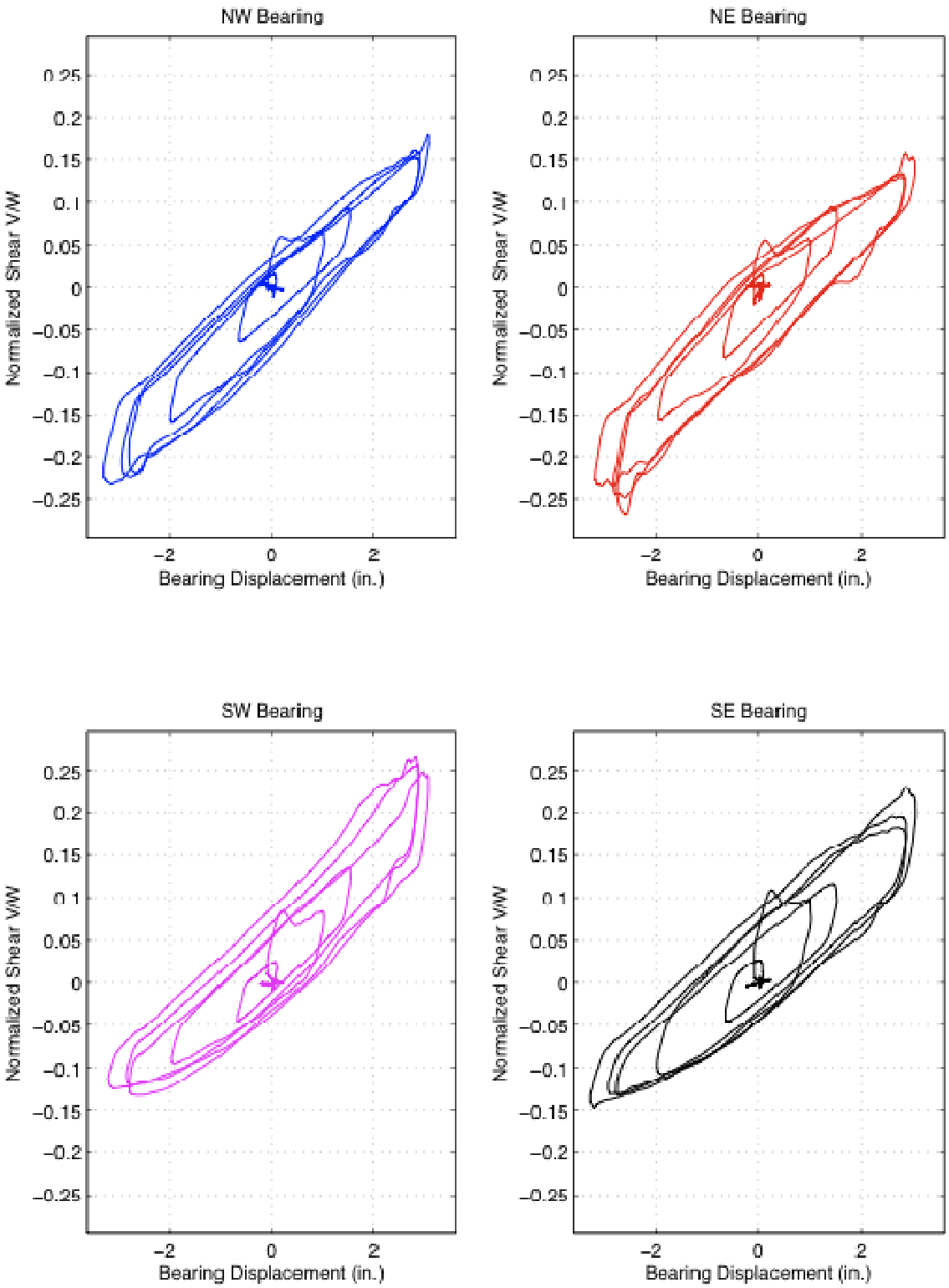

Figure 5.5: Cyclic behavior for all TP bearings in Sine-79 Test (ID 171402)

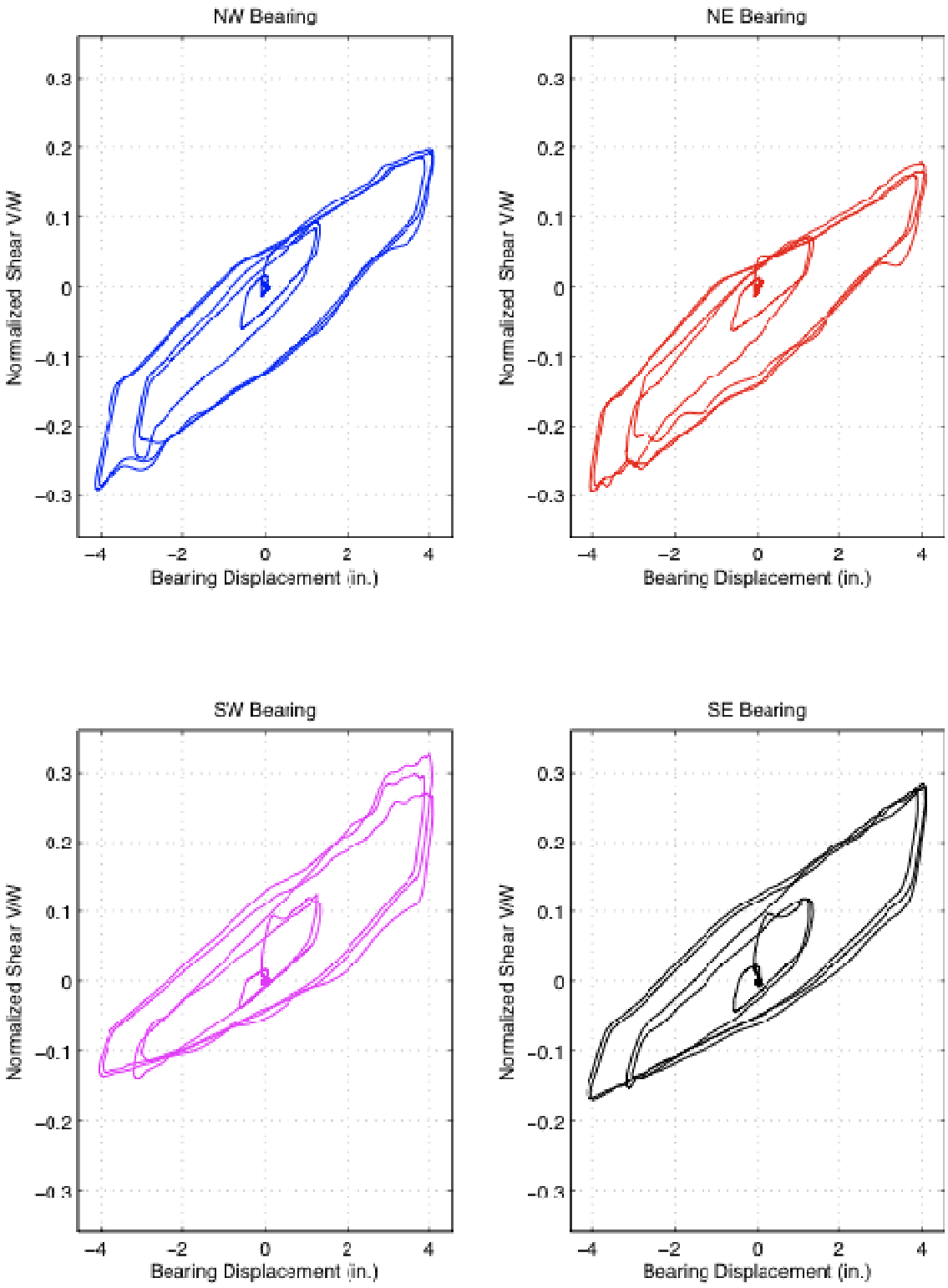

Figure 5.6: Cyclic behavior for all TP bearings in Sine-95 Test (ID 171519)

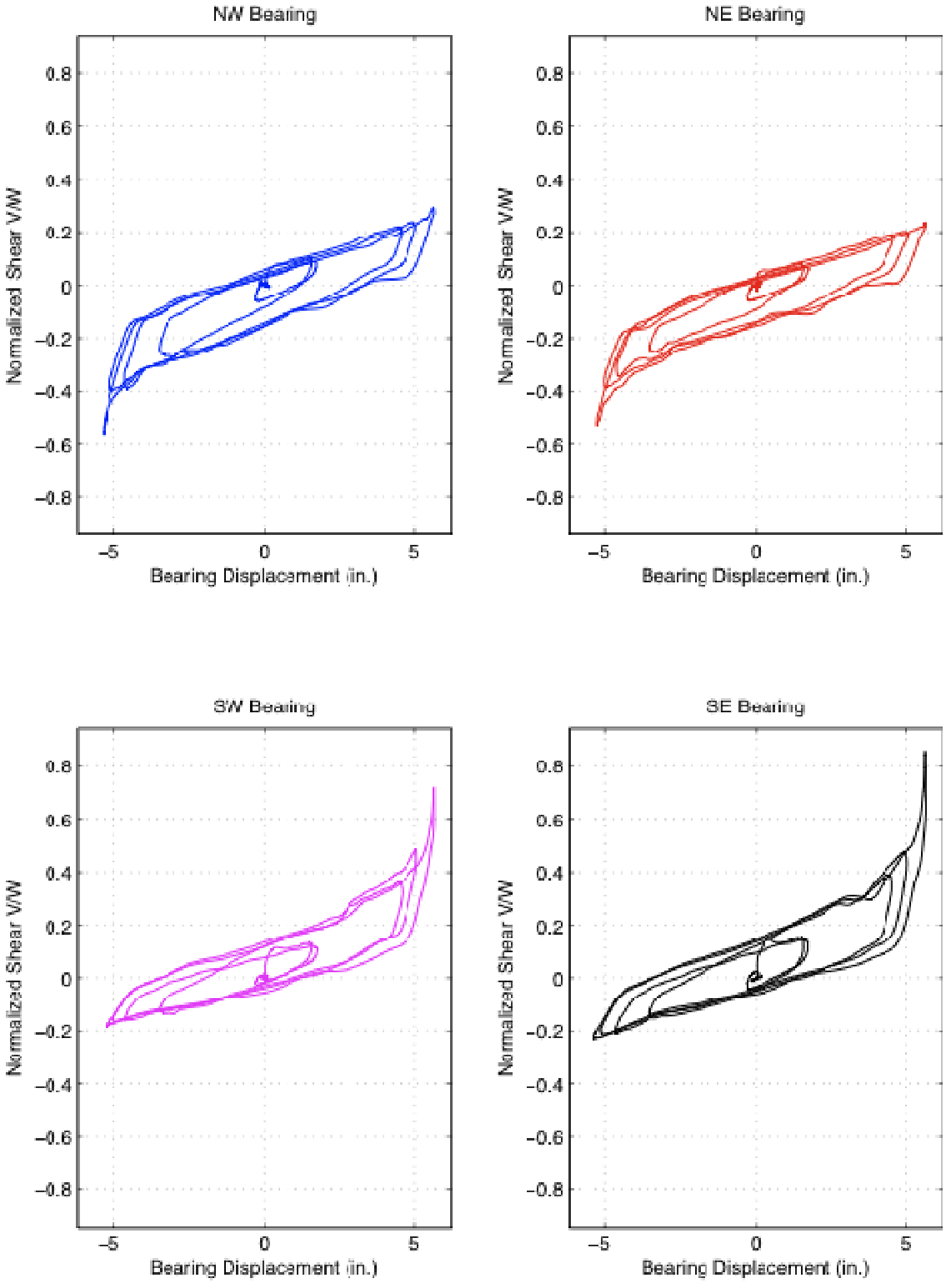

Figure 5.7: Cyclic behavior for all TP bearings in Sine-117 Test (ID 174624)

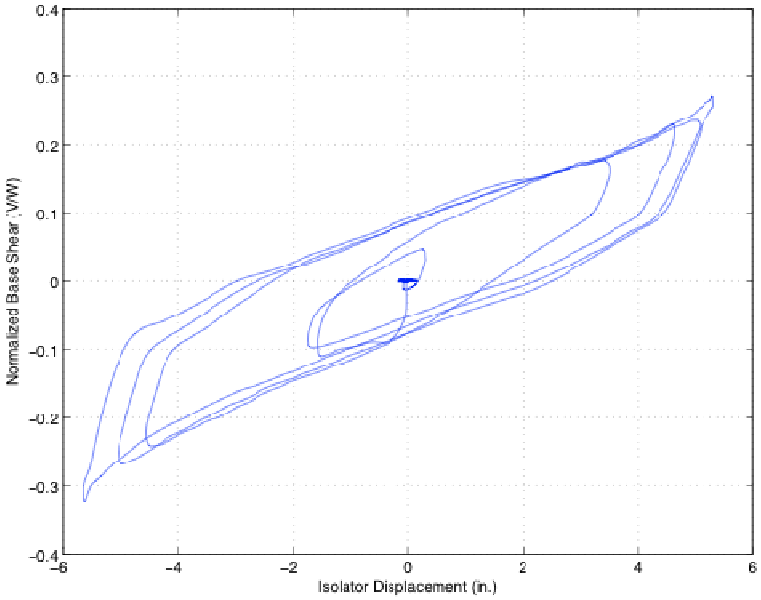

Figure 5.8: Cyclic behavior for overall TP isolation system in Sine-117 Test (ID 174624)

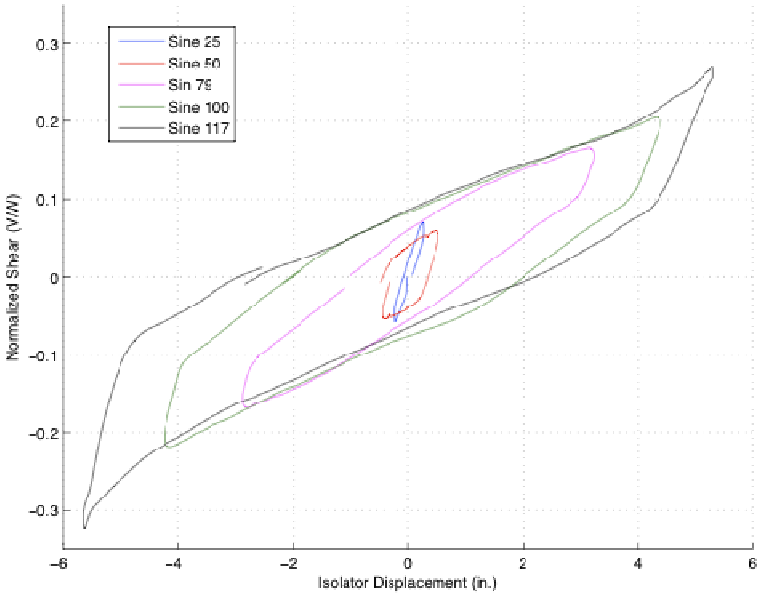

Figure 5.9: Single-cycle hysteresis for overall TP system considering multiple levels of displacement

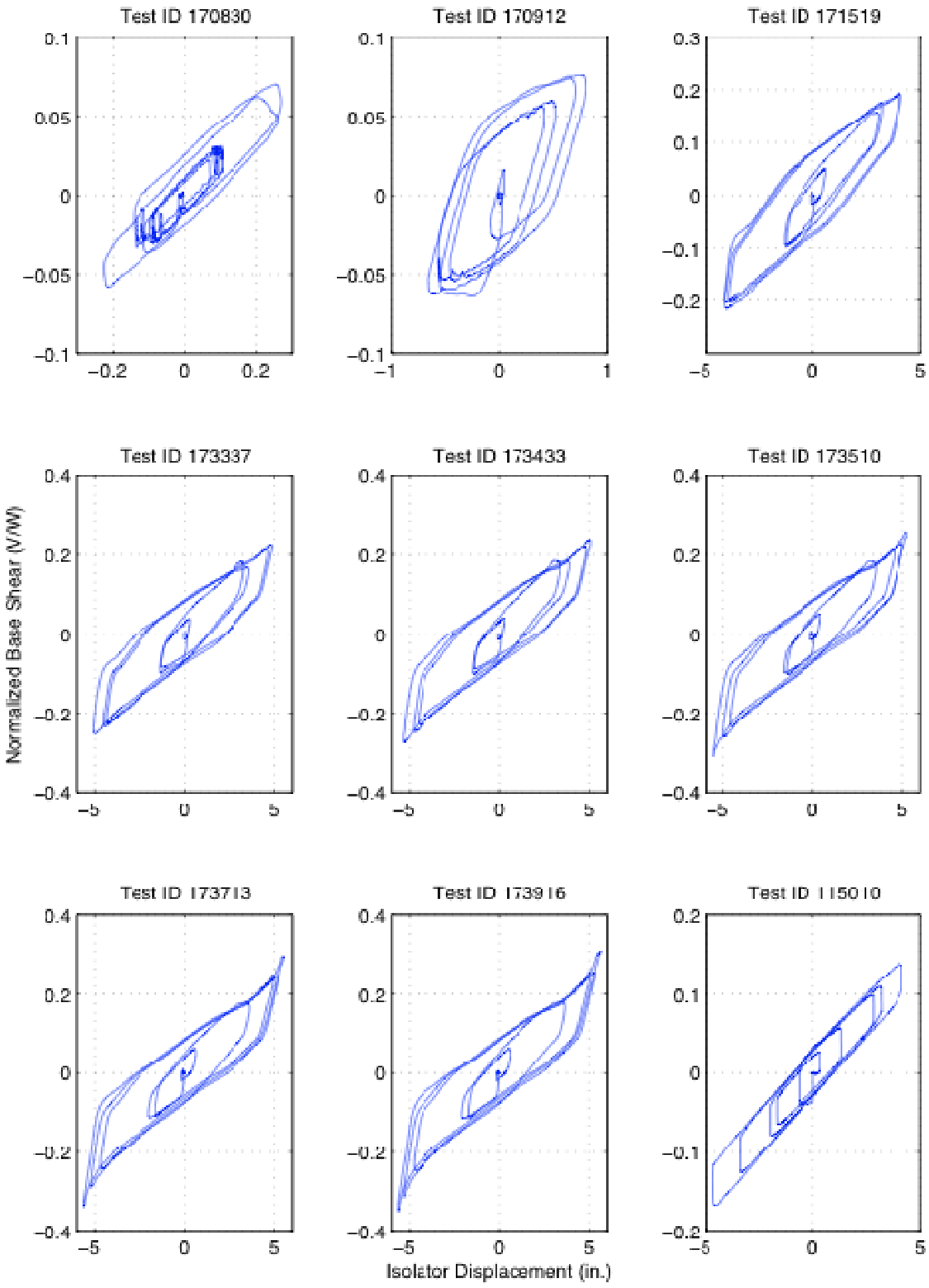

Figure 5.10: Summary of normalized experimental hysteresis for overall TP system, for select sinusoidal characterization tests (DP bearing shown lower right for comparison)

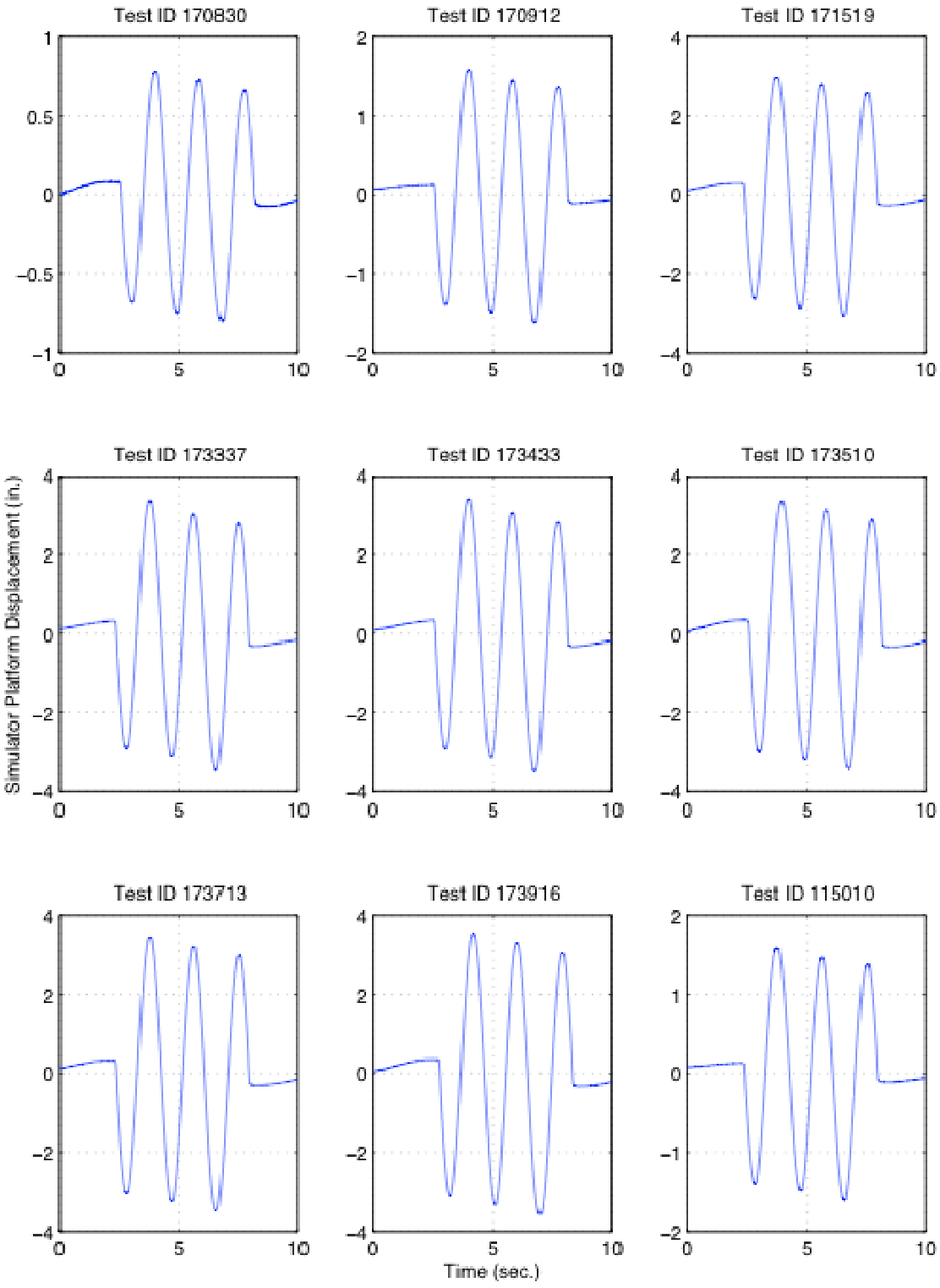

Figure 5.11: Summary of recorded simulator platform displacements for select sinusoidal characterization tests (experimental hysteresis for these tests shown in Figure 5.10)

5.1.2.2 Estimation of Friction Coefficients

The cyclic model for a TP bearing developed in Chapter 3 accepts the three pendulum lengths, L_1, L_2, and L_3, and the three friction coefficients, μ_1, μ_2, and μ_3, as input parameters. Therefore, for a particular bearing test specimen, it is necessary to estimate these parameters to calibrate a cyclic model for comparison. Whereas the pendulum lengths are each a function of two precise geometric quantities (dish radius and slider height), the friction coefficients can only be determined experimentally. In practice, these friction coefficients are specified by a range of acceptable values, and a prototype test program is conducted to verify that the measured friction is within this acceptable range. These prototype tests are generally conducted only in a single direction, on a bearing that is initially undeformed (and hence all mechanisms are aligned). A natural question therefore emerges: given a set of cyclic data, how is each friction coefficient measured? For the single-pendulum bearing, where there is only one friction coefficient, the measured friction coefficient is simply the measured shear force divided by the measured vertical load at the instant of zero lateral displacement. Where there are numerous displacement cycles, multiple samples of this friction coefficient are measured, and the "true" friction coefficient may be estimated as the mean of the sample. Where there are multiple distinct pendulum mechanisms, however, an alternate procedure is necessary to form estimates of each distinct friction coefficient. As with a *single*-pendulum bearing only *one* cyclic test is necessary to characterize the friction coefficient, it will be shown that for a *triple* pendulum bearing, *three* cyclic tests are necessary to characterize the three friction coefficients. In general, *n* independent cyclic tests are necessary to characterize a bearing with *n* independent pendulum mechanisms, so long as each test induces deformation on a distinct pendulum mechanism.

5.1.2.2.1 Friction Coefficient of Inner Slider (μ_1)

The task of estimating the friction coefficient of the inner slider is identical to that of the single-pendulum bearing, since the cyclic behavior is equivalent for both. From the harmonic tests that only activate sliding on the first pendulum mechanism, the measured friction coefficient is simply half the height of the hysteresis loop at a displacement of zero. That is, let H_1 be the height of the hysteresis loop, shown below in Figure 5.12. Then, an estimate of μ_1 is given as $\hat{\mu}_1 = H_1 / 2$, where the hat denotes a parameter that is measured experimentally.

The zero-displacement intercept is a particularly convenient measurement from experimental data since it is uniquely defined, and hence forms a basis for our measurements of friction in this section.

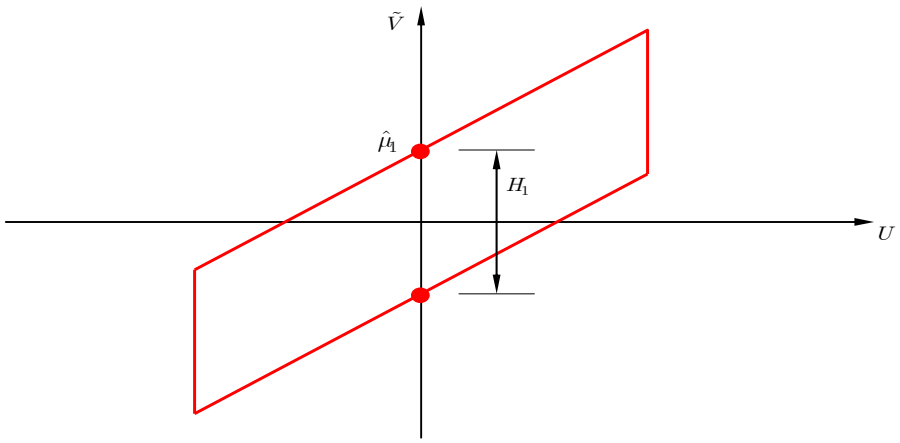

Figure 5.12: Idealized hysteresis loop for Stage I sliding, indicating the measured height H_1 at zero displacement

5.1.2.2.2 Friction Coefficient of Bottom Slider (μ_2)

Once the first friction coefficient has been estimated, it is then possible to estimate the second friction coefficient. A second cyclic test is required, the displacement amplitude of which must be such that sliding on the lower surface is initiated, but not so large as to induce sliding on the upper surface. The resulting hysteresis loop exhibits two zero-displacement intercepts, and the height between them is denoted H_2. We can define an *effective* second friction coefficient as $\hat{\mu}_{2e} = H_2 / 2$, where H_2 is shown below in Figure 5.13.

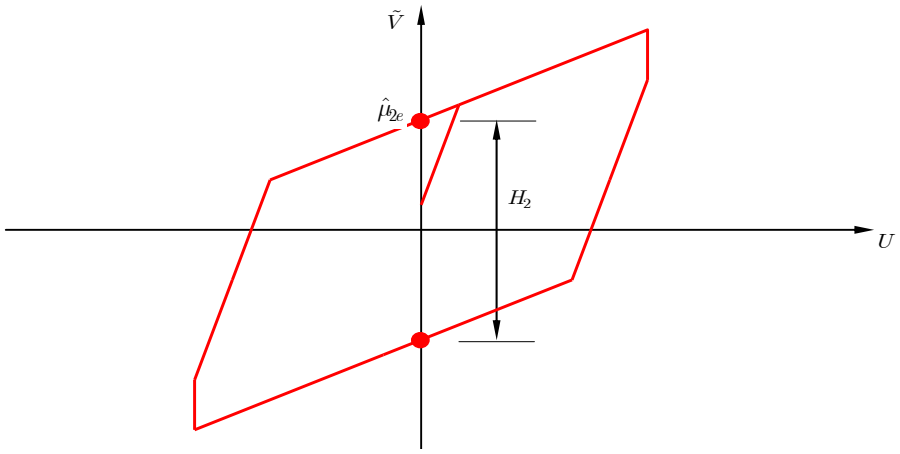

Figure 5.13: Idealized hysteresis loop for Stage II sliding, indicating the measured height H_2 at zero displacement

This effective friction coefficient $\hat{\mu}_{2e}$ is *not* equal to the second friction coefficient μ_2 since the force at which sliding initiates is slightly larger than the zero-displacement intercept (due to flexibility in the first pendulum mechanism). However, we are interested in estimating the second friction coefficient μ_2 as part of calibrating the cyclic model, so a minor computation is required. Knowing the pendulum lengths L_1 and L_2 (by geometry), and having obtained an experimental estimate of the first friction coefficient $\hat{\mu}_1$ above in Section 5.1.2.2.1, the second friction coefficient is estimated as

$$\hat{\mu}_2 = \frac{\hat{\mu}_{2e}\left(L_1 + L_2\right) - 2\hat{\mu}_1 L_1}{L_2 - L_1} \tag{5.6}$$

5.1.2.2.3 Friction Coefficient of Top Slider (μ_3)

After the first two friction coefficients have been estimated, it is possible to estimate the third and final friction coefficient μ_3 through an additional cyclic test where sliding on the upper surface is activated. The resulting hysteresis loop again exhibits two zero-displacement intercepts, and the height between them is denoted H_3. Similar to Stage II sliding above, we can define an *effective* third friction coefficient as $\hat{\mu}_{3e} = H_3 / 2$, where H_3 is shown below in Figure 5.14.

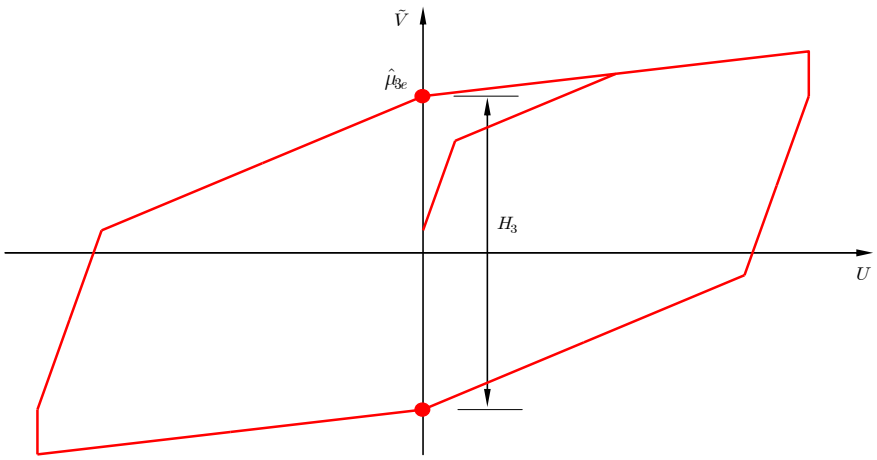

Figure 5.14: Idealized hysteresis loop for Stage III sliding, indicating the measured height H_3 at zero displacement

We are again interested in estimating the *actual* third friction coefficient μ_3 as part of calibrating the cyclic model, so another computation is required. Knowing the pendulum lengths L_1, L_2, and L_3, and having obtained experimental estimates of the first and second friction coefficients $\hat{\mu}_1$ and $\hat{\mu}_2$ above in Sections 5.1.2.2.1 and 5.1.2.2.2, the third friction coefficient is estimated as

$$\hat{\mu}_3 = \frac{\hat{\mu}_{3e}(L_2 + L_3) - \hat{\mu}_2(L_2 - L_1) - 2\hat{\mu}_1 L_1}{L_3 - L_1} \tag{5.7}$$

Given the estimates of all three friction coefficients, is it possible to fully calibrate, based on experimental results, the cyclic model previously developed. This friction coefficient estimation procedure is also useful in determining acceptance of the results of prototype and production tests compared to project specifications. Whereas the design engineer assumes a set of friction values (and their allowable variation) for design, the outlined procedure above can be used to verify that test results demonstrate compliance with the assumed friction coefficients.

5.1.2.3 Behavior Subject to Uplift

To investigate the stability of TP isolators under significant overturning-induced axial forces, including uplift, a series of harmonic tests was conducted along the transverse axis of the building specimen. This direction has a height-to-width aspect ratio of approximately 3:1, slender enough such that uplift in the bearings is possible given the performance limits of the

simulator platform. Figure 5.15 presents the axial force histories for each bearing, and instances of bearing uplift are noted. The duration of observed uplift did not exceed 0.25 seconds in any case. However, subsequent to uplift, each bearing underwent one full cycle of displacement, and ejection of the slider would be evident from the hysteresis. Figure 5.16 and Figure 5.17 present the hysteresis for each bearing and of the total isolation system, respectively, under the uplift test. It is clear that the cyclic behavior does not degrade or change significantly following the uplift excursion. The model was instantaneously supported by only two of the four isolators, exhibiting a rocking mode of behavior. Full-scale buildings have overturning restricted to only those columns engaged as part of the lateral force resisting system, whereas most columns resist gravity load only. As a result, the majority of isolators do not experience seismic-induced variation of axial load beyond that due to vertical acceleration. The importance of the uplift test was to demonstrate stability of the slider assembly in the event of short-duration uplift and re-engagement under a very rare earthquake.

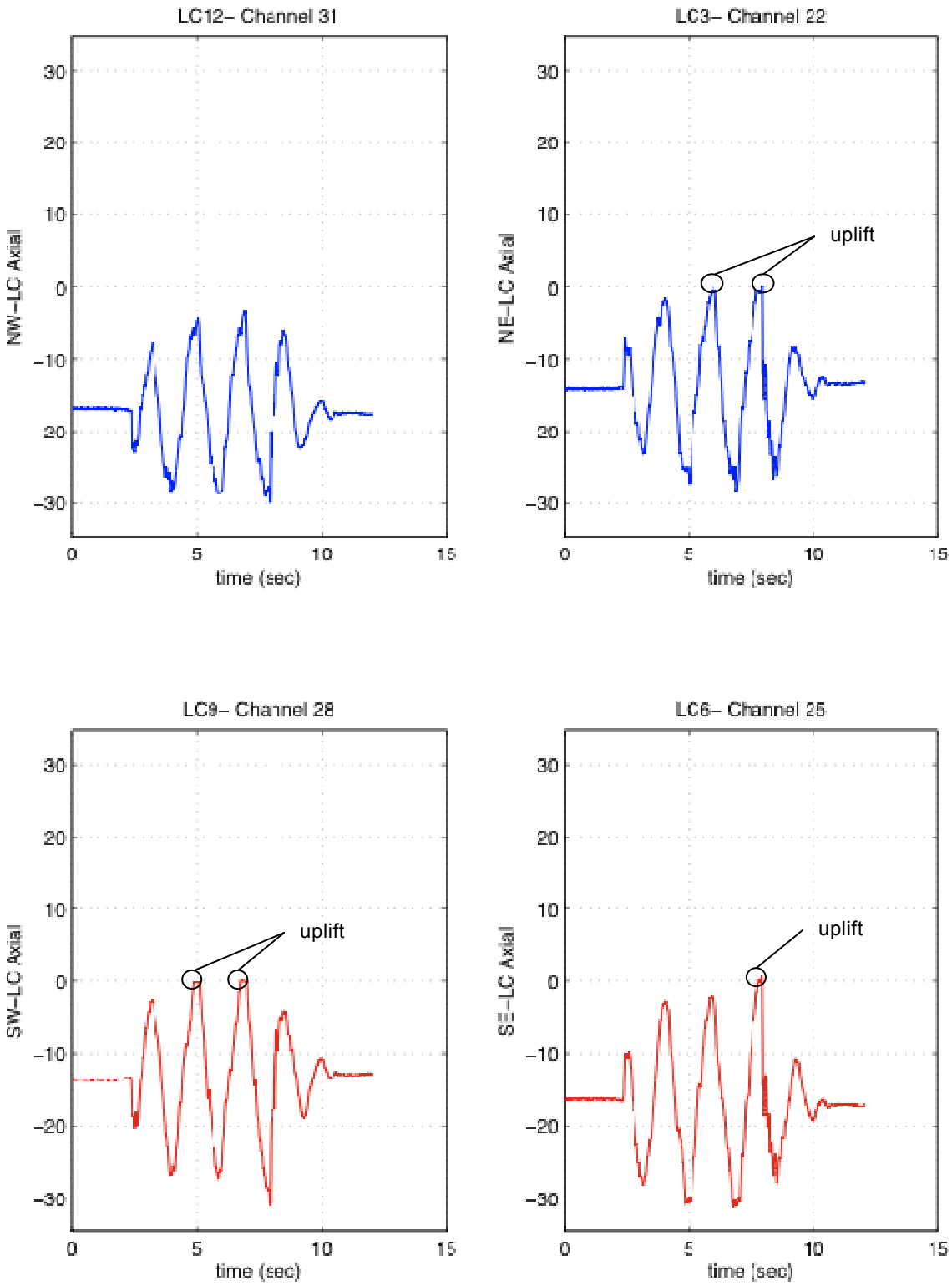

Figure 5.15: Axial loads for all bearings in uplift harmonic test (ID 181700)

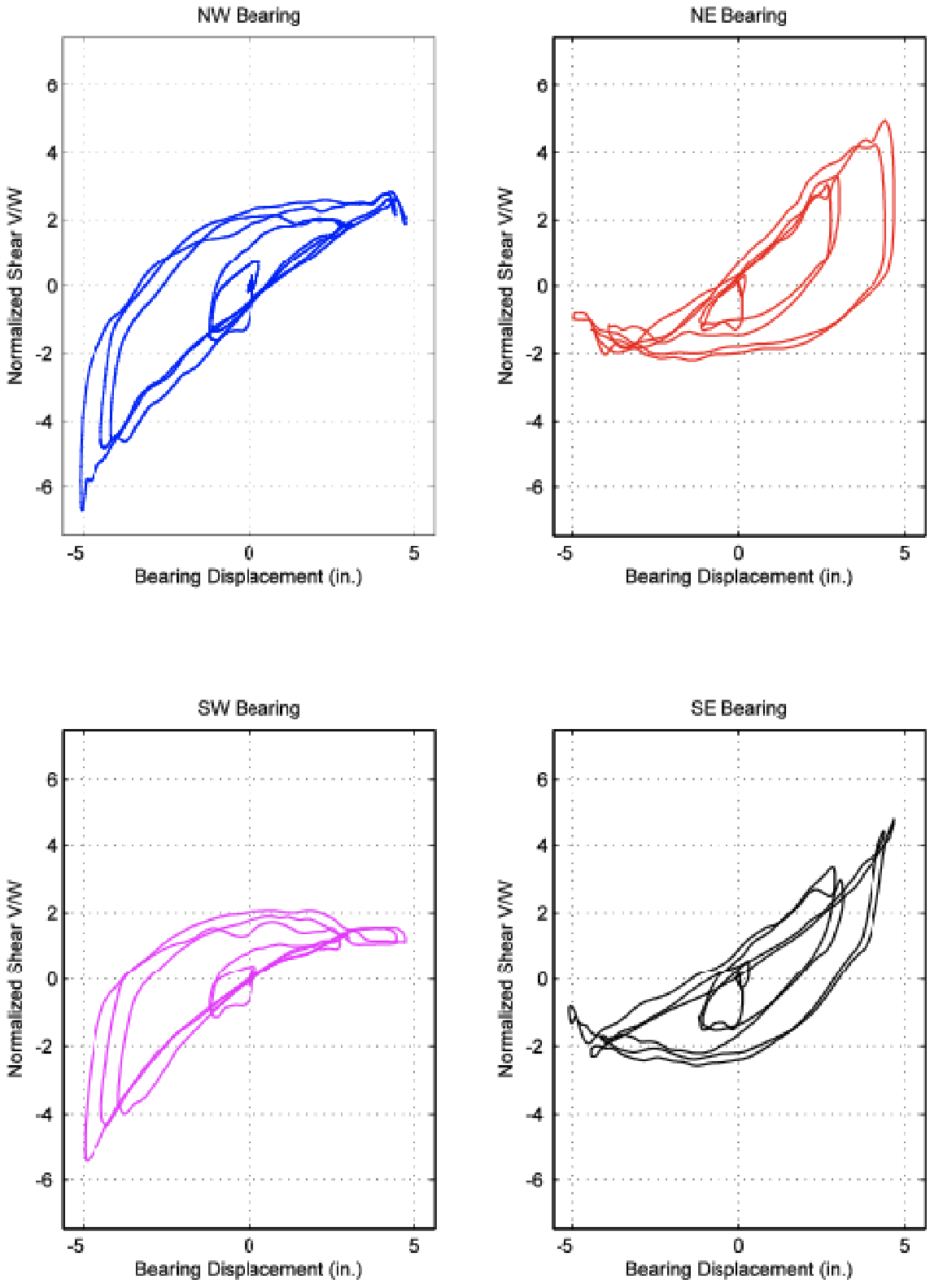

Figure 5.16: Cyclic behavior for all bearings in uplift harmonic test (ID 181700)

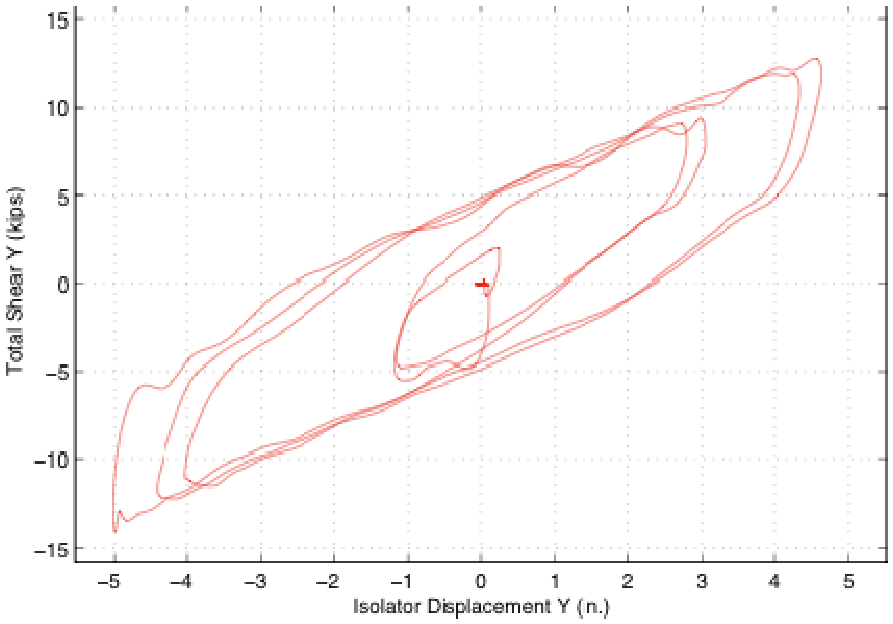

Figure 5.17: Cyclic behavior for overall isolation system in uplift harmonic test (ID 181700)

5.2 COMPARISON OF OBSERVED BEHAVIOR WITH CYCLIC MODEL OF THE TRIPLE PENDULUM BEARING

This section describes the cyclic response of the TP isolation system and compares the experimentally observed behavior with the analytical behavior determined from the Cyclic Series Model (CSM) developed in Section 3.3.4.

5.2.1 Stage I Sliding

A series of low-amplitude cyclic tests was performed to characterize the behavior of the inner pendulum mechanism. This mechanism defines the initial sliding phase described in Section 3.3.1.1 of this report. Under small excitation, from either wind, ambient lateral vibration, or low-level seismic activity, deformation of the bearings will occur entirely on the inner slider.

The necessary parameters to define the behavior of the inner slider are the effective pendulum length, L_1, and the coefficient of friction, μ_1. The cyclic behavior under small deformation is identical to the original single-pendulum FP bearing, and a method to estimate the first friction coefficient is described above in Section 5.1.2.2.1. This procedure leads to an estimate of friction coefficient $\hat{\mu}_1 = 0.012$. Figure 5.18 below shows a force-displacement

relationship from a low-level cyclic test (SINE-10) including both experimental and analytical results given this friction estimate.

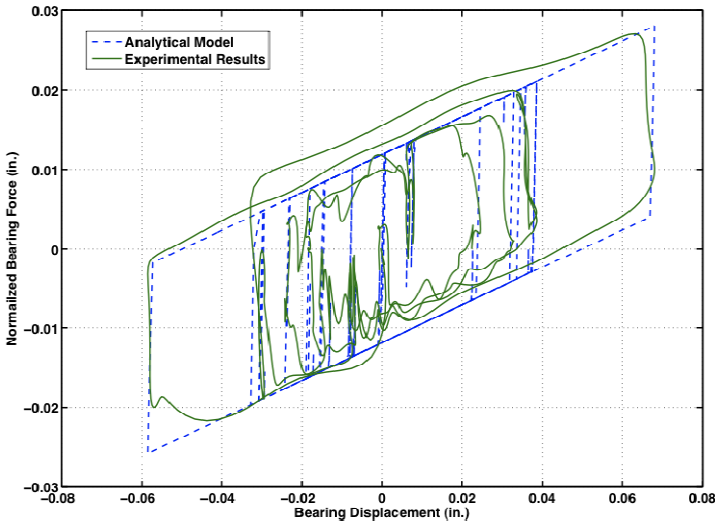

Figure 5.18: Comparison of experimental and analytical results of total system hysteresis for test SINE-10.

The same data are prepared using a typical displacement-based model, which can be implemented for a single-pendulum mechanism as

$$\tilde{V}(u,\dot{u}) = \frac{1}{L_1}u + \mu(\dot{u})\,\mathrm{sgn}(\dot{u}) \tag{5.8}$$

where $\tilde{V} = \tilde{V}/W$ is the normalized shear force introduced in Chapter 3, and $\mu(\dot{u})$ is the friction coefficient, which generally depends on the velocity. Setting $\mu(\dot{u}) = \mu$ is equivalent to the previous velocity-independent formulation. An alternate expression for the friction force can be taken as that of Equation (5.3). Implementing this model gives the alternate comparison of force-displacement loops shown below in Figure 5.19. For the remainder of the comparisons in this chapter, the slight velocity dependence of the friction force will be neglected.

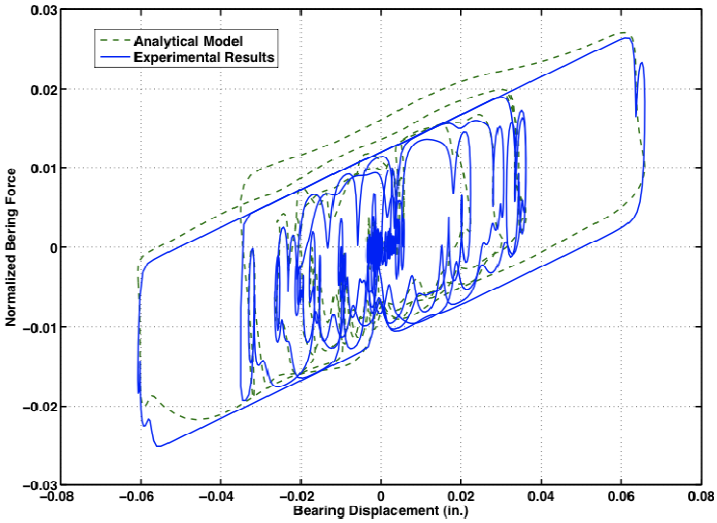

Figure 5.19: Comparison of experimental and analytical results of total system hysteresis for test SINE-10 (rate dependence of friction coefficient included)

5.2.2 Stage II Sliding

To evaluate the model for sliding in Phase II, or both the inner slider and bottom spherical surface, the data of the test SINE-50 is observed. In particular, a value of friction must be selected for the model that compares favorably with the experimental data. The friction coefficient estimation procedure of Section 5.1.2.2.2 is implemented. Based on the previous estimate of $\hat{\mu}_1 = 0.012$ and the data of the test SINE-50, an estimate of the second friction coefficient is $\hat{\mu}_2 = 0.052$. As a basis of evaluation of the adequacy of this estimate, the energy-dissipation history is computed for the model and the experimental data. This comparison is appropriate here since the energy dissipation history is entirely a function of the friction coefficients. Energy dissipation is defined as

$$E_d = \int_{\text{all } u} p(\hat{u})\, d\hat{u} = \int_{t_i}^{t_f} p(\tau)\, \dot{u}(\tau)\, d\tau \tag{5.9}$$

where p is the force, and u is the displacement. This may be specialized to the case of discrete time intervals by observing that the force at a time step may be approximated as the average force at the beginning and the end of the time step. So too can the differential displacement be approximated by the displacement step over the time step. Making these substitutions, Equation (5.9) becomes

$$E_d = \frac{1}{2}\sum_{i=1}^{n-1}(p_{i+1} + p_i)(u_{i+1} - u_i) \tag{5.10}$$

The above equation is used in subsequent calculations of energy dissipation over time.

Assuming a friction coefficient at the second sliding interface of $\mu_2 = 0.052$, a comparison of the force-displacement relation for the SINE-50 test is shown below in Figure 5.20, and the energy dissipation history is shown in Figure 5.21.

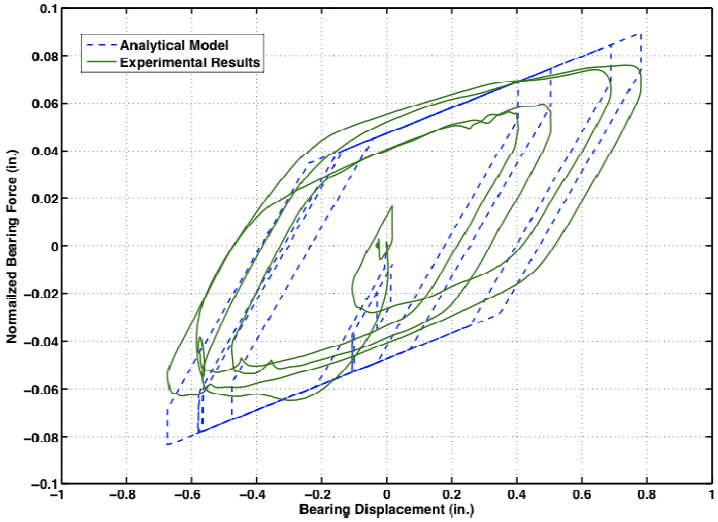

Figure 5.20: Comparison of experimental and analytical results of total system hysteresis for test SINE-50.

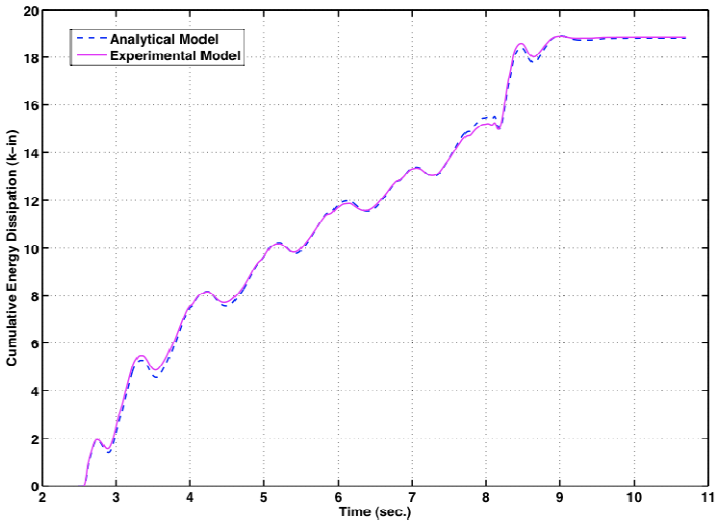

Figure 5.21: Comparison of experimental and analytical results of total energy dissipation for test SINE-50.

5.2.3 Stage III Sliding

The process of selecting a proper friction coefficient for the third and final slider is summarized above in Section 5.1.2.2.3. The SINE-95 test was used for this purpose because the imposed displacements were sufficient to cause sliding on both upper and lower concave surfaces, but not to the extent that stiffening was initiated. Given the previous estimates of $\hat{\mu}_1 = 0.012$ and $\hat{\mu}_2 = 0.052$, implementing the estimation procedure for the third friction coefficient yielded $\hat{\mu}_3 = 0.14$. A comparison of the force-displacement relation for the SINE-95 test is shown below in Figure 5.22, and the energy dissipation history is shown in Figure 5.23.

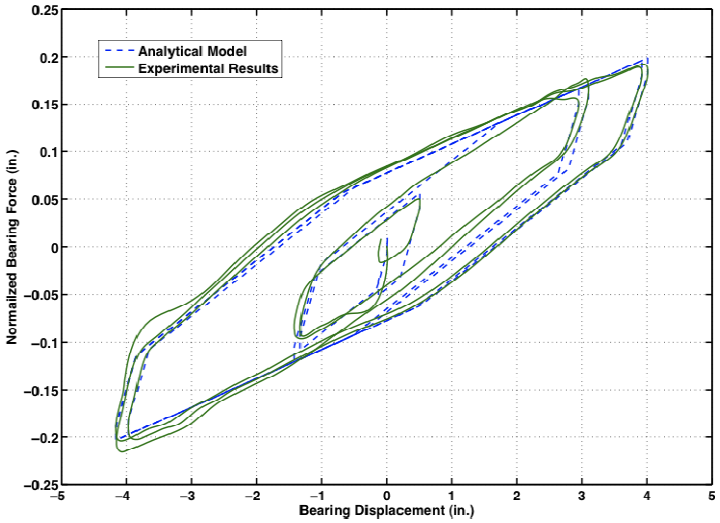

Figure 5.22: Comparison of experimental and analytical results of total system hysteresis for test SINE-95.

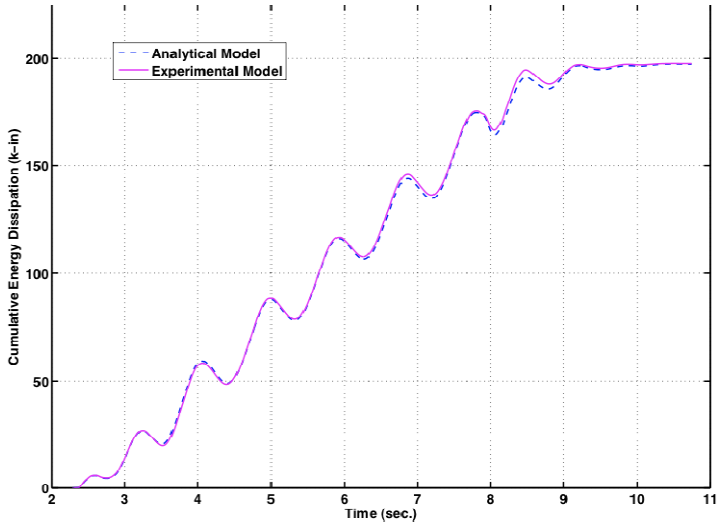

Figure 5.23: Comparison of experimental and analytical results of total energy dissipation for test SINE-95.

5.2.4 Stage IV Sliding

Given the above estimated friction coefficients and the geometry of the TP bearing specimen, the cyclic behavior under any displacement amplitude may be computed. Of particular interest is the stiffening regime of the TP bearing, since this mode of sliding is intended to control isolator displacements under very large earthquakes. A comparison of the experimental hysteresis and the analytical CSM under Stage IV sliding is shown below in Figure 5.24. Here it is evident that the transition to isolation system stiffening is correctly captured for both positive and negative displacement excursions greater than 4 inches.

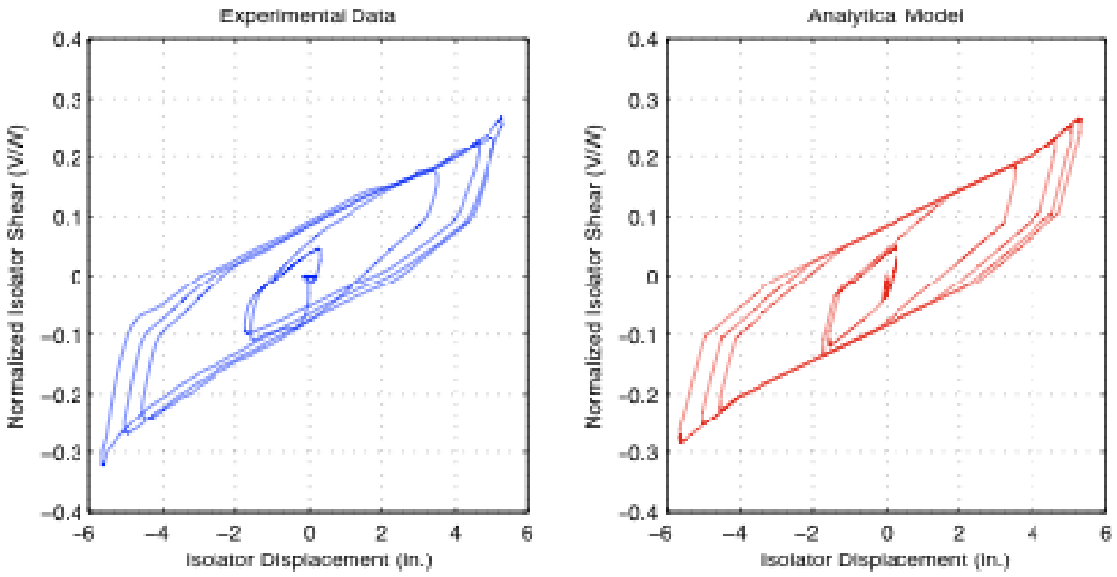

Figure 5.24: Comparison of experimental and force-based analytical results of total system hysteresis for test SINE-112 (ID 174624)

5.3 SEISMIC RESPONSE OF ISOLATION SYSTEMS

An extensive earthquake simulation program was described in Chapter 4 of this report. The observed response of both DP and TP isolation systems to this test program is reported here. The key behavioral characteristics investigated as part of the earthquake simulation program are (a) behavior of isolators under a range of levels of seismic intensity; (b) dependence of isolator behavior and demand parameters on presence of multi-component ground excitation; and (c) variation in frequency content of recorded floor accelerations over multiple amplitudes of ground excitation. In this section, the reported behavior of the isolation system is the combined response of all four bearing specimens.

5.3.1 Unidirectional Ground Motion

This section describes the cyclic properties of DP and TP bearing specimens under unidirectional ground-motion input for three levels of seismic hazard.

5.3.1.1 Service Level Earthquake (SLE)

To investigate the behavior of the DP and TP bearing specimens under moderate levels of seismic input, a series of shake table tests were conducted with ground motions scaled to

induce small isolator displacements. The input signal scale factor for each specimen is not equal because of the differences in cyclic properties for the two types of bearings, and therefore the expected displacement demand. However, the goal of the SLE test program was to capture isolator behavior under minor levels of shaking and, for the TP specimen, evaluate the response of each sliding mechanism.

The isolation system cyclic response for both DP and TP specimens under the CHY, G03, and SYL signals, scaled to an SLE intensity, are shown in Figure 5.25, Figure 5.26, and Figure 5.27, respectively. Several important observations are made. At the sliding velocity excited by the SLE signals, the effective friction coefficient under Stage II sliding is approximately 0.04, ignoring the first-cycle friction effect explained in Section 5.1.2.1. A similar effect is not observed for the DP specimen.

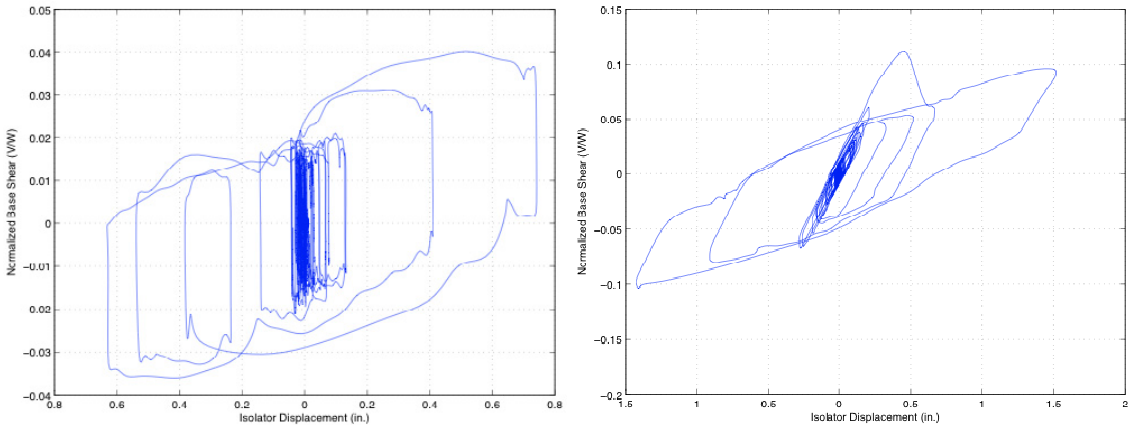

(a) DP bearings CHY-25 (ID 142803) (b) TP bearings CHY-35 (ID 151647)

Figure 5.25: Cyclic behavior of DP and TP isolation systems for CHY-SLE input

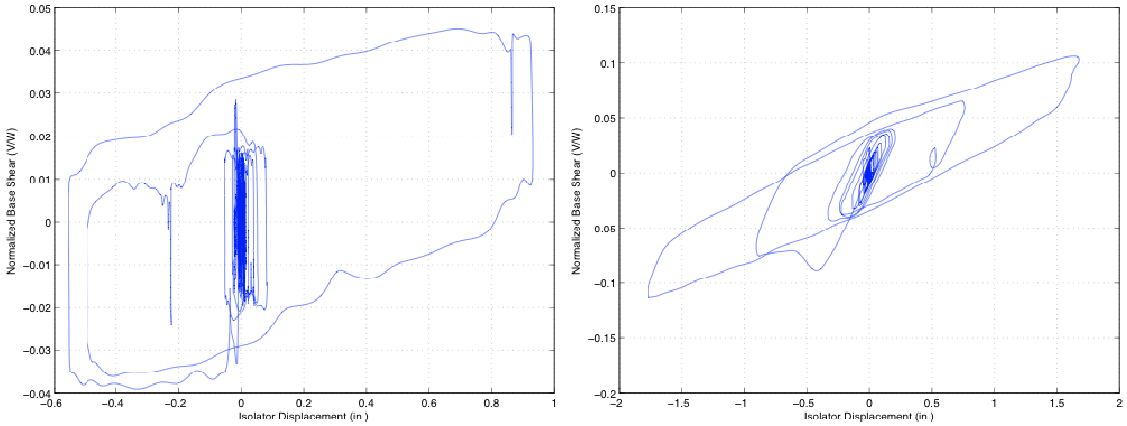

(a) DP bearings G03-25 (ID 150149) (b) TP bearings G03-35 (ID 153920)

Figure 5.26: Cyclic behavior of DP and TP isolation systems for G03-SLE input

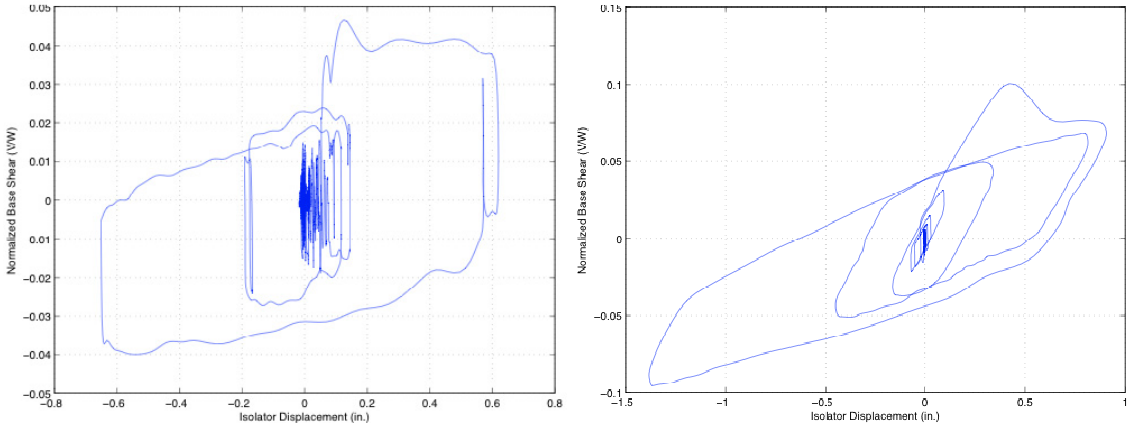

(a) DP bearings SYL-25 (ID 151716) (b) TP bearings SYL-35 (ID 153920)

Figure 5.27: Cyclic behavior of DP and TP isolation systems for SYL-SLE input

5.3.1.2 Design Basis Earthquake (DBE)

To investigate the behavior of the DP and TP bearing specimens under severe levels of seismic input, a series of shake table tests were conducted with ground motions scaled to induce an isolator displacement approximating that of a 475-year return period event.

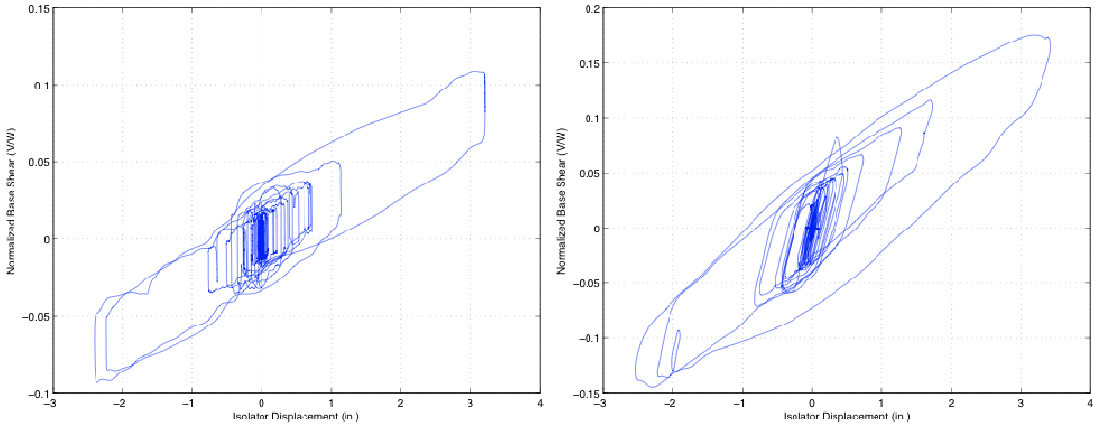

(a) DP bearings CHY-65 (ID 143439) (b) TP bearings CHY-65 (ID 151910)

Figure 5.28: Cyclic behavior of DP and TP isolation systems in CHY-DBE input

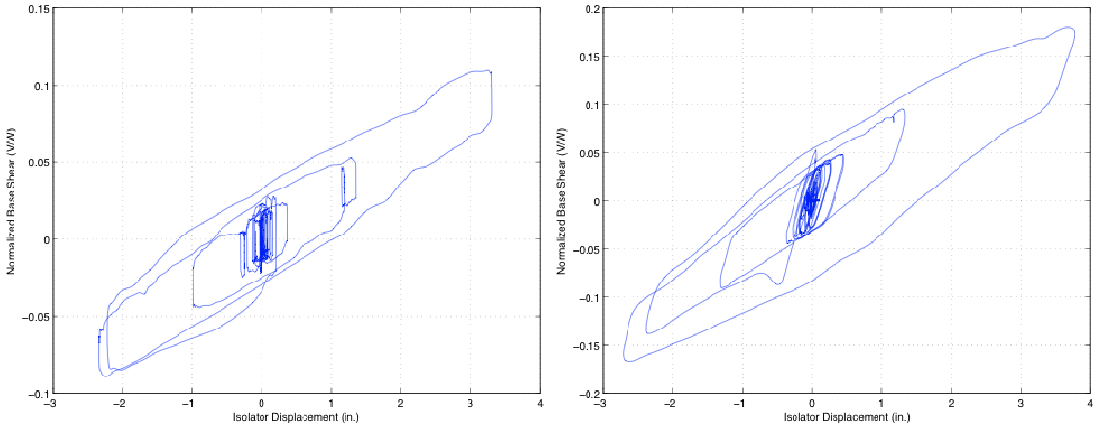

(a) DP bearings G03-65 (ID 150249) (b) TP bearings G03-65 (ID 155005)

Figure 5.29: Cyclic behavior of DP and TP isolation systems in G03-DBE input

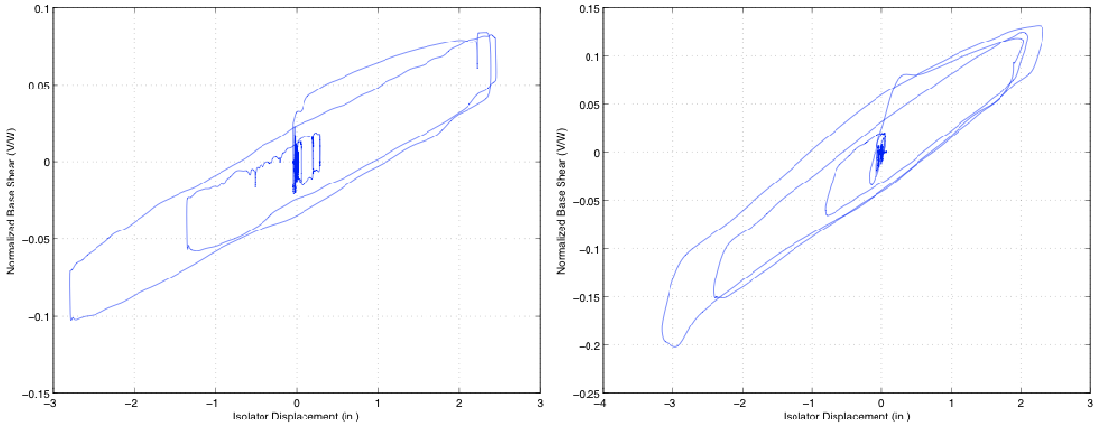

(a) DP bearings SYL-65 (ID 151806) (b) TP bearings SYL-65 (ID 160705)

Figure 5.30: Cyclic behavior of DP and TP isolation systems in SYL-DBE input

5.3.1.3 Maximum Considered Earthquake (MCE)

To investigate the behavior of the DP and TP bearing specimens under severe levels of seismic input, a series of shake table tests were conducted with ground motions scaled to induce an isolator displacement approximating those expected when the structure were subjected to a 2475-year return period event.

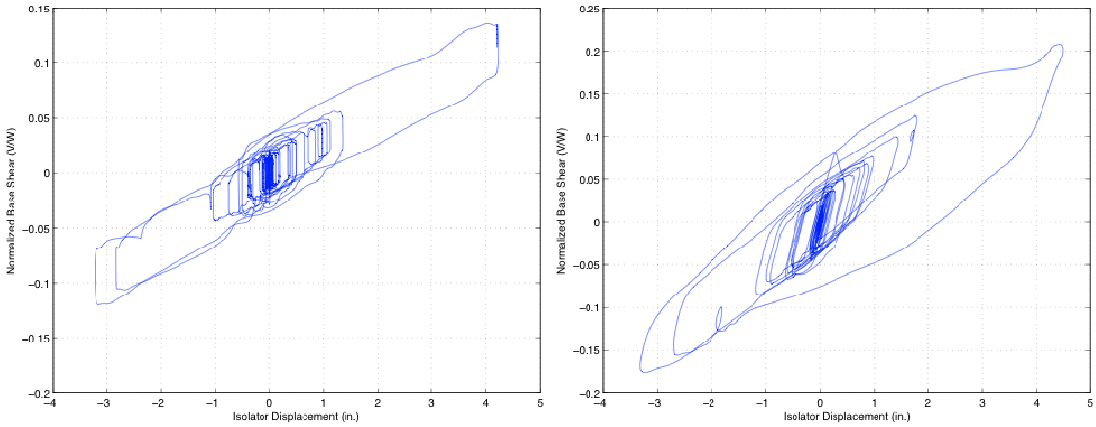

(a) DP bearings CHY-80 (ID 143915) (b) TP bearings CHY-85 (ID 152532)

Figure 5.31: Cyclic behavior of DP and TP isolation systems in CHY-MCE input

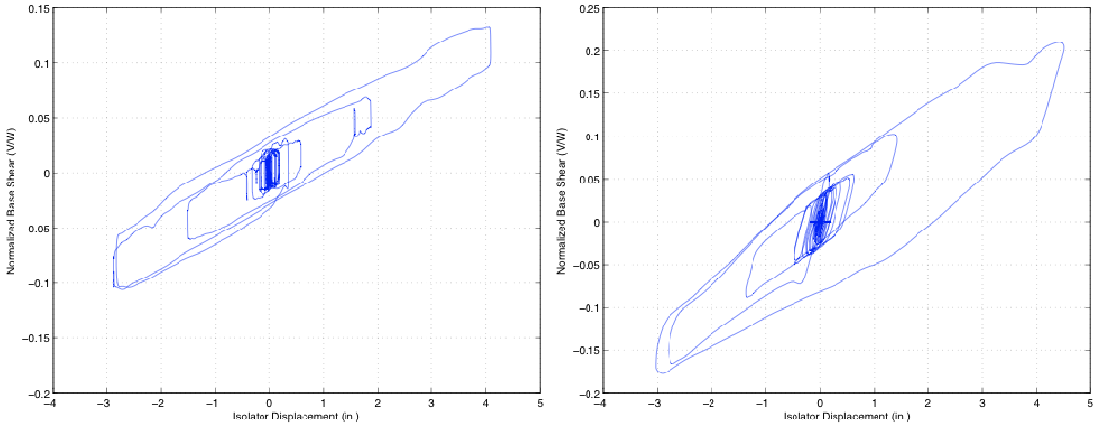

(a) DP bearings G03-80 (ID 150338) (b) TP bearings G03-75 (ID 154042)

Figure 5.32: Cyclic behavior of DP and TP isolation systems in G03-MCE input

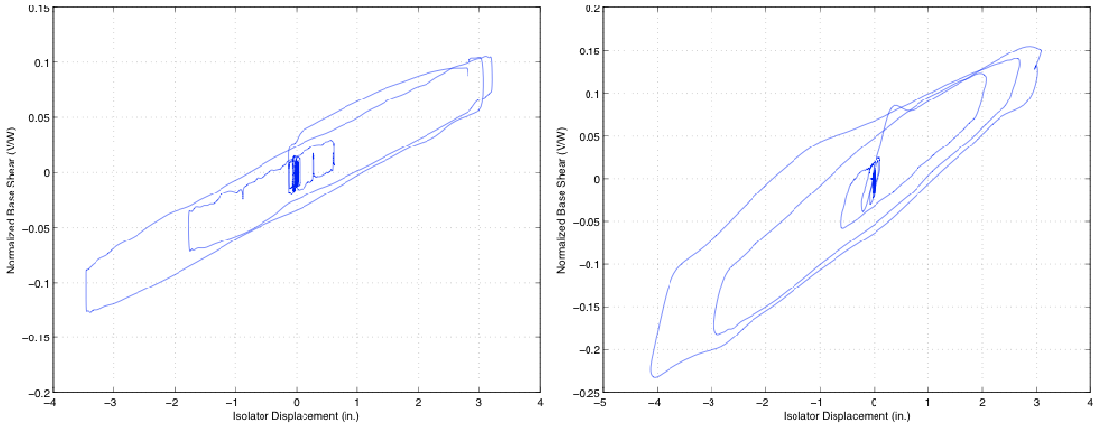

(a) DP bearings SYL-80 (ID 151905) (b) TP bearings SYL-90 (ID 161130)

Figure 5.33: Cyclic behavior of DP and TP isolation systems in SYL-MCE input

5.3.2 Effect of Vertical Ground Motion on Cyclic Behavior of Isolators

To investigate the effect of vertical ground motion on behavior of DP and TP bearings, a set of shake table experiments was conducted with the same horizontal input as that described above in Section 5.3.1, but with the addition of recorded vertical motion for each record under consideration. These tests allow for the direct comparison of important isolation system demand parameters, such a peak force output, peak isolator displacement, and total energy dissipation.

The results of nine pairs of experiments are available, for reviewers to evaluate the sensitivity of the DP isolation system to the presence of vertical ground acceleration. These

consist of three records, each at three excitation amplitudes. An example of pertinent experimental results for the CHY-80 input is shown below. For this record with and without vertical acceleration input, a comparison of the total vertical load on all isolators is shown in Figure 5.34. It is clear from this figure that the total vertical load W varies from 52 kips to 70 kips *without* vertical acceleration (or a variation of approximately $0.86 \le W / W_{DL} \le 1.16$, where W_{DL} is the total dead weight of the specimen). The same horizontal input is applied with vertical acceleration, and the total vertical load varies from 42 kips to 74 kips (or a variation of approximately $0.69 \le W / W_{DL} \le 1.22$). For the same pair of CHY-80 tests, a comparison of the cyclic behavior of the isolation system with and without vertical acceleration is shown in Figure 5.35. It is evident from these data that, even with a substantial variation in total axial load between the two tests, virtually no observable difference exists between the peak shear force, peak displacement demand, or total energy dissipation by including (or omitting) vertical acceleration input.

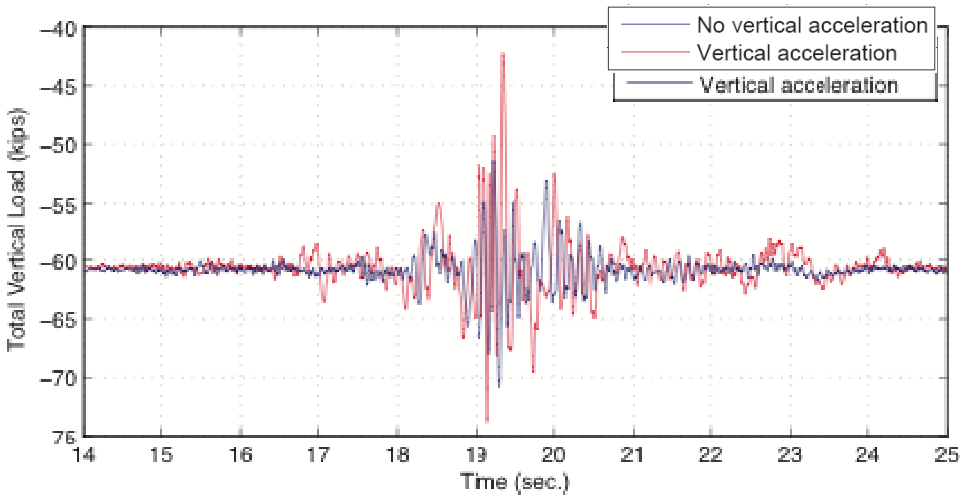

Figure 5.34: Comparison of total weight on DP isolation system, with/without vertical ground acceleration, CHY-80 (ID 143915/144942)

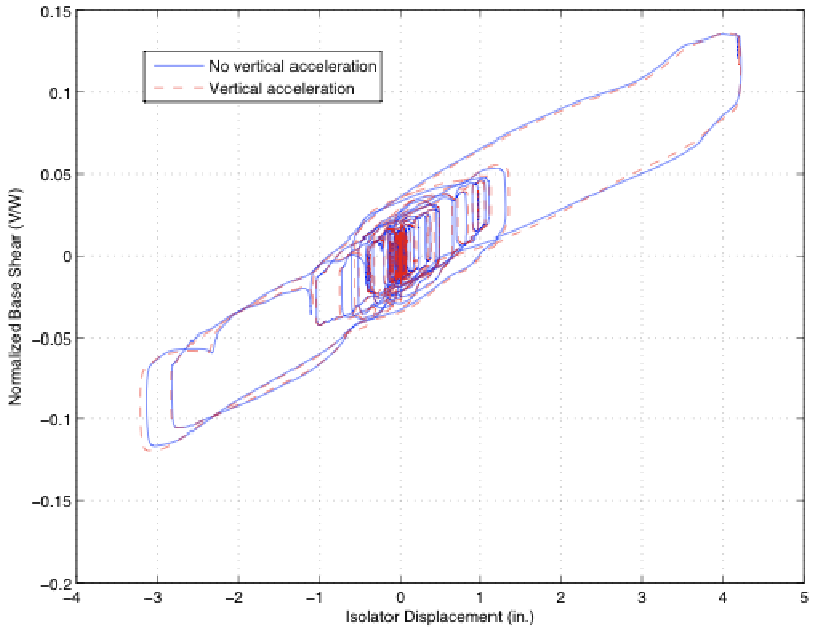

Figure 5.35: Comparison of cyclic behavior of DP isolation system, with/without vertical ground acceleration, CHY-80 (ID 143915/144942)

As with the DP specimen, the results of nine pairs of experiments are available, for reviewers to evaluate the sensitivity of the TP isolation system to the presence of vertical ground acceleration. An example of pertinent experimental results for the CHY-85 input is shown below. For this record with and without vertical acceleration input, a comparison of the total vertical load on all isolators is shown in Figure 5.36. It is clear from this figure that the total vertical load W varies from 50 kips to 70 kips *without* vertical acceleration (a variation of approximately $0.83 \le W / W_{DL} \le 1.16$). The same horizontal input is applied with vertical acceleration, and the total vertical load varies from 45 kips to 74 kips (a variation of approximately $0.74 \le W / W_{DL} \le 1.22$). For the same pair of CHY-85 tests, a comparison of the cyclic behavior of the isolation system with and without vertical acceleration is shown in Figure 5.37. It is evident from these data that, as with the DP bearing specimen, virtually no observable difference exists between the peak shear force, peak displacement demand, or total energy dissipation due to including (or omitting) vertical acceleration input.

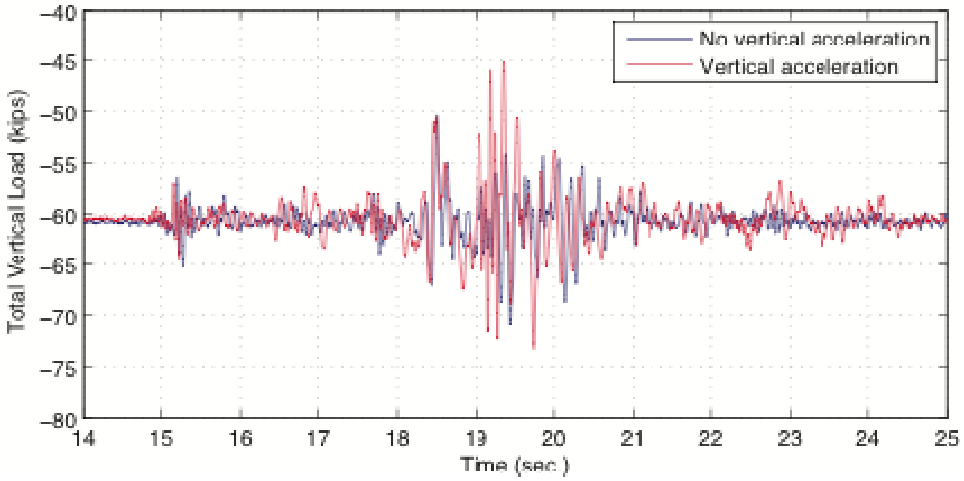

Figure 5.36: Comparison of total weight on TP isolation system, with/without vertical ground acceleration, CHY-85 (ID 152532/153252)

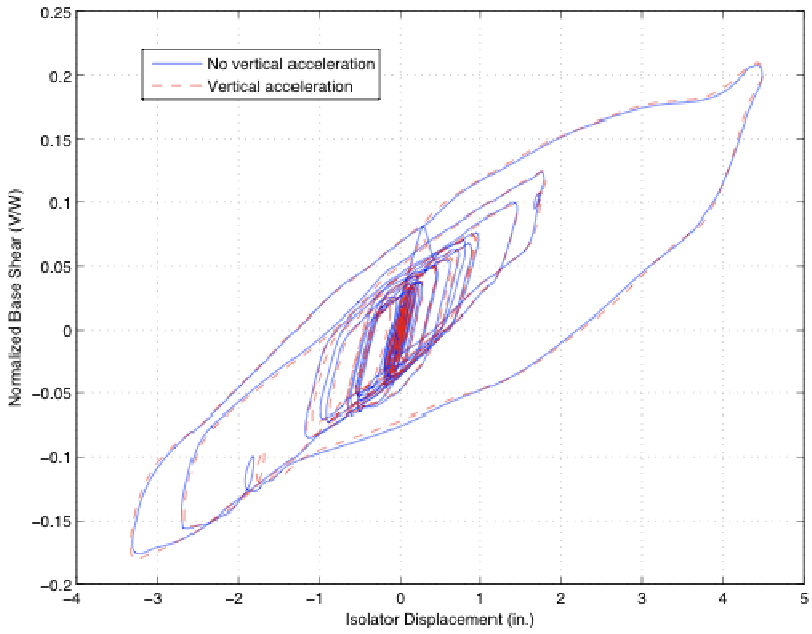

Figure 5.37: Comparison of cyclic behavior of TP isolation system, with/without vertical ground acceleration, CHY-85 (ID 152532/153252)

5.3.3 Effect of Tridirectional Ground Motion on Cyclic Behavior of Isolators

To investigate the effect of tridirectional ground motion on the performance of DP and TP bearings, a test was conducted for each record including three components of ground motion. This is an important consideration since, regardless of the assumptions, all seismic events induce such tridirectional motion, and isolation systems must be capable of responding in a robust and predictable manner under such motion.

For the DBE level of hazard, each of the three input signals was run with a single longitudinal component, a longitudinal and vertical component, and all three components. In Section 5.3.2, the insensitivity of the bearing response to the presence of vertical ground motion was established. It has been shown in previous experimental studies (e.g., Mosqueda et al. [2004]) that FP bearings generally follow a circular bidirectional interaction surface. A consequence of this is isotropic behavior in any planar direction, and coupling of orthogonal components of force under bidirectional displacement. This coupling is evident in the experimental results presented in this section. Figure 5.38 shows a comparison of cyclic behavior, along the longitudinal axis, for the CHY-65 record with one- and three-component excitation. The peak displacement shows an apparent increase due to the presence of orthogonal force, leading to decreased longitudinal force and hence less energy dissipation along this axis. In the absence of orthogonal coupling, there would be no difference in response between these two cases. Figure 5.39 shows the same comparison as described above subject to the CHY-65 signal, but for the TP specimen. A slight increase in longitudinal deformation is also evident due to orthogonal coupling of each pendulum mechanism. The data presented here are meant to establish evidence of coupling, however, they are also intended to validate future analytical models for TP bearings considering multi-component excitation.

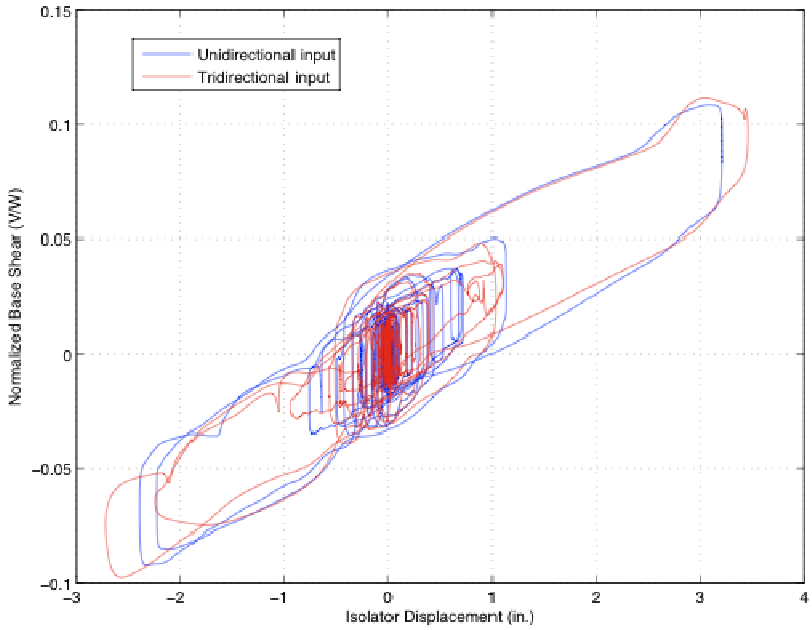

Figure 5.38: Comparison of cyclic behavior of DP isolation system, with/without tridirectional ground acceleration, CHY-65 (ID 143439/145554)

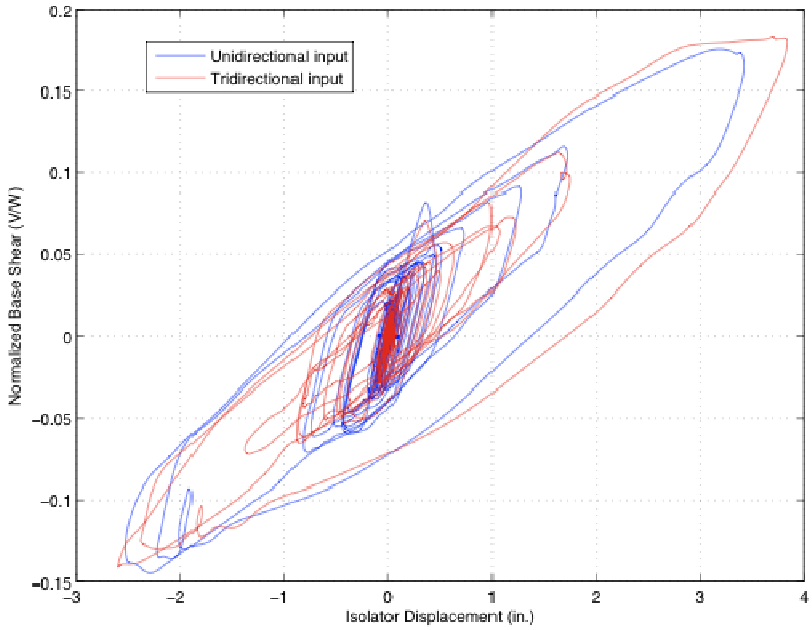

Figure 5.39: Comparison of cyclic behavior of TP isolation system, with/without tridirectional ground acceleration, CHY-65 (ID 151910/153452)

5.4 SEISMIC RESPONSE OF SUPPORTED STRUCTURE

5.4.1 System Identification of Steel Superstructure

An important consideration in evaluating the experimental data collected from the response of the steel superstructure is an estimate of its vibration properties. Specifically, the fundamental natural frequency and the associated damping in that mode of vibration are important system parameters since transmissibility of ground acceleration to the superstructure is a consideration in these experiments. Therefore, the identification of higher mode response can be readily identified from the acceleration transfer functions for each earthquake simulation test.

5.4.1.1 Fundamental Frequency of Vibration

To estimate the frequency of vibration in the steel frame specimen, the Fourier spectrum of the roof acceleration was computed over some duration where sliding on the supported bearings had clearly ceased. The test chosen for this identification is the low-amplitude sinusoidal excitation for the DP specimen, or Test ID 112603 (SINE-10, span setting = 63.) By observing the acceleration history at the end of the excitation, a signal was recorded that is uncontaminated by flexibility contribution by the isolation devices. Displacement records from the table to the bearings were observed to verify that no sliding occurs during this portion of the acceleration signal. By obtaining the Direct Fourier Transform by the FFT algorithm (Cooley and Tukey [1965]) the principal harmonic components of this signal may be obtained. The Fourier amplitude spectrum for the free vibration of the steel frame is shown below in Figure 5.40. From this, the lowest frequency of vibration is 5.316 Hz, or a fundamental period of 0.19 seconds. This corresponds to $T_n = 0.38$ sec in prototype scale, a reasonable period for a three-story braced frame structure. From Figure 5.40, the second and third mode frequencies are approximately 7.87 and 12.12 Hz, (or 0.127 seconds and 0.083 seconds), respectively.

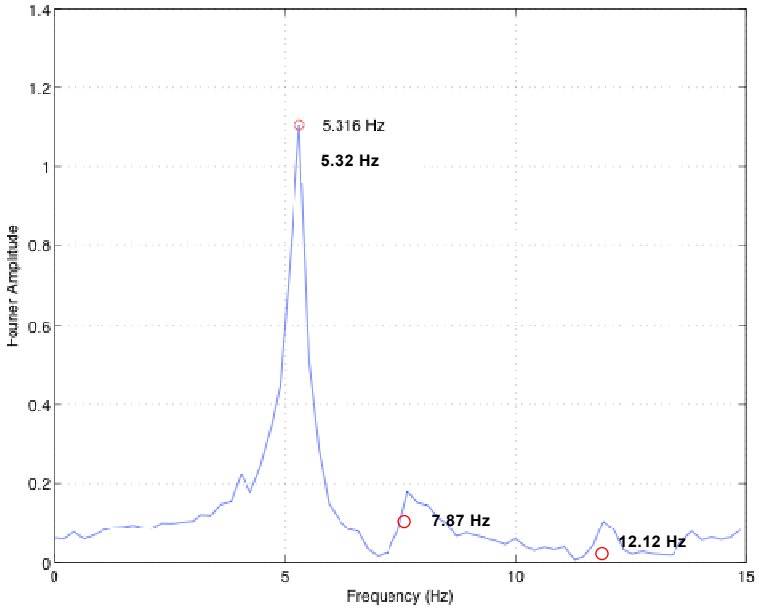

Figure 5.40: Fourier spectrum of roof acceleration under small-amplitude free vibration

5.4.1.2 Damping in First Mode

To estimate the inherent damping in the steel frame specimen, the decay of acceleration amplitude was observed over some duration where sliding on the supported bearings had ceased. To approximate the first-mode damping ratio, the log decrement approach was applied [Chopra, 2007]. This is an appropriate technique for estimating damping given this response since the structure undergoes free vibration. Using the log decrement approach, the damping ratio is estimating from a structure undergoing free vibration as

$$\zeta \approx \frac{1}{2\pi j} \ln\left(\frac{\ddot{u}_n}{\ddot{u}_{n+j}}\right) \tag{5.11}$$

where n is the number of the first peak acceleration, j is the total number of observed cycles, and $\ddot{u}_k$ is the acceleration of the kth peak. Given the free vibration data of Figure 5.41, this damping ratio is estimated as $\zeta = 0.025$ critical. This estimate is reasonable given commonly assumed damping ratios for bare steel frames. Also shown in Figure 5.41 is the superimposed exponential decay relationship of the acceleration envelope given a damping ratio of $\zeta = 0.025$. This comparison shows good agreement with the experimental data.

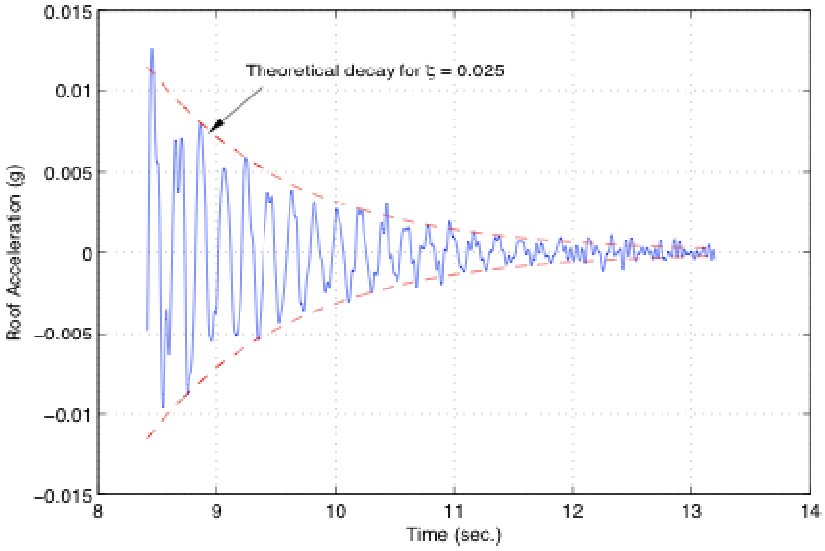

Figure 5.41: Roof acceleration history under small-amplitude free vibration (ID 112602)

5.4.2 Interstory Drifts

For all shake table tests, interstory deformations were measured at each of the three levels for the two longitudinal brace frames. As the structure is isolated from the shake table, the motion of each story was expected to follow essentially rigid-body behavior. Hence, very little interstory deformation was expected, and instrumentation was provided primarily to monitor any slippage of the slotted-bolted connections in the braces. In no test was there any observed bolt slippage, and measured interstory drift demands were negligible.

5.4.3 Floor Accelerations

5.4.3.1 Unidirectional Ground Motion

A key feature of multi-stage FP bearings is the ability to provide effective isolation under a range of ground-motion intensities. In particular, whereas traditional isolation systems exhibit high initial stiffness and strength, the inner slider of the triple pendulum bearing has very low strength and a stiffness that is defined by its geometry and may therefore be specified by the designer. An optimally tuned isolation system filters out high-frequency acceleration content over a broad range of intensities of ground shaking. To investigate the effectiveness of the bearing specimens to filter high-frequency acceleration, acceleration transfer functions are computed from experimental data at each story. The *j*th transfer

function, $H_j(\omega)$, is defined as the mapping of the Fourier spectrum of the table acceleration to the Fourier spectrum of the total acceleration at the *j*th level. Mathematically, this definition can be written as

$$H_j(\omega) = \frac{\mathcal{F}\left\{\ddot{u}_j^t(t)\right\}}{\mathcal{F}\left\{\ddot{u}_g(t)\right\}} \tag{5.12}$$

where $\mathcal{F}\{\cdot\}$ denoted the Discrete Fourier Transform. While this transfer function is generally complex-valued, a plot of its modulus, $\left|H_j(\omega)\right|^2$, versus frequency provides information as to the predominant frequencies of the accelerations transmitted to the superstructure from the ground by the isolation system. Figure 5.42 indicates the levels where floor accelerations are reported: Table (just below the isolation plane,) Base (just above the isolation plane), 1st, 2nd, and 3rd floors. At each floor, longitudinal accelerometers are mounted on the southwest (SW) and southeast (SE) corners.

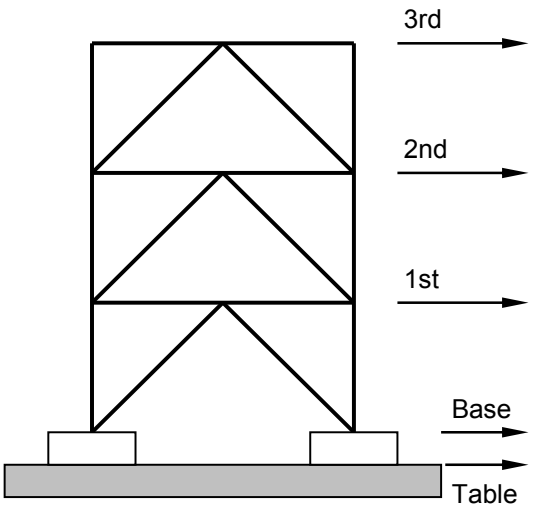

Figure 5.42: Floor labels for description of longitudinal acceleration data

To evaluate the frequency content of the acceleration response of the superstructure for both DP and TP specimens, the roof acceleration transfer function is computed and compared at the three intensity levels for the three input ground motions. The frequencies at which the peaks of these transfer functions occur indicate the nature of the filter that is provided by the isolation system. A transfer function with peaks only in the low frequency range is an indication of effective isolation under that particular input, and the limiting case

is an undamped linear spring, which has only one peak (at infinity) at precisely the natural frequency of the system.

Figure 5.43 shows a comparison of the roof acceleration transfer function amplitude, $|H_3(\omega)|^2$, for both the DP and TP specimens, and at three levels of scaling for the CHY input. In comparing the results from the SLE scaled record, it is evident that the DP specimen transmits significant frequency content between 5 and 10 Hz. This corresponds to the first and second fixed-base frequencies of the superstructure, indicating comparatively weak isolation effect for this input. For this same level of input, the TP acceleration transfer function shows virtually no transmission of acceleration above about 2 Hz, with small amplitude spikes around the fixed-base frequencies. Overall observation of the character of the transfer function for the CHY-SLE input indicates a more efficient low-frequency filter for the TP specimen as compared with the DP specimen. The efficiency of the DP isolator as a filter is shown to increase as the level of excitation becomes more severe, with the results of the CHY-MCE record indicating a low participation of high modes in the acceleration response relative to that of the isolated mode. It is noteworthy that the DP specimen shows significant excitation of first fixed-base mode response at the SLE hazard level, but virtually none at the DBE and MCE levels.

The data of Figure 5.44 and Figure 5.45 present the same comparison of roof acceleration transfer functions at discussed above, but for the G03 and SYL inputs, respectively. In both of these figures, there is clear high-frequency content in the acceleration response due to less efficient filtering by the DP bearing at the SLE hazard level. The capability of the DP system to filter high-frequency accelerations increases with more severe excitation, a trend observed for the CHY signal. For the TP specimen, there is some higher mode participation for the G03-MCE signal, though the exact source is not immediately clear. It is expected, however, that the stiffening properties of the TP system would lead to a reduction in isolation effectiveness at extreme displacement demands, though performance of acceleration-sensitive components is typically not a design consideration in such a rare seismic event.

5.4.3.2 Effect of Vertical Ground Motion on Floor Accelerations

A potential factor influencing the frequency content of floor accelerations in structures isolated with sliding-based bearings is the presence of vertical ground motion. Vertical

ground motion is generally dominated by high-frequency acceleration [Kramer, 1996], and while isolator peak forces, deformations, and energy dissipation appear insensitive to such motion, the frequency content of the bearings force output is likely to mimic the vertical acceleration. This is due to the direct relationship between shear output force and normal force, the latter of which is directly related to vertical acceleration. No studies have been directed at the experimental evaluation of the sensitivity to vertical ground motion of floor accelerations in isolated structures. This experimental program included nine such comparative tests for each of the two specimens. The results of a subset of these tests are presented in this section, however, the trend for all tests results matched those presented.

First, the effect of vertical ground acceleration is investigated for a moderate level of excitation. Consider the CHY input signal, scaled to the SLE hazard level. Figure 5.46 shows a comparison of the Fourier spectra of the total horizontal acceleration response at each floor level of the supported structure, with and without vertical acceleration input, for the DP specimen. From these data, there is no observable variation due to vertical ground motion in either the magnitude of each frequency contribution, or the predominant frequencies of response. While a direct comparison of acceleration response histories does not generally lead to clear conclusions, by converting each history to the frequency domain, substantial variations in the output become much clearer. Figure 5.47 shows the same comparison, but for the TP specimen. From these data, it is clear that the frequency content of each floor acceleration is less rich than the DP case, and the TP bearings focus much of the response in the low-frequency range. However, as with the DP case for the CHY-SLE input, there is very little discernable difference in either the magnitude of each frequency contribution, or the predominant frequencies of response with the inclusion of vertical ground motion.

It is necessary to perform the same comparison under a severe level of excitation, since the variation in axial load history becomes more substantial with higher vertical acceleration. Here we consider the CHY input signal, scaled to the MCE hazard level. Figure 5.48 shows a comparison of the Fourier spectra, with and without vertical acceleration input, for the DP specimen. From these data, the low-frequency acceleration content is much more pronounced than for the same record scaled to the SLE. This is an indication of the improved isolation effectiveness of the traditional Friction Pendulum as the displacement demand increases. However, there is also no observable variation in superstructure acceleration response due to vertical ground motion. These is some change in frequency content of base

level acceleration in the 6–8 Hz range, but the difference does not appear to be substantial. Figure 5.49 shows the same comparison, but for the TP specimen. From these data, it is clear that the frequency content of each floor acceleration is comparable to that of the DP specimen at the MCE, an indication of parity in achieving effective isolation. As with the DP case for the MCE input, there is very little discernable difference in characteristics of the acceleration response with the inclusion of vertical ground motion.

5.5 CONCLUSIONS

The experimental results summarized here confirm the behavior of the triple pendulum bearing presented in Chapter 3 of this report. Behavior was investigated under multiple amplitudes of both sinusoidal excitation and earthquake excitation. Key parameters investigated include: multiple levels of isolator displacement, variation of axial load, uplift of bearings, and multi-components of base excitation. The experimental results indicate cyclic behavior is predicted well by the cyclic model developed for TP bearings. The behavior of bearings subject to large overturning conditions shows stability under transient uplift and stable performance in the cycles that follow uplift. Additionally, both the isolation system and superstructure response appear largely insensitive to the presence of vertical ground acceleration.

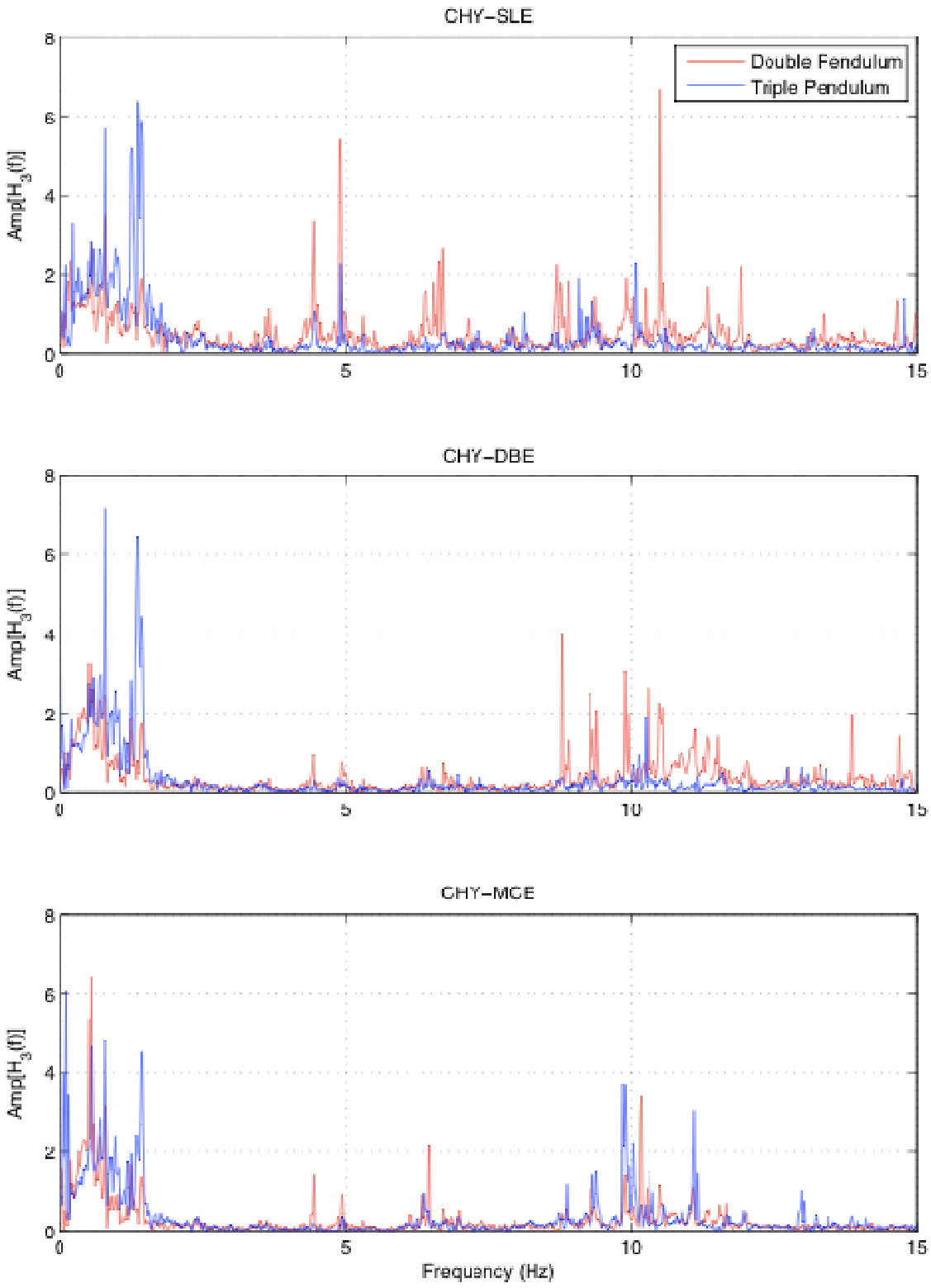

Figure 5.43: Comparison of DP and TP roof acceleration transfer functions for CHY inputs

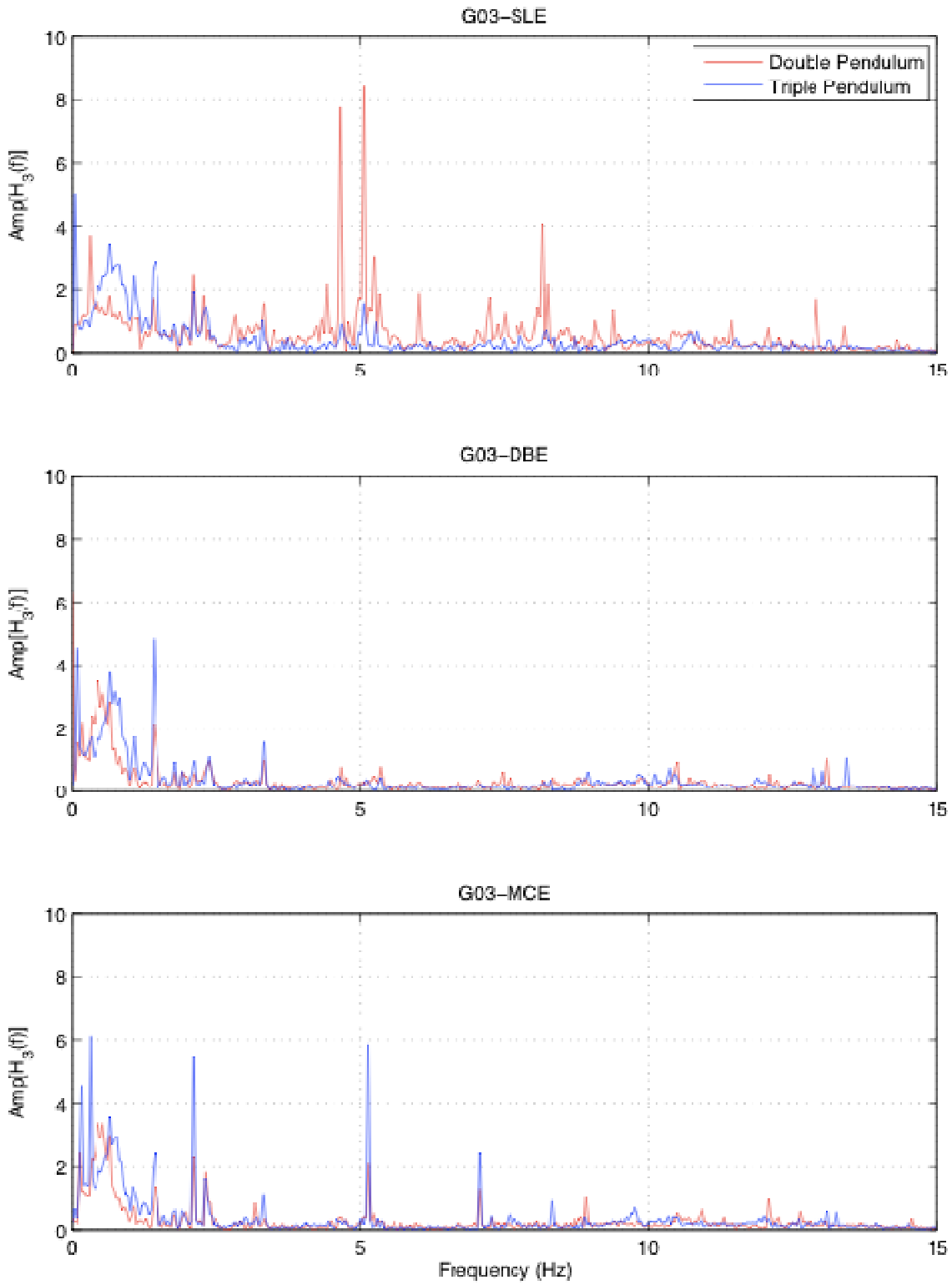

Figure 5.44: Comparison of DP and TP roof acceleration transfer functions for G03 inputs

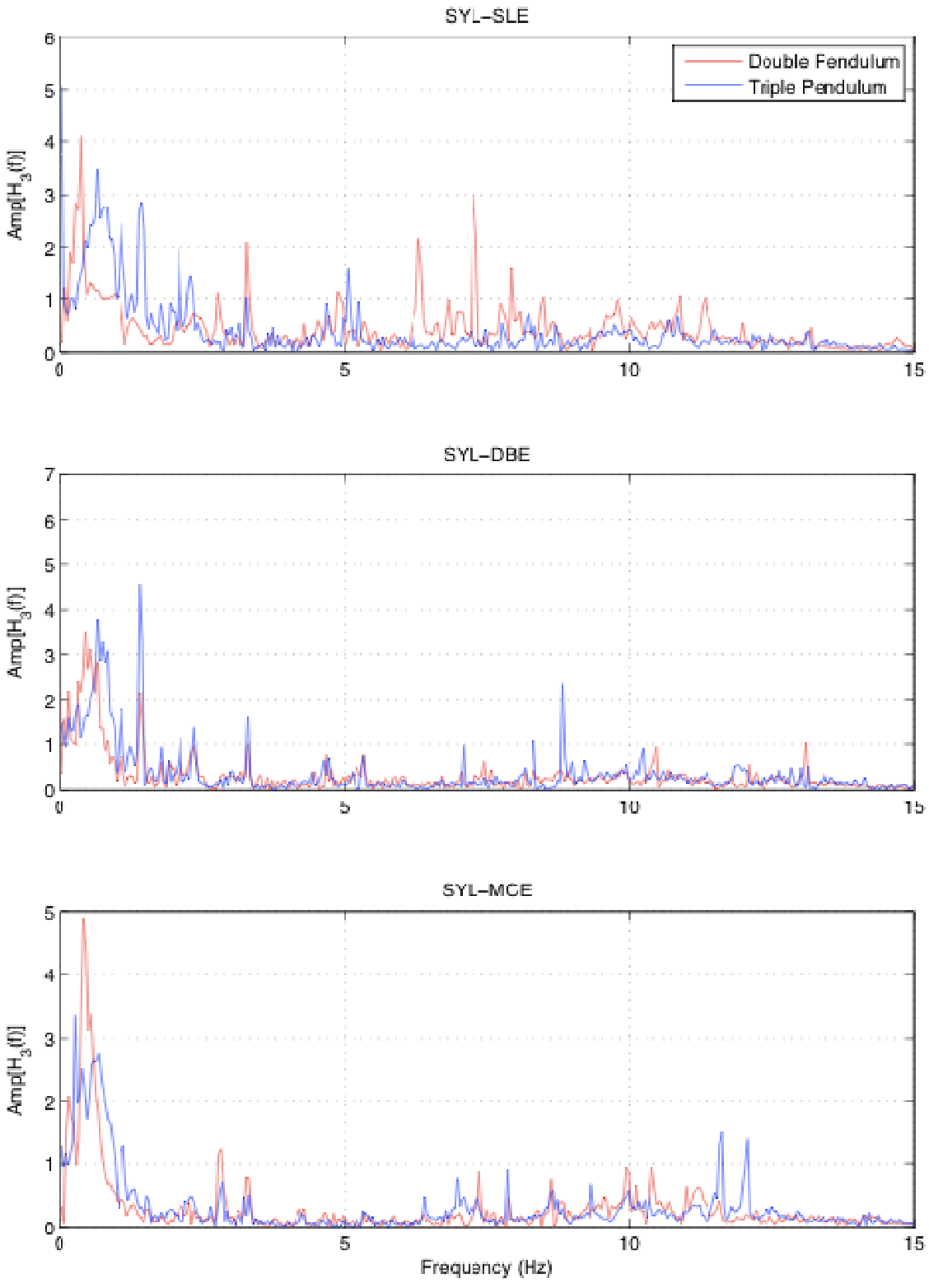

Figure 5.45: Comparison of DP and TP roof acceleration transfer functions for SYL inputs

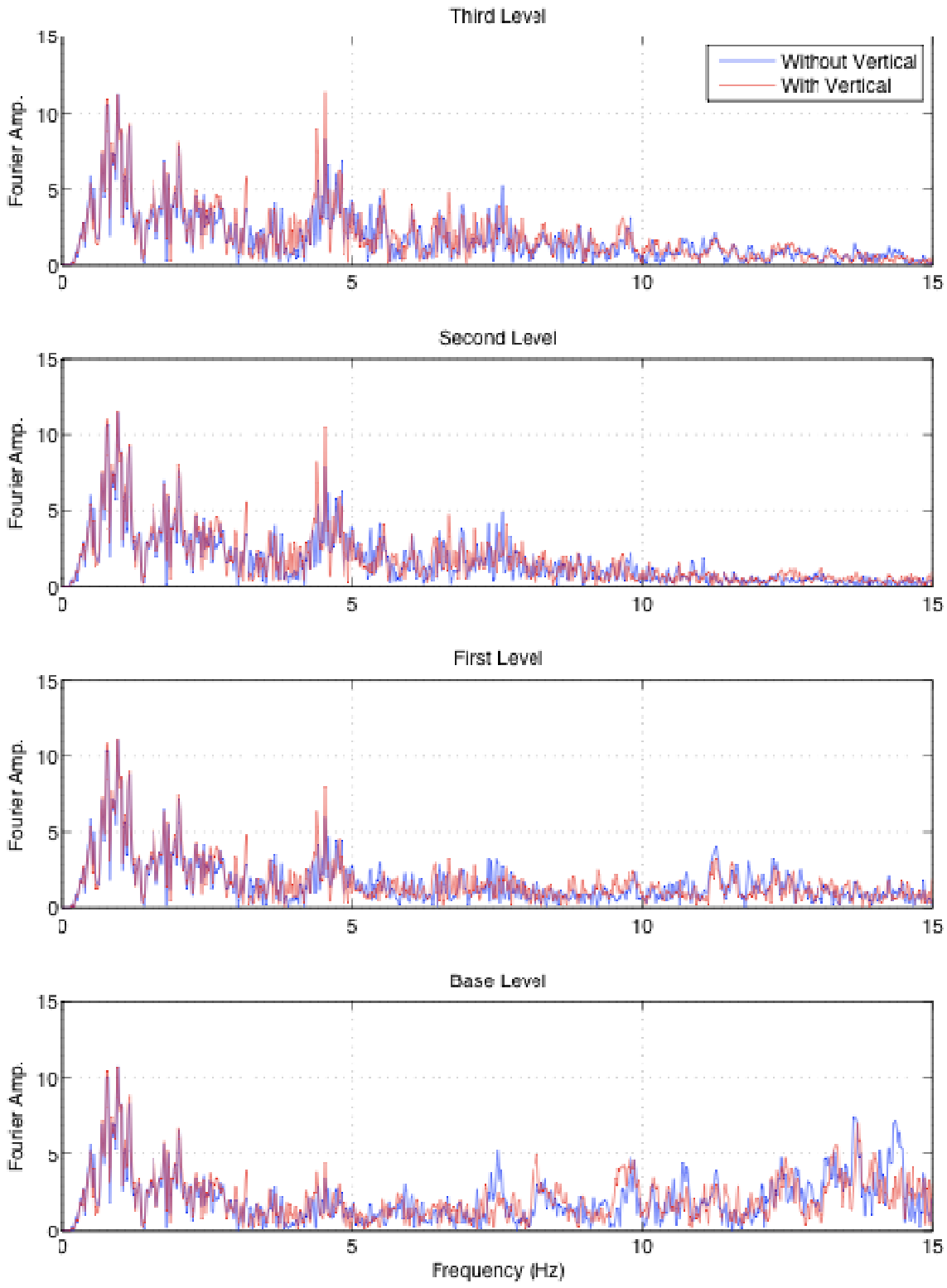

Figure 5.46: Comparison of Fourier spectra of total acceleration at each level for DP specimen, CHY-SLE input, with/without vertical input (ID 142803/144558)

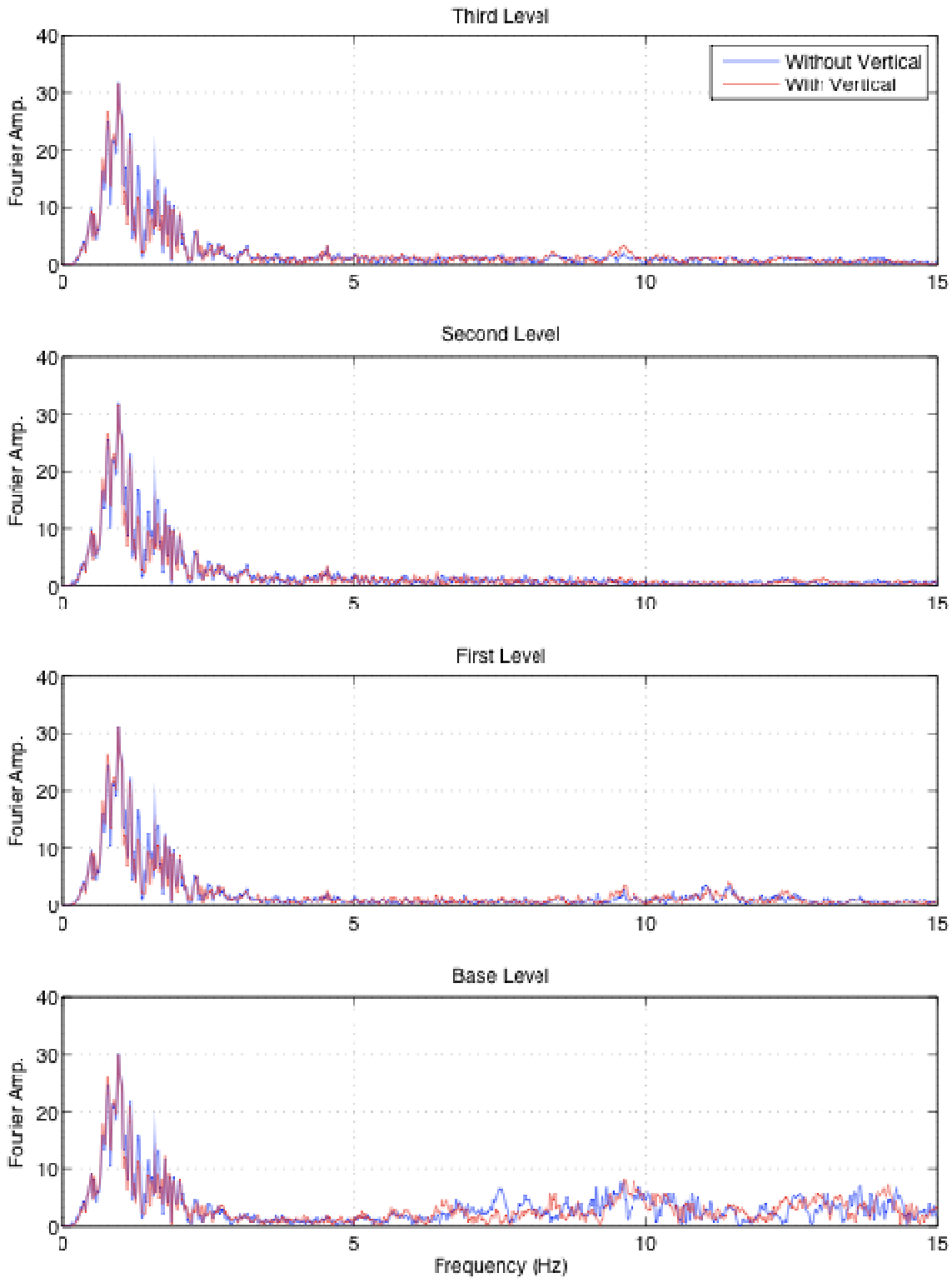

Figure 5.47: Comparison of Fourier spectra of total acceleration at each level for TP specimen, CHY-SLE input, with/without vertical input (ID 151647/152851)

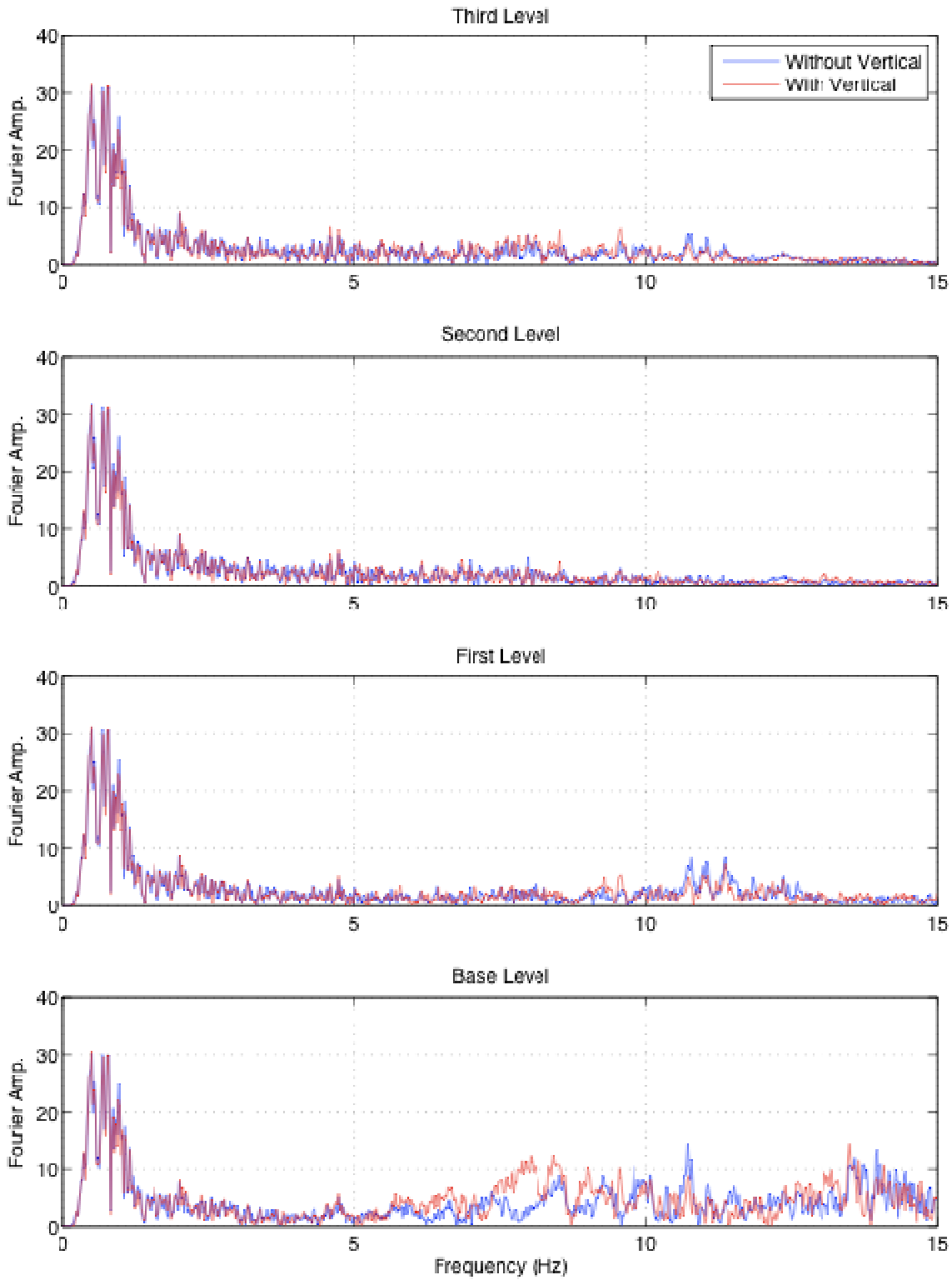

Figure 5.48: Comparison of Fourier spectra of total acceleration at each level for DP specimen, CHY-MCE input, with/without vertical input (ID 143915/144942)

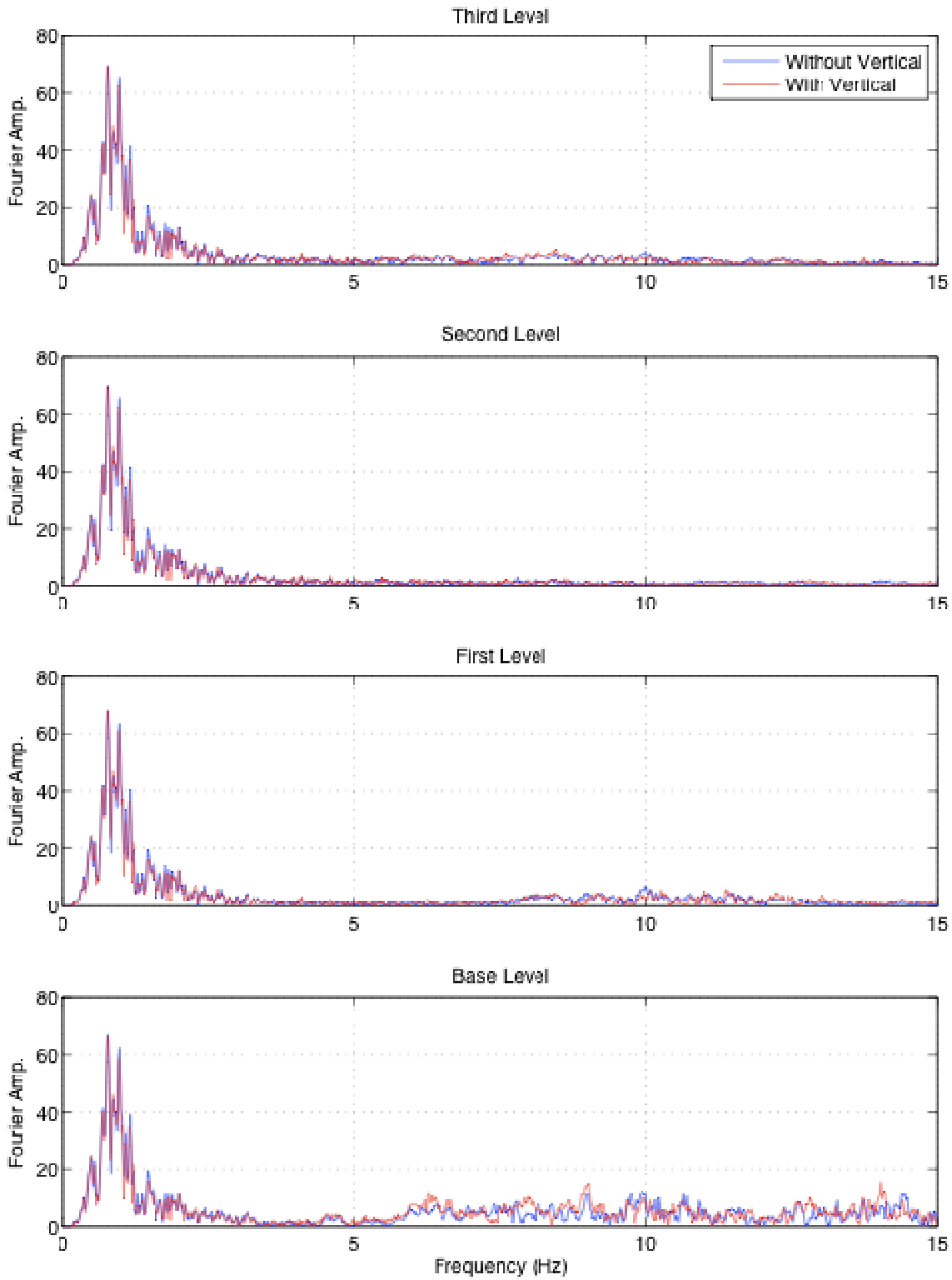

Figure 5.49: Comparison of Fourier spectra of total acceleration at each level for TP specimen, CHY-MCE input, with/without vertical input (ID 152532/153252)

6 Analytical Simulations

In this chapter, parametric numerical simulations are conducted to identify the effect of various isolation system characteristics on several engineering demand parameters of interest. Given the development and validation of an accurate model for the triple pendulum (TP) bearing in Chapters 3 through 5, it is important to generate a significant body of analytical results not only for the TP bearing, but also for other classes of isolation systems, so comparisons may be drawn. The goal of the studies described in this chapter is to provide the technical background against which a methodology can be devised for selecting isolation devices consistent with targeted performance objectives. Particular emphasis is given to the performance enhancement capabilities of TP bearings compared to more traditional isolation systems.

6.1 INTRODUCTION

The studies described first consider a canonical two-degree-of-freedom structure subjected to a single ground motion input. All isolation systems are studied with a range of parameters considered. These studies are meant to provide a rudimentary indication of the sensitivity of seismic demand on the intensity of excitation for all isolation systems under consideration. Subsequent to these simple analyses, parametric studies are conducted on three- and nine-story buildings, considering an ensemble of ground motions developed for multiple levels of seismic hazard. With the range of isolator types and properties considered, the results of these studies are appropriate to quantify isolation effectiveness of linear elastomeric systems with supplemental viscous dampers, lead-rubber isolation systems, traditional friction pendulum bearings, and the new triple pendulum bearing.

6.2 THE ROLE OF INTERSTORY DRIFT AND FLOOR ACCELERATION IN SEISMIC PERFORMANCE OF STRUCTURES

To evaluate the effect of various isolation system parameters on the seismic performance of the base-isolated structure, it is important to select a set of demand parameters that appropriately characterizes performance. Earthquake-induced damage to structures can often be related to global and local interstory deformations and floor level accelerations. Detailed treatment of the importance of these two demand parameters to performance-based earthquake engineering is given by Taghavi and Miranda [2003].

Even elastic deformation of a structure may induce damage in non-structural components that are unable to accommodate differential movement at their boundaries, or at the contact points of the nonstructural components to adjacent structural and nonstructural elements. Examples of such components include interior gypsum wall partitions, exterior glazing systems, precast concrete cladding, stairs, elevators, and vertical plumbing risers. Deformations that exceed the elastic limit of the structural components lead to greater nonstructural damage, but also to a variety of structural damage such as: buckling or fracture of steel beam-column connections and braces, spalling of exterior cover concrete, diagonal cracking of concrete piers, and cracking and dislocation of masonry walls. Additionally, severe inelastic deformations often lead to permanent deformations once seismic shaking has ceased. Such deformations are extremely expensive to rehabilitate, and in many cases may lead to a life-safety hazard if means of egress are rendered useless.

Accelerations in the structure induce inertial forces that must be resisted by either anchorage in components rigidly attached to the structure, or by overturning resistance in freestanding components. Additionally, accelerations induce forces in the primary structural elements such as diaphragms, chords, and collectors. Acceleration-sensitive components include exterior cladding, equipment, parapets, piping, and ceilings. Because flexible nonstructural components can amplify the forces imparted to them by the acceleration of their supports, several descriptors of acceleration are necessary. For essentially rigid components, the peak floor acceleration (PFA) is generally sufficient to characterize the potential for damage in those components. However, many nonstructural components are non-rigid, and as a result, a spectral representation of acceleration at a particular location in the structure is necessary. Such an acceleration spectrum at a point other than the ground

level is referred to as a *floor spectrum*. Given the likely natural frequency range of nonstructural components, a second descriptor of acceleration damage is peak floor acceleration, PFSA, which is implicitly taken here as the maximum floor spectral acceleration computed over the frequency range 2–10 Hz for a damping ratio of 5%.

Based on the above discussion, the engineering demand parameters considered in the subsequent analytical studies are peak interstory drift ratio (*PIDR*), peak floor acceleration (*PFA*), peak floor spectral acceleration (*PFSA*) and peak isolator displacement (U_{iso}).

6.3 PARAMETRIC STUDIES OF TWO-DEGREE-OF-FREEDOM SYSTEMS

The linear theory of seismic isolation as originally presented by Kelly [1996] considers a two-degree-of-freedom (2-DOF) isolated structure, one base mass just above the isolation system, and one structural mass connected to the base mass through an elastic structural system. Viscous damping is considered in the form of linear viscous elements in parallel with both the isolation system and the superstructure. A schematic representation of this 2-DOF structure is shown below in Figure 6.1. Such a simple formulation is useful because it facilitates the study of the response of seismically isolated structures by retaining the simplicity of the canonical single-degree-of-freedom (SDOF) system prevalent in the study of earthquake-resistant design. The theory presented by Kelly is a specialization of general modal dynamic analysis concepts for conditions where the stiffness of the isolation system is much less than that of the superstructure. In this section, this 2-DOF model is extended to assess the influence of nonlinear restoring force and energy dissipation characteristics of the isolation and structural system on demand parameters such as isolator displacement, interstory drift, and floor accelerations. Therefore, an extension of the initial model to treat nonlinear behavior is necessary. While response under dynamic excitation is not computed herein using linear modal expansion techniques, results from the nonlinear analyses will be examined in such a way that comparison with linear modal analysis is meaningful.

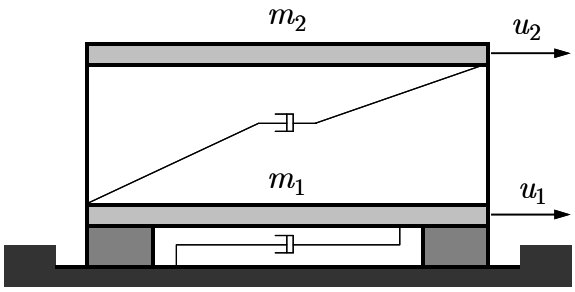

Figure 6.1: Schematic of 2-DOF isolated structure

Here it is useful to state the equations of motion for a 2-DOF isolated structure, considering *global* displacements at each DOF [that is, $u_j(t)$ is the displacement of the j^{th} DOF with respect to its undeformed position]. Here, the damping forces and spring forces are left general, in recognition of the possibility of nonlinear response in these elements. We let the masses at DOFs 1 and 2 be m_1 and m_2, respectively. Since the displacements $u_j(t)$ are relative to an absolute frame of reference, each entry of the mass matrix **m** is simply $\left[m_{ij}\right] = m_i \delta_{ij}$, where δ_{ij} is the standard Kronecker delta function. As a result, the vector of global inertial forces can be represented as $\mathbf{f}_i = \begin{bmatrix} f_{i1} & f_{i2} \end{bmatrix}^T = \mathbf{m}\ddot{\mathbf{u}}$. The vector of global damping forces at each DOF are represented by $\mathbf{f}_d = \begin{bmatrix} f_{d1} & f_{d2} \end{bmatrix}^T$ and the global spring forces by $\mathbf{f}_s = \begin{bmatrix} f_{s1} & f_{s2} \end{bmatrix}^T$. These two force vectors are the result of a mapping of local damping and spring element forces, respectively, to global coordinates by a transformation matrix

$$\mathbf{B} = \begin{bmatrix} 1 & -1 \\ 0 & 1 \end{bmatrix} \tag{6.1}$$

Note that the columns of **B** are linearly independent, which implies the existence of $\mathbf{B}^{-1}$. Given this transformation, $\mathbf{f}_d = \mathbf{B}\mathbf{q}_d$ and $\mathbf{f}_s = \mathbf{B}\mathbf{q}_s$ where $\mathbf{q}_d$ is a vector of element damper forces between each level, and $\mathbf{q}_s$ is a vector of element spring forces between each level. Both of these vectors are generally nonlinear. Writing the equations of motion at each DOF for base earthquake acceleration $\ddot{u}_g(t)$ yields the following system of equations

$$\mathbf{m}\ddot{\mathbf{u}}(t) + \mathbf{f}_d(t) + \mathbf{f}_s(t) = -\mathbf{m}\mathbf{1}\ddot{u}_g(t) \tag{6.2}$$

Substituting the expressions for the global damping and spring forces leads to

$$\mathbf{m}\ddot{\mathbf{u}}(t) + \mathbf{B}\mathbf{q}_d(\mathbf{u}, \dot{\mathbf{u}}, t) + \mathbf{B}\mathbf{q}_s(\mathbf{u}, \dot{\mathbf{u}}, t) = -\mathbf{m}\mathbf{1}\ddot{u}_g(t) \tag{6.3}$$

The damping and spring element forces are left general. The exact analytical form of $\mathbf{q}_d$ and $\mathbf{q}_s$ is described in the sections below.

6.3.1 Effect of Nonlinear Damping Elements

In classical dynamics, the damping force is assumed to be a linear function of velocity. Under this assumption, and in the notation introduced, the i^{th} damping force would be $q_{di} = c_i \dot{v}_i$ where $\dot{v}_i$ is the local velocity for the i^{th} damping element. In this case, the vector of global damping forces simplifies to

$$\begin{aligned} \mathbf{f}_d = \mathbf{B}\mathbf{q}_d &= \begin{bmatrix} 1 & -1 \\ 0 & 1 \end{bmatrix} \begin{pmatrix} c_1 \dot{v}_1 \\ c_2 \dot{v}_2 \end{pmatrix} = \begin{pmatrix} c_1 \dot{u}_1 + c_2 \left(\dot{u}_2 - \dot{u}_1 \right) \\ c_2 \left(\dot{u}_2 - \dot{u}_1 \right) \end{pmatrix} \\ &= \begin{bmatrix} c_1 + c_2 & -c_2 \\ -c_2 & c_2 \end{bmatrix} \begin{pmatrix} \dot{u}_1 \\ \dot{u}_2 \end{pmatrix} = \mathbf{c}\dot{\mathbf{u}} \end{aligned} \tag{6.4}$$

Here, **c** is the traditional global damping matrix, and although not necessarily classical (i.e., diagonal in the eigenspace), it defines a linear transformation between global velocity and global force. This formulation is a convenient approximation for systems with natural damping, which is a result of multiple sources of energy dissipation, such as friction associated with architectural elements and nominal inelastic material behavior. While these types of energy dissipation are not necessarily velocity dependent, they generally contribute small amounts of damping, and the error introduced is considered negligible. However, it is increasingly common in engineering practice to consider the implementation of manufactured damping devices, such as fluid viscous dampers (FVDs), to control structural response. An overview of the use of manufactured damping devices to control isolator deformations is discussed in Chapter 2.

In designing structural systems with FVDs, it is now common to investigate the use of damping elements manufactured to exhibit a nonlinear force-velocity relationship. A general class of nonlinear FVDs follows the force-velocity relationship

$$q_d(t) = c_d \left| \dot{v}(t) \right|^{\eta} \operatorname{sgn}\left[\dot{v}(t) \right] \tag{6.5}$$

where, as before, q_d and $\dot{v}$ are the damper element force and velocity, respectively. The exponent η defines what is known as the *damper power law*, and $\operatorname{sgn}(\cdot)$ is the signum

function. The coefficient c_d is the damping coefficient, whose magnitude describes the damper force output at some velocity demand. These types of dampers have been considered attractive because, at a particular output damper force capacity, the total energy dissipation per cycle is greater for a nonlinear FVD where $\eta < 1$ [Lin and Chopra, 2003].

Applying a transformation similar to Equation (6.4) above, the global damping force can be expressed as

$$\begin{aligned}\mathbf{f}_d(\mathbf{u},\dot{\mathbf{u}}) = \mathbf{B}\mathbf{q}_d &= \begin{bmatrix} 1 & -1 \\ 0 & 1 \end{bmatrix} \begin{pmatrix} c_1 \left|\dot{v}_1\right|^{\eta_1} \operatorname{sgn}(\dot{v}_1) \\ c_2 \left|\dot{v}_2\right|^{\eta_2} \operatorname{sgn}(\dot{v}_2) \end{pmatrix} \\ &= \begin{pmatrix} c_1 \left|\dot{v}_1\right|^{\eta_1} \operatorname{sgn}(\dot{v}_1) - c_2 \left|\dot{v}_2\right|^{\eta_2} \operatorname{sgn}(\dot{v}_2) \\ c_2 \left|\dot{v}_2\right|^{\eta_2} \operatorname{sgn}(\dot{v}_2) \end{pmatrix} \\ &= \begin{pmatrix} c_1 \left|\dot{u}_1\right|^{\eta_1} \operatorname{sgn}(\dot{u}_1) - c_2 \left|\dot{u}_2 - \dot{u}_1\right|^{\eta_2} \operatorname{sgn}(\dot{u}_2 - \dot{u}_1) \\ c_2 \left|\dot{u}_2 - \dot{u}_1\right|^{\eta_2} \operatorname{sgn}(\dot{u}_2 - \dot{u}_1) \end{pmatrix}\end{aligned} \tag{6.6}$$

6.3.1.1 Nonlinear Spring Elements

A similar extension of spring force to nonlinear behavior is described here. Under the assumption of spring linearity, and in the notation introduced, the i^{th} spring force would be $q_{si} = k_i v_i$ where v_i is the local deformation for the i^{th} spring element. In this case, the vector of global spring forces simplifies to

$$\begin{aligned}\mathbf{f}_s = \mathbf{B}\mathbf{q}_s &= \begin{bmatrix} 1 & -1 \\ 0 & 1 \end{bmatrix} \begin{pmatrix} k_1 v_1 \\ k_2 v_2 \end{pmatrix} = \begin{pmatrix} k_1 u_1 + k_2 \left(u_2 - u_1\right) \\ k_2 \left(u_2 - u_1\right) \end{pmatrix} \\ &= \begin{bmatrix} k_1 + k_2 & -k_2 \\ -k_2 & k_2 \end{bmatrix} \begin{pmatrix} u_1 \\ u_2 \end{pmatrix} = \mathbf{k}\mathbf{u}\end{aligned} \tag{6.7}$$

Here, **k** is the traditional global stiffness matrix, and it defines a linear transformation between a compatible global displacement field and global force field in equilibrium. It is noted that, due to the Maxwell-Betti reciprocity theorem, this matrix is strictly symmetric when rigid body modes of deformation are *not* considered (an implication of structural stability).

The response of structures to severe seismic excitation may extend elements of the lateral system beyond the elastic range. In this case, the stiffness matrix described above in Equation (6.7) is not valid. Instead, some model must be assumed that reasonably captures

the expected inelastic force-deformation properties of the subject structural element. One model that captures nonlinear cyclic behavior is the Bouc-Wen hysteretic constitutive relationship [Wen, 1976]. This model is appropriate for both superstructural yielding elements and a wide class of seismic isolation devices. This nonlinear spring element follows the force deformation relationship

$$q_s(t) = \underbrace{\alpha k v(t)}_{elastic} + \underbrace{(1-\alpha) q_y z(t)}_{hysteretic} \tag{6.8}$$

where q_s and v are the spring element force and deformation, respectively. The elastic and hysteretic portions of the force are explicitly identified. The parameter α defines the ratio of plastic stiffness to elastic stiffness ($\alpha < 1$) and q_y is the yield force at which the stiffness transition from elastic to plastic occurs. The non-dimensional hysteretic parameter $z(t)$ follows the differential equation

$$\dot{z}(t) = \frac{k}{q_y}\left[\dot{v}(t) - \gamma\left|\dot{v}(t)\right| z(t) \left|z(t)\right|^{n-1} - \beta \dot{v}(t) \left|z(t)\right|^{n}\right] \tag{6.9}$$

In this formulation, $z(t) \in [-1,1]$, where a value of ± 1 indicates positive or negative yielding. The parameters γ and β define the shape of the hysteresis loops, and the exponent n defines the rate of transition from elastic to plastic stiffness. A large value of n, say $n \geq 20$, corresponds to essentially bilinear hysteresis. For an isolation system with linear bearing stiffness k_b, the elastic portion of the Bouc-Wen model in Equation (6.8) can be rewritten as $k_b v(t) = \alpha k v(t)$. The nonlinear springs at the isolation interface could either represent bearings with inherent hysteretic behavior (such as single-concave friction pendulum or lead-rubber bearings), or linear bearings in parallel with hysteretic supplemental dampers (such as those with energy dissipation based on friction or metallic yielding).

Applying a transformation similar to Equation (6.7) above and substituting the expression for bearing stiffness as $k_b = \alpha_1 k_1$, the global spring force vector can be expressed as

$$
\begin{aligned}
\mathbf{f}_s(\mathbf{u},\dot{\mathbf{u}}) = \mathbf{B}\mathbf{q}_s &= \begin{bmatrix} 1 & -1 \\ 0 & 1 \end{bmatrix} \begin{pmatrix} k_b v_1(t) + (1-\alpha_1) q_{y1} z_1(t) \\ \alpha_2 k_2 v_2(t) + (1-\alpha_2) q_{y2} z_2(t) \end{pmatrix} \\
&= \begin{pmatrix} k_b v_1(t) + (1-\alpha_1) q_{y1} z_1(t) - \alpha_2 k_2 v_2(t) - (1-\alpha_2) q_{y2} z_2(t) \\ \alpha_2 k_2 v_2(t) + (1-\alpha_2) q_{y2} z_2(t) \end{pmatrix} \\
&= \underbrace{\begin{bmatrix} k_b + \alpha_2 k_2 & -\alpha_2 k_2 \\ -\alpha_2 k_2 & \alpha_2 k_2 \end{bmatrix}}_{\mathbf{k}_p} \begin{pmatrix} u_1 \\ u_2 \end{pmatrix} + \underbrace{\begin{bmatrix} (1-\alpha_1) q_{y1} & (\alpha_2 - 1) q_{y2} \\ 0 & (1-\alpha_2) q_{y2} \end{bmatrix}}_{\mathbf{q}_y} \begin{pmatrix} z_1 \\ z_2 \end{pmatrix} \\
&= \mathbf{k}_p \mathbf{u} + \mathbf{q}_y \mathbf{z}
\end{aligned}
\tag{6.10}
$$

where the vector **z** follows the differential equation

$$
\dot{\mathbf{z}} = \begin{pmatrix} \dfrac{k_b}{\alpha_1 q_{y1}} \left[\dot{u}_1(t) - \gamma \left| \dot{u}_1(t) \right| z_1(t) \left| z_1(t) \right|^{n-1} - \beta \dot{u}_1(t) \left| z_1(t) \right|^n \right] \\ \dfrac{k_2}{q_{y2}} \left[\dot{u}_2(t) - \dot{u}_1(t) - \gamma \left| \dot{u}_2(t) - \dot{u}_1(t) \right| z_2(t) \left| z_2(t) \right|^{n-1} - \beta \left(\dot{u}_2(t) - \dot{u}_1(t) \right) \left| z_1(t) \right|^n \right] \end{pmatrix}
\tag{6.11}
$$

6.3.1.2 Normalized Equations of Motion

Since the behavior of seismic isolated structures can be significantly affected by the nonlinear behavior of both spring and damping elements, it is convenient to recast the equations of motion in terms of parameters that relate to the strength of both the isolation system and the superstructure. These are parameters with which designers are often familiar. For example, an elastomeric isolation system may be designed with an aggregate lead core strength of $Q_d = 0.07 \times W$, where W is the seismic weight of the superstructure. For a friction pendulum bearing, this is equivalent to a design friction coefficient of 0.07. Similarly, the superstructure may be designed for a base shear of $V_b = 0.25 \times W$. This corresponds to a pushover curve for the superstructure that reaches a plateau at 25% of the structure's seismic weight. Such behavioral parameters are particularly convenient, because they are meaningful to designers even in cases where details of the supported structure are either unknown or approximate. It is useful, however, to non-dimensionalize the equations of motion used in the studies reported herein so that they can be applied to a broad class of structures rather than only specific ones such as the case just mentioned. Normalization of the equation of motion for SDOF oscillators with bilinear springs subjected to both harmonic pulse and near-field earthquake excitations was represented in Makris and Black [2004a, 2004b]. While this work showed self-similarity of the response for a fixed yield displacement, the normalization

below is for a 2-DOF structure, and is for the purpose of defining the nonlinear system of equations in terms of convenient non-dimensional design parameters.

To develop a system of equations of motion that are in terms of non-dimensional design parameters, we first express the structural displacements in terms of element deformations, rather than global displacements relative to an absolute frame of reference. This transformation was used by Kelly [1996] to approximate dynamic characteristics of linear isolated structures. The extension here is to nonlinear behavior in the isolation system and superstructure. Let $\mathbf{v} = \mathbf{B}^T\mathbf{u}$ where the square equilibrium transformation matrix $\mathbf{B}$ is defined in Equation (6.1). Recalling that $\mathbf{B}$ is both square and full rank, the global displacements can then be expressed as $\mathbf{u} = \mathbf{B}^{-T}\mathbf{v}$. Substituting this transformation into Equation (6.3) yields

$$\mathbf{m}\mathbf{B}^{-T}\ddot{\mathbf{v}}(t) + \mathbf{B}\mathbf{q}_d(\mathbf{v},\dot{\mathbf{v}},t) + \mathbf{B}\mathbf{q}_s(\mathbf{v},\dot{\mathbf{v}},t) = -\mathbf{m}\mathbf{1}\ddot{u}_g(t) \tag{6.12}$$

Premultiplying this by $\mathbf{B}^{-1}$ gives

$$\underbrace{\mathbf{B}^{-1}\mathbf{m}\mathbf{B}^{-T}}_{\tilde{\mathbf{m}}}\ddot{\mathbf{v}}(t) + \mathbf{q}_d(\mathbf{v},\dot{\mathbf{v}},t) + \mathbf{q}_s(\mathbf{v},\dot{\mathbf{v}},t) = -\mathbf{B}^{-1}\mathbf{m}\mathbf{1}\ddot{u}_g(t) \tag{6.13}$$

To obtain the transformed mass matrix on the right side of Equation (6.13), it is necessary to solve for a modified influence vector $\mathbf{r}$ from $\mathbf{B}^{-T}\mathbf{r} = \mathbf{1}$. Doing so yields $\mathbf{r} = \mathbf{B}^T\mathbf{1} = \begin{bmatrix}1 & 0\end{bmatrix}^T$, and; hence Equation (6.13) becomes

$$\tilde{\mathbf{m}}\ddot{\mathbf{v}}(t) + \mathbf{q}_d(\mathbf{v},\dot{\mathbf{v}},t) + \mathbf{q}_s(\mathbf{v},\dot{\mathbf{v}},t) = -\tilde{\mathbf{m}}\mathbf{r}\ddot{u}_g(t) \tag{6.14}$$

where

$$\tilde{\mathbf{m}} = \mathbf{B}^{-1}\mathbf{m}\mathbf{B}^{-T} = \begin{bmatrix} m_1 + m_2 & m_2 \\ m_2 & m_2 \end{bmatrix}, \quad \mathbf{r} = \begin{pmatrix} 1 \\ 0 \end{pmatrix} \tag{6.15}$$

The forces $\mathbf{q}_d(\mathbf{v},\dot{\mathbf{v}},t)$ and $\mathbf{q}_s(\mathbf{v},\dot{\mathbf{v}},t)$ are defined above in Equations (6.5) and (6.8), respectively. The linear portions of this system follow the results of Kelly [1996].

The system of equations in (6.14) is not in its most convenient form for parametric nonlinear analysis, since the explicit appearance of a mass matrix indicates that information about the supported structure is necessary. Additionally, in most common applications viscous damping associated with the supported structural elements may be considered small,

and therefore approximated as being linear. Therefore, the elements of $\mathbf{q}_d$ are simply $q_{di} = c_i \dot{v}_i$. To normalize this system of equations, each DOF is considered separately.

6.3.1.2.1 First Degree of Freedom

In developing a normalized system of equations of motion, consider the first row of Equation (6.14):

$$\left(m_1 + m_2\right)\ddot{v}_1(t) + m_2\ddot{v}_2(t) + c_1\dot{v}_1(t) + q_{s1}(t) = -\left(m_1 + m_2\right)\ddot{u}_g(t) \tag{6.16}$$

Diving by $\left(m_1 + m_2\right)$, this becomes

$$\ddot{v}_1(t) + \frac{m_2}{\left(m_1 + m_2\right)}\ddot{v}_2(t) + \frac{c_1}{\left(m_1 + m_2\right)}\dot{v}_1(t) + \frac{q_{s1}(t)}{\left(m_1 + m_2\right)} = -\ddot{u}_g(t) \tag{6.17}$$

Following the notation of Kelly [1996], the superstructure mass ratio is defined as $\gamma = m_2 / (m_1 + m_2)$. Recognizing the viscous damping ratio of the isolated structure, where the supported structure is completely rigid, as $\zeta_1 = c_1 / 2\left(m_1 + m_2\right)\omega_1$,

$$\ddot{v}_1(t) + \gamma\ddot{v}_2(t) + 2\zeta_1\omega_1\dot{v}_1(t) + \frac{q_{s1}(t)}{\left(m_1 + m_2\right)} = -\ddot{u}_g(t) \tag{6.18}$$

This formulation is practical, since the designer often wishes to establish the elastic isolated frequency of the structure, $\omega_1 = \sqrt{k_b / (m_1 + m_2)}$, before proceeding to a more detailed analysis. Here, we define a *frictional displacement* of the isolation system as $v_{f1} = q_{y1} / k_b$, or the ideal elastic displacement of the isolation system when subjected to the characteristic strength q_{y1}. This parameter has been introduced to solve the differential equation of Coulomb-damped oscillators [Jacobsen and Ayre, 1958]. Note that this frictional displacement v_{f1} is *not* the same as the traditional yield displacement, which we define for the superstructure as $y_2 = v_2 / v_{y2}$. The yield displacement of the superstructure is defined as $v_{y2} = q_{y2} / k_2$, noting that k_2 is the *elastic* stiffness of the superstructure. If normalized displacements $y_1 = v_1 / v_{f1}$ and $y_2 = v_2 / v_{y2}$ (for $v_{f1}, v_{y2} \neq 0$) are substituted into Equation (6.18), the equation of motion becomes

$$\ddot{y}_1(t)+\gamma\frac{v_{y2}}{v_{f1}}\ddot{y}_2(t)+2\zeta_1\omega_1\dot{y}_1(t)+\frac{q_{s1}(t)}{(m_1+m_2)v_{f1}}=-\frac{1}{v_{f1}}\ddot{u}_g(t) \tag{6.19}$$

Here, we define a normalized isolator spring force $\overline{q}_{s1}=q_{s1}/(m_1+m_2)g$, or the spring force as a fraction of the weight above the isolation system. This normalized spring force has the advantage of (a) being non-dimensional; and (b) approximating the pseudo-acceleration demand as a percentage of gravity. Therefore, a normalized yield strength follows the same definition, that is, $\overline{q}_{y1}=q_{y1}/(m_1+m_2)g$. The ratio of isolator spring force to yield force is defined as $\overline{R}_1=\overline{q}_{s1}/\overline{q}_{y1}$. Here, we also define a normalized ground acceleration $\ddot{\overline{u}}_g(t)=\ddot{u}_g(t)/g$. Applying these definitions, and substituting $v_{f1}=q_{y1}/k_1$ yields

$$\ddot{y}_1(t)+\gamma\frac{v_{y2}}{v_{f1}}\ddot{y}_2(t)+2\zeta_1\omega_1\dot{y}_1(t)+\omega_1^2\overline{R}_1(t)=-\omega_1^2\frac{1}{\overline{q}_{y1}}\ddot{\overline{u}}_g(t) \tag{6.20}$$

This equation of motion has units of [sec^{-2}], so it is desirable to multiply by ω_1^{-2}. Doing so leads to the non-dimensional nonlinear equation of motion below:

$$\frac{1}{\omega_1^2}\ddot{y}_1(t)+\frac{\gamma}{\omega_1^2}\frac{\overline{q}_{y2}}{\overline{q}_{y1}}\ddot{y}_2(t)+\frac{2\zeta_1}{\omega_1}\dot{y}_1(t)+\overline{R}_1(t)=-\frac{1}{\overline{q}_{y1}}\ddot{\overline{u}}_g(t) \tag{6.21}$$

6.3.1.2.2 Second Degree of Freedom

We now consider the second row of (6.14):

$$m_2\ddot{v}_1(t)+m_2\ddot{v}_2(t)+c_2\dot{v}_2(t)+q_{s2}(t)=-m_2\ddot{u}_g(t) \tag{6.22}$$

Dividing by m_2, and recognizing that the viscous damping ratio of the superstructure can be expressed as $\zeta_2=c_2/2m_2\omega_2$, this becomes

$$\ddot{v}_1(t)+\ddot{v}_2(t)+2\zeta_2\omega_2\dot{v}_2(t)+\frac{q_{s2}(t)}{m_2}=-\ddot{u}_g(t) \tag{6.23}$$

Recalling the normalized displacement $y_2=v_2/v_{y2}$ and substituting it into Equation (6.23), the equation of motion becomes

$$\frac{v_{f1}}{v_{y2}}\ddot{y}_1(t)+\ddot{y}_2(t)+2\zeta_2\omega_2\dot{y}_2(t)+\frac{q_{s2}(t)}{m_2}=-\frac{1}{v_{y2}}\ddot{u}_g(t) \tag{6.24}$$

It is noted that, by its above definition, the normalized displacement y_2 is also the superstructural ductility demand. It is also convenient to introduce a normalized superstructure spring force $\overline{q}_{s2} = q_{s2} / m_2 g$, or the spring force as a fraction of the weight of the superstructure (analogous to the spectral acceleration in units of *g).* Therefore, a normalized yield strength follows the same definition, that is, $\overline{q}_{y2} = q_{y2} / m_2 g$. The ratio of spring force to yield force is defined as $\overline{R}_2 = \overline{q}_{s2} / \overline{q}_{y2}$. Applying these definitions, and substituting $v_{y2} = q_{y2} / k_2$ yields

$$\frac{v_{f1}}{v_{y2}} \ddot{y}_1(t) + \ddot{y}_2(t) + 2\zeta_2 \omega_2 \dot{y}_2(t) + \omega_2^2 \overline{R}_2(t) = -\omega_2^2 \frac{1}{\overline{q}_{y2}} \ddot{\overline{u}}_g(t) \tag{6.25}$$

Premultiplying by ω_2^{-2} leads to the non-dimensional equation of motion below:

$$\frac{1}{\omega_2^2} \frac{v_{f1}}{v_{y2}} \ddot{y}_1(t) + \frac{1}{\omega_2^2} \ddot{y}_2(t) + \frac{2\zeta_2}{\omega_2} \dot{y}_2(t) + \overline{R}_2(t) = -\frac{1}{\overline{q}_{y2}} \ddot{\overline{u}}_g(t) \tag{6.26}$$

6.3.1.2.3 Results of Normalization

Combining the developed normalized equations of motion in a convenient matrix form gives the following non-dimensional system of nonlinear differential equations

$$\begin{bmatrix} \frac{1}{\omega_1^2} & \frac{\overline{q}_{y2}}{\overline{q}_{y1}} \frac{\gamma}{\omega_2^2} \\ \frac{\overline{q}_{y1}}{\overline{q}_{y2}} \frac{1}{\omega_1^2} & \frac{1}{\omega_2^2} \end{bmatrix} \begin{pmatrix} \ddot{y}_1(t) \\ \ddot{y}_2(t) \end{pmatrix} + \begin{bmatrix} \frac{2\zeta_1}{\omega_1} & 0 \\ 0 & \frac{2\zeta_2}{\omega_2} \end{bmatrix} \begin{pmatrix} \dot{y}_1(t) \\ \dot{y}_2(t) \end{pmatrix} + \begin{pmatrix} \overline{R}_1(t) \\ \overline{R}_2(t) \end{pmatrix} = -\begin{pmatrix} \frac{1}{\overline{q}_{y1}} \\ \frac{1}{\overline{q}_{y2}} \end{pmatrix} \ddot{\overline{u}}_g(t) \tag{6.27}$$

Substituting definitions for each matrix and vector above, we express compactly as

$$\overline{\mathbf{m}} \ddot{\mathbf{y}}(t) + \overline{\mathbf{c}} \dot{\mathbf{y}}(t) + \overline{\mathbf{R}}(t) = -\overline{\mathbf{r}} \ddot{\overline{u}}_g(t) \tag{6.28}$$

This non-dimensional form may be implemented in a numerical integration algorithm to determine the nonlinear response to ground acceleration given parameters that are generally of practical interest to the designer and have important physical interpretations. These equations form the basis for the analyses presented in subsequent 2-DOF parametric studies.

6.3.2 Effect of Linear Viscous Energy Dissipation on Seismic Performance

To investigate the effect on the performance of base isolated structures to linear supplemental viscous damping devices acting in parallel with linear isolators, a methodology must be developed to select appropriate damping parameters. This investigation is important for the studies described herein, as the linear viscous isolation system forms a basis of comparison for other isolation system incorporating either bilinear hysteretic or triple pendulum behavior.

6.3.2.1 Selection of Isolation System Parameters

Based on the previous formulation in Section 6.3.1, a designer can choose the following parameters to characterize a linear isolation system with supplemental nonlinear fluid viscous dampers: ω_1, c_d, and η. Recall that ω_1 defines the natural frequency of the isolated building assuming superstructure rigidity, and c_d and η define the damping coefficient and velocity power law, respectively, of the generally nonlinear damper. Here it is assumed that all energy dissipation in the isolation system is due to the supplemental dampers, and therefore ω_1 is the only parameter needed to characterize the isolation bearings.

The properties of the isolation system should be selected considering the seismic environment in which the structure is located, and the desired response. For any location in the U.S., a set of seismic hazard curves has been developed by the United States Geological Survey [USGS, 2007.] From these hazard curves, spectral ordinates (such as spectral displacement at damping ζ = 0.05) may be computed at any natural frequency ω_n, and for any mean annual frequency (MAF) ν. In current model building codes in the United States [ASCE, 2005] the isolation system and all interconnected components must remain stable under a Maximum Considered Event (MCE) ground motion. The level of hazard, where not controlled by a fault scenario-based deterministic event, is defined as a seismic event having a 2% probability of exceedance in a 50-year interval, or a 2475-year return period. This event corresponds to $\nu_{MCE} = 4.04 \times 10^{-4}$. Therefore, the seismic hazard curve for the site provides the parameter $S_d(\omega_1, \nu_{MCE})$, which approximates the 5% damped MCE isolator displacement for a linear isolation system having natural frequency ω_1.

Typically, the isolation frequency is selected to provide substantial frequency separation from the superstructural natural frequency, and to minimize the base shear in the Design Basis Event (DBE). If we take ω_1 as a result of the structural design and treat it as given, the bearing stiffness is simply $k_b = \omega_1^2 m$, where m is the total mass of the isolated structure. This selection of ω_1 leads to an estimate of the MCE isolator displacement, $u_M = S_d\left(\omega_1, \nu_{MCE}\right)$. However, this spectral displacement is typically computed at a damping of $\zeta = 0.05$, which is generally considered appropriate for fixed-base structures with cladding, partitions, and other sources of nominal energy dissipation under small vibration. For a linear isolation system, composed of either natural rubber bearings or lubricated spherical sliding bearings, damping is very close to zero, so the estimate of MCE isolator displacement must be modified in the absence of supplemental energy dissipation. An approximation for the IBC-based damping reduction factor is given by Christopolous et al. [2006] as

$$S_d\left(\omega, \zeta_t\right) = \frac{S_d\left(\omega, 0.05\right)}{B} = S_d\left(\omega, 0.05\right)\frac{1 - \ln \zeta_t}{4} \tag{6.29}$$

where S_d is the spectral displacement and ζ_t is the target damping ratio of the isolation system. If a displacement limit of the isolation system is defined as $\overline{u}_M$, then it is feasible to estimate the target viscous damping ratio for supplemental linear viscous dampers by imposing the constraint

$$S_d^{5\%}\left(\omega_1, \nu_{MCE}\right)\frac{1 - \ln \zeta_t}{4} \le \overline{u}_M \tag{6.30}$$

If we assume a damping ratio in the linear isolation system without supplemental energy dissipation as being negligibly small, Equation (6.30) can be rearranged to solve for the target damping as

$$\zeta_t \ge \exp\left[1 - 4\frac{\overline{u}_M}{S_d^{5\%}\left(\omega_1, \nu_{MCE}\right)}\right] \tag{6.31}$$

This estimate of the target damping ratio for a linear supplemental energy dissipation system can be used to compute the parameters c_d and η for a nonlinear system by assuming the energy dissipation by the nonlinear supplemental dampers during a representative cycle equals the energy dissipated by the linear system with viscous damping ration ζ_t.

For a system comprised of nonlinear viscous damping elements having the same power for the velocity, recall that the damping force of the system is given by

$$f_d = c_d \left|\dot{u}\right|^{\eta} \operatorname{sgn}\left(\dot{u}\right) \tag{6.32}$$

where c_d is the damping coefficient of all dampers in the system. Here we will estimate the peak velocity by considering a representative cycle of response having a frequency $\bar{\omega}$ and peak displacement u_0 of the isolation system. Given the force-velocity relationship of Equation (6.32), and assuming one cycle of displacement demand is given by $u(t) = u_0 \sin \bar{\omega} t$, the viscous damping force can be expressed as

$$f_d(t) = c_d \left|u_0 \bar{\omega} \cos \bar{\omega} t\right|^{\eta} \operatorname{sgn}\left(u_0 \bar{\omega} \cos \bar{\omega} t\right), \quad t \in \left[0, \frac{2\pi}{\omega}\right] \tag{6.33}$$

We wish to compute the total energy dissipated in one cycle of displacement, and recognizing that, for an infinitesimal displacement *du*, the energy accumulation over that displacement is $dE = f_d \, du$. Integrating over some displacement interval $\left[u_0, u_1\right]$ gives the expression for total energy dissipation in one cycle as

$$E_d = \int_{u_0}^{u_1} f_d(u) du \tag{6.34}$$

However, substituting $du = \dot{u} \, dt$, this integral becomes

$$E_d = \int_0^{2\pi/\omega} f_d(t) \dot{u}(t) dt \tag{6.35}$$

Substituting the expressions for damper force and velocity yields

$$E_d = \int_0^{2\pi/\omega} c_d \left|u_0 \bar{\omega} \cos \bar{\omega} t\right|^{\eta} \operatorname{sgn}\left(u_0 \bar{\omega} \cos \bar{\omega} t\right) u_0 \bar{\omega} \cos \bar{\omega} t \, dt \tag{6.36}$$

The cosine function is positive-valued for $t \in \left[0, \pi/2\right]$ and $t \in \left[3\pi/2, 2\pi\right]$, and negative-valued for $t \in \left[\pi/2, 3\pi/2\right]$, so Equation (6.37) may be expressed as

$$E_d = c_d \left(u_0 \bar{\omega}\right)^{\eta+1} \left[\int_0^{\pi/2\omega} \cos^{\eta+1} \bar{\omega} t \, dt + \int_{3\pi/2\omega}^{2\pi/\omega} \cos^{\eta+1} \bar{\omega} t \, dt - \int_{\pi/2\omega}^{3\pi/2\omega} \cos^{\eta+1} \bar{\omega} t \, dt \right] \tag{6.37}$$

This summation of integrals has a closed form solution, and is given by Soong and Constantinou [1994] as

$$E_d = \lambda(\eta)\, c_d u_o^{1+\eta} \bar{\omega}^{\eta} \tag{6.38}$$

where $\lambda(\eta)$ is defined by the Gamma function, and is given by

$$\lambda(\eta) = 4\left(2^{\eta}\right)\frac{\Gamma^2\left(1+\eta/2\right)}{\Gamma\left(2+\eta\right)}, \quad \Gamma(x) = \int_0^{\infty} u^{x-1} e^{-u}\, du \tag{6.39}$$

For the above displacement cycle, the peak damper force is $f_{d0} = c_d\left(u_0\bar{\omega}\right)^{\eta}$ for a peak displacement of u_0. From Equation (6.38), E_d may be expressed as

$$E_d = \lambda\left(\eta\right) f_{d0} u_o \tag{6.40}$$

The variable $\lambda(\eta)$ may be interpreted as a shape modification factor for the damper hysteresis. Taking two natural cases of the velocity exponent: $\eta = 0$ (velocity independent) and $\eta = 1$ (linear viscous), computing λ for each gives $\lambda(0) = 4$ and $\lambda(1) = \pi$. This same result is found by recognizing that for velocity-independent damping force, the hysteresis is rectangular, and for linear viscous damping force, the hysteresis is elliptical. In the former case, the peak damper force is in-phase with the peak displacement, whereas for the latter, it is exactly out of phase by $\pi/2$ radians. The implications of this for isolation structures will become clear in subsequent discussions regarding different mechanisms of energy dissipation at the isolation interface.

The final goal of this section is to compute a required set of damper parameters c_d and η such that a nonlinear viscous damper dissipates the same energy as a linear one having a target damping ratio ζ_t. The approach is to equate the energy dissipation for linear viscous and nonlinear cases for a cycle of displacement having the same peak displacement and frequency. In light of the above derivations, this is a straightforward process. While this approach has been derived assuming rigid superstructure, it may be extended to the case of the non-rigid superstructure so long as there is sufficient period separation that earthquake-induced deformation is primarily concentrated at the isolation interface.

Consider the canonical 2-DOF isolated structure, having total mass $m_1 + m_2 = m$, isolated frequency ω_1, and negligible inherent damping. If a linear viscous damper is installed to act in parallel with the isolators, the viscous damping ratio is defined as $\zeta = c/2m\omega_1$. From Equation (6.38), taking $\eta = 1$, the peak displacement as u_0 and the

frequency of response as $\bar{\omega}$, the energy dissipation per cycle is given as $E_d = c\pi\bar{\omega}u_0^2$. Therefore, the damping ratio may be expressed as

$$\zeta = \frac{E_d}{2\pi m\bar{\omega}\omega_1 u_0^2} \tag{6.41}$$

While only valid for linear viscous damping, the expression above is often used to approximate the equivalent linear viscous damping coefficient for a nonlinear damping element if the proper energy dissipation per cycle, E_d, is substituted. This approach was first taken by Jacobsen and Ayre [1958] in their definition of equivalent viscous damping for inelastic systems subjected to harmonic vibrations. Substituting E_d from Equation (6.38) into Equation (6.41) yields

$$\zeta = \frac{\lambda(\eta)}{2\pi}\frac{c_d u_o^{\eta-1}\bar{\omega}^{\eta-1}}{m\omega_1} \tag{6.42}$$

For earthquake excitation of isolated structures, the frequency of response is normally very close to the structure's natural frequency during strong shaking. Therefore, it is reasonable for the level of approximation we are seeking here to assume that $\bar{\omega} \approx \omega_1$. Making this substitution and solving for the required normalized damping coefficient $\bar{c}_d$ (as a fraction of the supported weight) to achieve a target effective damping ratio ζ_t gives

$$\bar{c}_d = \frac{c_d}{mg} = \zeta_t \frac{2\pi}{\lambda(\eta)}\frac{1}{u_o^{\eta-1}\omega_1^{\eta-2}g} \tag{6.43}$$

It is useful to define a new coefficient $\beta(\eta) = 2\pi / \lambda(\eta)$ and examine its properties. The functional form of $\beta(\eta)$ is

$$\beta(\eta) = \frac{\pi}{2^{\eta+1}}\frac{\Gamma(2+\eta)}{\Gamma^2(1+\eta/2)} \tag{6.44}$$

While this may be computed with relative ease using digital computers, a more tractable form amenable to preliminary design is preferred. A plot of $\beta(\eta)$ for $\eta \in [0,2]$, a likely bound on values for structural engineering applications, is shown below in Figure 6.2. Observation of the values of this function indicates a nearly linear relationship between $\beta(\eta)$ and η over the given range. Also shown in Figure 6.2 is the linear least-squares

estimate of $\beta(\eta)$ over the same range. As a result, an appropriately accurate simplification of the required nonlinear damping exponent to achieve target damping ratio ζ_t is

$$\overline{c}_d = \frac{\zeta_t \left(0.4\eta + 1.6\right) u_o^{1-\eta} \omega_1^{2-\eta}}{g} \tag{6.45}$$

Importantly, for the linear case of η = 1, the actual damping coefficient is computed as $c_d = 2\zeta_t m\omega_1$, the result from classic linear dynamics. For a velocity-independent device having η = 0, such as one based on metallic yielding or friction, the required normalized coefficient is $\overline{c}_d = \zeta_t \pi u_0 \omega_1^2 / 2g$. However, for such a device, the damping coefficient is equal to the yield (or slip) force of the device, and the term $mu_0\omega_1^2$ is close to the maximum restoring force of the isolation system, f_{s0}, for small amounts of added damping force. Therefore, the necessary yield force of the device can be computed as $f_y = \frac{\zeta_t \pi}{2} f_{s0}$. This can be taken a step further, since the restoring force of the isolator can be taken directly from the spectral acceleration at the natural frequency and target damping, or $f_{so} = mS_a\left(\omega_1, \zeta_t\right)$. Therefore, the necessary normalized yield force can be obtained from

$$\overline{f}_y = \frac{f_y}{mg} = \frac{\zeta_t \pi}{2} \frac{S_a\left(\omega_1, \zeta_t\right)}{g} \tag{6.46}$$

This is a very useful form for the designer, since the yield force coefficient normalized yield force can be taken directly from the elastic response spectrum for the given site. By Equation (6.46), for an isolated structure with an elastic spectral acceleration of 0.2*g* at a target equivalent damping ratio of 0.15, the supplemental devices must be designed to yield at 0.047*mg*, or about 5% of the structure's weight.

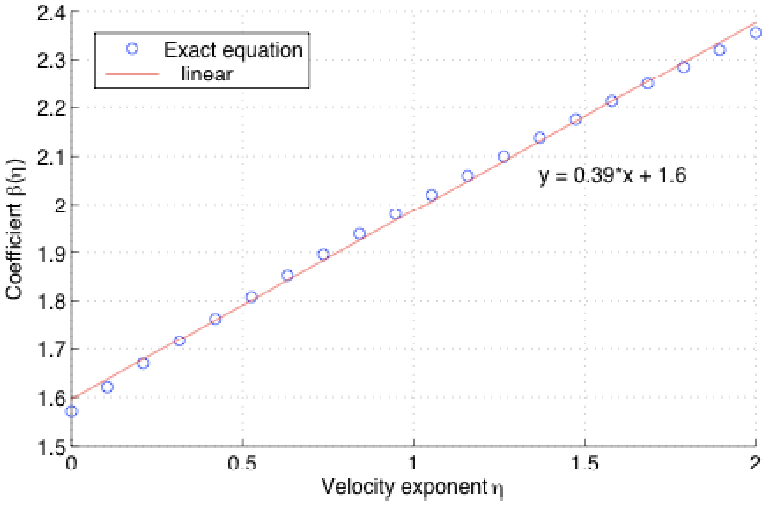

Figure 6.2: Exact equation for $\beta(\eta)$ compared with linear approximation

Finally, we combine the discussion of target damping for a particular isolator displacement limit with equivalent damping for nonlinear viscous damping systems. Setting the expression for equivalent damping in Equation (6.42) equal to the target damping computed in Equation (6.31), we have the inequality

$$\frac{\overline{c}_d u_o^{\eta-1}\omega_1^{\eta-2} g}{0.4\eta+1.6} \geq \exp\left[1-4\frac{\overline{u}_M}{S_{d,MCE}^{5\%}}\right] \tag{6.47}$$

Since the target displacement is generally equal to the displacement limit of the isolation system in the MCE, it can be assumed that $u_0 = \overline{u}_M$. The required normalized damping coefficient becomes

$$\overline{c}_d \geq \frac{(0.4\eta+1.6)\overline{u}_M^{1-\eta}\omega_1^{2-\eta}}{g}\exp\left[1-4\frac{\overline{u}_M}{S_{d,MCE}^{5\%}}\right] \tag{6.48}$$

Careful inspection on the above relation reveals a possible further simplification. Noting that the *target* MCE spectral acceleration, in units of *g*, can be expressed as $S_{a,t} = \omega_1^2 \overline{u}_M / g$, Equation (6.48) becomes

$$\overline{c}_d \geq (0.4\eta+1.6)\omega_1^{\eta} S_{a,t}^{1-\eta}\exp\left[1-4\frac{\overline{u}_M}{S_{d,MCE}^{5\%}}\right] \tag{6.49}$$

where $S_{a,t} = S_a(\omega_1, \zeta_t)/g$, and is the target MCE spectral acceleration. This form allows the designer to estimate the required damping coefficient of the nonlinear viscous damping

system as a function of the structure's weight, which is conveniently analogous to the specification of the required base shear of a structure.

6.3.2.2 Sensitivity of Demand Parameters to Viscous Damping

In the previous section, a simplified method of selecting generalized nonlinear viscous damping parameters to meet particular isolation system displacement limits was presented. The performance characteristics of the supported structure were not considered, since the primary function of supplemental damping at the isolation interface is usually prevention of excessive deformation of the isolators. In this section, a specialization to linear viscous damping is made in order to form a baseline to which subsequent studies may be compared.

Consider the idealized isolated structure depicted in Figure 6.1. The equations of motion for this structure were developed for both nonlinear spring and nonlinear damper properties at both the isolation level and the superstructure level. To identify the effect of linear damping on superstructure performance, both the isolation system and superstructure are assumed linear.

The engineering demand parameters (EDPs) considered are the following:

1. U_{iso} : isolator displacement
2. δ_s: story drift of superstructure
3. PFA_s : peak floor acceleration at the second floor
4. $PFSA_s$: peak floor spectral acceleration of superstructure over the frequency range $f \in [2\,\text{Hz}, 10\,\text{Hz}]$

To clarify the sensitivity of these EDPs to ground-motion intensity, a single ground motion was selected and scaled incrementally to different intensities. For the purposes of the sensitivity analysis presented here, the characteristics of the acceleration record may be considered to be arbitrary. Here, the LA01 record developed by Somerville et al. [1996] as part of the FEMA/SAC Steel Project was used as the basis of the response history analyses. This motion, having a peak ground acceleration of 0.46 g, was part of an ensemble of records scaled to represent the 10% in 50-year hazard level on firm ground conditions in metropolitan Los Angeles. Ground-motion intensity is characterized herein as the scale factor by which the input acceleration record is amplified. The scale factor, SF, is varied to crudely simulate various levels of seismic hazard. This type of analysis has been termed Incremental Dynamic Analysis (IDA) by previous researchers (e.g., Vamvatsikos and Cornell [2006]),

and provides a clear method of observing the magnitude of changes to the EDPs of nonlinear systems as a function of linear increases in demand input. While it is not generally acceptable to model differences in seismic hazard with ground-motion scale factors due to the relationship between dynamic characteristics and earthquake magnitude, IDA can provide general insight as to the interrelationships between intensity of input and important response parameters such as acceleration and deformation.

To gain understanding of the effect of linear fluid viscous damping parameters on seismic performance over a range of seismic hazard, a number of viscous damping ratios, superstructure periods, and isolation periods. The primary objective of this study is to observe trends of each EDP as a function of the intensity measure for a given set of isolation system and superstructure parameters are considered.

Three fixed-base natural periods are considered in this study: T_{fb} = 0.5 sec, 1.0 sec, and 1.5 sec. Additionally, two isolated periods are considered: T_{iso} = 3 sec and 4 sec. Finally, two levels of isolation system viscous damping are considered: ζ_t = 0.10 and 0.25. Damping in the superstructure is taken as 0.05. In relation to the non-dimensional equations developed for the 2-DOF system in Section 6.3.1.2, $T_{iso} = 2\pi / \omega_1$ and $T_{fb} = 2\pi / \omega_2$. For illustrative purposes, sample hysteresis loops of several cases of the combined linear isolation system with dampers is shown in Figure 6.3. Figure 6.4 and Figure 6.5 present analytical results of the above-described IDA, where the scale factor defines the intensity measure. The EDPs reported are peak isolator displacement, peak interstory drift, and peak floor spectral acceleration. Each plot compares the evolution of the EDP with SF for the levels of damping considered.

Consider the data presented in Figure 6.4, which presents EDP versus SF for T_{iso} = 3 sec. All EDPs exhibit a linear relationship with respect to the scale factor (SF) of the input ground motion. This is expected, due to the linearity of the system. Whereas the isolator displacement appears equally sensitive to damping regardless of the superstructure period, the sensitivity of drift demand to damping is more significant for T_{fb} = 0.5 sec and 1.0 sec, and less significant for T_{fb} = 1.5 sec. The peak floor spectral acceleration does not appear sensitive to the damping in the isolation system for all fixed-base periods.

Inspection of the data of Figure 6.5 for T_{iso} = 4 sec. shows similar trends to those of Figure 6.4 for the sensitivity of isolator displacement to viscous damping. However, the

trends for peak interstory drift and peak floor spectral acceleration are *opposite* of those observed for the 3 sec isolation system. The drift demand shows virtually no sensitivity to isolation system viscous damping, whereas the floor spectral acceleration shows similar sensitivity to damping regardless of the fixed-base period.

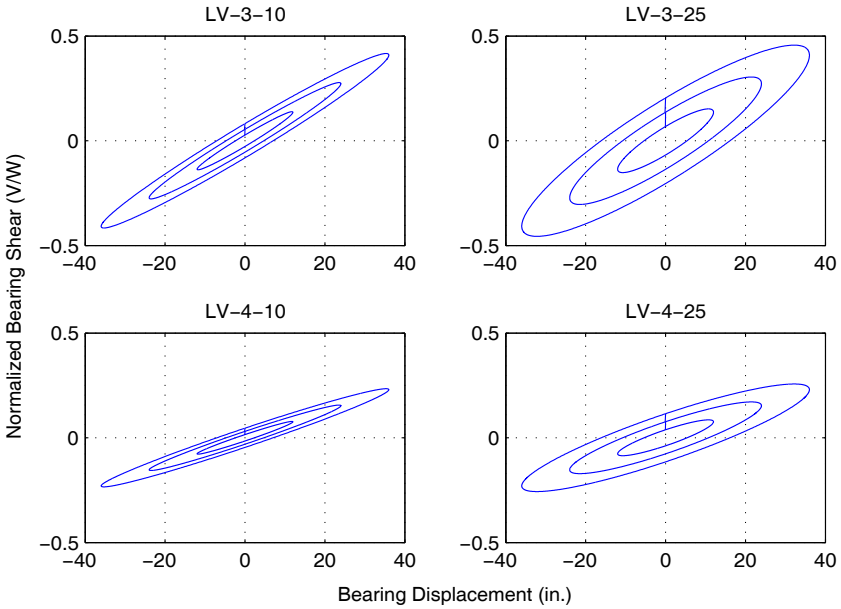

Figure 6.3: Sample cyclic behavior for several cases of linear viscous isolation systems considered in parametric studies

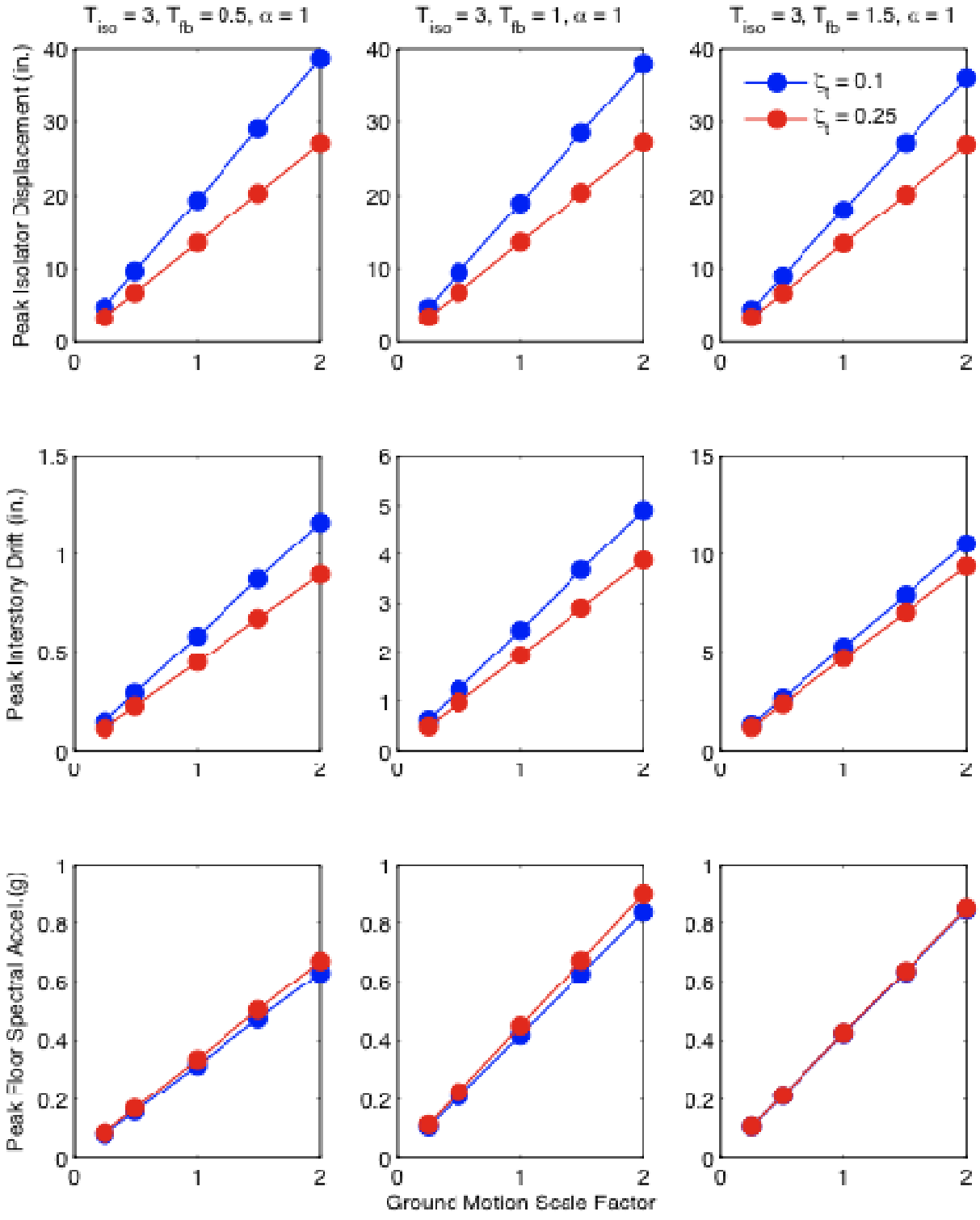

Figure 6.4: Comparison of peak isolator displacement, interstory drift, and peak floor spectral acceleration for linear viscous T_{iso} = 3 sec and the LA01 record

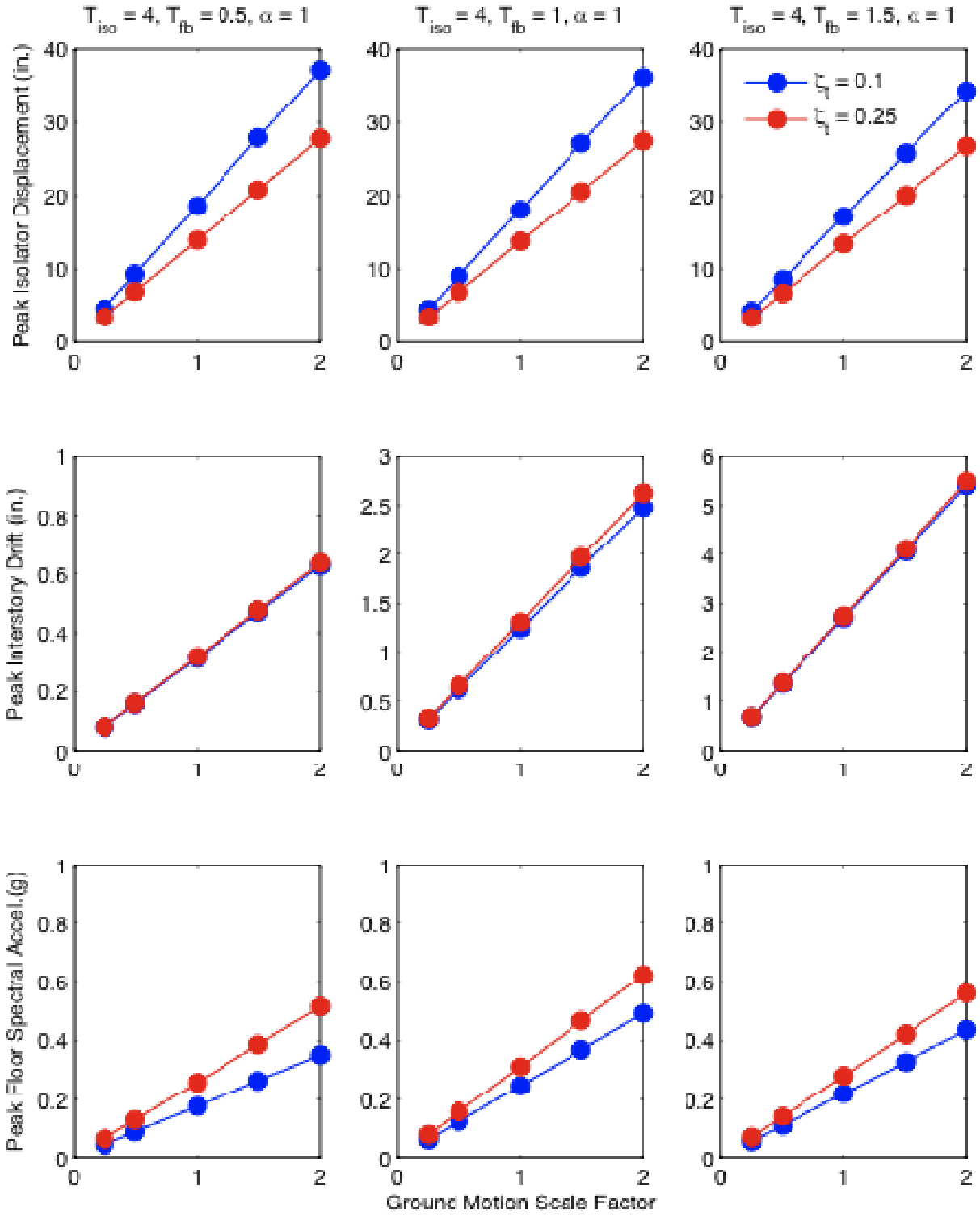

Figure 6.5: Comparison of peak isolator displacement, interstory drift, and peak floor spectral acceleration for linear viscous T_{iso} = 4 sec and the LA01 record

6.3.3 Effect of Bilinear Hysteretic Energy Dissipation on Seismic Performance

An investigation similar to that for linear isolation systems with nonlinear viscous damping is conducted here for linear isolation systems having purely bilinear hysteretic damping, and superstructure damping of 0.05. Such mechanisms have seen wide implementation in seismic isolation design, principally due to the ease of incorporating hysteretic damping within the isolation device. Two main sources of hysteretic damping internal to isolation bearings are (a) yielding of lead for the lead rubber (LR) bearing and (b) friction for the friction pendulum (FP) bearing. In Japanese design practice, there is prominent use of supplemental hysteretic damping devices. Such devices include helical and U-shaped steel dampers, lead dampers, and sliding dampers, the characteristics of which are summarized by Higashino and Okamoto [2006]. To investigate the effect of supplemental hysteretic damping devices on the performance of base-isolated structures, a method must be developed to select the behavioral parameters for the isolation system subject to a particular seismic environment.

6.3.3.1 Selection of Isolation System Parameters

The following parameters characterize a linear isolation system with hysteretic damping: ω_1, $\bar{q}_y$, and v_y. Recall from Section 6.3.1.1 that ω_1 defines the natural frequency of the isolation system assuming a rigid superstructure and no hysteretic damping, and $\bar{q}_y$ and v_y define the normalized yield strength and yield displacement, respectively, of the hysteretic damping mechanism. Here it is assumed that all energy dissipation in the isolation system is due to the supplemental damping mechanism, and therefore ω_1 is the only parameter characterizing the isolation bearings. However, if a LR or single-concave FP isolation system is considered, the friction or lead yield force is taken into account by the damping parameters.

The derivations of Section 6.3.2 for nonlinear viscous dampers can be specialized to hysteretic dampers by recognizing the implications of rate-independence of both metallic yielding and friction. Additionally, energy dissipation per cycle, E_d, is virtually independent of yield displacement and therefore may be omitted from subsequent discussions on parameter selection. By Equation (6.46), the following relationship was established to determine the necessary normalized yield force of a hysteretic damping system given a target

effective isolated natural frequency $\omega_{1,eff}$ and target equivalent damping ζ_t , and a spectral acceleration $S_a\left(\omega_{1,eff},\zeta_t\right)$:

$$\bar{f}_y = \frac{\zeta_t \pi}{2}\frac{S_a\left(\omega_{1,eff},\zeta_t\right)}{g} = \frac{\zeta_t \pi}{2}\frac{\omega_{1,eff}^2 u_t}{g} \tag{6.50}$$

where u_t is the assumed isolator displacement at the target effective natural frequency and damping ratio.

By equating the target equivalent damping ratio of Equation (6.31) to the damping resulting from a hysteretic system with normalized yield force $\bar{f}_y$, the following inequality results from substituting $\eta = 0$ into Equation (6.49):

$$\bar{f}_y \geq \frac{\pi}{2}\frac{S_{a,t}}{g}\exp\left[1-4\frac{\bar{u}_M}{S_{d,MCE}^{5\%}}\right] \tag{6.51}$$

where $S_{a,t} = S_a\left(\omega_{1,eff},\zeta_t\right)/g$, and is the target MCE spectral acceleration. This form allows the designer to specify the yield force of the hysteretic damping system as a function of the structure's weight, which is conveniently analogous to the specification of the minimum base shear of a structure. In this case, the assumed isolator displacement $\bar{u}_M$ can be taken as the equivalent linear viscous MCE isolator displacement $S_d\left(\omega_{1,eff},\zeta_t\right)$, which is readily available from the target MCE elastic spectrum under consideration.

6.3.3.2 Sensitivity of Demand Parameters to Hysteretic Damping

In the previous section, a simplified method of selecting hysteretic damping parameters to meet particular isolation system displacement limits was presented. In this section, an investigation of the implications of hysteretic damping on the performance of isolated superstructures is conducted.

As with the viscous damping system investigation in the previous section, consider the idealized isolated structure depicted in Figure 6.1. To identify the effect of hysteretic damping on superstructure performance, the superstructure is assumed linear, and only hysteretic damping in the isolation system in considered. The remaining aspects of the analysis methodology remain identical to that presented above in Section 6.5.2.2.

For each level of target damping, the yield force of the damper is selected based on Equation (6.50) above, assuming as in the previous case that the target effective isolated frequency and damping ratio is achieved at an isolator displacement equal to that of the equivalent linear viscous case. The primary objective is to observe trends of each EDP as a function of the intensity measure for a given set of isolation system and superstructure parameters.

Figure 6.7 and Figure 6.8 present analytical results of the above-described IDA, where the LA01 ground motion defines the seismic input, and the scale factor defines the intensity measure. As before, the EDPs reported are peak isolator displacement, peak interstory drift, and peak floor spectral acceleration. Each plot compares the evolution of the EDP with SF for a set of target damping ratios, ζ_t = 0.10 and 0.25. Three fixed-base natural periods are considered in this study: T_{fb} = 0.5 sec, 1.0 sec, and 1.5 sec. Additionally, two effective isolated periods are considered: T_{iso} = 3 sec and 4 sec. The yield displacement is assumed to be fixed at 0.02 inches, or nearly rigid. For illustrative purposes, sample hysteresis loops of several cases of the combined linear isolation system with hysteretic damping are shown in Figure 6.6.

The first case considered is the moderate-period isolation system, T_{iso} = 3 sec. These data are presented in Figure 6.7, and each plot shows a comparison of the two levels of target damping considered. It is an expected result that increased target damping results in a lower peak isolator displacement, and the effect of hysteretic damping on isolator displacement is not noticeably sensitive to the fixed-base period of the structure. However, the drift demand appears quite sensitive to the damping for a range of levels of excitation and fixed-based periods. For T_{fb} = 0.5 sec, there is a marked increase in drift demand for SF < 1.5, and this amplification can be as high as 50% for an increase in target damping from 0.10 to 0.25. For longer fixed-base period structures, this increase, for the same change in damping, can approach twofold. This indicates a high sensitivity of deformation in the superstructure to the amount of hysteretic damping in the isolation system. There is also an increase in peak floor spectral acceleration due to the addition of hysteretic damping. For T_{fb} = 0.5 sec, there is a greater than twofold increase on acceleration demand for a change in hysteretic damping of 0.10 to 0.25, and this amplification does not appear sensitive to the ground-motion intensity. As the fixed-base period increases, this amplification in peak spectral acceleration is less

pronounced for the low intensity ground motions, and for SF = 0.25 (the lowest intensity considered), there is virtually no increase in PFSA as the damping increases from 10% to 25%. However, for SF = 0.5, there is no sensitivity in PFSA to damping for T_{fb} = 1.5 sec, however there is significant sensitivity for T_{fb} = 1.0 sec.

From the data of Figure 6.8, the above-described trends in EDP as a function of intensity are similar for the case of T_{iso} = 4 sec. It appears, based on comparison of the isolator displacements with those of Figure 6.7 (in which T_{iso} = 3 sec), that the addition of hysteretic damping shows less significant reduction for the long-period isolation system relative to the moderate-period system. For the case of T_{iso} = 3 sec and T_{fb} = 0.5 sec, an increase in damping from 0.1 to 0.25 results in a 35% decrease in peak isolator displacement for SF = 2. In contrast, for the case of T_{iso} = 4 sec and T_{fb} = 0.5 sec, the same increase in damping results in only a 20% decrease in peak isolator displacement. For both of the above parameter cases, the same increase in damping results in an increase in interstory drift of about 100% for low intensity ground motion ($SF \leq 0.5$). This increase in drift becomes less pronounced as the intensity increases for both moderate and long period isolation systems. Interestingly, the increase in drift demand at low-intensity shaking becomes less significant as the fixed-base period of the superstructure elongates. Expectedly, the amplitude of the peak drift demand increases significantly with elongation of the fixed-base period. Lastly, the peak floor spectral acceleration shows significant sensitivity to the presence of hysteretic damping, as was the case for the moderate-period isolation system. While the amplitude of the PFSA is lower than for the moderate-period isolation system, the amplification with the increase in damping is similar. For the case of T_{iso} = 3 sec and T_{fb} = 0.5 sec, an increase in damping from 0.1 to 0.25 results in a 230% increase in PFSA at SF = 1. For the case of T_{iso} = 4 sec and T_{fb} = 0.5 sec, the same increase in damping results in a 180% increase in PFSA. Both also show similar trends in PFSA with elongation of fixed-base period. The amplification tends to be lower as T_{fb} increases. This can likely be attributed to the tendency of the superstructural properties to drive the system response as the period separation decreases. As a result, where acceleration response is dominated by the behavior of the superstructure (e.g., at low intensities of ground motion), the isolation system properties become less influential.

A general conclusion regarding the use of hysteretic dampers to control isolator displacements is that, particularly for long isolation periods, such devices are inefficient at

large levels of displacement response. That is, the reduction in displacement at large levels of shaking (where isolator displacement control is a performance goal) is quite modest. In contrast, the increase is response in the superstructure due to the presence of hysteretic damping is significant, particularly at low and moderate levels of shaking. As a result, the investigation of innovative seismic isolation systems that substantially reduce isolator displacements in very large earthquakes while optimally limiting superstructural deformation and acceleration response in more frequent earthquakes is warranted.

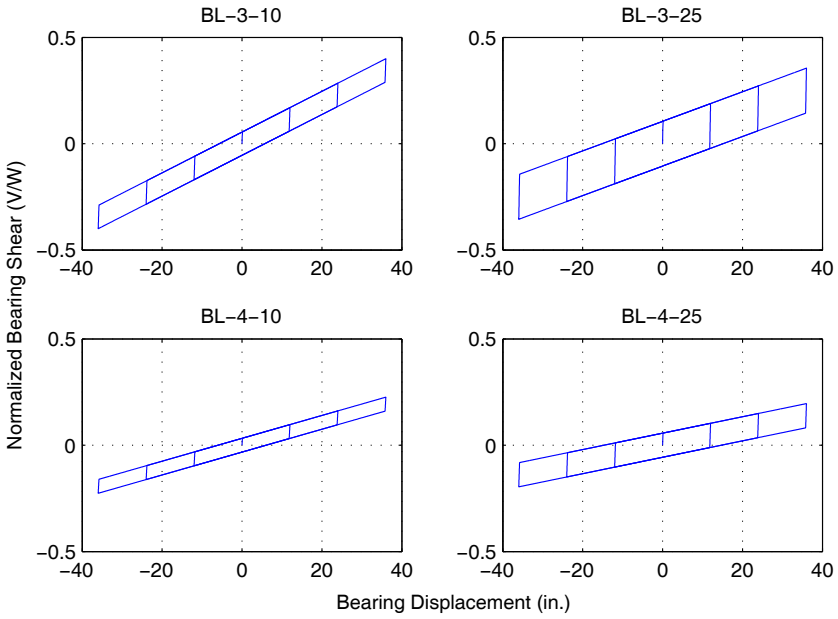

Figure 6.6: Sample cyclic behavior for several cases of bilinear hysteretic isolation systems considered in parametric studies

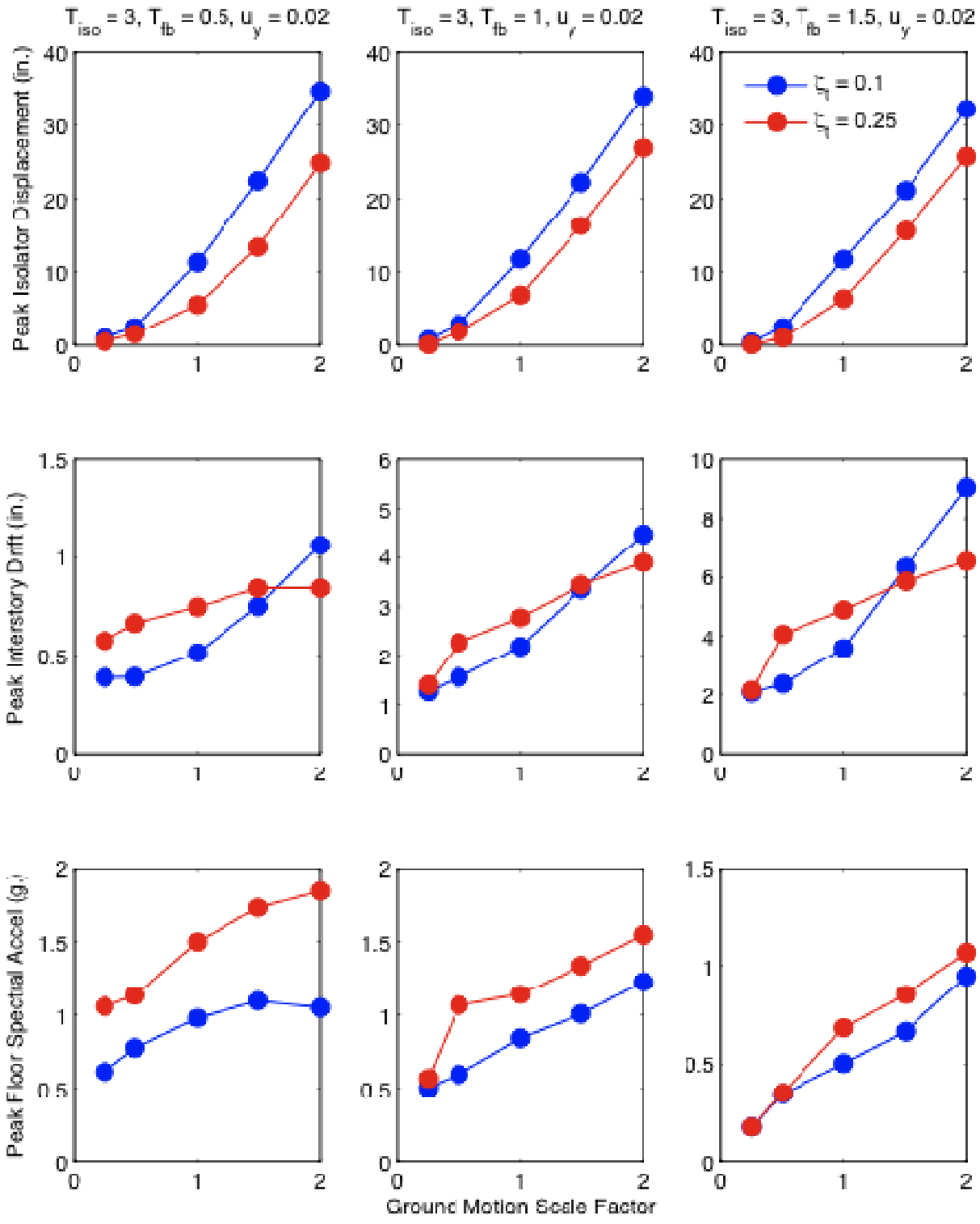

Figure 6.7: Comparison of peak isolator displacement, interstory drift, and peak floor spectral acceleration for bilinear hysteretic T_{iso} = 3 sec and the LA01 record

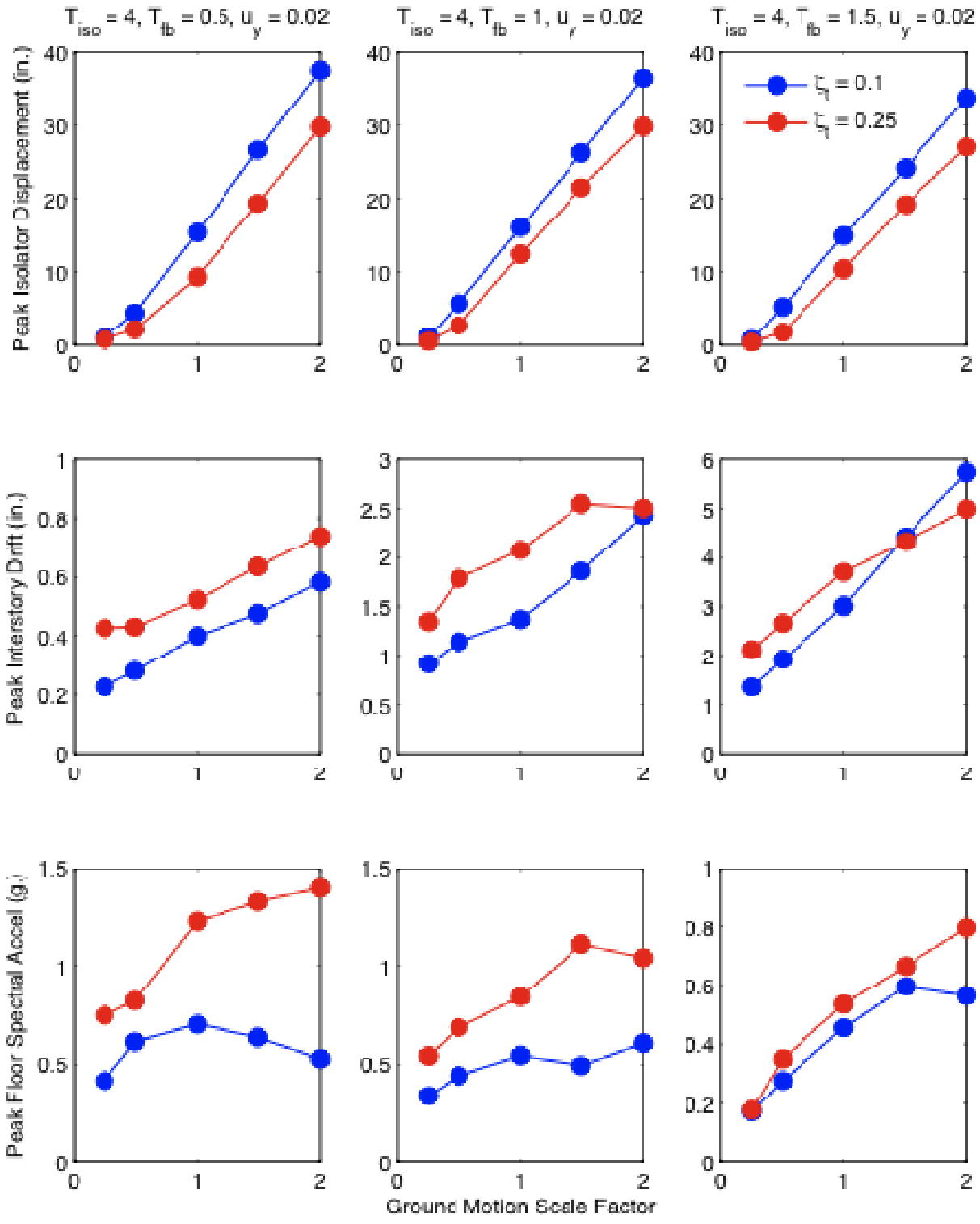

Figure 6.8: Comparison of peak isolator displacement, interstory drift, and peak floor spectral acceleration for bilinear hysteretic T_{iso} = 4 sec and the LA01 record

6.3.3.3 Frequency Content of Total Accelerations for Hysteretic Damping

An important consideration for isolated structures is the degree to which high frequency acceleration are attenuated in the superstructure by the isolation system. It is well known that a purely linear, undamped isolation system filters virtually all frequency content of acceleration not near the natural frequency of the structure, so long as the period separation is sufficiently large. Since this isolated natural frequency is typically quite low, these accelerations do not generally pose a risk to non-structural elements and building contents that resonate at higher frequencies. However, it has also been shown that the presence of hysteretic damping significantly amplifies the high-frequency accelerations in the isolated structure, particularly for low to moderate levels of ground shaking. The causes for this are investigated further to identify potentially beneficial aspects of an isolation system that would effectively isolate the structure from high-frequency accelerations over a range of ground-motion intensity.

Consider the following equation of motion for an SDOF structure isolated on a linear isolation system with a hysteretic damper of yield strength q_d, and negligibly low yield displacement:

$$m\ddot{u}(t) + c\dot{u}(t) + k_b u(t) + q_d \operatorname{sgn}\left[\dot{u}(t)\right] = -m\ddot{u}_g(t) \tag{6.52}$$

Dividing by m and substituting the natural frequency ω_n we obtain

$$\ddot{u}(t) + 2\zeta\omega_n\dot{u}(t) + \omega_n^2 u(t) + \frac{q_d}{m}\operatorname{sgn}\left[\dot{u}(t)\right] = -\ddot{u}_g(t) \tag{6.53}$$

Since Equation (6.53) is *almost* a linear differential equation, we move the hysteretic component to the right-hand side to obtain

$$\ddot{u}(t) + 2\zeta\omega_n\dot{u}(t) + \omega_n^2 u(t) = -\left[\ddot{u}_g(t) + \frac{q_d}{m}\operatorname{sgn}\left[\dot{u}(t)\right]\right] \tag{6.54}$$

If we define some new displacement $\bar{u}(t) = nu(t)$, then (6.54) becomes

$$\ddot{\bar{u}}(t) + 2\zeta\omega_n\dot{\bar{u}}(t) + \omega_n^2\bar{u}(t) = -n\left[\ddot{u}_g(t) + \frac{q_d}{m}\operatorname{sgn}\left[\dot{u}(t)\right]\right] \tag{6.55}$$

But $\mathrm{sgn}(n\dot{u}) = \mathrm{sgn}(\dot{u})$, so

$$\ddot{\bar{u}}(t) + 2\zeta\omega_n\dot{\bar{u}}(t) + \omega_n^2\bar{u}(t) = -n\left[\ddot{u}_g(t) + \frac{q_d}{m}\mathrm{sgn}\left[\dot{\bar{u}}(t)\right]\right] \tag{6.56}$$

Comparing Equations (6.54) and (6.56), it is clear that in multiplying *both* the ground acceleration and yield strength by the same factor *n*, the response becomes $\bar{u}(t) = nu(t)$, or, in other words, each response quantity (displacement, velocity, acceleration) scales up by the same *n*. However, the time variation of the response (and hence the frequency content) remains unchanged due to the scaling of both the ground motion and yield strength by the exact same amount. This is an important result because, if the objective of isolation were to preserve equal frequency content in superstructural accelerations over a range of seismic intensity, one strategy would be to devise a hysteretic device whose effective yield force varies depending on the amplitude of the ground-motion input. Such a device with a variable effective yield force is the triple pendulum (TP) bearing, whose behavior has been described extensively in this report. The next section contains analytical studies for 2-DOF structures isolated on TP bearings.

6.3.4 Effect of Triple Pendulum Bearings on Seismic Performance

A third investigation, similar to those described for isolation systems with either viscous or hysteretic damping, is conducted and described here for triple pendulum (TP) isolation systems. To investigate the effect of TP bearings on the performance of base-isolated structures, a set of parameters must be selected that highlights the sensitivities of each demand parameter to the properties of the isolation system. For proper comparison with the above parameter studies, the same IDA approach is taken, and the same EDPs (isolator displacement, interstory drift, and peak floor spectral acceleration) are reported.

A feature of the TP isolation system is the multiple geometric and frictional parameters that characterize its cyclic behavior. The parameters open to selection by the designer include spherical radii (R_1, R_2, R_3), slider heights (h_1, h_2, h_3), pendulum displacement capacities ($\bar{u}_1, \bar{u}_2, \bar{u}_3$), and friction coefficients (μ_1, μ_2, μ_3). In practice, these parameters do not assume arbitrary and necessarily distinct values, but are selected based on standard manufactured sizes and specialized to the particular seismic environment. In this

investigation, parameters are selected to achieve practical design properties that are equivalent to the viscous and hysteretic isolation systems described in the previous sections.

The four sets of radii and slider heights selected for this investigation are summarized below, and are classified as Type X-YY where X is the effective period and YY is the percent of critical damping at a displacement equal to that of the equivalent linear viscous system.

$$R_{3-10} = [27" \quad 67" \quad 67"], \quad h_{3-10} = [6" \quad 8" \quad 8"]$$
$$R_{3-25} = [15" \quad 118" \quad 118"], \quad h_{3-25} = [6" \quad 8" \quad 8"]$$
$$R_{4-10} = [47" \quad 109" \quad 109"], \; h_{4-10} = [6" \quad 8" \quad 8"]$$
$$R_{4-25} = [19" \quad 160" \quad 160"], \; h_{4-25} = [6" \quad 8" \quad 8"]$$

In general, the order of entries in the above vector notation denotes the parameters for the first, second, and third pendulum mechanisms. The spherical radii and slider heights are based on representative sizes used by the manufacturer, EPS, Inc. Recalling from Chapter 3 that $L_j = R_j - h_j$, these correspond to the following pendulum lengths for each mechanism:

$$L_{3-10} = [24" \quad 63" \quad 63"]$$
$$L_{3-25} = [12" \quad 114" \quad 114"]$$
$$L_{4-10} = [44" \quad 105" \quad 105"]$$
$$L_{4-25} = [16" \quad 156" \quad 156"]$$

Recalling the effective stiffness for each stage of sliding described in Chapter 3, the natural period for each stage of sliding is summarized below in Table 6.1.

Table 6.1: Pendulum natural periods for parametric study

Classification	Stage I	Stage II	Stage III
TP-3-10	1.06 sec	2.58 sec	3.32 sec
TP-3-25	1.24 sec	3.24 sec	4.24 sec
TP-4-10	2.12 sec	4.12 sec	4.99 sec
TP-4-25	1.30 sec	4.12 sec	5.54 sec

Additionally, four sets of friction coefficients are selected for each bearing type, and are summarized below.

$$\mu_{3-10} = \begin{bmatrix} 0.01 & 0.06 & 0.14 \end{bmatrix}$$
$$\mu_{3-25} = \begin{bmatrix} 0.02 & 0.09 & 0.20 \end{bmatrix}$$
$$\mu_{4-10} = \begin{bmatrix} 0.01 & 0.035 & 0.065 \end{bmatrix}$$
$$\mu_{4-25} = \begin{bmatrix} 0.02 & 0.05 & 0.08 \end{bmatrix}$$

Finally, three sets of displacement capacities are selected for one of the *outer* spherical surfaces. The inner pendulum mechanism is assumed to have no deformation limit, since reaching this limit implies the bearing has exceeded its overall displacement capacity and the structure therefore is subject to pounding. Additionally, the third pendulum mechanism is assumed to have no deformation limit, since the last stage of sliding is intended to function as a "soft stop" that gradually increases the shear resistance as the isolator reaches its displacement capacity. Since this stage of sliding functions as a displacement restraint, it is not included in the analysis because performance beyond the isolator displacement capacity is not considered for any systems investigated in this Chapter. While important to the ultimate performance of isolated structures, this limit state is not considered here; it is assumed that sufficient capacity has been provided by the designer based on analysis. The three displacement capacities considered for the outer surfaces are

$$\bar{u}_{3-10} = \begin{bmatrix} NL & 13.8" & NL \end{bmatrix}$$
$$\bar{u}_{3-25} = \begin{bmatrix} NL & 13.1" & NL \end{bmatrix}$$
$$\bar{u}_{4-10} = \begin{bmatrix} NL & 17.5" & NL \end{bmatrix}$$
$$\bar{u}_{4-25} = \begin{bmatrix} NL & 11.0" & NL \end{bmatrix}$$

where *NL* = "no limit" and denotes the lack of consideration of loss of total bearing travel in the analyses. Recall from Chapter 3 that the selection of these parameters defines the transitions to the hardening regime of Stage IV sliding. Sample hysteretic behavior for each of the four bearing types is summarized in Figure 6.9.

First we consider the moderate isolation period T_{iso} = 3 sec. These data are presented in Figure 6.10, and each plot shows the variation of all three EDPs with intensity for the two levels of effective damping considered. An interesting result is that, while the high damping bearing exhibits a reduction in isolator displacements over the low damping bearing (a decrease of about 20% for SF = 2 and T_{fb} = 0.5 sec), this increase in damping leads to virtually no amplification of drift except at the lowest levels of shaking ($SF \leq 1$) for T_{fb} = 0.5 sec. It is apparent from the data for peak floor spectral acceleration that there is amplification

due to the increase in damping. However, the magnitude of the PFSA and the associated amplification both appear to be less significant than that for the equivalent bilinear hysteretic isolation system.

Figure 6.11 presents analytical results for the long isolation period system T_{iso} = 4 sec. An observation regarding the isolator displacements is that, for the low damping bearing, the isolators appear to be activated even at the smallest level of excitation. This response was not observed for any other system studied. This is an indication of effective isolation even under small and moderate seismic events. Compared to the TP isolation system with T_{iso} = 3 sec, the sensitivity of both drift and peak floor spectral acceleration to the increase in damping is more significant. However, for both TP systems studied, the magnitude and amplification of the drift and PFSA demands are less than for the equivalent bilinear hysteretic system.

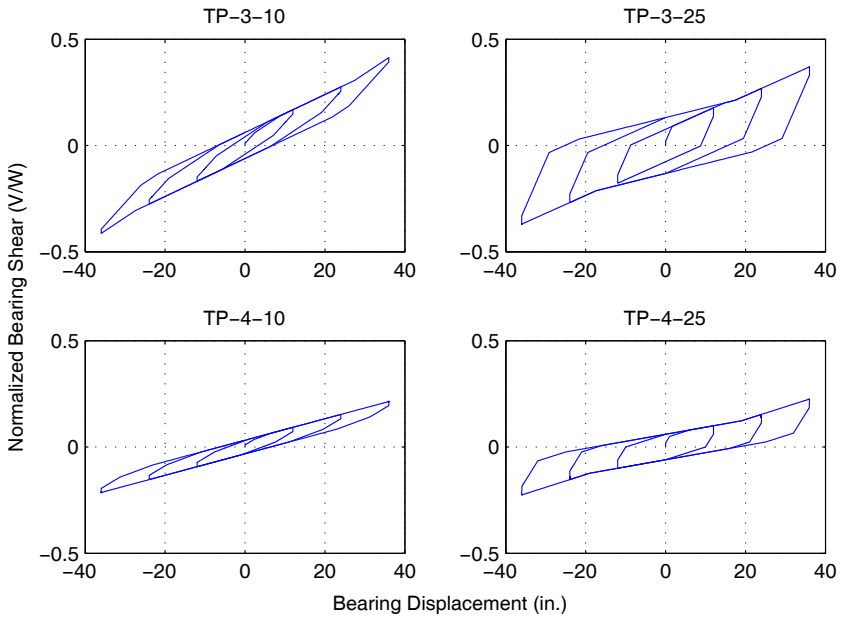

Figure 6.9: Sample cyclic behavior for TP bearings considered in parametric studies

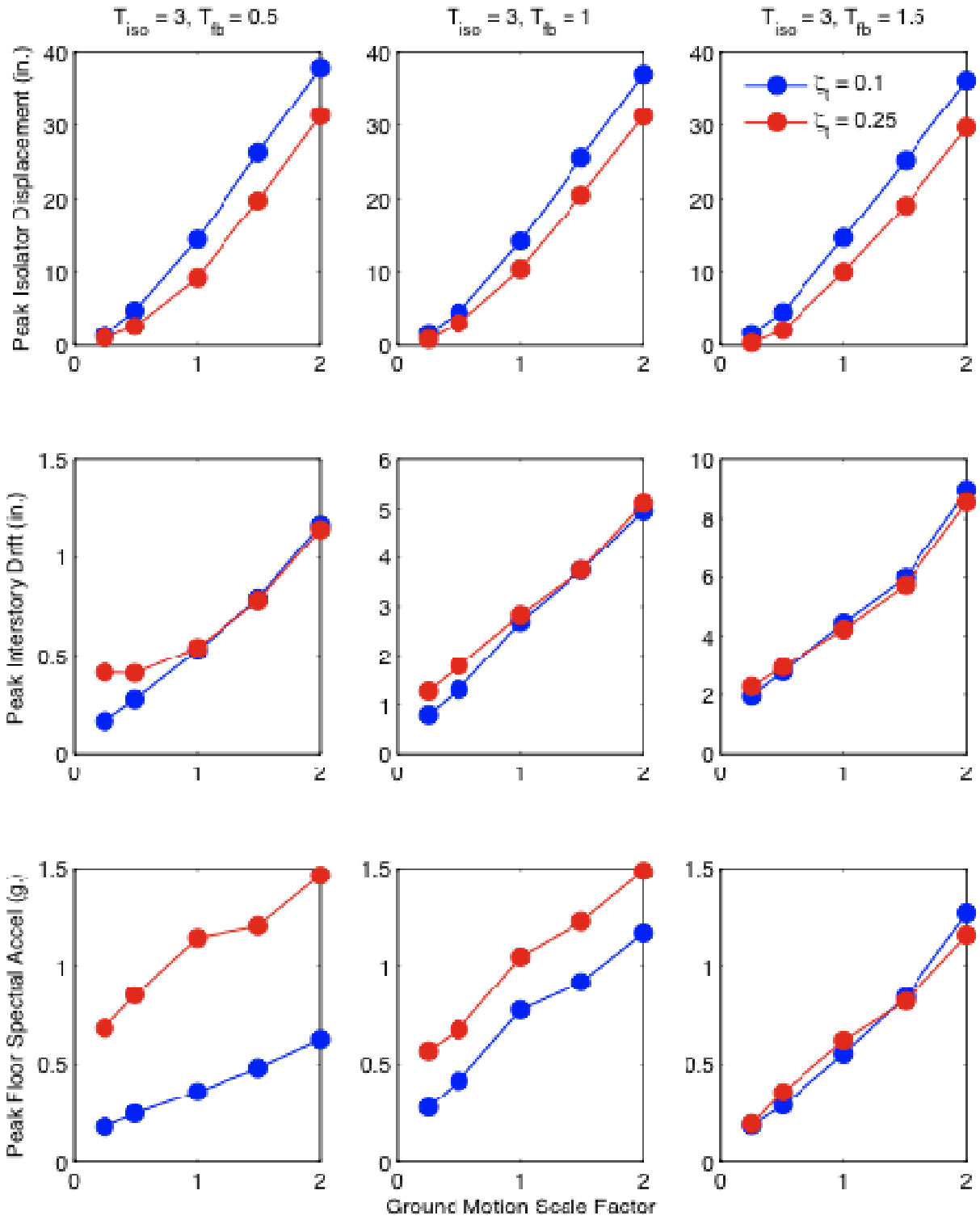

Figure 6.10: Comparison of peak isolator displacement, interstory drift, and peak floor spectral acceleration for TP T_{iso} = 3 sec and the LA01 record

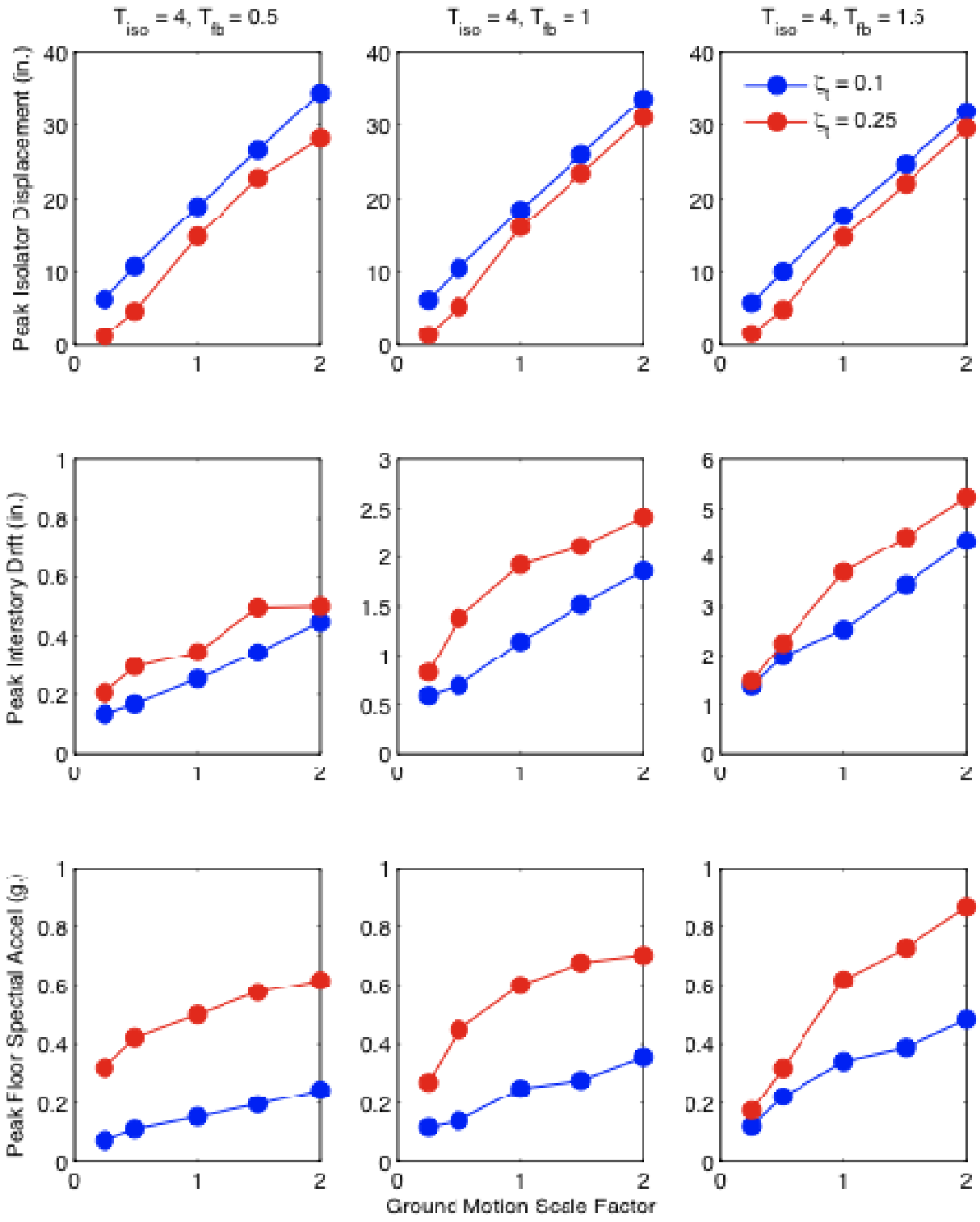

Figure 6.11: Comparison of peak isolator displacement, interstory drift, and peak floor spectral acceleration for TP T_{iso} = 4 sec and the LA01 record

6.4 SEISMIC RESPONSE OF MULTI-STORY ISOLATED STRUCTURES

The objectives of the previous section were to identify relationships between isolation system parameters and important engineering demand parameters. To provide clarity to the results of these investigations, a 2-DOF structure subjected to a single ground-motion input was selected as representing the structure and its seismic demand. The intensity was modeled as a scale factor applied to the ground motion, a simple but ultimately inaccurate reflection of varying seismic hazard. To study the above-described parametric relationships for multi-story isolated structures subject to a variety of ground motions, a study is undertaken here to evaluate the previously drawn conclusions considering more realistic models of the system and the associated variability in seismic input.

6.4.1 Ground-Motion Selection

To both facilitate the development of statistical descriptions of EDPs and to consider a variety of seismic characteristics, an ensemble of ground motions was selected to represent possible realizations of ground motion at a site. As part of the SAC Steel Project, several ensembles of ground motions were developed for the Los Angeles basin. Since the objectives of these studies are to identify demand parameter sensitivities to inputs having multiple frequencies of occurrence, three ground-motions ensembles were selected. Each of the three ensembles contains 10 pairs of acceleration records, and was developed for return periods of 72 years, 475 years, and 2475 years. The selected records and their amplitudes have magnitude-distance pairs that are compatible with the disaggregation of the probabilistic seismic hazard at the subject site [Barroso, 1999]. Further details of the development of the SAC ground motions are described by Somerville et al. [1997].

Figures Figure 6.12 through Figure 6.14 show the elastic response spectra for each ground motion for the 72-year, 475-year, and 2475-year ensembles, respectively. Figure 6.15 shows a comparison of the median spectra for all three return periods, including an overlay of the USGS prescriptive spectra with best-fit parameters. These parameters are described in Table 6.2. Best-fit parameters are determined by selecting S_{DS} and S_{D1} such that the error between the median spectrum and the USGS spectrum is minimized for both constant acceleration and constant velocity regions, for all three return periods.

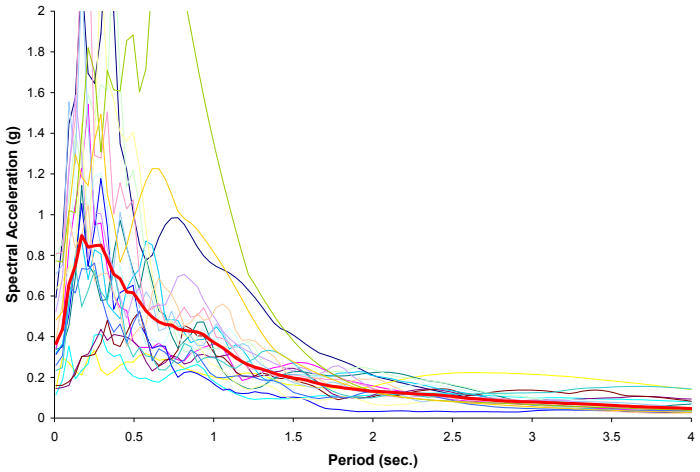

Figure 6.12: Elastic response spectra for 72-year records (median shown red and bold)

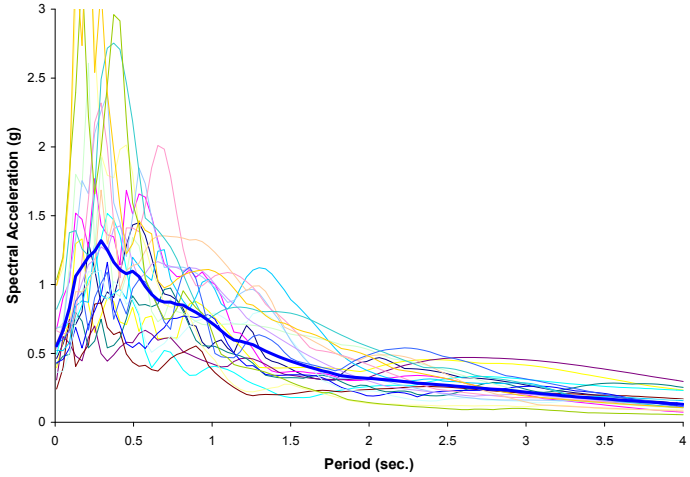

Figure 6.13: Elastic response spectra for 475-year records (median shown blue and bold)

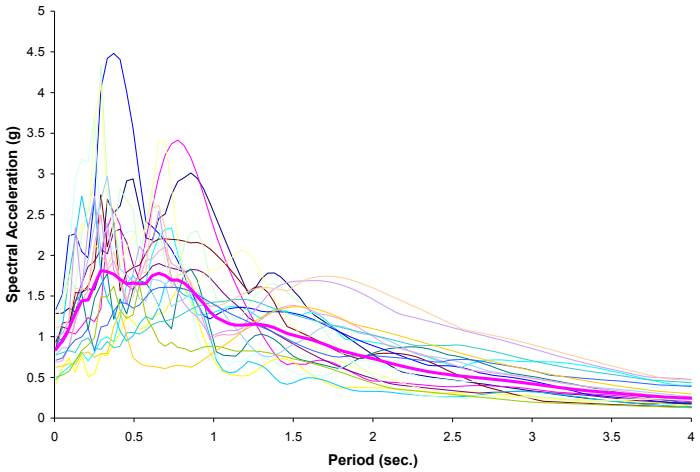

Figure 6.14: Elastic response spectra for 2475-year records (median shown magenta and bold)

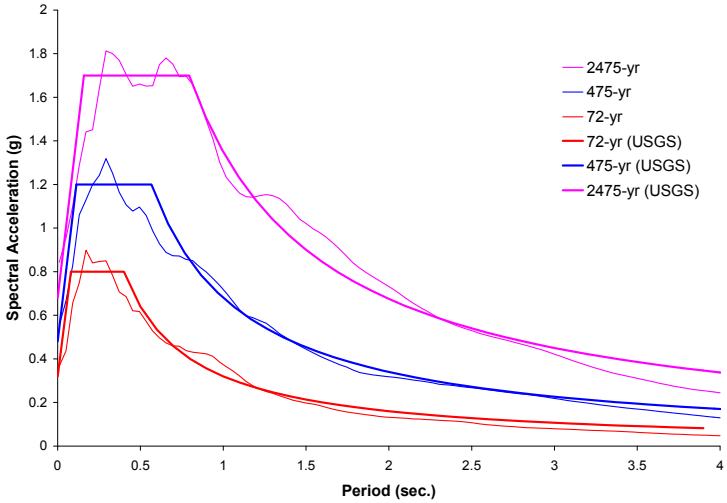

Figure 6.15: Median elastic response spectra for all three ground-motion ensembles, including overlay of best-fit USGS prescriptive spectra

Table 6.2: Best-fit USGS spectral parameters

T_R	PGA (g)	S_{DS} (g)[1]	S_{D1} (g)[2]	T_o (sec.)[3]
72-yr	0.32	0.8	0.32	0.40
475-yr	0.48	1.2	0.68	0.57
2475-yr	0.68	1.7	1.35	0.79

[1] Spectral acceleration at 0.2-sec

[2] Spectral acceleration at 1.0-sec

[3] Transition period from const. accel to const. veloc.

6.4.2 Methodology for System Parameter Selection

A procedure is described in this section for selecting structural system parameters given general information about the structure and the seismic environment in which it is located. Consider the task of developing generally nonlinear shear spring elements for an *n*-story shear building. Each story has mass m_j and interstory height h_j ($j = 1, \ldots, n$) and may be generally distinct (although often they are approximately equal for vertically regular structures).

The following notation is used throughout this section:

$\mathbf{p} = [p_1 \cdots p_n]^T$: global force vector

$\mathbf{u} = [u_1 \cdots u_n]^T$: global displacement vector

$\mathbf{q} = [q_1 \cdots q_n]^T$: local spring force vector

$\mathbf{v} = [v_1 \cdots v_n]^T$: local spring deformation vector

For the *n*-story shear building, the equilibrium matrix mapping local spring forces to global forces, $\mathbf{p} = \mathbf{B}\,\mathbf{q}$, can be determined by inspection as

$$\mathbf{B} = \begin{bmatrix} 1 & -1 & 0 & 0 \\ 0 & 1 & \ddots & 0 \\ \vdots & \ddots & \ddots & -1 \\ 0 & \cdots & 0 & 1 \end{bmatrix}_{n \times n} \tag{6.57}$$

By contragradience, it can be stated that the global displacements are mapped to the spring deformations by the equation $\mathbf{v} = \mathbf{B}^T\mathbf{u}$. Additionally, each spring has a constitutive relation $q_j = k_j v_j$, where $q_j \le q_{yj}$, the yield spring force of the *j*th shear spring. It is noted, however, that structural systems generally have a yield drift ratio that is independent of strength, and is noted as θ_y. This yield drift ratio is assumed constant for all stories. It will be shown that steel concentric braced frames have $\theta_y \approx 0.003$. Recall that the yield drift at the *j*th story is defined as $\theta_j = v_j / h_j$. A necessary definition is the strength reduction factor *R*. Here, the nominal design base shear for the structure is computed by dividing the elastic base shear demand by *R*. The R factor may be considered the product of two independent factors, and can be written as $R = R_\mu R_\Omega$ [SEAOC, 1999]. The factor R_μ is the ductility-based component, and R_Ω is the overstrength-based component. In this procedure, the ductility-based portion R_μ must be specified. Some guidance is given by modern building codes (such as the IBC [2006]) as to how to select these for a particular structural system. For isolated structures, essentially elastic behavior is generally assumed to result on average from setting $R_\mu = 1.0$.

With the above definitions, it is possible to uniquely determine the nonlinear spring properties of a general *n*-story shear building. For the seismic demand, some site-specific response spectrum must be defined. This procedure is independent of the type of spectrum (e.g., uniform hazard, attenuation model given M_w, R_{JB}, etc.). This spectrum is defined as $S_a(\omega,\zeta)$ for some frequency ω and damping ζ. Hence, to get a first-pass estimate of the global elastic seismic forces applied to our shear building, we need a first-pass estimate of the fundamental frequency, ω_1, and some shape function, Ψ_1, that defines an estimate of the first mode shape. The selection of ω_1 is nearly arbitrary, since iteration will be employed to find its solution. However, an estimate implied by the building code is $\omega_1 = 2\pi\left(C_t H^{3/4}\right)^{-1}$ where C_t depends on the system but in this case could simply be called $C_t = 0.03$, and $H = \Sigma_{j=1}^{n} h_j$ is the total building height (which must be in feet for this equation). The initial estimate of the shape function Ψ_1 could be taken as triangular, and therefore is mathematically expressed as $\Psi_1 = \begin{bmatrix} 1/n & 2/n & \cdots & n \end{bmatrix}^T$. With all these definitions, the first mode global force vector is simply

$$\mathbf{p}_1 = \Gamma_1 \mathbf{m} \Psi_1 S_a(\omega_1, \zeta), \quad \Gamma_1 = \frac{\Psi_1^T \mathbf{m1}}{\Psi_1^T \mathbf{m} \Psi_1} \approx 1.3 \tag{6.58}$$

From equilibrium, $\mathbf{p} = \mathbf{B}\mathbf{q}$, and noticing that **B** is both square and full rank, the elastic spring forces are simply $\mathbf{q}_e = \mathbf{B}^{-1}\mathbf{p}_1$. Assuming the equal-displacement rule[2] from Newmark and Hall [1982], $q_e = R_\mu q_y$, and the yield spring force vector is $\mathbf{q}_y = \left(1/R_\mu\right)\mathbf{q}_e$. This defines the yield forces for each of the *n* nonlinear shear springs. In finding the elastic stiffness of each spring, we need only notice that each spring has the identical yield displacement $v_{yj} = \theta_y h_j$. Therefore each elastic spring's stiffness may be computed as $k_j = q_{yj} / v_{yj} = q_{yj} / \theta_y h_j$. This gives an element stiffness matrix

$$\mathbf{k}_e = \frac{1}{\theta_y} \begin{bmatrix} \frac{q_{y1}}{h_1} & 0 & 0 \\ 0 & \ddots & 0 \\ 0 & 0 & \frac{q_{yn}}{h_n} \end{bmatrix} \tag{6.59}$$

Applying the compatibility relation $\mathbf{v} = \mathbf{B}^T \mathbf{u}$, the global stiffness matrix **k** mapping **u** to **p** is computed as $\mathbf{k} = \mathbf{B}\mathbf{k}_e\mathbf{B}^T$. Now, we have a mass matrix **m** and a global stiffness matrix **k**, so by eigenvalue analysis we obtain a first iteration of the *n* mode shapes and *n* natural periods. Our next iteration of global earthquake forces is, for each mode $k = 1 \ldots n$.

$$\mathbf{p}_k = \Gamma_k \mathbf{m} \phi_k S_a\left(\omega_k, \zeta\right), \quad \Gamma_k = \frac{\phi_k^T \mathbf{m1}}{\phi_k^T \mathbf{m} \phi_k} \tag{6.60}$$

The elastic spring forces *for each mode* are computes as $\mathbf{q}_{ek} = \mathbf{B}^{-1}\mathbf{p}_k$, and the modal combination of spring forces is simply the SRSS of each mode, or

$$\mathbf{q}_e = \begin{pmatrix} \sqrt{\sum_{k=1}^{n} q_{ek,1}^2} \\ \vdots \\ \sqrt{\sum_{k=1}^{n} q_{ek,n}^2} \end{pmatrix} \tag{6.61}$$

[2] This is not strictly required if we apply an appropriate *R*-μ-*T* relationship.

The current iteration of spring yield forces becomes $\mathbf{q}_y = \left(1/R_\mu\right)\mathbf{q}_e$, which by Equation (6.59) gives a new element stiffness matrix $\mathbf{k}_e$. Applying $\mathbf{k} = \mathbf{B}\mathbf{k}_e\mathbf{B}^T$ provides an updated global stiffness matrix, which in turn yields a new set of frequencies and mode shapes. This iteration continues until the previous trial set of natural frequencies converges suitably close to the currently computed set.

The converged shear building design consists of a set of spring stiffnesses and yield forces for each of the *n* springs. Assuming some hardening parameter $\alpha = k_p / k_e$, which defines the ratio of plastic-to-elastic stiffness, this is sufficient to specify bilinear (or Bouc-Wen plasticity) springs at each story and conduct parametric studies with a suite of ground motions. For parametric studies described in this section, however, only the isolation systems are nonlinear, and therefore the masses, spring stiffnesses, and assumed damping matrix completely characterize the response of the superstructure.

6.4.2.1 Yield Story Drift Ratio of Braced Frame Structures

An important input parameter for the above design procedure is the yield story drift ratio. For a concentric braced frame structure, it can be shown that the yield drift ratio is a function only of material and geometric properties, and not the selected design strength or stiffness. First, observe that the strength and stiffness of a particular story are perfectly coupled. Consider a one-story, single-bay subassemblage having axially inextensible beams and columns with ideal pin connections at their ends. Given a typical story height, *h*, and a typical bay width, *b*, equations for both the story stiffness, k_s, and the story strength, q_y, may be derived in terms of the brace cross-sectional area, A_{br}. From the geometry of a single diagonal braced bay, the story stiffness and story strengths can be described by the equations below,

$$k_s = \frac{E_s A_{br} b^2}{\beta\left(b^2 + h^2\right)^{3/2}}, \quad q_y = \frac{A_{br}\sigma_y b}{\left(b^2 + h^2\right)^{1/2}} \tag{6.62}$$

where E_s is the Young's modulus of steel, σ_y is the yield stress of the brace material, and β is a modification factor to account for the flexible length of a brace that is less than the work-point length (i.e., $L_{eff} = \beta L_{wp}$) and therefore increases the effective axial stiffness. Where brace strengths are controlled by bucking (that is, $\sigma_{cr} < \sigma_y$) the same reasoning applies,

however, for simplicity, that case is not considered here. By combining Equations (6.62) above, we get an equation for the story strength directly in terms of the story stiffness:

$$q_y = \underbrace{\left[\frac{\beta\sigma_y\left(b^2+h^2\right)}{E_s b}\right]}_{v_y} k_s \tag{6.63}$$

The term in brackets is the yield displacement, and is only a function of either material properties or geometric assumptions. Dividing by the story height gives the interstory drift ratio at yield as

$$\theta_y = \frac{\beta\sigma_y}{E_s}\frac{\left(b^2+h^2\right)}{bh} \tag{6.64}$$

For example, given a brace fabricated from ASTM A36 material (with expected yield stress σ_y = 42 ksi), a bay width of 24', a story height of 12', and a yield length modification factor of 0.8, the yield drift is computed by Equation (6.64) as $\theta_y = 0.00272$ radians. Such a formulation is convenient because the stiffness of each story may be computed considering strength *or* drift limitations alone, and the resulting parameters may then be incorporated for use with nonlinear response-history analysis to compute statistics of engineering demand parameters such as ductility demands, interstory drifts, and floor accelerations.

6.4.3 Parametric Studies

Given the above-described ensemble of ground motions and methodology for selecting parameters for a multi-story structure, it is possible to gain understanding of the effect of isolation system properties on key demand parameters. Of primary interest is the comparison of key EDPs for a variety of isolator types and, within each type, a variety of parameters. Trends in these key EDPs as a function of intensity were studied in Section 6.2.4 for the canonical 2-DOF isolated structure subject to a single ground motion. Here, we extend this simple analysis to MDOF structures subject to an ensemble of ground motions.

6.4.3.1 Superstructure

In assigning parameters to the superstructure, three-story and nine-story shear buildings are considered. All floor weights and interstory heights are assumed equal over the height of the

building. The buildings are designed assuming $R_\mu = 1$, and according to a prescriptive elastic spectrum with parameters equal to those in Table 6.2 for the 475-year event. This follows the design provisions of the 1997 UBC whereby structural elements are proportioned according to a seismic event having this return period. Note there is an implicit assumption here that the isolated *R*-factor, R_I, is equal to the overstrength, Ω_0. However, in subsequent analyses, inelastic behavior of the superstructure in not considered, and the design strength is used for the purpose of developing estimates of the member sizes, and hence story stiffnesses. For all buildings, braced frame construction is assumed based on predominant practice for isolated buildings. From the discussion in Section 6.3.2.1, a yield drift ratio of $\theta_y = 0.003$ is assumed and selection of story stiffnesses is according to the iterative response-spectrum analysis method described in Section 6.3.2. Masses were assumed to be equal at each floor, and may be arbitrarily set equal to one. Viscous damping is based on Rayleigh damping matrix with 1% critical in the fundamental mode (isolated mode) and 5% in the second mode (which corresponds to significant deformation in the superstructure.) Damping or nonlinearity in the isolation layer is accounted for separately in the isolator elements, and is not included as Rayleigh damping. Response history analysis was carried out using a custom Matlab® [Mathworks, 2006] script. Implicit Newmark time integration was implemented, and a time step of dt = 0.0025 was used for improved convergence of nonlinear isolator elements.

Given the above design assumptions, the properties of the three- and nine-story buildings are summarized below:

Three-Story Building

Equivalent design base shear: $0.168W$

First three natural periods: T_1 = 0.83 sec, T_2 = 0.35 sec, T_3 = 0.21 sec

Nine-Story Building

Equivalent design base shear: $0.163W$

First three natural periods: T_1 = 1.36 sec, T_2 = 0.58 sec, T_3 = 0.37 sec

6.4.3.2 Linear Isolation System with Viscous Damping

Parameters considered for studies on linear isolation systems with linear viscous damping include variations of both target effective isolation period and damping ratio. The isolation

periods and damping are equivalent to those considered in Section 6.3, that is, effective isolation periods of $T_{eff} = 3$ sec and $T_{eff} = 4$ sec and target isolator damping ratios considered are $\zeta_{eq} = 0.10$ and $\zeta_{eq} = 0.25$ m in addition to the above-described Rayleigh damping. The isolator displacements at which these effective properties are targeted are taken from the median elastic MCE spectrum at the appropriate level of damping. The isolation systems are denoted LV-3-10, LV-3-25, LV-4-10, and LV-4-25, where LV-X-Y denotes a linear viscous system with period X and viscous damping Y%. Properties for LV systems are summarized in Table 6.3.

6.4.3.3 Bilinear Hysteretic Isolation System

Parameters considered for studies on hysteretic isolation systems include variations of effective isolation period and target damping ratio for a fixed yield displacement. As for the viscous isolation system, effective isolation periods of $T_{eff} = 3$ sec and $T_{eff} = 4$ sec are considered. Target isolator damping ratios considered are $\zeta_{eq} = 0.10$ and $\zeta_{eq} = 0.25$. Yield displacement is fixed at $u_y = 0.02"$. The isolation systems are denoted BL-3-10, BL-3-25, BL-4-10, and BL-4-25, where BL-X-Y denotes a bilinear hysteretic system with effective period X and equivalent viscous damping Y% at the respective median isolator displacement observed for the equivalent linear viscous system described in Section 6.4.3.2. Properties for BL systems are summarized in Table 6.3.

6.4.3.4 Triple Pendulum Isolation System

Parameters considered for studies on triple pendulum isolation systems include variations of both slider friction coefficients and slider displacement capacities. Four sets of surface radii, slider heights, and friction coefficients were considered for TP parameter studies. This is based on achieving equivalent period and damping properties to those selected for the viscous and hysteretic systems described above. Properties of each of the four TP systems selected are described above in Section 6.3.4, and are denoted TP-3-10, TP-3-25, TP-4-10, and TP-4-25, where TP-X-Y denotes a triple pendulum system with effective period X and equivalent viscous damping Y% at the respective median isolator displacement observed for the equivalent linear viscous system described in Section 6.4.3.2. Properties for TP systems are summarized in Table 6.3.

Table 6.3: Summary of isolation system properties

		Linear Viscous (LV)		Bilinear Hysteretic (BL)		Triple Pendulum (TP)		
T_{eff}	ζ_{eff}	$\bar{k}_{iso}$ [1]	$\bar{c}_d$ [2]	$\bar{k}_{iso}$ [1]	$\bar{f}_y$ [3]	L_{eff}	μ	$\bar{u}_2$
3 sec	0.10	0.01135	0.00108	0.00960	0.05460	24" / 63" / 63"	0.01 / 0.06 / 0.14	13.8"
3 sec	0.25	0.01135	0.00271	0.00691	0.10520	12" / 114" / 114"	0.02 / 0.09 / 0.20	13.1"
4 sec	0.10	0.00639	0.00081	0.00540	0.03240	44" / 105" / 105"	0.01 / 0.035 / 0.065	17.5"
4 sec	0.25	0.06386	0.00203	0.00388	0.05667	16" / 156" / 156"	0.02 / 0.05 / 0.08	11.0"

Units: [1]1/in, [2]sec/in, [3]nondimensional

6.4.4 Analytical Results

To investigate the response of multi-story base-isolated structures, a parametric study is conducted to identify sensitivity of structural response to the cyclic characteristics of the isolation system. This study is also useful in evaluating the newly developed triple pendulum (TP) system relative to other available isolation systems. In this section, analytical results are presented and described for three general classes of isolation system: 1) linear isolators with linear supplemental dampers, 2) bilinear hysteretic isolators, and 3) triple pendulum isolators. The parameters included and subjected to variation are described above in Section 6.3.3.

6.4.4.1 Linear Viscous Isolation System

This section presents results of the parametric studies on linear isolation systems with linear viscous damping mechanisms. This presentation is divided into two sections, one for each of the two buildings considered.

6.4.4.1.1 Linear Isolators, Three-Story Building

Figure 6.16 presents empirical probabilistic data describing the distribution of peak isolator displacement for seismic events having three return periods: 72-year, 475-year, and 2475-year. Also shown for each isolation system is the CDF of the lognormal distribution with parameters estimated from the observed data. From these data, the median linear viscous MCE isolator displacements as a function of isolation system are as follows: U_{iso}(LV-3-10) = 29.2 in., U_{iso}(LV-3-25) = 23.1 in., U_{iso}(LV-4-10) = 31.3 in., and U_{iso}(LV-4-25) = 21.6 in. These displacements are useful for subsequent comparisons with nonlinear isolation systems.

Figure 6.17 presents peak interstory drift ratio (PIDR) response over the height of the isolated building for all linear viscous systems considered. Additionally, for each hazard level, the median response is reported along the middle column with the 16^{th} and 84^{th} percentile response reported to the right and left, respectively. This gives an indication of the dispersion in response and therefore identifies conditions under which significant variation from the median may exist. A clear result of the PIDR data presented is that, for all return period events, there is an insignificant sensitivity of drift to damping at all floor levels except the third story. The third floor drift demand shows amplification due to increased damping, likely a result of excitation of higher modes. Note that where drifts exceed 0.3%, yielding of the structure is not accounted for. Nonetheless, the results are useful in showing trends and indentifying sensitivity of drifts to various damper characteristics.

Figure 6.18 presents similarly organized data as for PIDR above, but for peak floor acceleration (PFA). Floor accelerations appear to be more sensitive to isolation viscous damping compared to drift demands. Interestingly, median PFA for the 475- and 2475-year events shows negligible sensitivity to the isolation period for a fixed level of damping. This suggests that, to reduce rare- and very-rare event PFA in an isolated structure, it is preferable to specify lower viscous damping and shorter isolation period rather that higher viscous damping and longer isolation period. This effect is less pronounced for the 72-year event, where LV-3-0.10 and LV-4-0.25 give comparable median PFA results.

While PFA is a commonly adopted EDP for evaluating the potential for damage to non-structural components, the frequency content of floor accelerations is important for non-rigid secondary systems. To investigate the effect of linear viscous damping mechanisms on the response on such non-rigid components, floor response spectra are developed at the roof for all isolation systems investigated. The median of these spectra are shown in Figure 6.19 for all levels of seismic hazard considered in this study. In examining the roof spectra for the 72-year event, it is clear that that an increase in damping from 10% to 25% leads to approximately a 50% increase in peak floor spectral acceleration in above 1 Hz. This may be an important consideration when isolating a structure for protection of secondary components that have a variety of dynamic characteristics.

6.4.4.1.2 Linear Isolators, Nine-Story Building

Figure 6.20 through Figure 6.23 show the peak isolator displacement, PIDR, PFA, and roof acceleration spectra for the nine-story building isolated by a linear isolation system with a nonlinear viscous damping mechanism. Variation in the observed response trends relative to the three-story model are identified and discussed.

From Figure 6.28, the median MCE isolator displacements as a function of isolation system are as follows: U_{iso}(LV-3-10) = 27.8 in., U_{iso}(LV-3-25) = 22.8 in., U_{iso}(LV-4-10) = 31.3 in., and U_{iso}(LV-4-25) = 21.6 in. From these data, there is very little observable difference in median estimates of isolator displacement relative to the three-story case. There is a slight decrease in the nine-story median isolator displacement in the 72- and 475-year events due to the relative increase in flexibility of the superstructure. However, this decrease becomes less pronounced for the 2475-year event, which is the level of hazard at which isolator displacement is generally a critical response quantity.

Evaluating the PIDR and PFA response data of Figure 6.21 and Figure 6.22, respectively, many observed trends remain unchanged relative to the discussion of the three-story building above. The effect of increased target isolator damping on the excitation of higher-mode response is clear, but *less pronounced* for the nine-story building compared to the three-story building. There is increased amplification of roof acceleration and drift demand compared to lower stories, likely due to higher mode effects and the associated increase in effective roof inertia. Despite this higher-mode excitation, the overall amplitude of PIDR and PFA response is similar between both the three- and nine-story buildings. This is an indication of the general effectiveness of the selected isolation systems in controlling drift demands and acceleration response for buildings of varying height and natural period.

In examining the median roof acceleration spectra shown in Figure 6.23, it is evident that the 72-year predominant frequency content shows a similar level of sensitivity to the level of damping compared to the three-story building. The increase in 72-year peak roof spectral acceleration above 1 Hz due to increasing damping is about 50%.

It is evident from the above discussion that the effect of the parameters of linearly viscously damped isolation systems is consistent for the three- and nine-story buildings designed according to response spectrum analysis. The effects of increased viscous damping for the moderate- and long-period isolation systems were not observed to be significant for the demand parameters investigated.

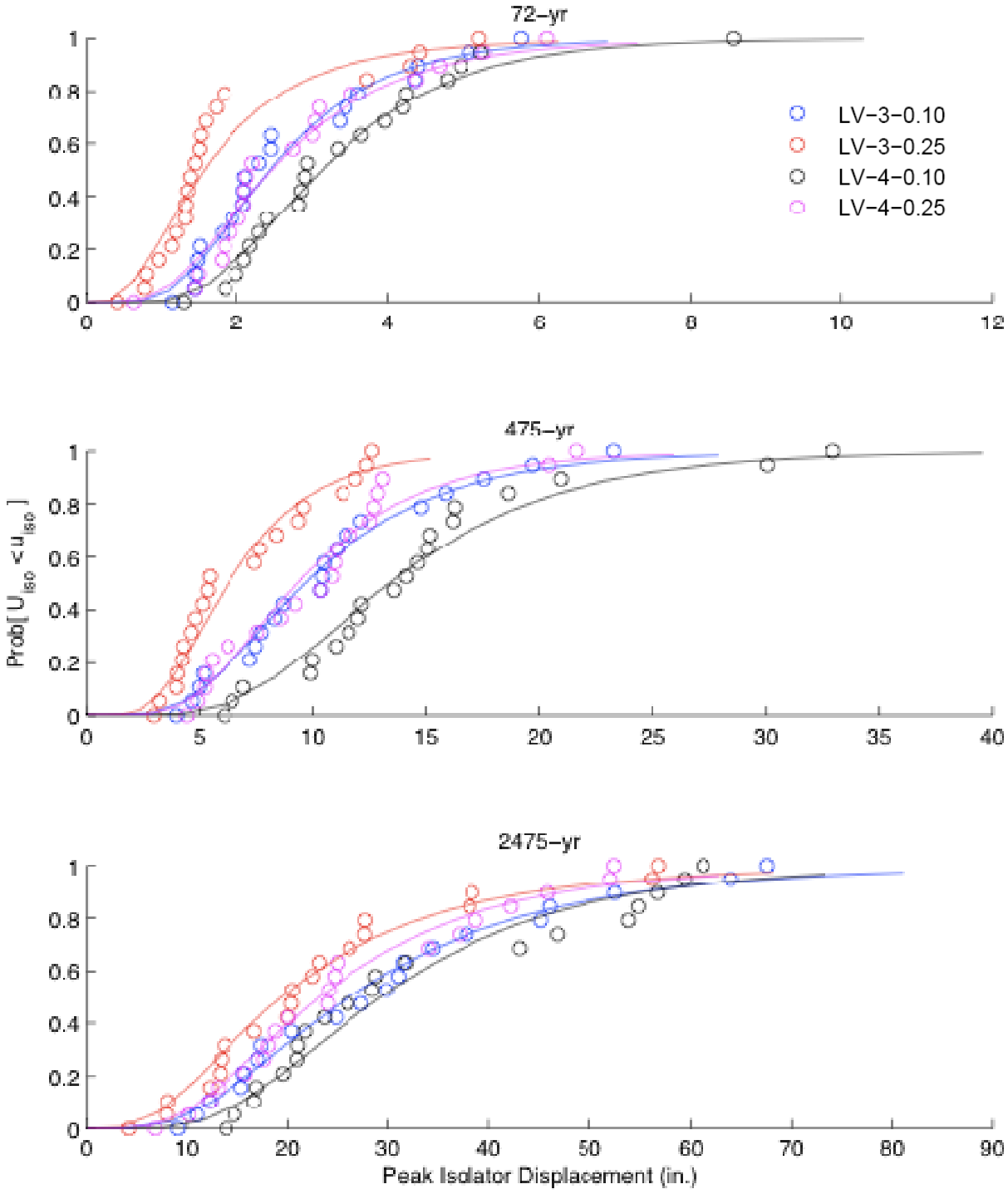

Figure 6.16: Comparison of empirical CDFs of isolator displacement for three levels of seismic hazard (fitted lognormal CDF shown solid), 3-story building on linear viscous damped isolation system

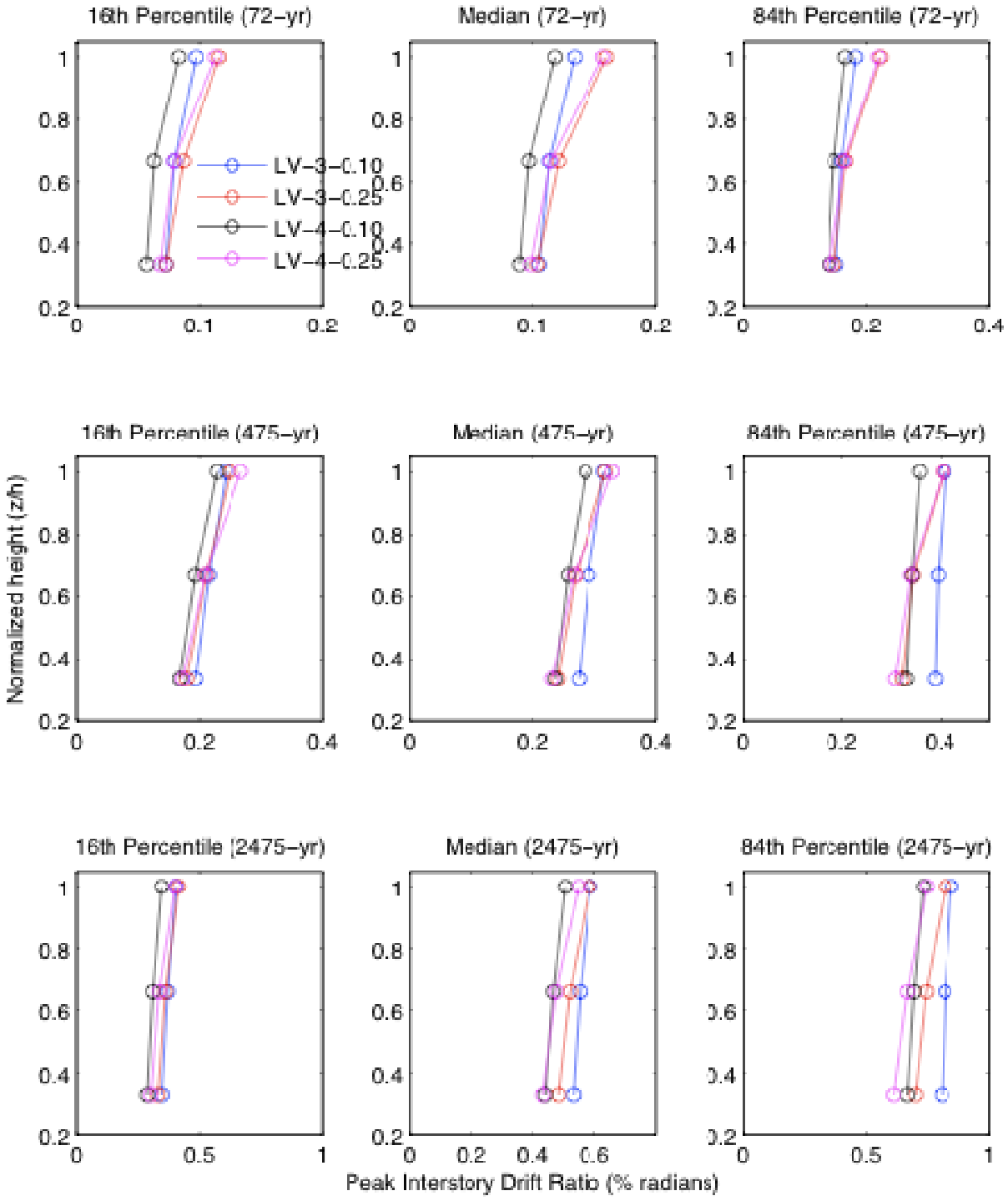

Figure 6.17: Comparison of peak interstory drift ratio (PIDR) at each floor level for 3-story building on linear viscous damped isolation system

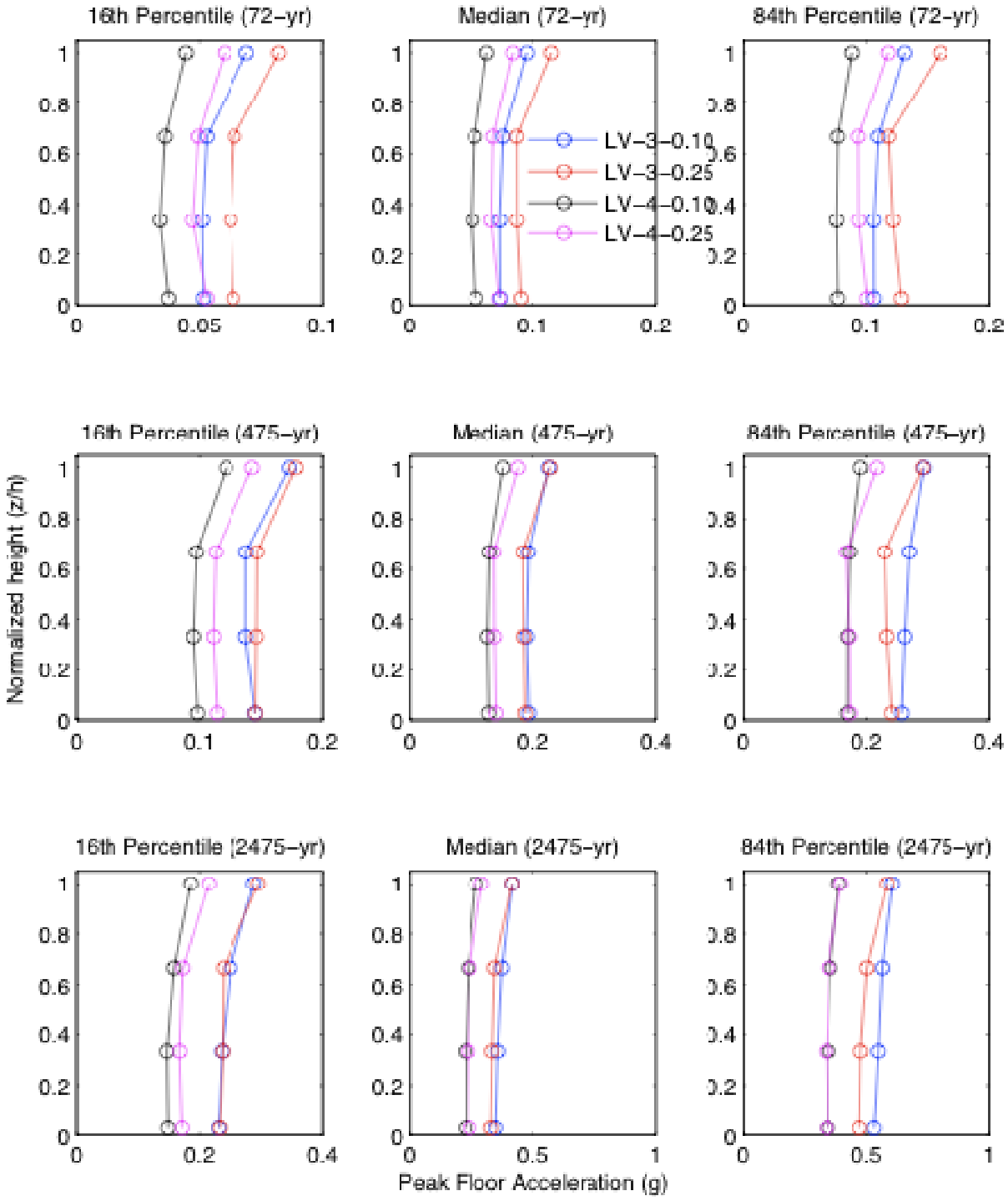

Figure 6.18: Comparison of peak floor acceleration (PFA) at each floor level for 3-story building on linear viscous damped isolation system

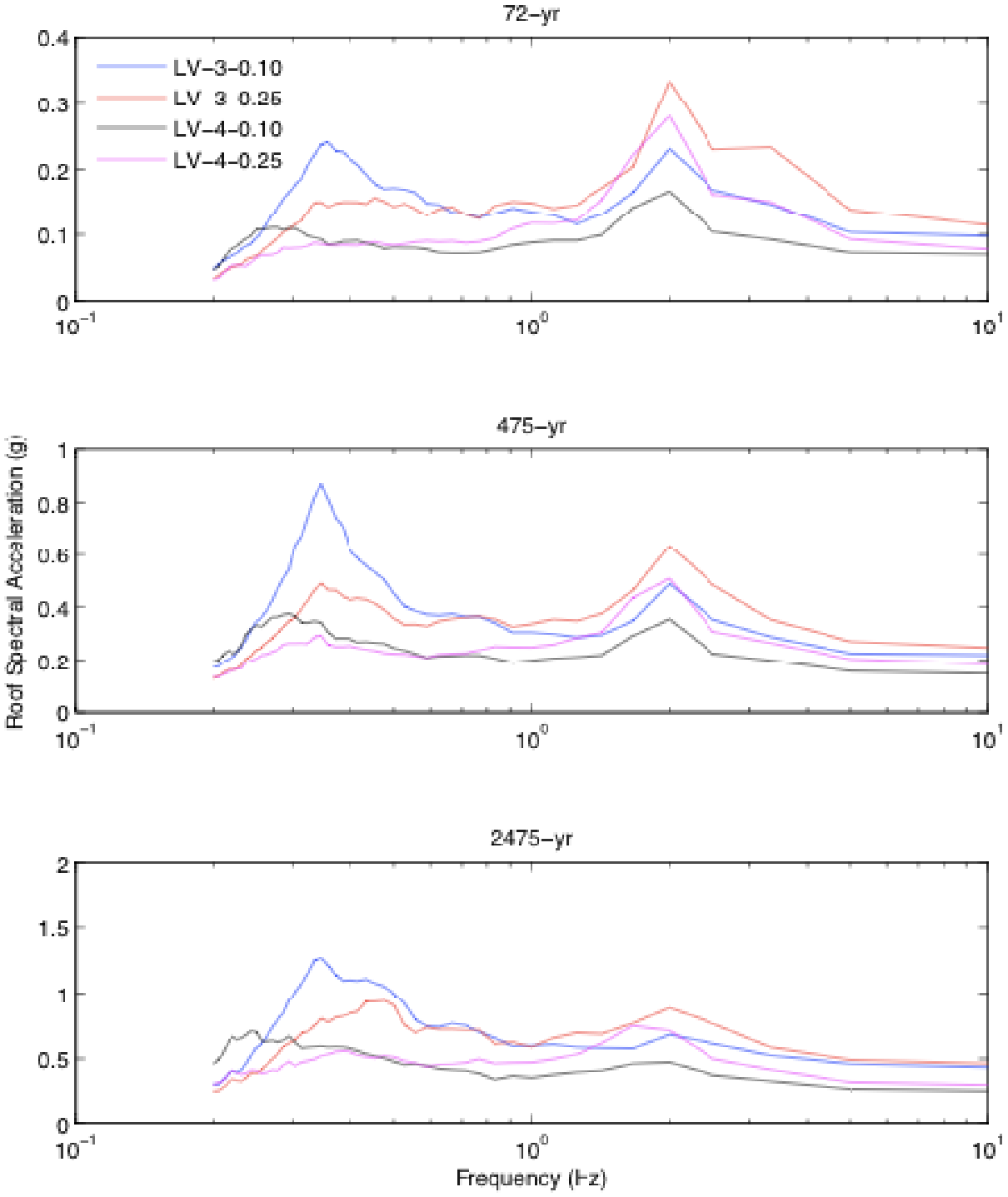

Figure 6.19: Comparison of median roof acceleration spectra for 3-story building isolated on linear viscous damped isolation system

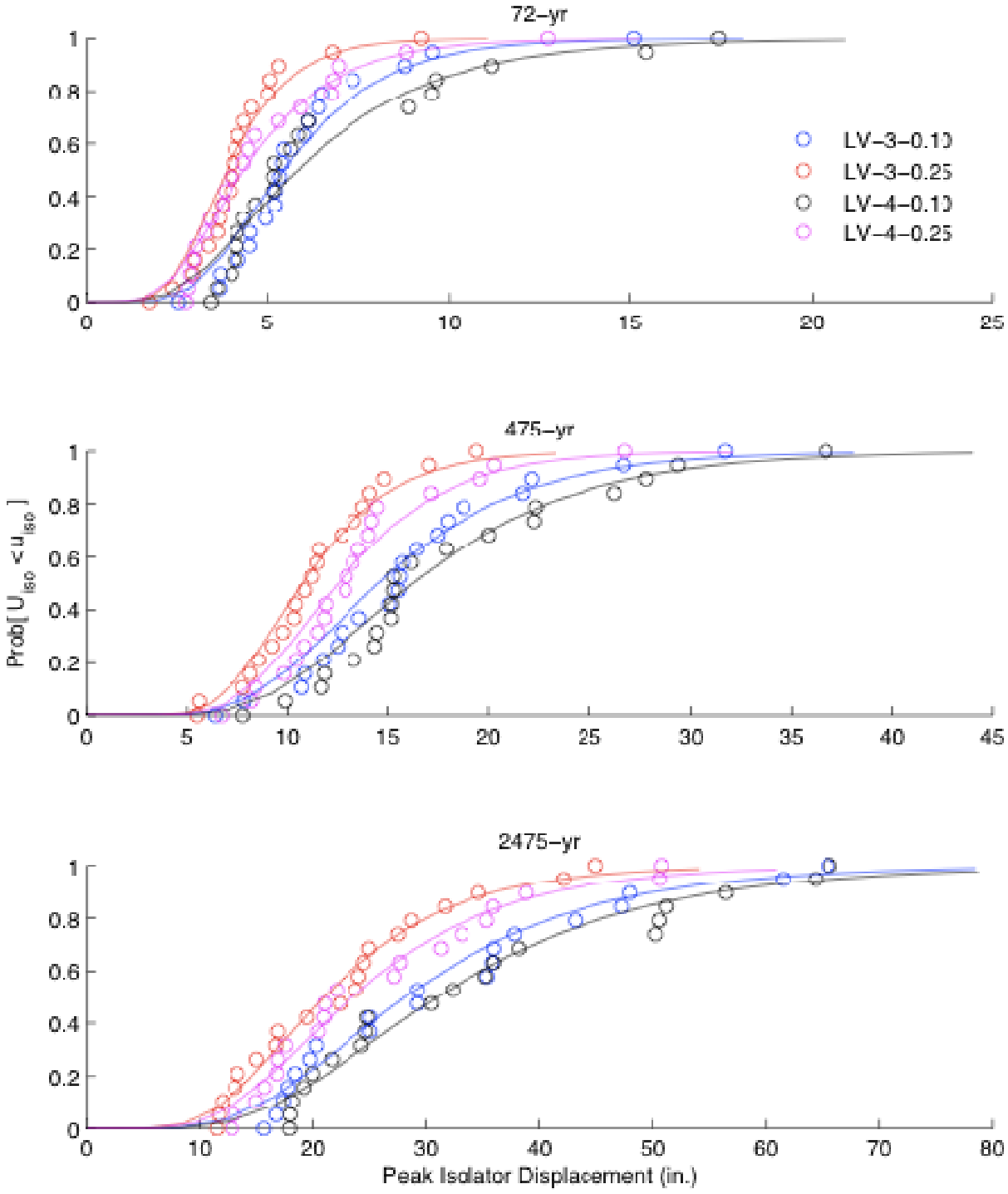

Figure 6.20: Comparison of empirical CDFs of isolator displacement for three levels of seismic hazard (fitted lognormal CDF shown solid), 9-story building on linear viscous damped isolation system

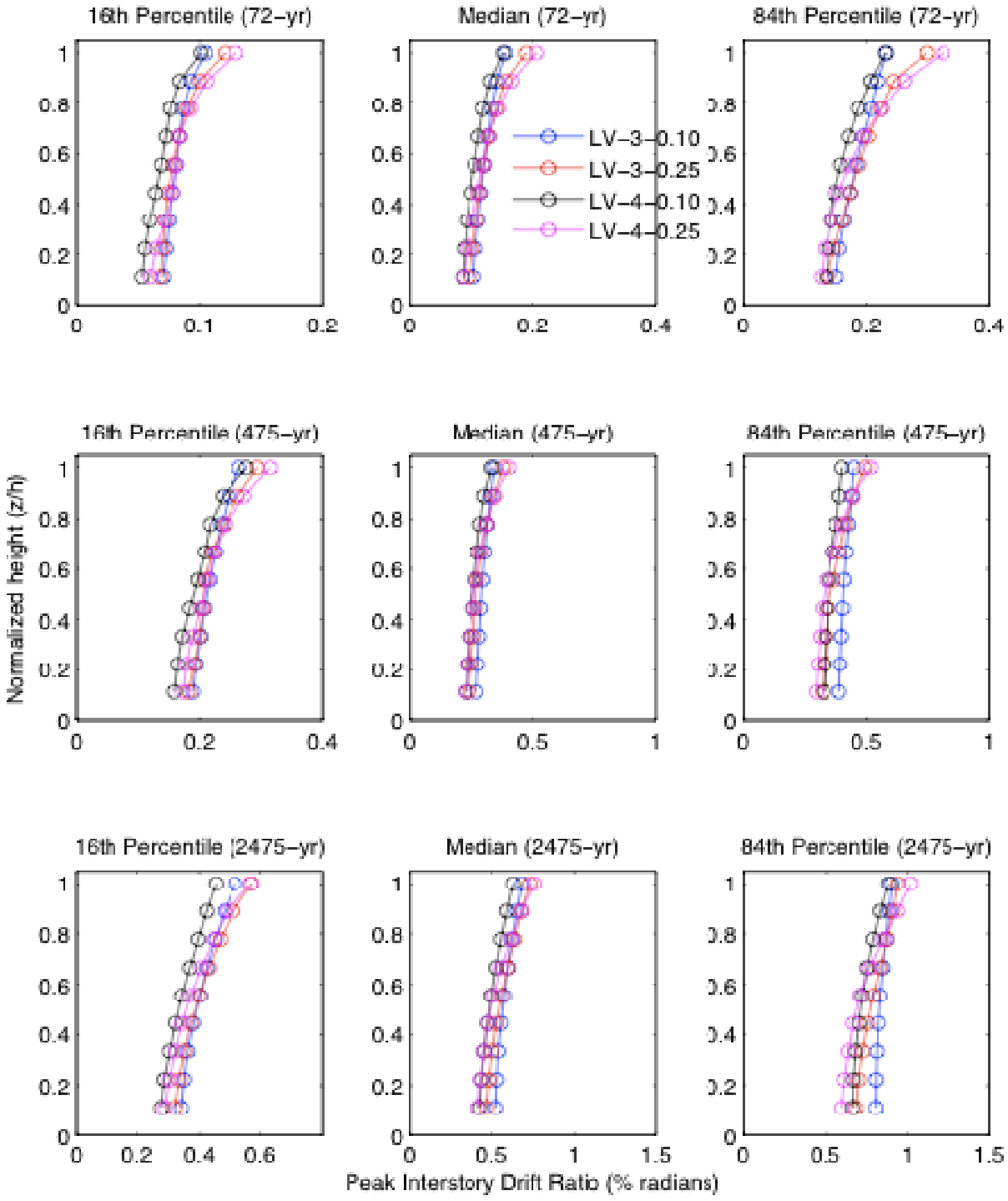

Figure 6.21: Comparison of peak interstory drift ratio (PIDR) at each floor level for 9-story building on linear viscous damped isolation system

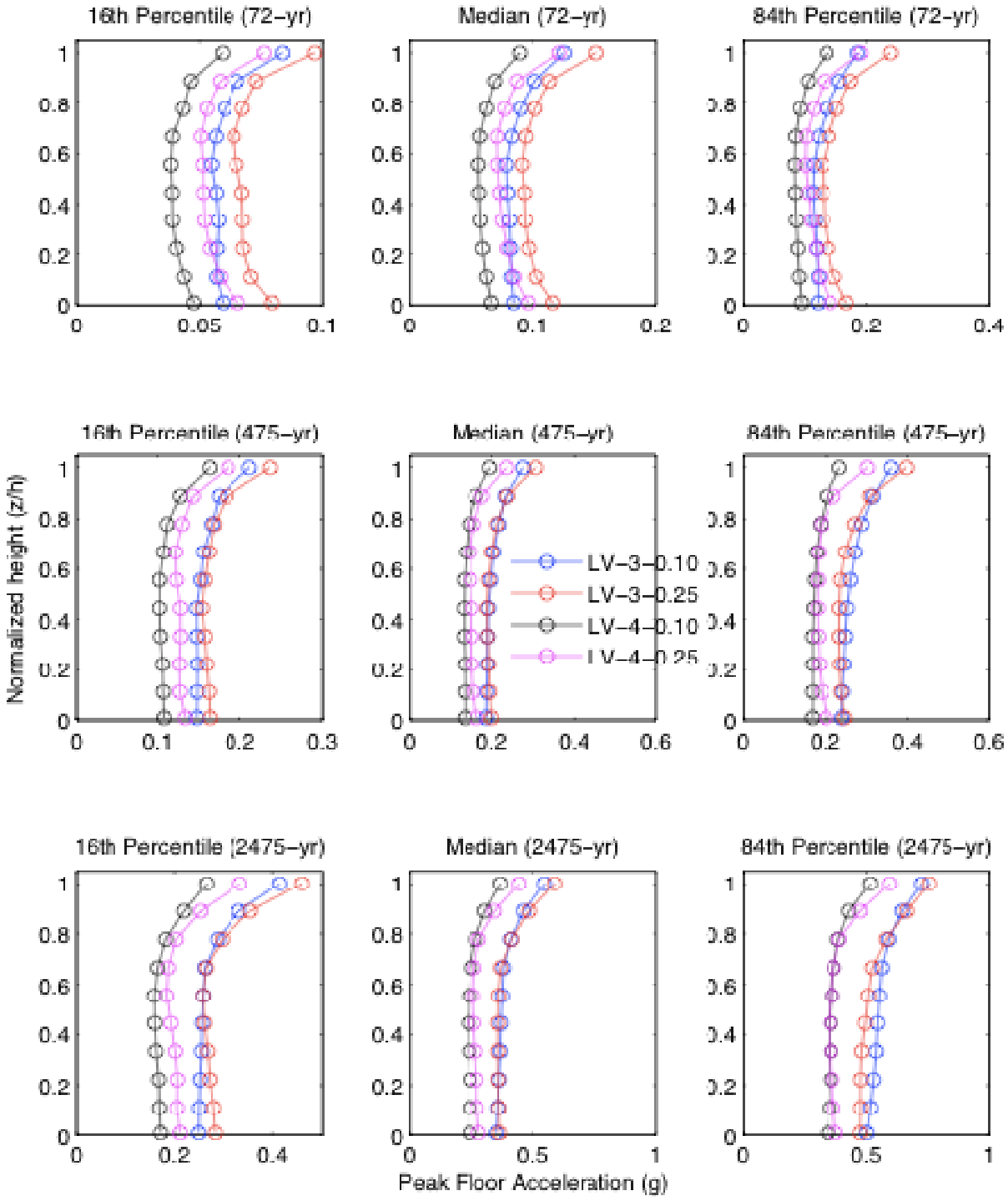

Figure 6.22: Comparison of peak floor acceleration (PFA) at each floor level for 9-story building on linear viscous damped isolation system

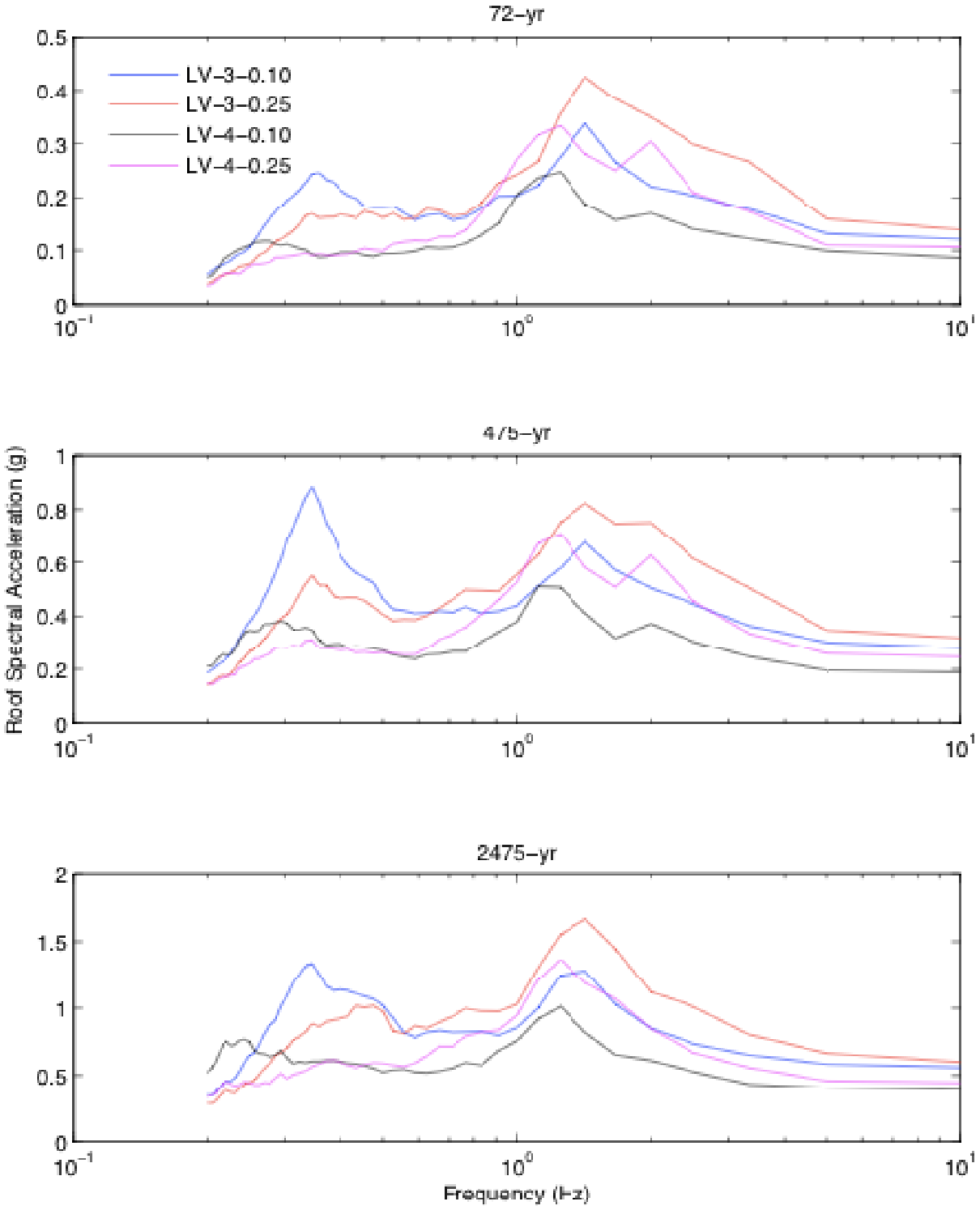

Figure 6.23: Comparison of median roof acceleration spectra for 9-story building isolated on linear viscous damped isolation system

6.4.4.2 Bilinear Hysteretic Isolation System

This section presents results of the parametric studies on bilinear hysteretic isolation systems. This presentation is divided into two sections, one for each for each of the two buildings considered.

6.4.4.2.1 Bilinear Hysteretic Isolators, Three-Story Building

Figure 6.24 presents empirical probabilistic data describing the distribution of peak isolator displacement for seismic events having three return periods: 72-year, 475-year, and 2475-year. Also shown for each isolation system is the CDF of the lognormal distribution with parameters estimated from the observed data. From these data, the median MCE bilinear hysteretic isolator displacements as a function of isolation system are as follows: U_{iso}(BL-3-10) = 28.6 in., U_{iso}(BL-3-25) = 20.4 in., U_{iso}(BL-4-10) = 27.2 in., and U_{iso}(LV-4-25) = 24.0 in. These displacements are comparable in magnitude to those medians observed for the linear viscous isolation system in Section 6.4.4.1.

Figure 6.25 presents peak interstory drift ratio (PIDR) response over the height of the isolated building for all bilinear hysteretic systems considered. Additionally, for each hazard level, the median response is reported along the middle column with the 16^{th} and 84^{th} percentile response reported to the right and left, respectively. An interesting result of the PIDR data presented is that, for the 72- and 475-year return period events, there is an insignificant sensitivity of drift to a change in effective isolation period of 3 to 4 sec. However, for these moderate and rare levels of excitation, there is a noticeable effect on PIDR due to an increase in damping from 10% to 25%, and this effect is similar for both 3- and 4-sec effective isolation periods. For the 2475-year event, the third floor median drift demand shows significant amplification due to increased damping, however, the amplification to decreased effective isolation period is similar for all floors. This is an indication that the increased damping has a more pronounced effect on higher-mode excitation relative to decreased period.

Figure 6.26 presents similarly organized data as for PIDR above, but for peak floor acceleration (PFA). Floor accelerations appear to show sensitivity to both effective isolation period and equivalent damping for all levels of seismic hazard considered. For both 72- and 475-year events, the median PFA is nearly identical for the BL-3-0.10 and BL-4-0.25 isolation systems. Whereas the profile of PFA indicates higher-mode participation for all

isolation systems, this effect is most pronounced for the systems with 25% damping. It is worthwhile to note that, for all isolation systems considered, the magnitude of both PIDR and PFA observed for the bilinear hysteretic systems is significantly larger than the equivalent linear viscous system described above.

To investigate the effect of bilinear hysteretic damping mechanisms on the response on non-rigid components, floor response spectra are developed at the roof for all isolation systems investigated. The median of these spectra are shown in Figure 6.27 for all levels of seismic hazard considered in this study. From these data, there is very little acceleration frequency content near the effective isolation frequency compared to the linear viscous system. However, there is noticeable acceleration content at higher frequencies, which correspond to higher modes of the isolated structure. Such behavior is an indication that the bilinear hysteretic isolation system does not serve as an efficient filter for acceleration in higher modes compared to the linear viscous system.

6.4.4.2.2 Bilinear Hysteretic Isolators, Nine-Story Building

Figure 6.20 through Figure 6.31 show the peak isolator displacement, PIDR, PFA, and roof acceleration spectra for the nine-story building isolated by a bilinear hysteretic isolation system. Variation in the observed response trends relative to the three-story model are identified and discussed.

From Figure 6.28, the median MCE isolator displacements as a function of isolation system are as follows: U_{iso}(BL-3-10) = 27.5 in., U_{iso}(BL-3-25) = 20.4 in., U_{iso}(BL-4-10) = 24.2 in., and U_{iso}(BL-4-25) = 22.0 in. From these data, there is a slight decrease in the nine-story median isolator displacement compared to three-story for all levels of seismic hazard. This is an expected result given the increase in superstructure flexibility.

In evaluating the PIDR and PFA response data of Figure 6.29 and Figure 6.30 respectively, many observed trends remain unchanged relative to the discussion of the three-story building above. As with the linear viscous case, the effect of increased target damping on the excitation of higher-mode response is clear, but *less pronounced* for the nine-story building compared to the three-story building.

In examining the median roof acceleration spectra shown in Figure 6.31, it is evident that the 72-year predominant frequency content shows a similar level of sensitivity to the level of damping compared to the three-story building. For the 72-year event, there appears

to be excitation of multiple higher modes of the superstructure, further indicating the inefficiency of bilinear systems in filtering higher-mode accelerations.

As with linear viscous systems, it is evident from the above discussion that the effect of the parameters of bilinear hysteretic isolation systems is consistent for the three- and nine-story buildings designed according to response spectrum analysis. For both buildings there appears to be significant amplification of both drift and acceleration response due to an increase in equivalent hysteretic damping regardless of the effective isolation period considered.

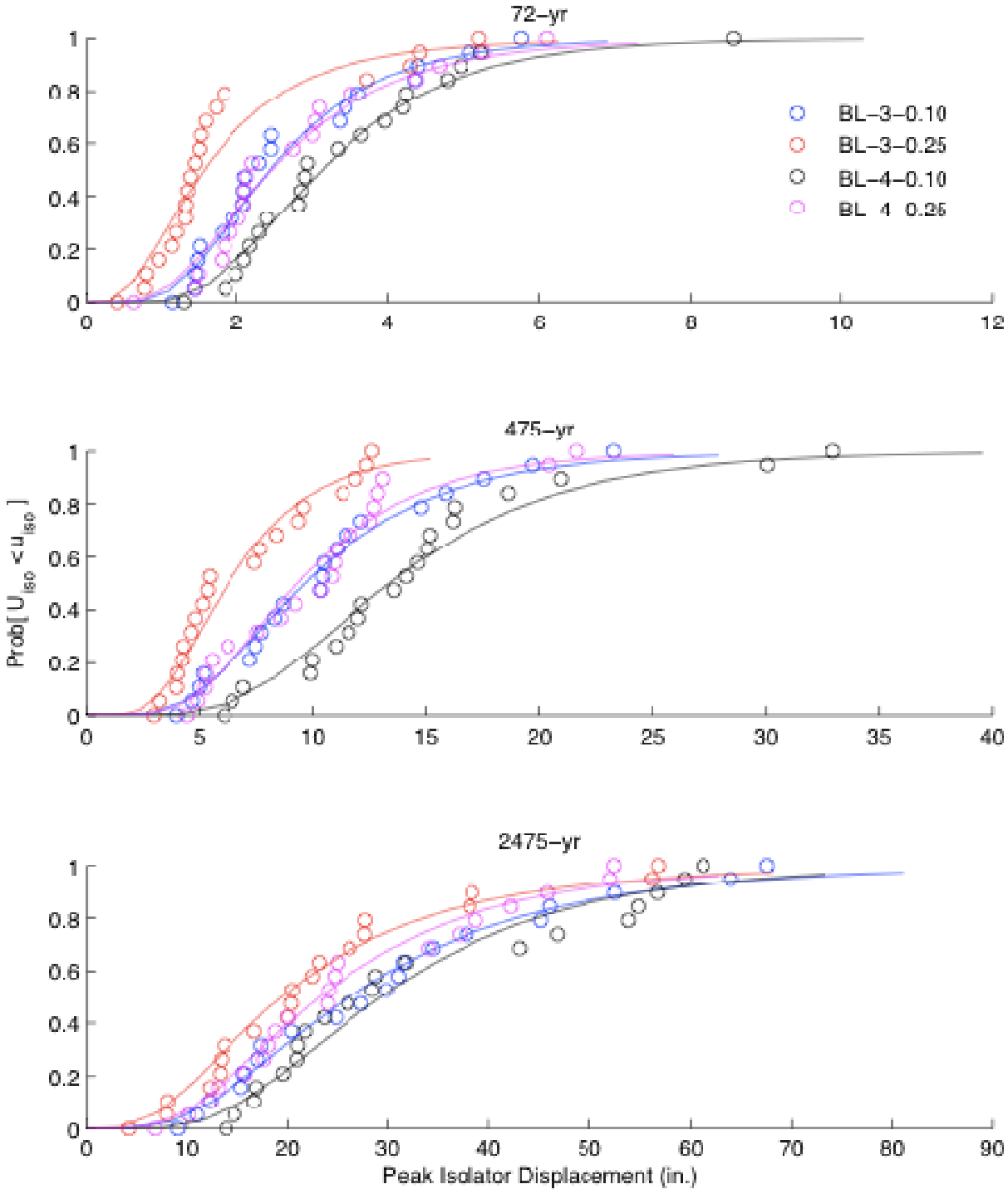

Figure 6.24: Comparison of empirical CDFs of isolator displacement for three levels of seismic hazard (fitted lognormal CDF shown solid), 3-story building on hysteretic isolation system

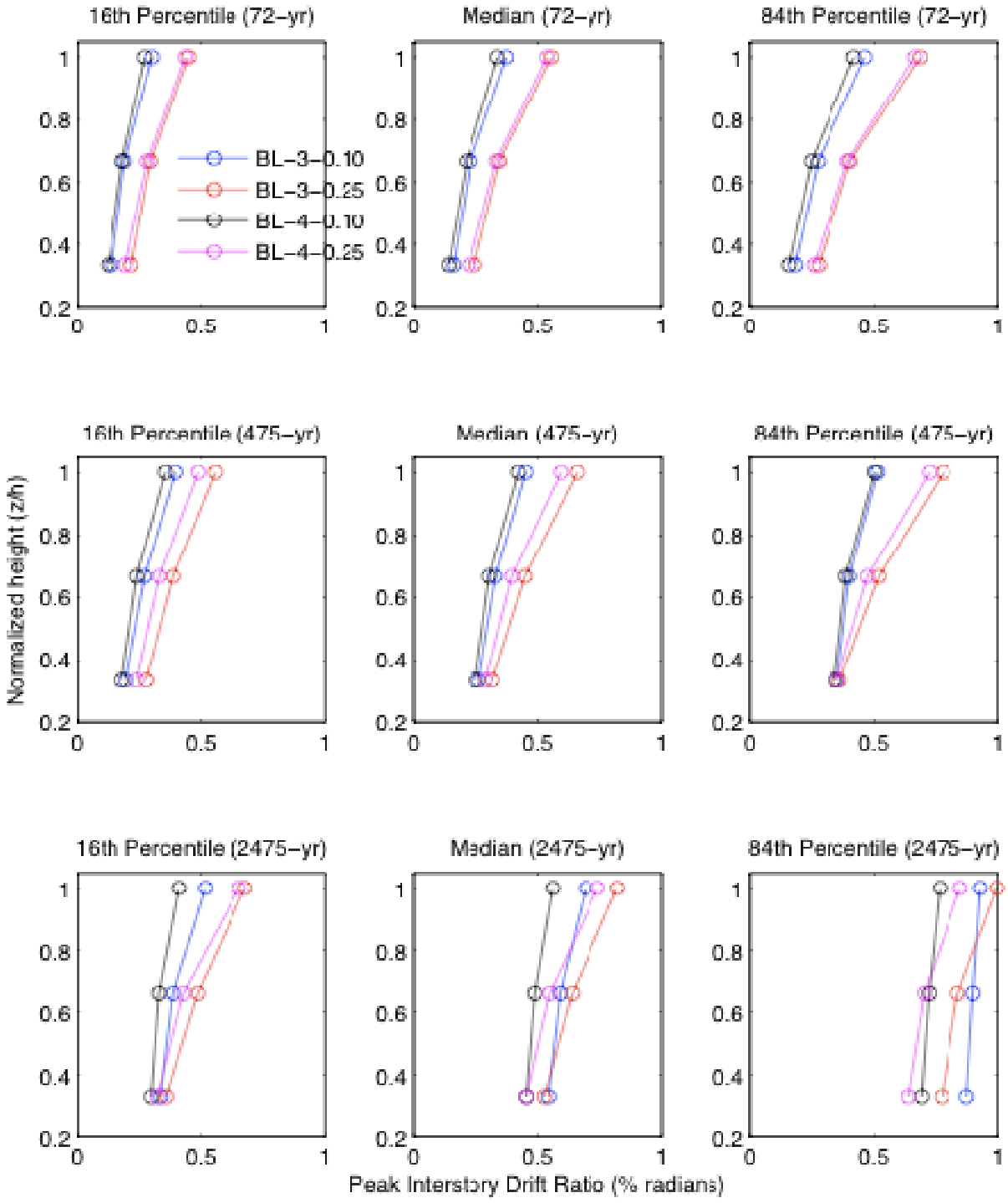

Figure 6.25: Comparison of peak interstory drift ratio (PIDR) at each floor level for 3-story building on bilinear hysteretic isolation system

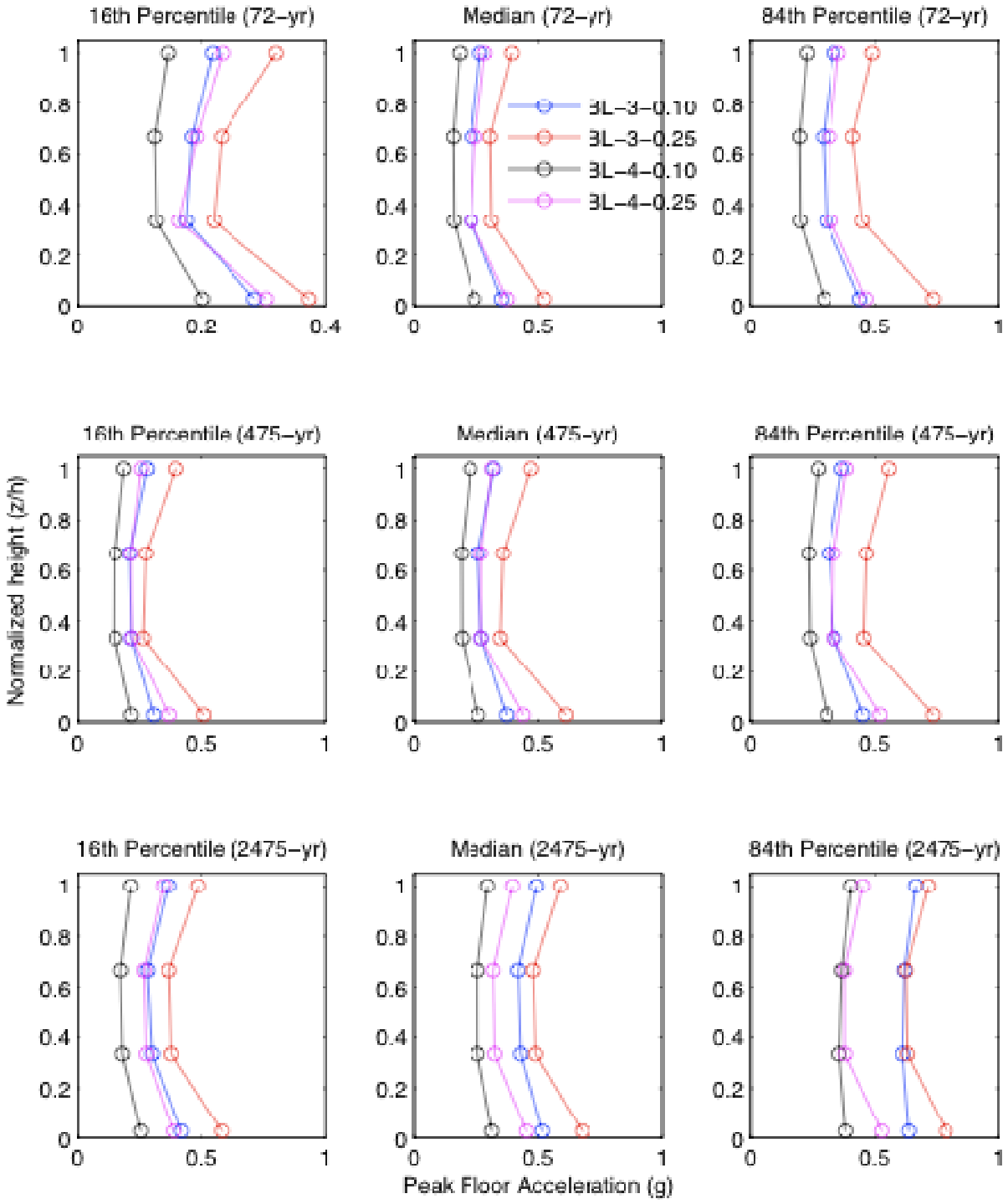

Figure 6.26: Comparison of peak floor acceleration (PFA) at each floor level for 3-story building on bilinear hysteretic isolation systems

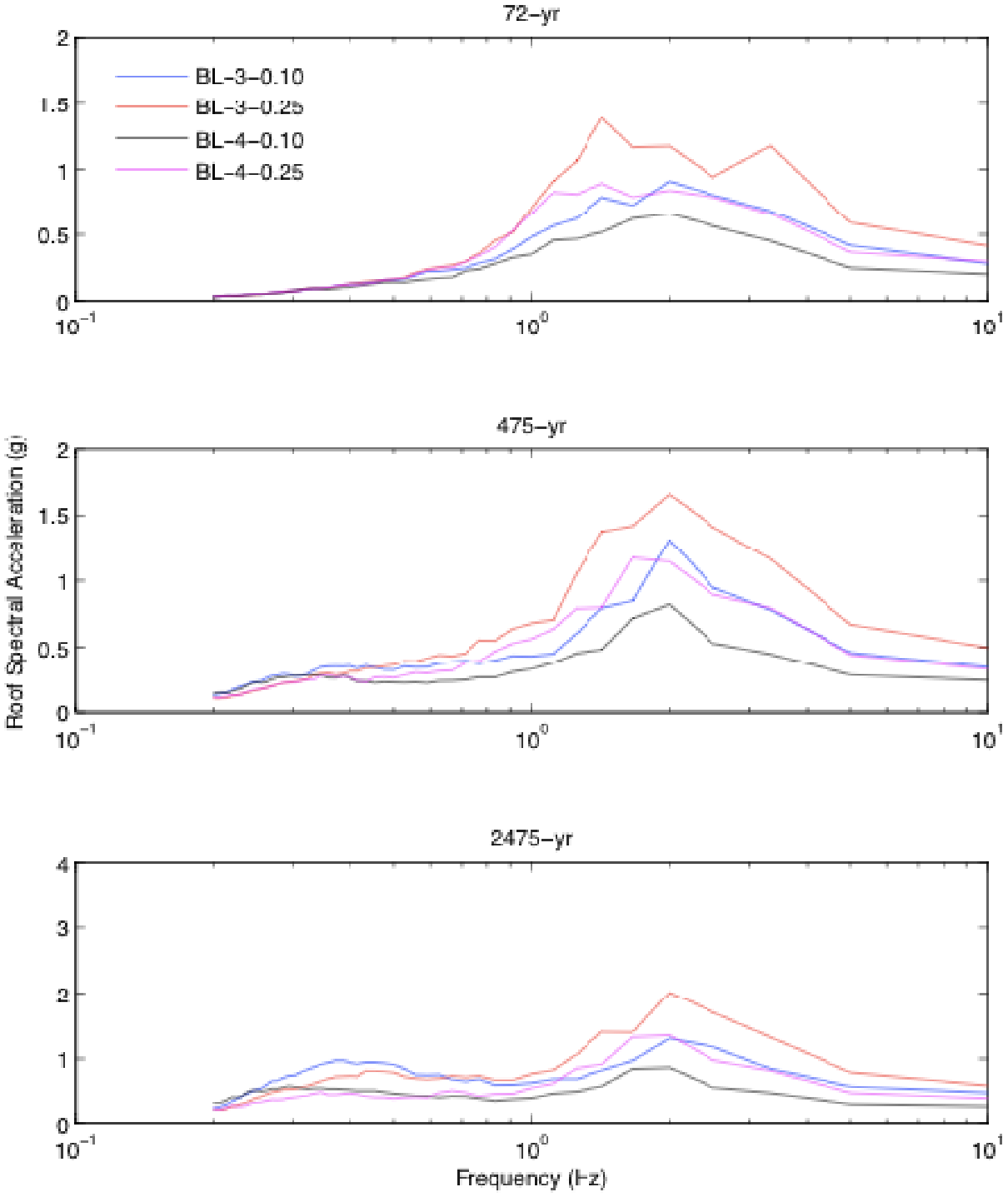

Figure 6.27: Comparison of roof acceleration spectra for 3-story building isolated on bilinear hysteretic isolation system

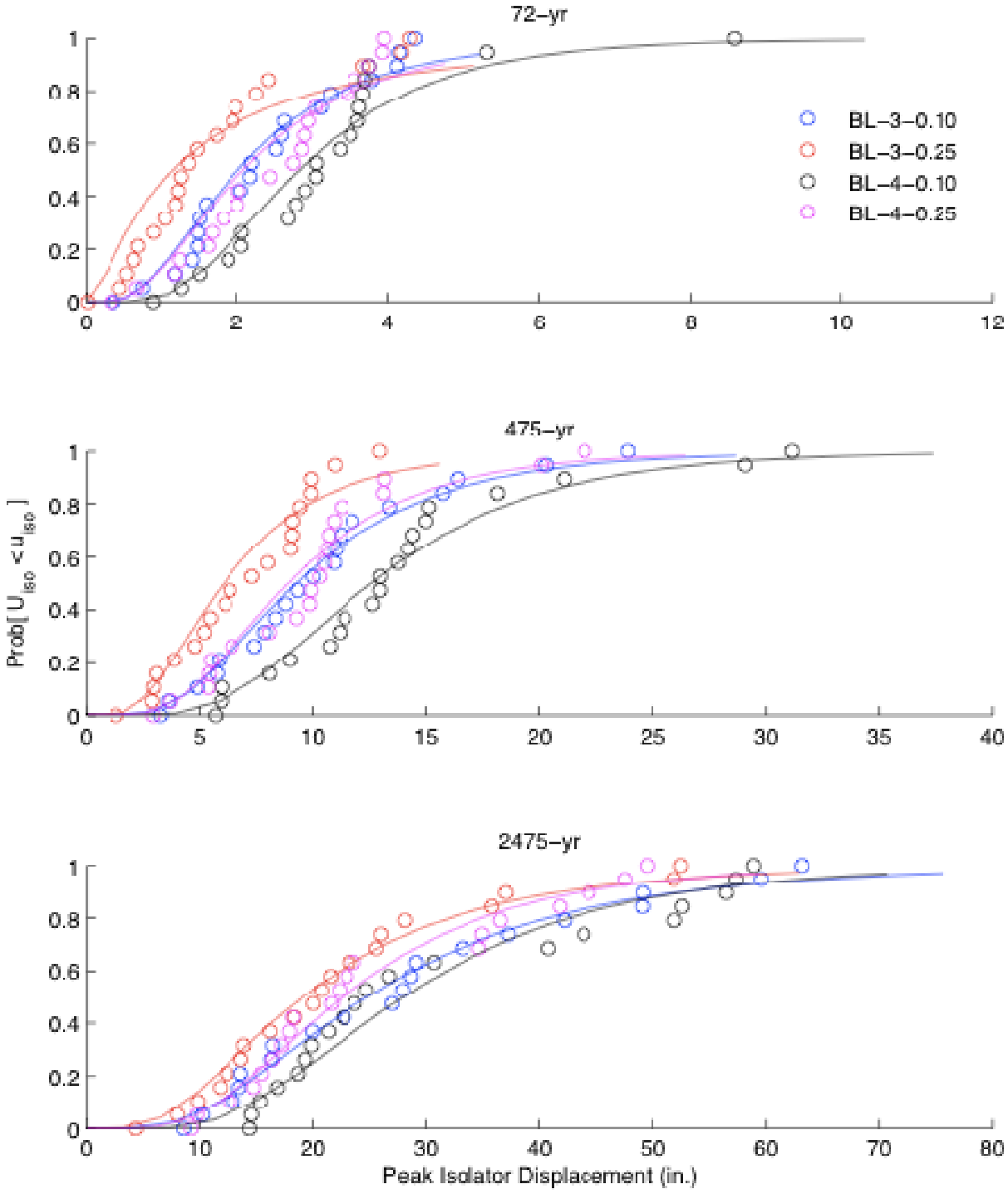

Figure 6.28: Comparison of empirical CDFs of isolator displacement for three levels of seismic hazard (fitted lognormal CDF shown solid), 9-story building on bilinear hysteretic isolation system

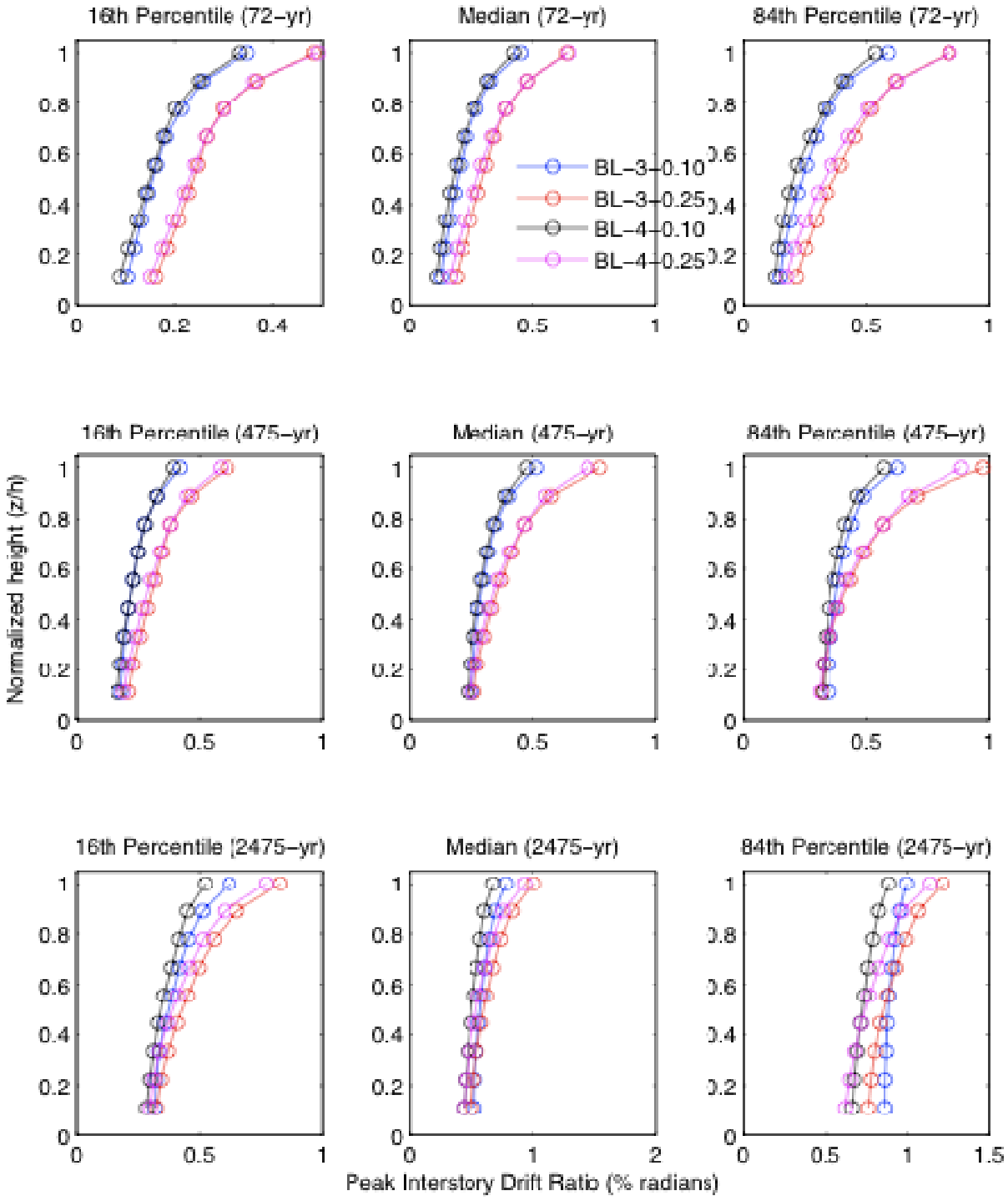

Figure 6.29: Comparison of peak interstory drift ratio (PIDR) at each floor level for 9-story building on hysteretic isolation system

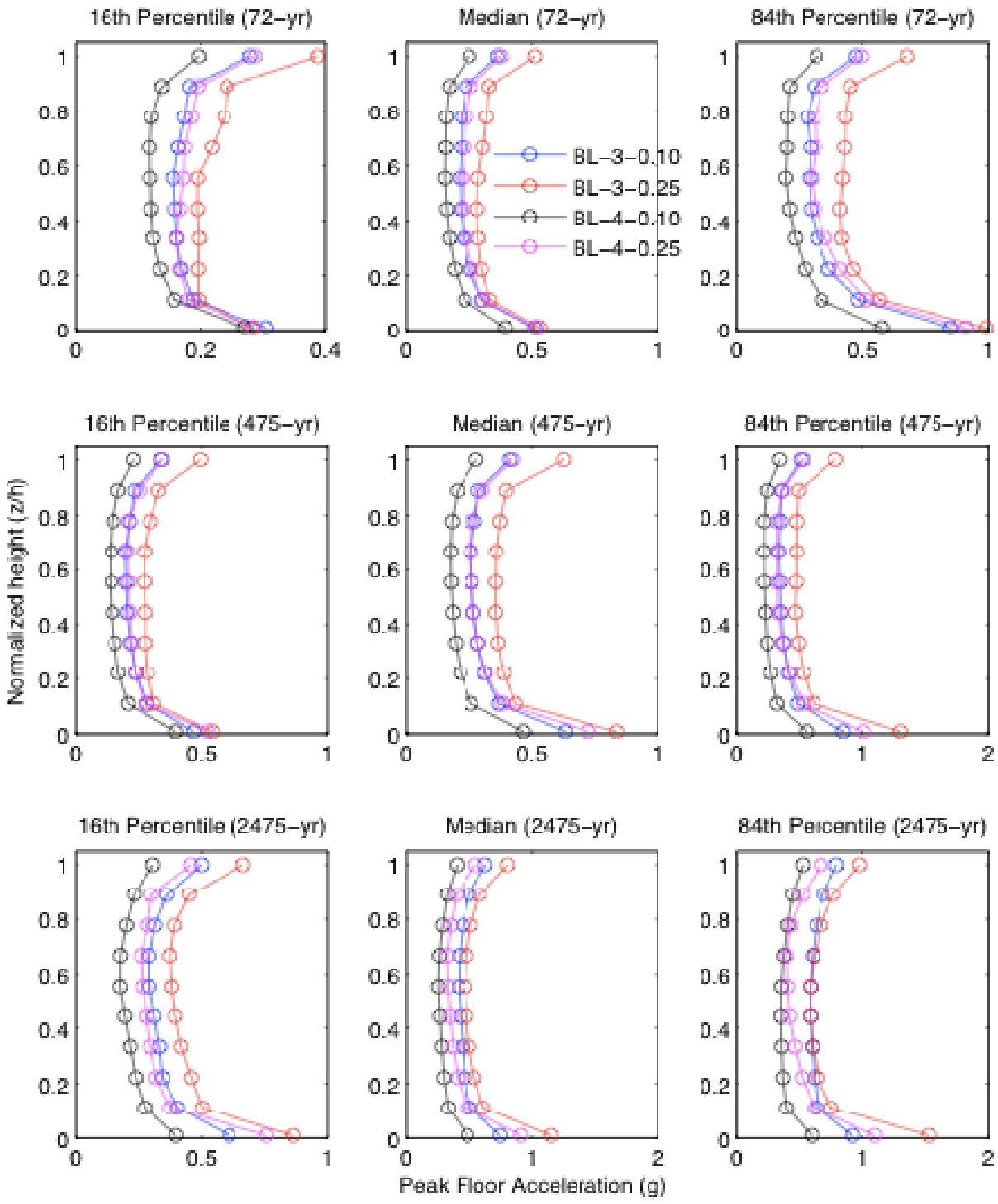

Figure 6.30: Comparison of peak floor acceleration (PFA) at each floor level for 9-story building on hysteretic isolation system

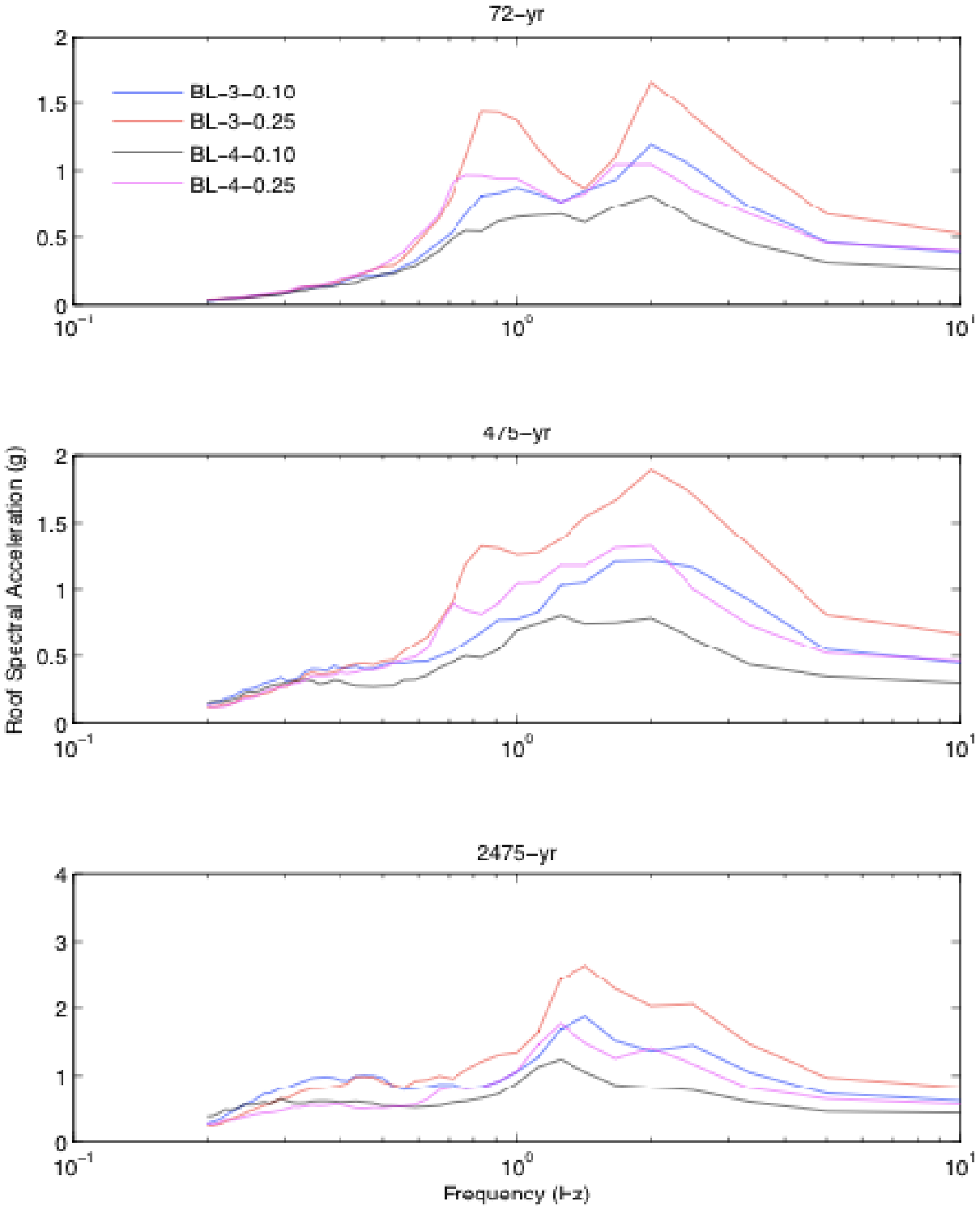

Figure 6.31: Comparison of roof acceleration spectra for 9-story building isolated on hysteretic isolation system

6.4.4.3 Triple Pendulum Isolation System

This section presents results of the parametric studies on triple pendulum (TP) isolation systems. This presentation is divided into two sections, one for each of the two buildings considered.

6.4.4.3.1 Triple Pendulum Isolators, Three-Story Building

Figure 6.32 presents empirical probabilistic data describing the distribution of peak isolator displacement for seismic events having three return periods: 72-year, 475-year, and 2475-year. Also shown for each isolation system is the CDF of the lognormal distribution with parameters estimated from the observed data. From these data, the median MCE triple pendulum isolator displacements as a function of isolation system are as follows: U_{iso}(TP-3-10) = 30.2 in., U_{iso}(TP-3-25) = 25.9 in., U_{iso}(TP-4-10) = 31.8 in., and U_{iso}(LV-4-25) = 24.5 in. As with the bilinear hysteretic systems, these displacements are comparable in magnitude to those medians observed for the linear viscous isolation system in Section 6.4.4.1.

Figure 6.33 presents peak interstory drift ratio (PIDR) response over the height of the isolated building for all TP systems considered. Additionally, for each hazard level, the median response is reported along the middle column with the 16^{th} and 84^{th} percentile response reported to the right and left, respectively. For the PIDR data presented, there is sensitivity of drift to a change in both effective isolation period and equivalent viscous damping, particularly at the roof level. This is in contrast to the bilinear system, for which very little sensitivity to the effective isolation period was observed. However, for all cases considered, the peak interstory drift for the TP isolated structure is smaller than that observed for the equivalent bilinear isolation system.

Figure 6.34 presents similarly organized data as for PIDR above, but for peak floor acceleration (PFA). As with bilinear systems, floor accelerations appear to show sensitivity to both effective isolation period and equivalent damping for all levels of seismic hazard considered, which high-damping systems leading to amplified acceleration under 72- and 475-year events. However, median PFA shows little sensitivity to damping at the 2475-year event. As with PIDR, for all isolation systems considered, the magnitude of PFA observed for the TP isolation systems is less than that observed for the equivalent bilinear hysteretic system described above.

To investigate the effect of TP isolation systems on the response of non-rigid components, floor response spectra are developed at the roof for all isolation systems investigated. The median of these spectra is shown in Figure 6.35 for all levels of seismic hazard considered in this study. From these data, there is more observable acceleration frequency content near the effective isolation frequency compared to the bilinear hysteretic system. Additionally, the magnitude of the roof spectral acceleration in the 1–10 Hz range is significantly lower than that for the bilinear hysteretic system, especially for the 72- and 475-year events. These observations are an indication that the TP isolation system serves as a more efficient filter for acceleration in higher modes compared to the bilinear hysteretic system, particularly for low- and moderate levels of shaking.

6.4.4.3.2 Triple Pendulum Isolators, Nine-Story Building

Figure 6.36 through Figure 6.39 show the peak isolator displacement, PIDR, PFA, and roof acceleration spectra for the nine-story building isolated by a TP isolation system. Variation in the observed response trends relative to the three-story model are identified and discussed.

From Figure 6.36, the median MCE isolator displacements as a function of isolation system are as follows: U_{iso}(TP-3-10) = 29.4 in., U_{iso}(TP-3-25) = 25.5 in., U_{iso}(TP-4-10) = 30.9 in., and U_{iso}(TP-4-25) = 23.5 in. As with the other isolation systems investigated, there is a slight decrease in the nine-story median isolator displacement compared to three-story for all levels of seismic hazard.

In evaluating the PIDR and PFA response data of Figure 6.37 and Figure 6.38 respectively, many observed trends remain unchanged relative to the discussion of the three-story building above. As with both the linear viscous and bilinear hysteretic cases, the effect of increased target damping on the excitation of higher-mode response is clear, but *less pronounced* for the nine-story building compared to the three-story building. Compared to the bilinear system, there is also an increased higher-mode PFA response, particularly for the 72- and 475-year events.

In examining the median roof acceleration spectra shown in Figure 6.39, it appears that the 72-year predominant frequency content shows a similar level of sensitivity to the level of damping compared to the three-story building. For the 72-year event, there is evidence of excitation of multiple higher modes of the superstructure, but the amplitude of

this higher-mode spectral acceleration is less than that for the equivalent bilinear hysteretic system.

As with both linear viscous and bilinear hysteretic isolation systems, it is evident from the above discussion that the effect of parametric variation of triple pendulum isolation systems is consistent for the three- and nine-story buildings designed according to response spectrum analysis. For both buildings there appears to be some amplification of both drift and acceleration response due to an increase in equivalent hysteretic damping at a particular effective isolation period. However, the amplitude of all response quantities considered is less for triple pendulum isolation systems compared to the equivalent bilinear isolation system.

6.5 CONCLUSIONS

This chapter summarizes the results of a series of parametric studies on single- and multi-story isolated buildings. Isolation systems considered were linear bearings in combination with either linear viscous or bilinear hysteretic energy dissipation mechanisms, and the newly developed triple-pendulum isolation system. For the purpose of this study, no maximum limit of isolator displacement was imposed. These studies show that high-damping isolation systems, while effective in limiting isolator displacements, tend to produce relatively large superstructural demands compared to low-damping isolation systems, particularly in low- and moderate-level events. A remarkable result is that the triple-pendulum bearing is generally effective at limiting isolator displacements in very rare earthquakes while controlling drifts and accelerations for low- and moderate-level excitations when compared to the equivalent bilinear hysteretic isolation system.

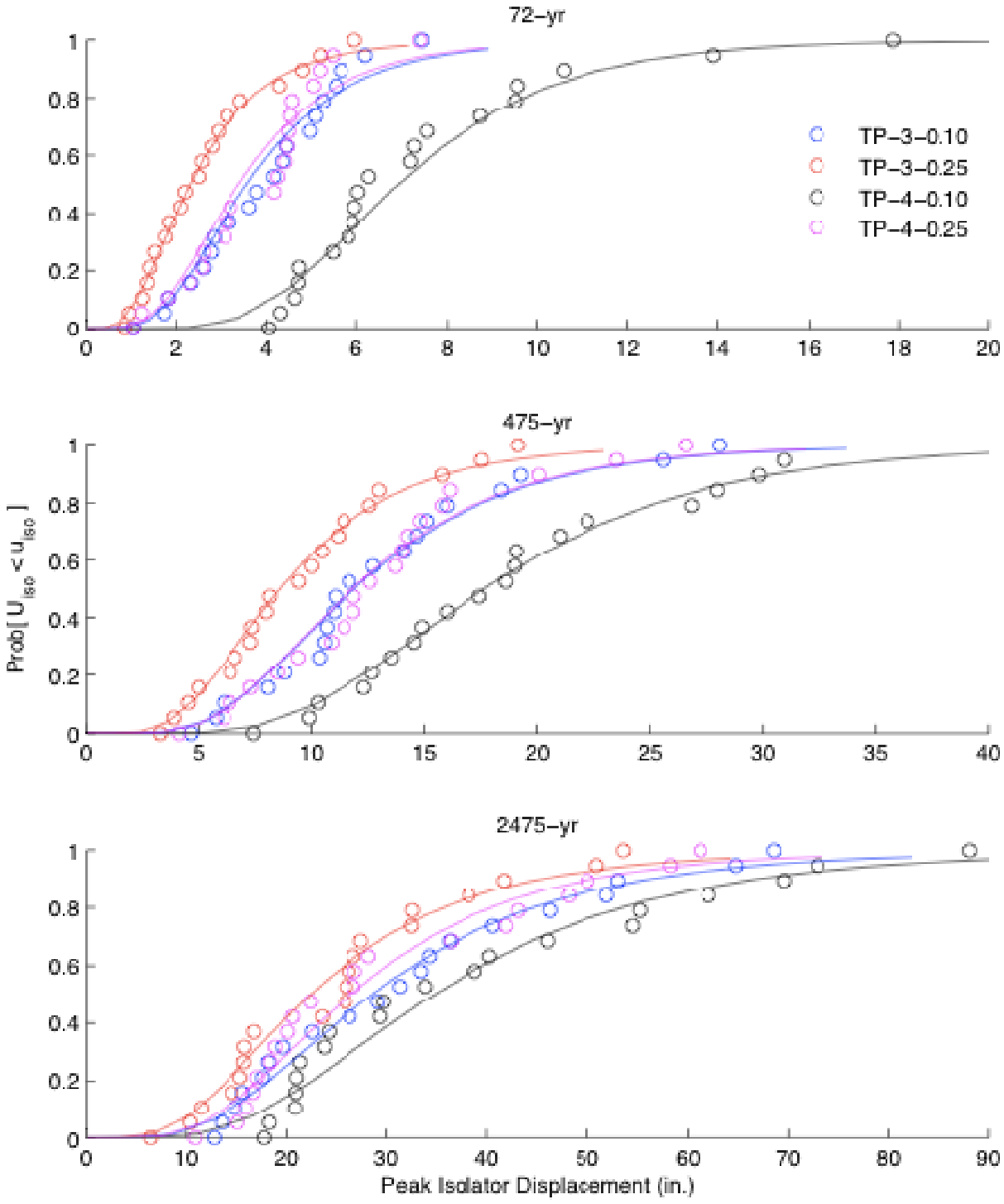

Figure 6.32: Comparison of empirical CDFs of isolator displacement for three levels of seismic hazard (fitted lognormal CDF shown solid), 3-story building on TP isolation system

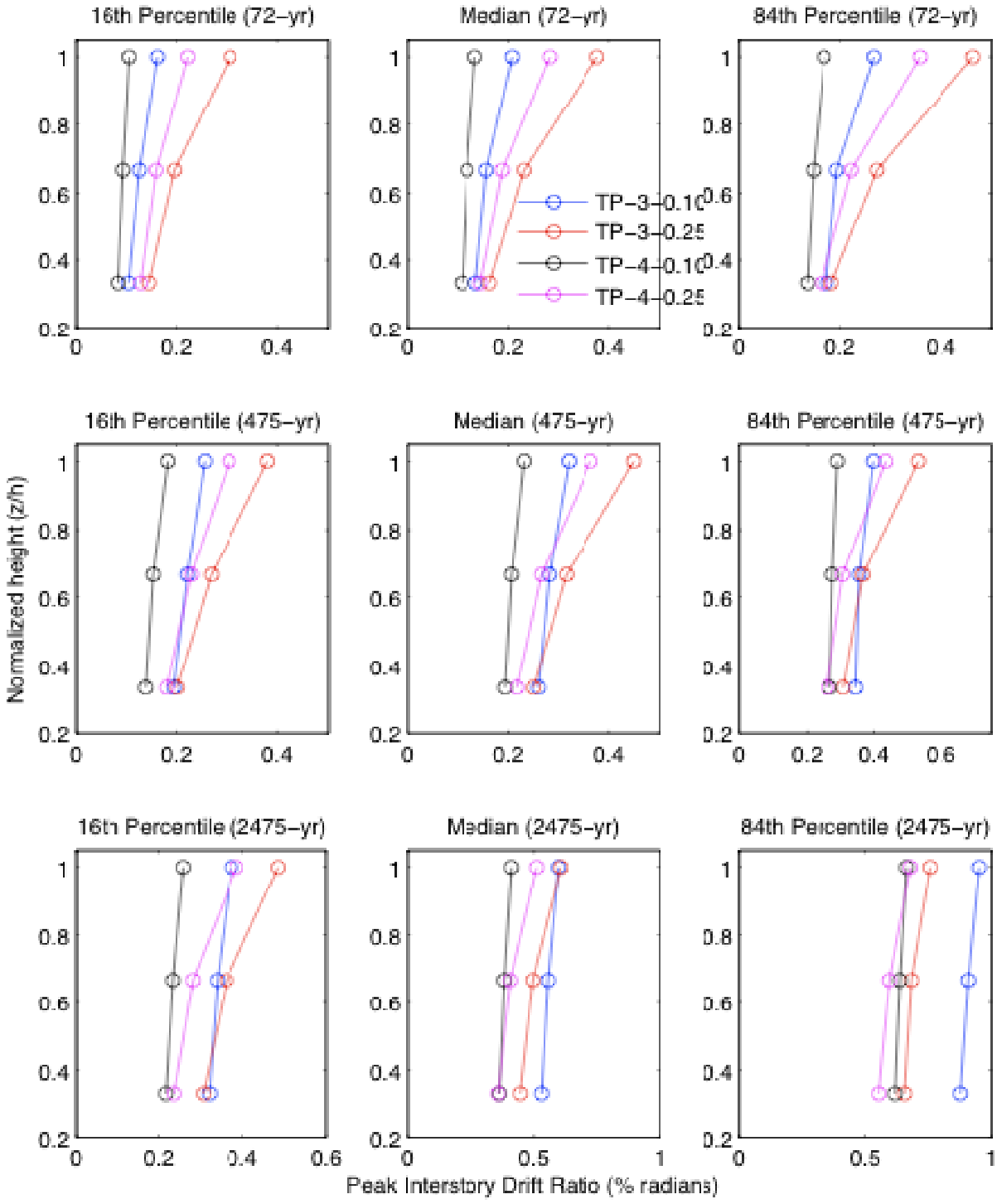

Figure 6.33: Comparison of peak interstory drift ratio (PIDR) at each floor level for 3-story building on TP isolation system

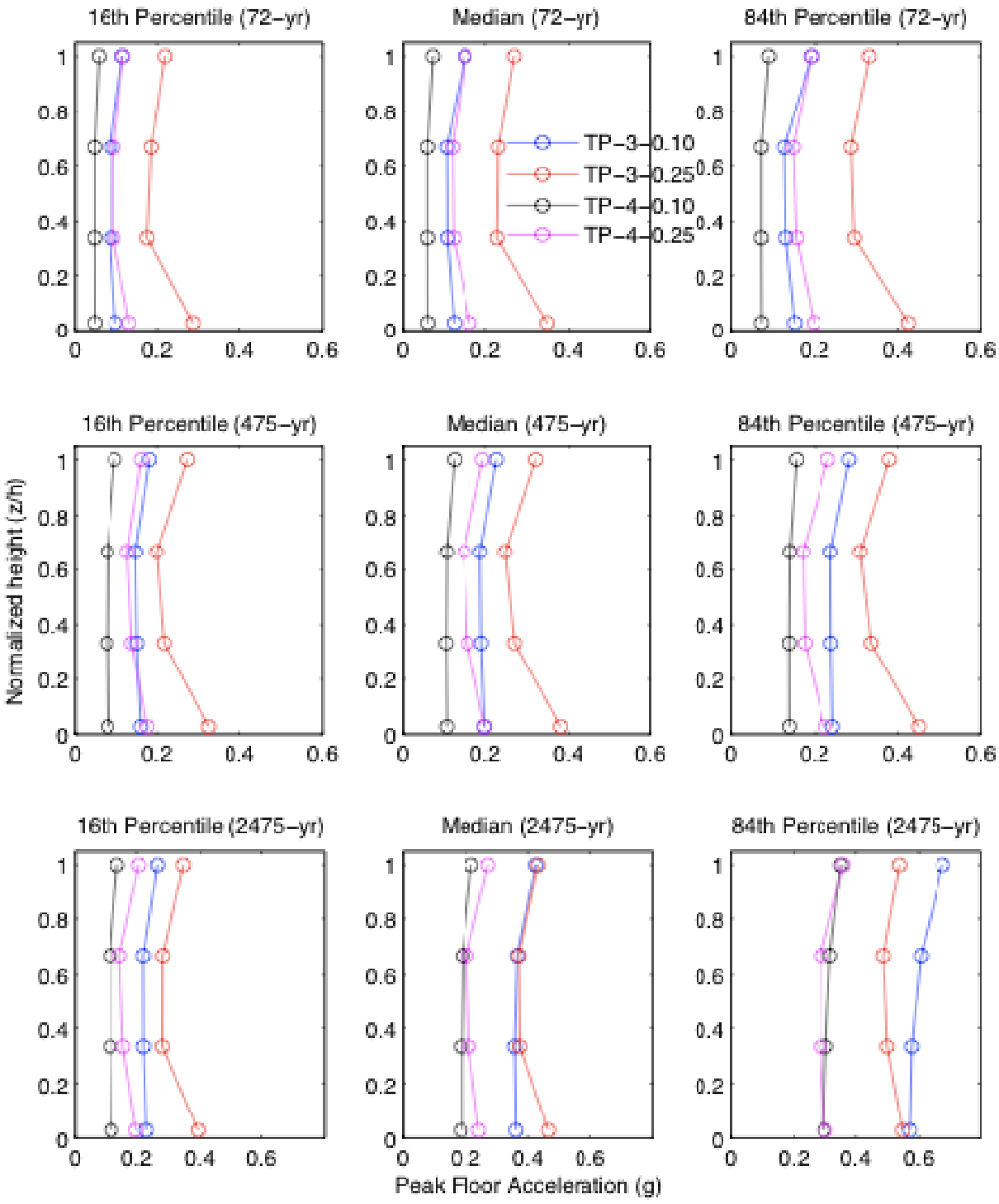

Figure 6.34: Comparison of peak floor acceleration (PFA) at each floor level for 3-story building on TP isolation system

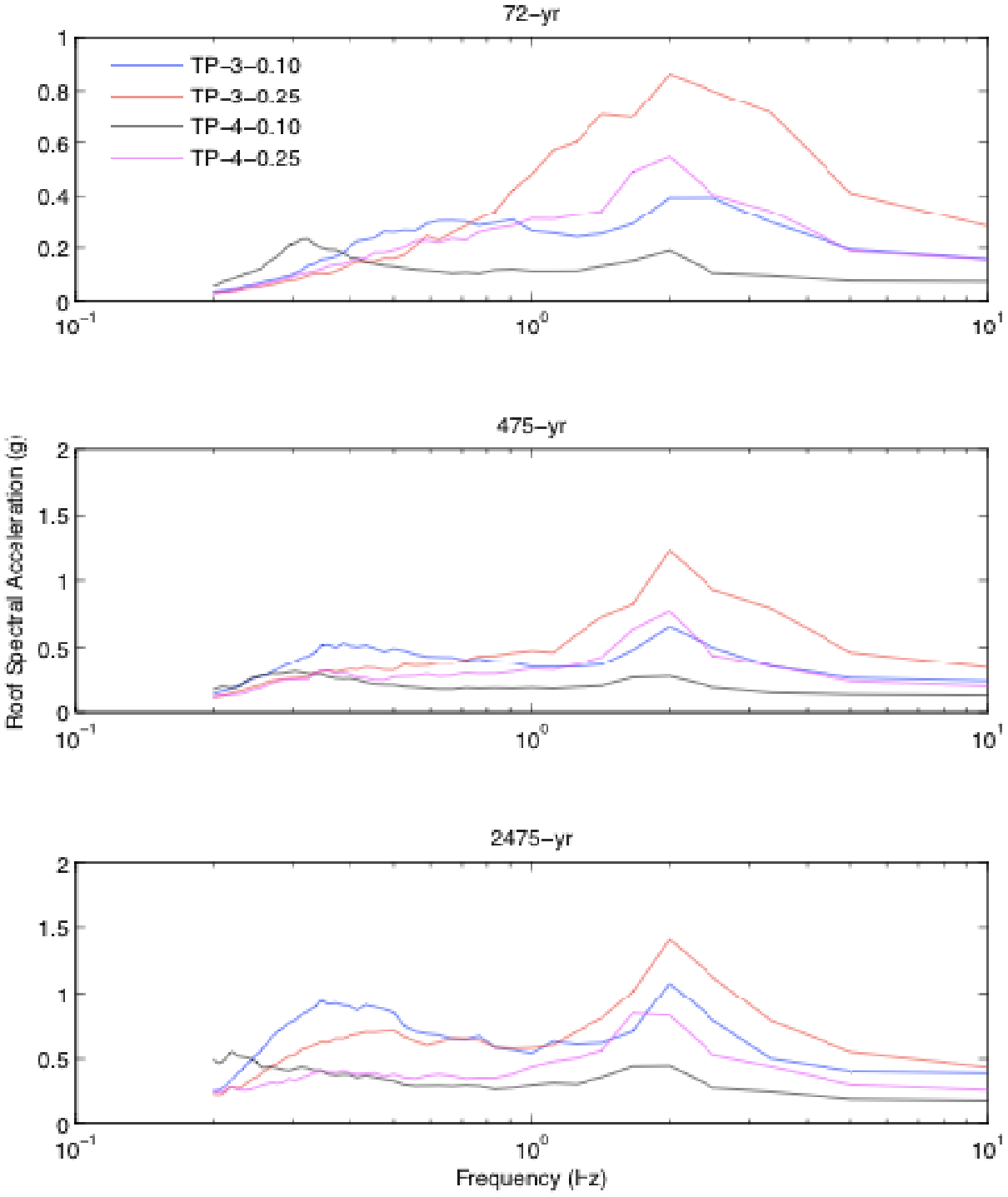

Figure 6.35: Comparison of roof acceleration spectra for 3-story building isolated on TP isolation system

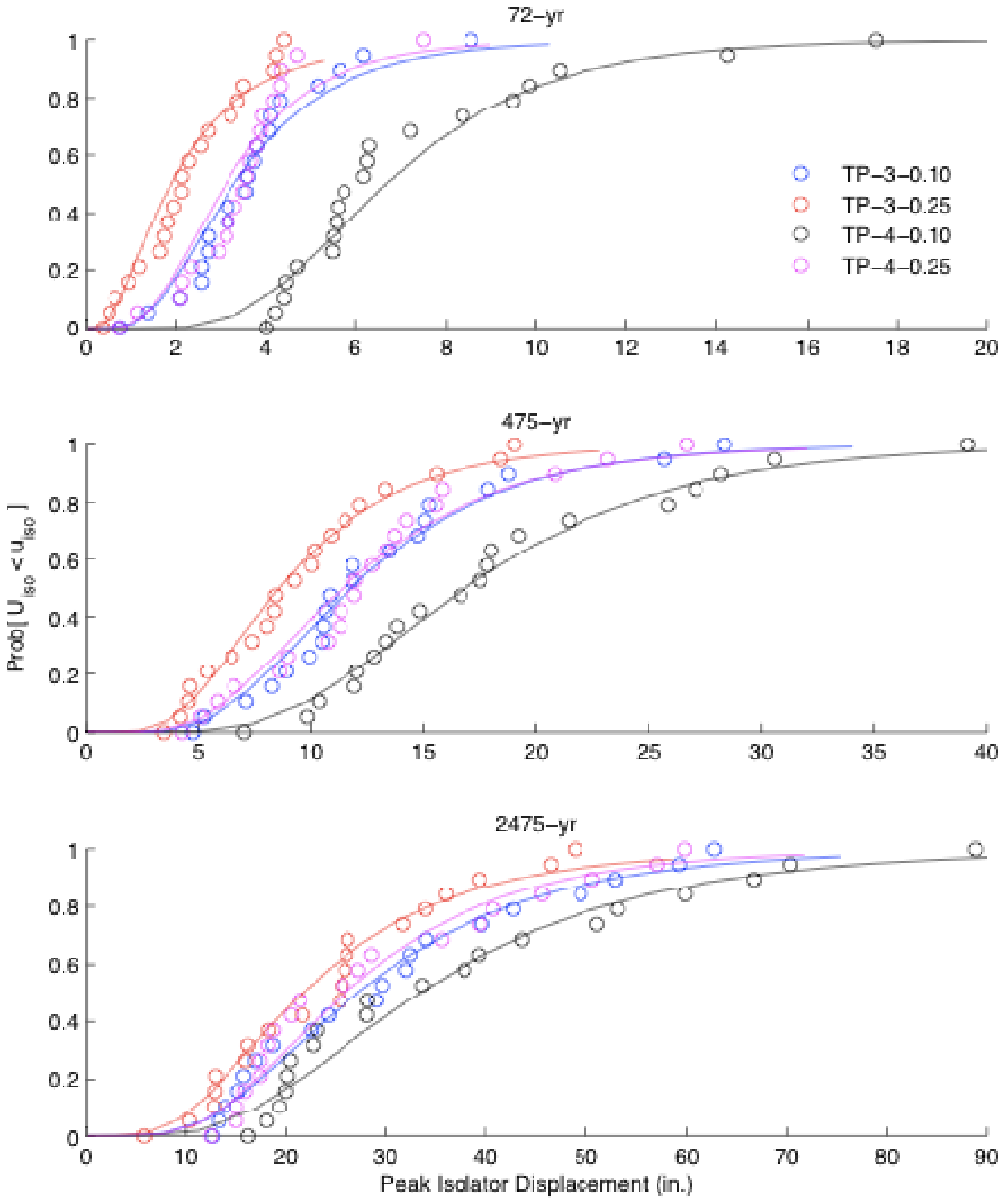

Figure 6.36: Comparison of empirical CDFs of isolator displacement for three levels of seismic hazard (fitted lognormal CDF shown solid), 9-story building on TP isolation system

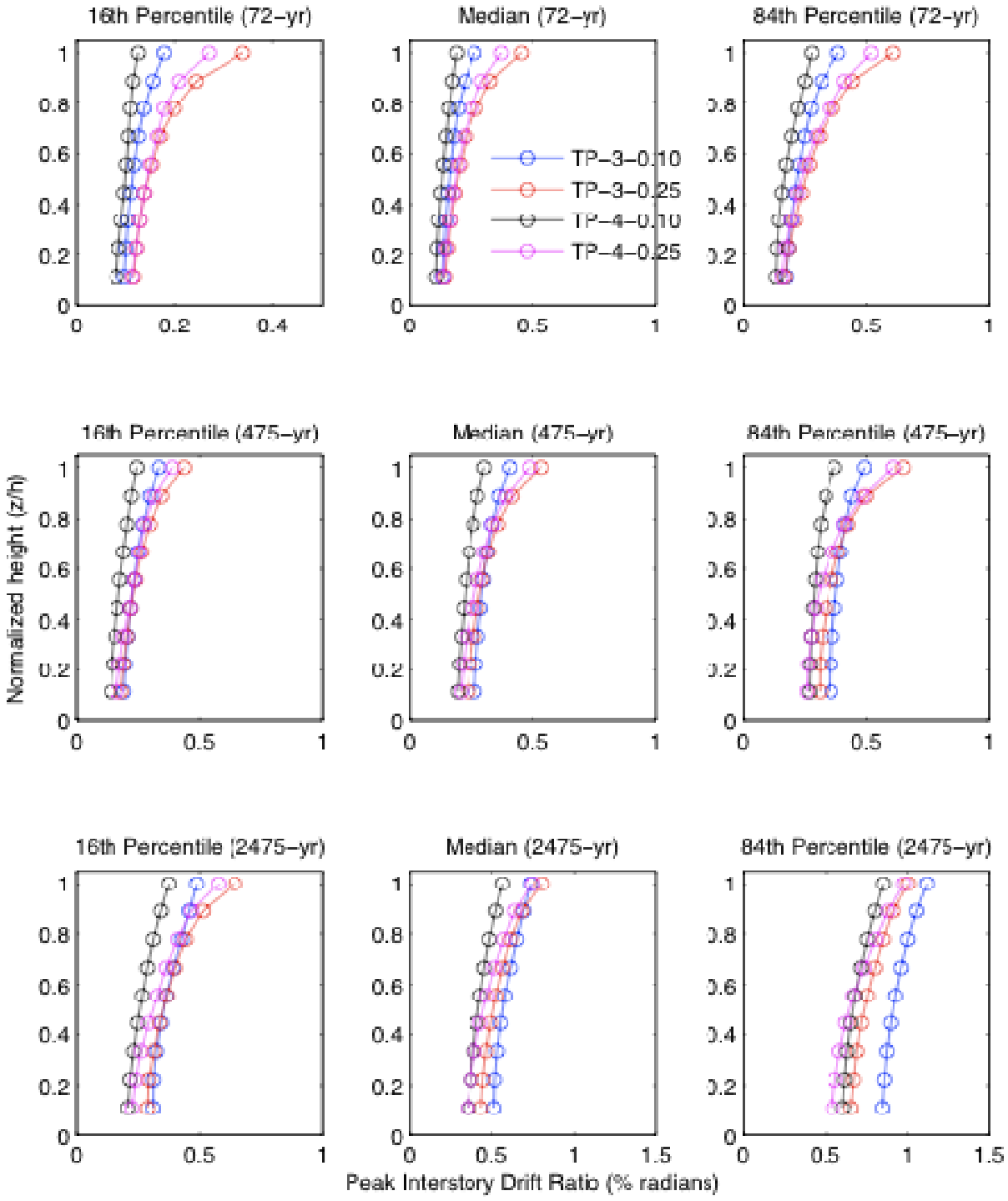

Figure 6.37: Comparison of peak interstory drift ratio (PIDR) at each floor level for 9-story building on TP isolation system

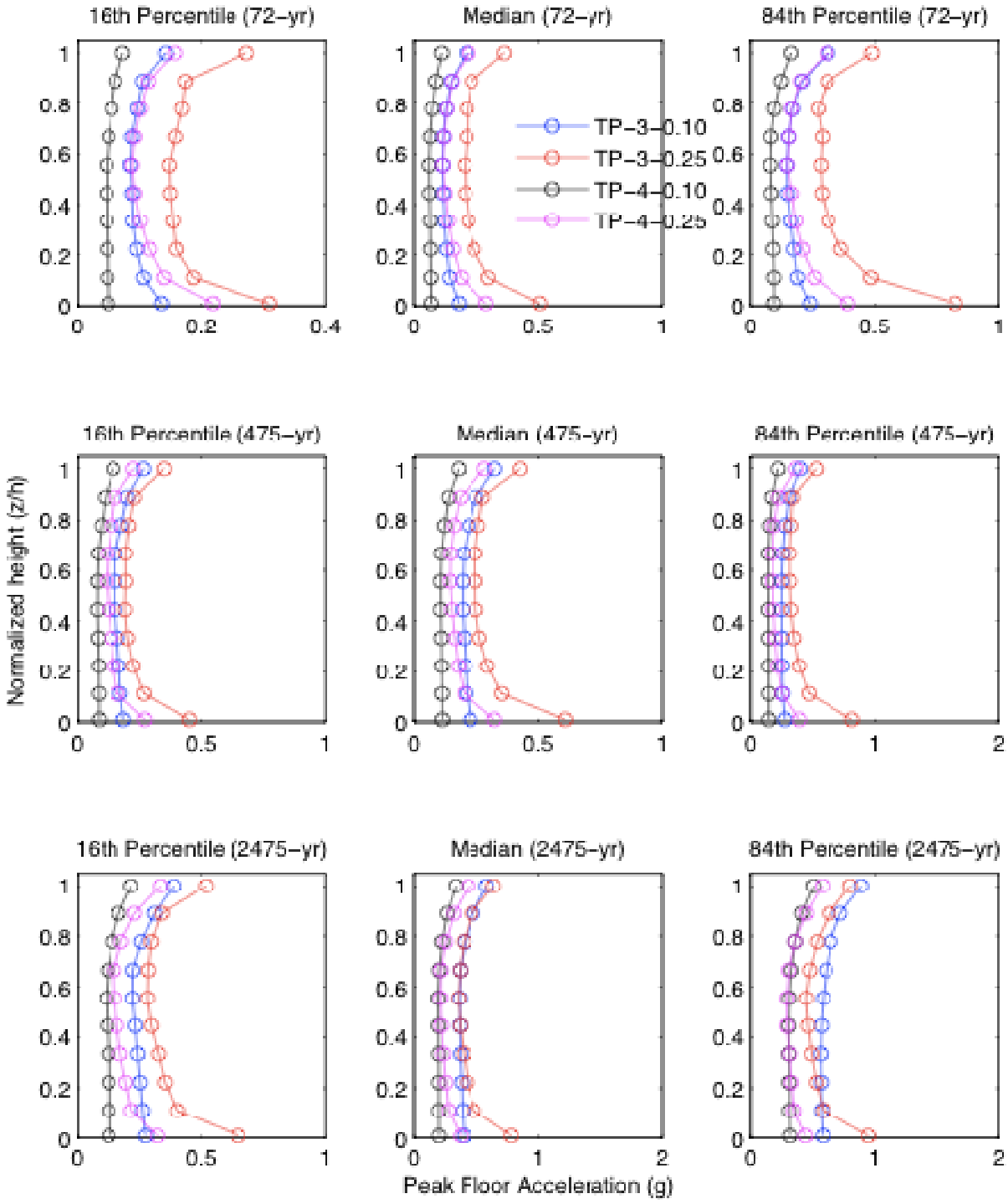

Figure 6.38: Comparison of peak floor acceleration (PFA) at each floor level for 9-story building on TP isolation system

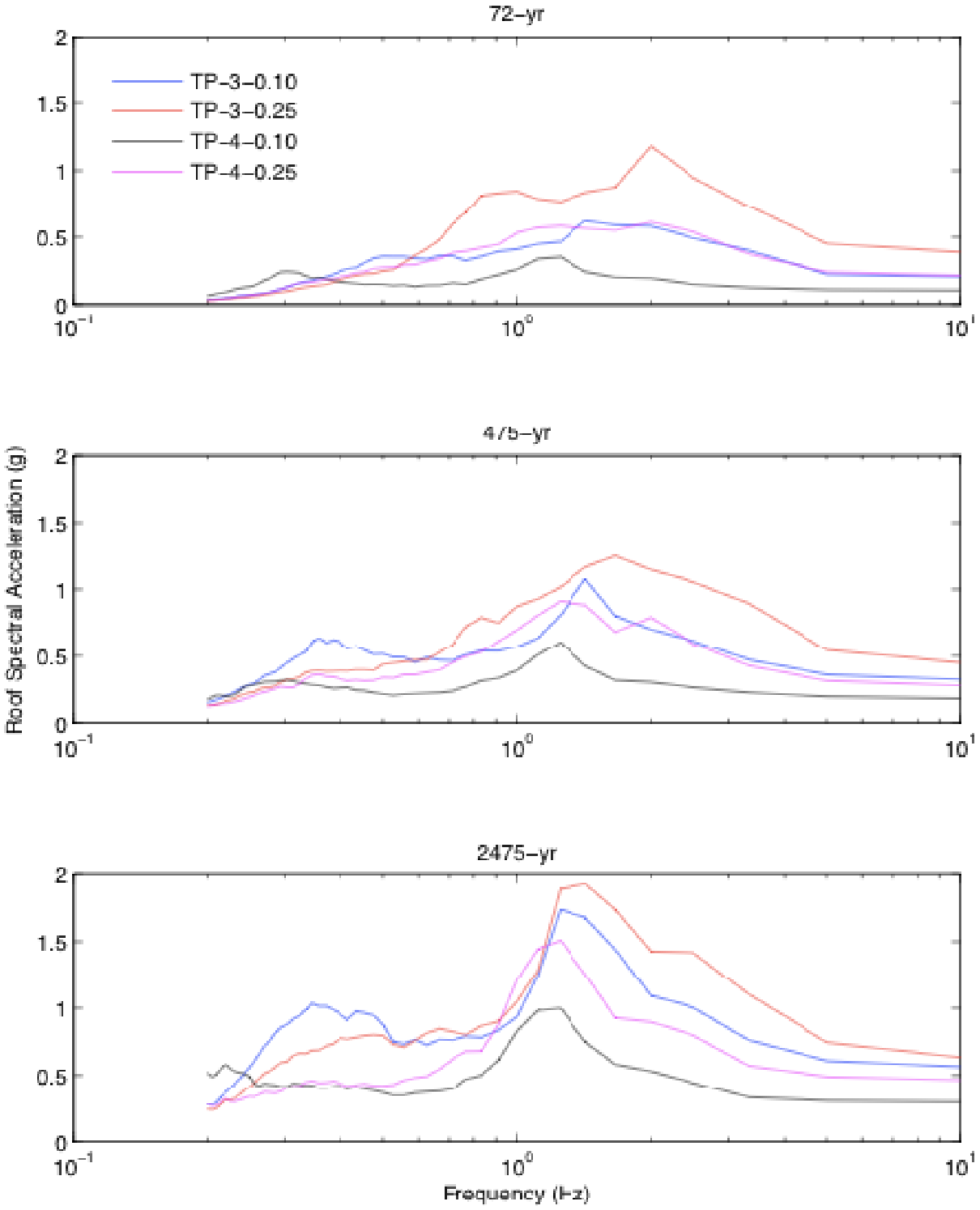

Figure 6.39: Comparison of roof acceleration spectra for 9-story building isolated on TP isolation system

7 Performance-Based Seismic Design Methodology for Base Isolated Structures

In selecting a seismic design strategy for any facility, the cost of a particular structural system must be weighed against the desired performance given the expected earthquake hazard at the site. In this chapter, a methodology is introduced for the selection of a base isolation system given the goal of achieving some complex performance objective. Herein, a complex performance objective is defined as one having a set of potentially distinct damage state limits at a corresponding set of seismic hazard levels. The methodology generally follows that developed for performance-based earthquake engineering by the Pacific Earthquake Engineering Research Center [Deierlein, 2004] with notable deviations and simplifications described within each section as appropriate.

7.1 INTRODUCTION

In identifying the parameters that frame the problem of earthquake resistant design of structures, the two main factors are the location of the site relative to sources of fault rupture, and the nature of the facility being considered. The site location determines the seismic hazard curves, and hence the probabilistic description of ground shaking that can be described in terms of either response spectra or an ensemble of ground acceleration records. The nature of the facility dictates geometric considerations such as story masses, number of stories, floor heights, and other parameters necessary even for preliminary structural analysis. Additionally, the nature of the facility provides some indication of the target seismic performance following a level of seismic hazard. Whereas owners of conventional structures may be able to tolerate some degree of damage in an earthquake having a 72-year return period, the interest of public welfare likely requires a hospital or fire station to be completely functional following such an event.

An effective seismic design and evaluation framework considers the above factors of site location and facility type, and allows for the selection of structural system parameters (both type and proportion) that satisfy some complex performance objective with a quantifiable level of confidence. To develop such a framework, the following are described in subsequent sections of this chapter:

- probabilistic methods of computing the reliability of some random vector of engineering demand parameters (such as peak forces and deformations associated with a seismic event) being below a prescribed damage state limit
- estimation of the parameters describing the uncertainty associated with the above random vector given an ensemble of analytical results
- definition of a multi-objective Seismic Performance Classification for a facility
- establishment of limits on engineering demand parameters to satisfy some target damage state

The above framework requires the generation of analytical results to estimate engineering demand parameters and both their uncertainty and correlation. The analytical data presented in Chapter 6 of this report forms the basis of an application of the framework to base isolated buildings. Both three- and nine-story buildings are considered, and three isolation systems are studied: nonlinear viscous, bilinear hysteretic, and triple pendulum. This application begins with a description of the seismic hazard environment based on the SAC ground motions, and presents the analytical data in terms of median EDP at each seismic hazard level considered. Given median EDPs and their dispersion and correlation, the reliability of meeting a target complex performance objective is estimated for each building, isolation system and its parameters. From this assessment, conclusions are drawn as to favorable attributes of base isolation to meet a target Seismic Performance Classification.

7.2 PROBABILISTIC ASSESSMENT OF SEISMIC PERFORMANCE

Given the occurrence of a seismic event, a structure will be subjected to a set of engineering demand parameters (EDPs), each of which generally describes some peak response of interest. A set or vector of EDPs could be a combination of global or local response peak amplitudes that are of interest to the designer or that can be used to estimate severity or cost of damage. Examples of EDPs include peak interstory drift ratios, peak floor accelerations, peak or cumulative plastic deformation demands, peak column axial loads, etc. A set of limit states can be defined for each EDP that describes the transition between damage states for

that category of EDP. For example, for a conventional steel brace we may have limit states related to having no damage, minor damage not requiring repair, moderate damage requiring limited repair to the element and adjacent nonstructural components, major damage requiring extensive repair or replacement of components, and severe damage leading to possible instability of the structure as a whole. While it is possible to track damage in each element individually, it is more common to reduce the number of EDPs to a more manageable number, by relating them approximately to other response parameters. As noted in Chapter 6, it is possible, for example, to relate deformations in individual braces, beam-to-column connections and so on to interstory drift. As such, it is convenient to use the peak interstory drift at each story or, more simply, the maximum peak interstory drift over all stories as a measure of potential damage. Given a probabilistic description of a set of EDPs, and appropriate threshold values corresponding to the occurrence of various damage limit states, it is of interest to assess the likelihood of the structure experiencing some damage state for a given level of seismic hazard.

Consider a vector of engineering demand parameters (EDPs) given the occurrence of a seismic event having a prescribed probability of exceedance. That is, from the observed or computed response of the facility to an earthquake having a return period of T_R years, a vector of n EDPs, $\mathbf{X} \in \mathbb{R}^n$, is formed. We can also define a vector of limit states $\overline{\mathbf{x}}^{\Upsilon} \in \mathbb{R}^n$ whose entries define the joint limits on $\mathbf{X}$ to meet Damage State (DS) Υ. The variable Υ may take on descriptive values that indicate the level of damage (i.e., DS-F = Functional, DS-IO = Immediate Occupancy, DS-LS = Life Safety, etc). It follows that, given the occurrence of an earthquake with return period T_R, the condition of a structure suffering damage classified by the state DS-Υ is mathematically defined as the event

$$\left\{ \bigcap_{j=1}^{n} X_j^R \leq \overline{x}_j^{\Upsilon} \right\} \tag{7.1}$$

This event is defined as each observed EDP simultaneously *not* exceeding the prescribed limit set for DS-Υ. The uncertainty in the definition of each damage state is not considered, and therefore the limits are treated as deterministic quantities. This approach is taken so that each isolation system can be compared without obfuscation by uncertainties related to damage.

7.2.1 Multivariate Probability Density

Here we introduce the definition of the multivariate density function for a vector of random variables, $f_{\mathbf{X}}(\mathbf{x})$, where $\mathbf{X}$ is a random vector defined on $\mathbb{R}^n$, and is generally continuous. This density function is required to describe not only the uncertainty in each EDP, but also any potential correlations between EDPs. Later, this uncertainty is used to estimate the probability of some set of EDPs simultaneously exceeding a prescribed limit (and hence failing to meet a designated performance objective).

Following Stone [1996], we can define the probability that $\mathbf{X} \in B$ where B is some subset of $\mathbb{R}^n$ as

$$P[\mathbf{X} \in B] = \int_B f_{\mathbf{X}}(\mathbf{x})\, d\mathbf{x} \tag{7.2}$$

This definition of probability is quite general. However, it is made less abstract when the set B is defined as some n-dimensional hypercube[3] of infinitesimal size. That is, let

$$B = \{\mathbf{x} \in (x_1, \ldots, x_n) \times (x_1 + dx_1, \ldots, x_n + dx_n)\} \tag{7.3}$$

The subset B is therefore an n-hypercube cornered at $(x_1, \ldots, x_n)$ having volume equal to $dx_1 dx_2 \cdots dx_n$. The probability defined in Equation (7.2) therefore becomes

$$P\left\{\bigcap_{j=1}^{n} X_j \in [x_j, x_j + dx_j]\right\} = f_{\mathbf{X}}(\mathbf{x})\, dx_1 \cdots dx_n \tag{7.4}$$

or the probability of the random vector $\mathbf{X}$ being within the n-hypercube B is the probability density of $\mathbf{X}$ multiplied by the volume of B. If we are interested in the probability of some element $X_j \in \mathbf{X}$ not exceeding some deterministic threshold $\bar{x}_j$, this corresponds to $P[X_j \le \bar{x}_j]$. By considering all elements of $\mathbf{X}$ simultaneously not exceeding the associated threshold vector $\bar{\mathbf{x}} = (\bar{x}_1, \ldots, \bar{x}_n)$, this probability can be expressed by integrating Equation (7.4) up to and including $\bar{\mathbf{x}}$, or

$$P\left[\bigcap_{j=1}^{n} X_j \le \bar{x}_j\right] = \int_{-\infty}^{\bar{x}_n} \cdots \int_{-\infty}^{\bar{x}_1} f_{\mathbf{X}}(\mathbf{x})\, dx_1 \cdots dx_n \tag{7.5}$$

[3] A hypercube is simply a generalization of a three-dimensional cube to n-dimensions. For example, a square is a two-dimensional hypercube, and higher than three dimensions is a challenge to visualize.

The right-hand-side of (7.5) is the cumulative density function (CDF), and is formally written as

$$F_{\mathbf{X}}(\bar{\mathbf{x}}) = \int_{-\infty}^{\bar{x}_n} \cdots \int_{-\infty}^{\bar{x}_1} f_{\mathbf{X}}(\mathbf{x})\, dx_1 \cdots dx_n \tag{7.6}$$

To be explicit about the form of the CDF, this function is characterized by parameters that are defined depending on the assumed distribution function. If we let the vector of parameters characterizing the CDF be $\boldsymbol{\theta} = (\theta_1, \ldots, \theta_r)$, then we formally write the CDF as $F_{\mathbf{X}}(\bar{\mathbf{x}} | \boldsymbol{\theta})$. These parameters may be assumed based on prior experience, left unknown, or estimated based on a sample of data. Returning to the original task of estimating the probability of the event that each observed EDP simultaneously does not exceed the prescribed limit state vector set for DS-Υ, as first presented above in Equation (7.1), we can state this probability as

$$P\left[\bigcap_{j=1}^{n} X_j \le \bar{x}_j^{\Upsilon}\right] = F_{\mathbf{X}}(\bar{\mathbf{x}}^{\Upsilon} | \boldsymbol{\theta}) \tag{7.7}$$

A consequence of this formulation is that the probability of failure to meet the damage state defined by DS-Υ is the complementary CDF, or

$$P_f^{\Upsilon} = P\left[\bigcap_{j=1}^{n} X_j > \bar{x}_j^{\Upsilon}\right] = 1 - F_{\mathbf{X}}(\bar{\mathbf{x}}^{\Upsilon} | \boldsymbol{\theta}) \tag{7.8}$$

As a result, the probability of meeting a damage state for a particular seismic hazard scenario becomes a function of a) the limit states $\bar{\mathbf{x}}^{\Upsilon}$ defining the transitions between damage states and b) the joint CDF of the demand parameters, including the distribution model and associated parameters $\boldsymbol{\theta}$.

7.2.2 Estimation of Demand Parameter Distribution

Consider first the task of estimating the joint CDF of the demand parameters, including distribution model and associated parameters $\boldsymbol{\theta}$. As described in Chapter 6, an ensemble of ground-motion records can be developed for a number of levels of seismic hazard. In our previous study, a total of 20 records were used for each of three hazard levels: T_R = 72 years, T_R = 475 years, and T_R = 2475 years. We wish to estimate the probabilistic structure of the

EDP vector **X** for each level of hazard. Here, this EDP vector is left general, but the entries are a mixture of peak accelerations, deformations, ductility demands, or other EDPs that are of interest in describing the state of damage of the structural system under consideration. In subsequent sections, this EDP vector is infused with actual peak response parameters relevant to the multi-story base isolated buildings under investigation.

7.2.2.1 Selection of Distribution Function

To form an estimate of the parameters characterizing the probabilistic structure of a random variable, a distribution model must first be selected that adequately describes the uncertainty inherent in the process that produces the response of interest. Often, the selection of a distribution model is inherent to a physical process. For example, the number of coin flips landing either heads or tails out of a fixed number of trials follows the binomial distribution. This is a consequence of the underlying mathematical process of Bernoulli trials from which the binomial distribution arises. Since a single coin flip constitutes a Bernoulli trial (where the observation of "success" and "failure" have equal probability for a fair coin,) estimating the probability that fewer than x heads are observed in n coin flips is naturally taken from the binomial distribution. In the case of an assumed fair coin, no estimation of the binomial parameter p (describing the success rate of a single trial) is necessary. However, if one were interested in testing the bias of a coin of unknown attribute, it would be necessary to conduct many trials, observe the number of successes over some large number of trials, and estimate the binomial parameter $\hat{p} = s / n$ where s is the number of observed heads and n is some (large) number of trials[4]. Despite the need for estimation in this simple example, the selection of assumed distribution is obvious from the underlying physical process.

It is often the case, however, that no feature of a random process reveals the appropriate distribution for which parameters should be estimated. In the case of structural response to input ground motion, there is a special case where the normal (Gaussian) distribution appropriately characterizes the output response. This case is the time-variant response of a linear structural system subjected to stationary Gaussian ground acceleration input [Lutes and Sarkani, 2004]. Here, there is a physical process that might reasonably lead to an assumption of Gaussian ground input. The successive reflection and refraction of

[4] A carat over a variable designates it as an estimate of some otherwise unknown parameter.

seismic waves through various strata of rock and soil leads to a surface response, which is the superposition of many randomly occurring seismic waves. By the Central Limit Theorem [Stone, 1996] a random process that is the summation of random variables having a common (but unknown) distribution becomes normally distributed as the number in the summation becomes very large. Despite the convenience of the Gaussian distribution for the above special case, the type of response quantities we are concerned with do not fit the necessary conditions described. First, the assumption of structural linearity is clearly violated, since highly nonlinear isolation systems are the focus of these studies. Additionally, we are concerned with peak responses over the duration of a single trial (ground motion) repeated over many trials. Finally, the ground motion inputs cannot be characterized as a Gaussian stationary signal. There is nothing inherent in these three significant departures from the original linear Gaussian assumption that would make the selection of distribution model clear.

It has been suggested in the available literature (Miranda and Aslani [2003] and McGuire [2004], among others) that the EDPs of peak interstory drift ratio (PIDR) and peak floor acceleration (PFA) are both lognormally distributed given some level of ground motion intensity. Based on the abundance of work suggesting the lognormality of EDPs, this distribution is assumed *a priori* to characterize the elements of the EDP vector **X**. Two significant consequences of the lognormal assumption are (a) the demand parameters are necessarily non-negative and (b) the distribution is characterized by positive skew. Both of these attributes of the lognormal distribution are appealing in their description of peak structural response of nonlinear systems because (a) peaks are non-negative by their definition, and (b) nonlinear response excursions tend to produce a few observations that are significantly larger than the majority of the sample. Moreover, since the EDP vector **X** contains multiple random variables, something must be stated regarding their dependence. Clearly, the peak response of the two demand parameters (e.g., deformation and acceleration) are subject to the same, uncertain seismic input, exhibit statistical dependence. Without compelling evidence to suggest strong independence, the potential for correlation must be accounted for in the estimation of probabilistic structure. For this reason, the EDP vector **X** is assumed to be jointly lognormal for a particular level of seismic hazard.

7.2.2.2 Multivariate Lognormal Density Function

Now that the assumption of joint lognormal distribution of **X** has been established, it is possible to estimate the necessary parameters characterizing the distribution. Consider the general problem of determining a joint CDF for a vector of multivariate lognormally distributed random variables. As before, let $\mathbf{X} \in \mathbb{R}^n$ be a random vector of EDPs. The expectation of $\ln \mathbf{X}$ is given as $E[\ln \mathbf{X}] = \boldsymbol{\Lambda} = [\lambda_1 \cdots \lambda_n]^T$, and the covariance matrix is defined as

$$\boldsymbol{\Psi} = E\left[(\ln \mathbf{X} - \boldsymbol{\Lambda})(\ln \mathbf{X} - \boldsymbol{\Lambda})^T\right] \tag{7.9}$$

That is, given a transformation $\mathbf{Y} = \ln \mathbf{X}$, the random vector **Y** is multivariate *normal* with mean vector $\boldsymbol{\Lambda}$ and covariance matrix $\boldsymbol{\Psi}$. This definition of the distribution of **Y** and its parameters is written $\mathbf{Y} \sim MN(\boldsymbol{\Lambda}, \boldsymbol{\Psi})$. Equivalently, the distribution of **X** is written as $\mathbf{X} \sim MLN(\boldsymbol{\Lambda}, \boldsymbol{\Psi})$. From Stone [1996] it follows that the joint PDF of the multivariate normal random vector **Y** is

$$f_{\mathbf{Y}}(\mathbf{y}) = \frac{1}{(2\pi)^{n/2}|\boldsymbol{\Psi}|^{1/2}} \exp\left[-\frac{1}{2}(\mathbf{y} - \boldsymbol{\Lambda})^T \boldsymbol{\Psi}^{-1}(\mathbf{y} - \boldsymbol{\Lambda})\right] \tag{7.10}$$

The multivariate normal joint CDF is computed in the standard way, as described in Equation (7.6). Noting that the probability of each random vector **X** and **Y** being within some infinitesimal *n*-hypercube is equal (due to one being a transformation of the other), we have

$$P\left[\bigcap_{j=1}^{n} X_j \in [x_j, x_j + dx_j]\right] = P\left[\bigcap_{j=1}^{n} Y_j \in [y_j, y_j + dy_j]\right] \tag{7.11}$$

From the definition of probability density in Equation (7.4) this gives

$$f_{\mathbf{X}}(\mathbf{x})\, dx_1 \cdots dx_n = f_{\mathbf{Y}}(\mathbf{y})\, dy_1 \cdots dy_n \tag{7.12}$$

According to the change of variable theorem for injective mapping, the density of **X** becomes

$$f_{\mathbf{X}}(\mathbf{x}) = f_{\mathbf{Y}}(\mathbf{y}) \left|\frac{\partial(y_1, \ldots, y_n)}{\partial(x_1, \ldots, x_n)}\right| = f_{\mathbf{Y}}(\mathbf{y}) \left|\mathbf{J}_{\mathbf{y},\mathbf{x}}\right| \tag{7.13}$$

where $\mathbf{J}_{\mathbf{y},\mathbf{x}}$ is the standard Jacobian matrix. Given the transformation $y_j = \ln x_j$ implies $dy_j = dx_j / x_j$, and the determinate of the Jacobian above is therefore $\left|\mathbf{J}_{\mathbf{y},\mathbf{x}}\right| = \left(\prod_{j=1}^{n} x_j\right)^{-1}$. Substituting this determinate and the variable change $\mathbf{y} = \ln \mathbf{x}$ into (7.13) gives the multivariate lognormal density as

$$f_{\mathbf{X}}(\mathbf{x}) = \frac{1}{(2\pi)^{n/2}\left|\mathbf{\Psi}\right|^{1/2}\prod_{j=1}^{n} x_j} \exp\left[-\frac{1}{2}\left(\ln \mathbf{x} - \mathbf{\Lambda}\right)^T \mathbf{\Psi}^{-1}\left(\ln \mathbf{x} - \mathbf{\Lambda}\right)\right] \tag{7.14}$$

7.2.2.3 Estimation of Joint Lognormal Parameters

To characterize the joint PDF of **X**, it is necessary to estimate the mean vector and covariance matrix, respectively denoted $\hat{\mathbf{\Lambda}}$ and $\hat{\mathbf{\Psi}}$, for each considered level of seismic hazard. Here we consider three hazard levels (72 years, 475 years, 2475 years), so for a particular set of structural system parameters, the estimation of three mean vectors, $\hat{\mathbf{\Lambda}}_{72}, \hat{\mathbf{\Lambda}}_{475}, \hat{\mathbf{\Lambda}}_{2475}$, and three covariance matrices, $\hat{\mathbf{\Psi}}_{72}, \hat{\mathbf{\Psi}}_{475}, \hat{\mathbf{\Psi}}_{2475}$, is required.

Consider an ensemble of *p* ground motions developed to represent a single level of seismic hazard of return period T_R. From nonlinear response history analysis, we obtain a set of observed demand vectors, $\mathbf{x}_1, \ldots, \mathbf{x}_p$, where $\mathbf{x}_j \in \mathbb{R}^n$. In general, let the quantity x_{ij} be the *i*th EDP that is observed in the *j*th ground motion ($i = 1, \ldots, n$ and $j = 1, \ldots, p$). Since each random EDP X_i is assumed to be lognormal, $\ln X_i$ is normally distributed, and the *i*th logarithmic mean can be estimated by the sample mean of the *p* observations

$$\hat{\lambda}_i = \frac{\sum_{j=1}^{p} \ln x_{ij}}{p}, \quad i = 1, \ldots, n \tag{7.15}$$

By taking the exponential of both sides of Equation (7.15), a measure of central tendency of the random variable X_i is

$$\hat{x}_i = \left[\prod_{j=1}^{p} x_{ij}\right]^{1/p} \tag{7.16}$$

which is the standard definition of the *geometric mean* of a sample. From these results, the estimated logarithmic mean vector is simply $\hat{\mathbf{\Lambda}} = \left[\hat{\lambda}_1 \cdots \hat{\lambda}_n\right]^T$.

Similarly, recognizing potential correlation between elements of **X**, the covariance matrix for **X** based on observations $\mathbf{x}_1,\ldots,\mathbf{x}_p$ must be estimated. The *ij*th entry of the covariance matrix **Ψ** is defined as

$$\begin{aligned}\boldsymbol{\Psi}_{ij} &= E\left[\left(\ln X_i - \lambda_i\right)\left(\ln X_j - \lambda_j\right)\right] \\ &= E\left[\ln X_i \ln X_j\right] - \lambda_i\lambda_j\end{aligned} \tag{7.17}$$

For $i = j$, the diagonal entry is simply the variance of X_i. An unbiased estimator of this variance is given as [Stone, 1996]

$$\hat{\zeta}_i^2 = \frac{\sum_{j=1}^{p}\left(\ln x_{ij} - \hat{\lambda}_i\right)^2}{p-1} \tag{7.18}$$

For $i \neq j$, it is convenient to introduce a dimensionless statistical measure termed the *correlation coefficient*. This coefficient is defined as

$$\rho_{ij} = \frac{E\left[\left(\ln X_i - \lambda_i\right)\left(\ln X_j - \lambda_j\right)\right]}{\zeta_i\zeta_j} \tag{7.19}$$

Hence, we can write $\boldsymbol{\Psi}_{ij} = \rho_{ij}\zeta_i\zeta_j$. Since an estimate of $\hat{\zeta}_i^2$ is given in Equation (7.18), obtaining an estimate of ρ_{ij} is sufficient to form a complete estimate of the covariance matrix **Ψ**. For this purpose, the Pearson product-moment correlation coefficient is useful. This estimator of ρ_{ij} is given as [Weisstein, 2006]

$$\hat{\rho}_{ij} = \frac{\sum_{k=1}^{p}\left(\ln x_{ik} - \hat{\lambda}_i\right)\left(\ln x_{jk} - \hat{\lambda}_j\right)}{\left(p-1\right)\hat{\zeta}_i\hat{\zeta}_j} \tag{7.20}$$

In summary, the covariance matrix **Ψ** is estimated as

$$\hat{\boldsymbol{\Psi}} = \begin{bmatrix} \hat{\zeta}_1^2 & \cdots & \hat{\rho}_{1n}\hat{\zeta}_1\hat{\zeta}_n \\ \vdots & \ddots & \vdots \\ \hat{\rho}_{n1}\hat{\zeta}_n\hat{\zeta}_1 & \cdots & \hat{\zeta}_n^2 \end{bmatrix} \tag{7.21}$$

where $\hat{\zeta}_i^2$ and $\hat{\rho}_{ij}$ are given in Equations (7.18) and (7.20), respectively. With the distribution of **X** selected and its parameters estimated based on observed response data, it is possible to compute the probability of the response given some level of earthquake hazard exceeding a prescribed vector of limit states.

7.2.2.4 Quantiles

Given the lognormal PDF of Equation (7.14) and specializing to the univariate case, it is straightforward to compute any *p*th quantile $x_p = \{x : F_X(x) = p\}$. For example, it may be of interest to determine the demand *x* at which there is a 16% probability of exceedance. This is called the 84th percentile and is denoted $x_{0.84}$. For a lognormally distributed random variable with estimated parameters $\hat{\lambda}$ and $\hat{\zeta}$

$$F_X(x_p) = \Phi\left(\frac{\ln x_p - \hat{\lambda}}{\hat{\zeta}}\right) = p \tag{7.22}$$

Solving for x_p leads to

$$x_p = \exp\left[\hat{\lambda} + \hat{\zeta}\,\Phi^{-1}(p)\right] \tag{7.23}$$

The values of $\Phi^{-1}(p)$ are well known and widely tabulated, and several important examples are:

$$\Phi^{-1}(0.0228) = -2,\ \Phi^{-1}(0.159) = -1,\ \Phi^{-1}(0.5) = 0,\ \Phi^{-1}(0.841) = 1,\ \Phi^{-1}(0.977) = 2$$

Therefore, the demand that has a 16% probability of exceedance, $x_{0.84}$, is computed as $x_{0.84} = \exp\left(\hat{\lambda} + \hat{\zeta}\right)$. Similarly, the inner 95% confidence interval is computed as

$$\begin{aligned} 95\%\ C.I. &= \left[x_{0.023}, x_{0.977}\right] \\ &= \left[\exp\left(\hat{\lambda} - 2\hat{\zeta}\right), \exp\left(\hat{\lambda} + 2\hat{\zeta}\right)\right] \end{aligned} \tag{7.24}$$

7.2.3 Computation of Failure Probability

Once the distribution parameters of the lognormally distributed random EDP vector **X** have been estimated for a given level of seismic hazard, it is mathematically possible to compute

the probability that the structure exceeds a limit state vector $\bar{\mathbf{x}}$. This failure probability is defined as $P_f = 1 - F_{\mathbf{X}}(\bar{\mathbf{x}})$, and computing this for practical applications is the subject of this section. The failure probability P_f is

$$P_f = 1 - F_{\mathbf{X}}(\bar{\mathbf{x}}) = 1 - \int_{-\infty}^{\bar{x}_n} \cdots \int_{-\infty}^{\bar{x}_1} f_{\mathbf{X}}(\mathbf{x})\, dx_1 \cdots dx_n \tag{7.25}$$

While a closed-form solution does not exist for this integral, a number of algorithms have been developed to numerically compute the multivariate normal CDF given a mean vector and covariance matrix. Therefore, it is convenient to transform the limit state vectors to the normal space. Doing so and explicitly recognizing the necessary parameters to characterize the multivariate normal distribution, Equation (7.25) becomes

$$P_f = 1 - F_{\mathbf{Y}}(\ln \bar{\mathbf{x}} \,|\, \boldsymbol{\Lambda}, \boldsymbol{\Psi}) \tag{7.26}$$

Recognizing the existence of potentially distinct limit state vectors for each performance classification, and an estimated mean vector $\hat{\boldsymbol{\Lambda}}$ and covariance matrix $\hat{\boldsymbol{\Psi}}$ that depends on the level of hazard, a general statement of the probability that a structure meets Damage State Υ in an earthquake having return period T_R is given as

$$P_R^{\Upsilon} = F_{\mathbf{Y}}(\ln \bar{\mathbf{x}}^{\Upsilon} \,|\, \hat{\boldsymbol{\Lambda}}^R, \hat{\boldsymbol{\Psi}}^R) \tag{7.27}$$

This multivariate normal CDF can be numerically computed by a quasi-Monte Carlo integration algorithm described by Genz [1992] and implemented in Matlab® [Mathworks, 2006]. This algorithm employs a simulation technique whereby uniform random numbers are transformed to uncorrelated standard Gaussian random numbers in the usual way. By Cholesky decomposition of the covariance matrix $\boldsymbol{\Psi}$, an uncorrelated standard Gaussian random vector may be rotated into the correlated Gaussian space with a prescribed mean $\boldsymbol{\Lambda}$ and covariance $\boldsymbol{\Psi}$. This simulation continues until a stable Monte Carlo estimate of the probability expressed in Equation (7.27) converges within some selected error tolerance.

7.3 APPLICATIONS TO PERFORMANCE-BASED EARTHQUAKE ENGINEERING

The section provides a specific framework within which the subject three- and nine-story isolated buildings from Chapter 6 are evaluated. First, the concept of a multi-objective

Seismic Performance Classification (SPC) is defined. This definition is contrasted with the procedures contained in modern building code provisions, which explicitly consider a single performance objective at a single level of seismic hazard. Since an important component of determination of the SPC for a facility is the set of limits defining damage state transitions, explicit limit state vectors are defined for each damage state considered. Lastly, a set of SPC designations is defined in the multi-objective context. These definitions are applied to isolated buildings in Section 7.4 to compute reliability estimates.

7.3.1 A Multiple-Objective Seismic Performance Classification

The form of Equation (7.27) is sufficiently general to allow evaluation of the reliability of a particular structural system to meet some complex performance objective. This performance objective is termed "complex" because it need not be a single damage state limit for a single return period event (i.e., Life Safety damage state for T_R = 475 years, as is the case for traditional building codes). It is possible to specify multiple performance criteria, and subsequently assign a performance objective to each level of seismic hazard considered. In this case, the Seismic Performance Classification (SPC) is a function of simultaneously meeting each deterministic damage state limit at the level of hazard prescribed. Given the mathematical expression of Equation (7.1) that describes the event of meeting Damage State Υ for a seismic event having return period T_R, this notion of multiple-objective SPC is defined as the simultaneous satisfaction (or nonexceedance) of k damage states at the corresponding k levels of seismic hazard, expressed as the event

$$\underbrace{\left\{\bigcap_{j=1}^{n} X_j^{R_1} \le \overline{x}_j^{\Upsilon_1}\right\}}_{DS-\Upsilon_1|R_1} \bigcap \cdots \bigcap \underbrace{\left\{\bigcap_{j=1}^{n} X_j^{R_k} \le \overline{x}_j^{\Upsilon_k}\right\}}_{DS-\Upsilon_k|R_k} \tag{7.28}$$

Note that each damage state need not be distinct, as the same damage limit could be targeted for multiple levels of hazard. Indeed, the same damage state could be targeted for *all* levels of seismic hazard in which case the SPC framework remains general. Additionally, some damage states may rely on the same EDP, such as partition damage and structural damage both relating to interstory drift. This framework is described further in this section, including implicit consideration of multiple performance objectives that appear in modern building codes.

7.3.2 Treatment of Performance Objectives in Building Codes

The design of structures in the United States and throughout the world is governed by minimum standards documented in building codes. The design provisions that appear in these codes have historically represented professional consensus without the consideration of explicit performance states. The commentary to the 2003 NEHRP provisions for new buildings [BSSC, 2003] states

> *Although the Provisions explicitly require design for only a single level of ground motion, it is expected that structures designed and constructed in accordance with these requirements will generally be able to meet a number of performance criteria, when subjected to earthquake ground motions of differing severity.*

This is clearly an implicit multi-level performance objective, as there is an expectation of satisfying multiple performance criteria for each level of seismic hazard considered. However, no methodology is described for either estimating the probability of exceeding or improving the reliability of achieving the intended multi-level performance objective.

The shortcomings of existing building codes were recognized by the structural engineering community, and a set of interim recommendations were developed to promote what was termed "Performance-Based Seismic Engineering" [SEAOC, 1995]. The intent of these recommendations, titled *Vision 2000*, was to define the following series:

1. standard seismic performance levels
2. reference seismic hazard levels
3. uniform design performance objectives for buildings depending on their occupancy classification and importance
4. recommendations for engineering practice

Vision 2000 promoted a holistic treatment of earthquake resistant design, and identified many key research needs to achieve such a design methodology. Many of the research areas identified remain active today. Based on the move toward performance-based seismic design, current building code provisions are more explicit about the intended seismic performance of structures designed in their accordance. The 2006 International Building Code largely adopts the provisions of the 2003 NEHRP Recommended Provisions for Seismic Regulations for New Buildings and Other Structures [BSSC, 2003], which presents

the expected building performance in a matrix, recreated in Figure 7.1. A qualitative description of each damage state in terms of structural and non-structural damage is contained in Table 7.1.

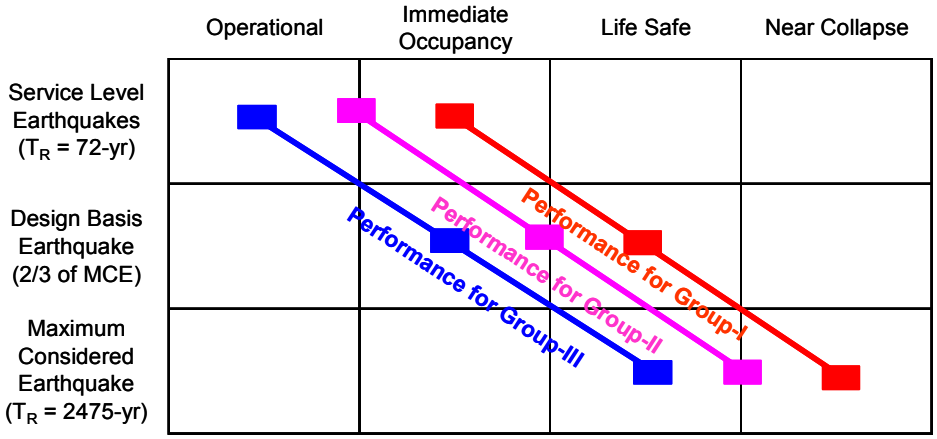

Figure 7.1: Expected building seismic performance as expressed in 2003 NEHRP Recommended Provisions [BSSC, 2003]

In the above performance matrix, the Seismic Performance Classification (denoted "Group" in 2003 NEHRP) can be interpreted within the framework introduced in this section. A facility could be designated Group III if the following intersection of events occurs:

$$\underbrace{\left\{\bigcap_{j=1}^{n} X_j^{72-yr} \le \bar{x}_j^{O}\right\}}_{DS-O|72-yr} \bigcap \underbrace{\left\{\bigcap_{j=1}^{n} X_j^{475-yr} \le \bar{x}_j^{IO}\right\}}_{DS-IO|475-yr} \bigcap \underbrace{\left\{\bigcap_{j=1}^{n} X_j^{2475-yr} \le \bar{x}_j^{LS}\right\}}_{DS-LS|2475-yr} \tag{7.29}$$

Table 7.1: Damage state definitions (adopted and expanded from ASCE-41 [2006])

	Functional	Immediate Occupancy	Life Safety	Collapse Prevention
Overall Damage	Very Light	Light	Moderate	Severe
Structural	No permanent drift. Structure substantially retains original strength and stiffness.	No permanent drift. Structure substantially retains original strength and stiffness.	Residual strength and stiffness remain at all stories. Gravity load system intact. No out-of-place wall or para- pet failure. Some permanent drift	Virtually no residual strength of stiffness remains. Gravity load system functioning. Large permanent drift. Failure of parapets and out-of-place wall anchorages.
Nonstructural	Minor cracking of facades, partitions, and ceilings. Power and utilities available. All systems important to normal operation are functional.	Minor cracking of facades, partitions, and ceilings. Elevators can be restarted. Equipment and contents generally secure but may not operate due to mechanical failure or loss of power.	Extensive damage to facades, partitions, and ceilings. Falling hazards mitigated. No loss of egress.	Extensive damage to all nonstructural systems, falling hazards not mitigated.

7.3.3 Establishment of Limit State Vectors

A crucial step in the assessment of seismic performance is the establishment of limits on demand parameters that identify a transition between damage states. A simple example is the deformation of a wall partition consisting of gypsum board attached to light-gage metal studs. If a partition specimen is placed in a loading frame, and an actuator imposes monotonically increasing deformation, several damage states may be observed throughout the deformation history. As some stage of deformation, cracking will occur in the brittle outer gypsum that would require patching and painting (and hence labor and materials). At some greater level of deformation, the board will experience opening of cracks that requires replacement of the outer gypsum, but does not compromise the integrity of the metal studs. Even greater deformation triggers buckling of the metal studs and hence replacement of the entire wall partition. Each of these increasing damage states has repair costs associated with it that escalate with the deformation demand. As a result, limits may be imposed on the allowable deformation to prevent the triggering of these repair costs in a particular seismic event. The definition of these damage states as a function of the imposed demand (termed “fragility function”) is a subject of significant research. Such fragility functions are being developed for structural elements, deformation-sensitive nonstructural elements, acceleration-sensitive

nonstructural elements, and contents. The form of a fragility function is always an estimate of exceeding a particular damage state given the occurrence of a demand. In our example of a partition wall, a fragility function for that wall (based on experimentation on many samples) may indicate that, at an interstory deformation of 1.5", there is a 50% chance the gypsum will have cracked, a 10% chance the gypsum needs to be replaced, and a 2% chance the metal studs need to be replaced. This information can be used to associate an economic or downtime loss triggered by the occurrence of a deformation demand, since each damage state causes either expense to repair, some duration of time where a portion of the facility may not be occupied, or often both. Aslani and Miranda [2003, 2005] provide excellent discussions on fragility functions and provide references to several developmental sources. Given the variety of fragility functions that currently exist, the rate at which new ones are being developed, and their dependence on facility type and occupancy, the studies described herein do not attempt to develop specific damage state limits, as might be done for an actual building project, nor do they account for dispersion in observing some damage state given the occurrence of an EDP value.

In these studies, a vector of EDPs must be selected that can be compared to their associated damage state limit. To capture the effect of various demand types on the overall damage state on the structure, the following demand parameters have been chosen:

1. peak interstory drift ratio (*PIDR*)
2. peak floor acceleration (*PFA*)
3. peak isolator displacement (U_{iso})
4. peak floor spectral acceleration at the roof level (*PFSA*) over the frequency range [1 Hz, 10 Hz] at 5% damping

Thus, the EDP vector **X**, which is assumed to be jointly lognormal, is defined for the following studies as:

$$\mathbf{X} = \begin{bmatrix} PIDR & PFA & U_{iso} & PFSA \end{bmatrix}^T \tag{7.30}$$

In an actual building, this set of EDPs would be expanded or truncated as called for by the project specifics. A set of limit state vectors, $\bar{\mathbf{x}}^{\Upsilon}$, must be constructed to describe the transition of each EDP to each damage state Υ.

To select limit state vectors for specific damage states, a generic approach is taken herein, employing representative numerical values for the specific damage states considered.

There are a number of recommended nonstructural damage state limits that are non-specific to the type of structure, but are based on the widely available research and include median and dispersion estimates to account for the uncertainty, assuming the customary lognormal distribution. Aslani and Miranda [2005] have developed statistical parameters for fragility functions of generic nonstructural drift-sensitive and acceleration-sensitive components. These are summarized below in Table 7.2. Recall that some quantile for a lognormal distribution, x_p, is given above as $x_p = \exp\left[\hat{\lambda} + \hat{\zeta}\,\Phi^{-1}(p)\right]$. Therefore, in the simplest probabilistic formulation of the limit state vector, we could choose to limit the demand to the 50th, 16th or other percentile estimate of the tabulated value to meet a particular damage state, depending on the desired level of reliability. It should be recognized that nonstructural elements having fragility functions far different from those tabulated below can be used in a structure, which could result in more or less robust performance. Therefore, the observations made below regarding performance of various isolated systems are conditioned on this particular set of damage states, and other conclusions might be reached if other numerical values were selected.

Table 7.2: Statistical parameters for fragility functions of generic nonstructural drift-sensitive and acceleration-sensitive components [Aslani and Miranda, 2005]

	Peak Interstory Drift Ratio		Peak Floor Acceleration	
Damage State	Median (%)	Dispersion[1]	Median (g)	Dispersion[1]
DS1: Slight damage	0.4	0.5	0.25	0.6
DS2: Moderate damage	0.8	0.5	0.50	0.6
DS3: Extensive damage	2.5	0.5	1.00	0.6
DS4: Complete damage	5.0	0.5	2.00	0.6

[1] Defined as the logarithmic standard deviation of the demand

Damage states must also be established to assess performance of the structure. These damage states are generally defined to identify transitions to modes of failure that either cause a significant increase in repair cost, or have the potential to compromise the gravity load-carrying ability of the structure. Limiting the former category of damage is often targeted for more frequent events, while the latter is mandated by building codes for rare events.

The studies conducted in Chapter 6 are focused primarily on steel braced frame construction. This was chosen because stiff structural systems are often utilized for isolated buildings to maximize the separation of the fixed base and isolated periods. Therefore, damage state limits assumed for the structural system will correspond in some fashion to those developed for steel braced frames.

A study by Kinali [2007] examined fragility functions for various steel frames in the central and eastern United States. For steel concentric X-braced frames, the performance levels and their associated drift limits considered in this study are summarized below in Table 7.3. These performance limits are adopted for the studies conducted here. These damage states are for a single class of braced frames, and may not represent all types of detailing and configurations. However, the limits can be incorporated in further analysis with the realization of their limitations. Clearly, other drift ratios and their estimated dispersions would be appropriate for other structural systems and detailing.

Table 7.3: Performance limits for X-braced steel (after Kinali [2007])

Damage State	Peak Interstory Drift Ratio (%)
IO: Immediate Occupancy	0.4
SD: Structural Damage	1.3
CP: Collapse Prevention	5.0

For isolated buildings, an important damage state is that of the peak isolator displacement exceeding the seismic gap provided by the surrounding moat. The moat size can be selected by the designer, and is therefore not a function of the isolation system used. However, in practical situations, the designer is encouraged by the owner and architect to limit the size of the moat because of architectural impact and cost considerations. Therefore, the minimum code provisions often dictate the final size of the moat. Using modern code provisions, the moat size must be greater than the expected isolator displacement (including the effects of real and accidental torsion) for the seismic event having a return period T_R = 2475 years. For simplicity, the same moat size (28 inches) is assumed for all isolation system considered in this study, since the penalty for excessive isolator displacement should be captured in the limit state vector. This limit is based on the 2475-year spectral displacement at 4 seconds, modified by a factor to account for 25% damping in the isolation system. For the results presented, this limit is only included to evaluate the ability of the various isolation systems

considered to limit the isolator displacement to a reasonable moat size. However, for simplicity of this conceptual demonstration, the effect of impact of the base of the structure against the moat wall has not been included in the estimates of story drifts, floor accelerations, and floor spectra accelerations, as would be required for an actual evaluation. Further consideration of the moat size and its role in probabilistic performance assessment is given in Section 7.4.3.

Given the discussions above, and recalling the definition of the random demand vector from Equation (7.30), the limit state vectors chosen are summarized below:

$$\overline{\mathbf{x}}^{F} = \begin{pmatrix} 0.4\% \\ 0.25g \\ 28" \\ 1.0g \end{pmatrix}, \quad \overline{\mathbf{x}}^{IO} = \begin{pmatrix} 0.8\% \\ 0.5g \\ 28" \\ 2.0g \end{pmatrix}, \quad \overline{\mathbf{x}}^{LS} = \begin{pmatrix} 1.5\% \\ 1.0g \\ 28" \\ 4.0g \end{pmatrix}, \quad \overline{\mathbf{x}}^{NC} = \begin{pmatrix} 5.0\% \\ 2.0g \\ 28" \\ 8.0g \end{pmatrix}$$

where F = Functional, IO = Immediate Occupancy, LS = Life Safety, and NC = Near Collapse. The definition of each damage state is qualitatively defined in Table 7.1. The PFSA limit is chosen as a constant multiplier of four applied to PFA. This is a result of typical anchorage forces computed as four times the floor acceleration. In practical applications, these values would be selected according to project-specific conditions.

7.3.4 Definition of Seismic Performance Classifications

A set of multiple-objective Seismic Performance Classifications (SPC) can be defined as an intersection of damage state nonexceedance events, shown in Equation (7.29). Table 7.4 describes the selected SPC designations, approximately following the definitions of Seismic Use Group in NEHRP 2003. SPC-I corresponds to the intended performance classification of a typical facility. SPC-II is an enhanced performance classification, and may be appropriate for buildings of vital importance to the economic viability of an organization. SPC-III is a safety-critical performance classification, and would be expected for facilities having emergency-response function such as acute-care hospitals, fire stations, and government agency headquarters. SPC-IV is the highest performance classification considered, and might be appropriate for facilities storing extremely hazardous materials, the release of which could lead to significant and widespread public health concerns.

Table 7.4: Definition of Seismic Performance Classifications as a function of required damage state limit following a seismic event of given return period

Seismic Event	T_R	SPC-I	SPC-II	SPC-III	SPC-IV
Frequent	72-yr	IO	F	F	F
Rare	475-yr	LS	IO	F	F
Very Rare	2475-yr	NC	LS	IO	F

T_R: Earthuake Return Period, SPC: Seismic Performance Classification
F: Functional, IO: Immediate Occupancy, LS: Life Safety, CP: Collpase Prevention

Given the procedure described to estimate the joint density function of the demand vector at a level of seismic hazard, and the definition of limit state vectors describing transition between damage states, it is possible to compare the isolated buildings studied in Chapter 6 within the context of performance assessment.

7.4 RELIABILITY ANALYSIS OF SEISMIC ISOLATION SYSTEMS

With a multiple-objective performance-based seismic assessment procedure defined, it is possible to evaluate a wide class of isolation systems as to their ability to satisfy specified complex performance objectives. The assessment is designed to address not only *if* a particular isolated building will satisfy a given SPC designation, but also the probability of exceeding this SPC designation. This is an important decision-making tool for engineers and building stakeholders in their selection of the appropriate set of isolation system parameters to economically achieve the desired building performance considering multiple levels of seismic hazard.

As described above, the analytical results of Chapter 6 form the basis for the probabilistic seismic demand analyses conducted in this section. These demands are combined with the limit state vectors developed in the previous section to identify damage states in the three seismic hazard levels considered in Chapter 6: 72-year, 475-year, and 2475-year. First, trends for each EDP as a function of seismic hazard are identified for all isolation systems considered. This identifies sensitivities that exist between EDPs and isolation system parameters. These EDPs are then compared to deterministic limits assumed for each damage state. The probabilistic description of the vector of EDPs is combined with

the damage state limits to estimate the probability of achieving a series of Seismic Performance Classifications, defined in Section 7.3.4. Conclusions are drawn as to isolation systems and parameters capable of achieving enhanced SPC designations.

7.4.1 Probabilistic Seismic Hazard Analysis

The first step towards assessing the seismic demands on a structural system is the development of probabilistic estimates of the expected ground motions at a site. The process of developing these estimates is broadly defined as Probabilistic Seismic Hazard Analysis (PSHA). The background of PSHA is described by Kramer [1996] and is based on the work of Cornell [1968] and others. In performing a PSHA for a particular site, an inventory is taken of all faults, their potential moment magnitude (M_w) and their distance (R) to the site under investigation. Then, using recurrence relationships for each fault, the mean rate (in events/year) of earthquakes having a moment magnitude exceeding some threshold is computed. Given some magnitude and distance, a median measure of seismic intensity (such as spectral acceleration at some natural vibration frequency), and its dispersion can be estimated from attenuation models of the form $S = \mathcal{F}\left(M_w, R\right)$. Assuming all possible earthquake magnitudes and distances and their probabilistic distributions, a probability of exceeding a threshold seismic intensity is computed. Finally, given the recurrence relationships of earthquake arrivals for each fault, total probability theory can be applied to find the chance of a seismic intensity exceeding a threshold value in a time period of one year. This is known as the mean annual frequency (MAF) of exceedance, or the hazard rate, and if we define some random spectral acceleration *S,* the MAF can be mathematically defined as

$$\nu_S(\bar{s}) = P\left[S > \bar{s} \,\middle|\, T = 1\ \text{yr}\right] \tag{7.31}$$

The larger the threshold intensity $\bar{s}$, the lower the probability of exceeding $\bar{s}$ in a one-year period. For this reason, $\nu_S(\bar{s})$ is always a monotonically decreasing function. It has been suggested [Cornell, 1996] that $\nu_S(\bar{s})$ may be approximated by the function $\nu_S(\bar{s}) = a\bar{s}^{-b}$, which is linear in log-log space. In the case of this form, knowing the median spectral acceleration at two mean annual frequencies is sufficient to completely describe the hazard curve. This form is generally a good approximation for closely spaced values of ν; however,

the shape of the hazard curve is of little importance since our methodology is concerned with discrete mean annual frequencies.

The SAC ensemble of ground motions has been developed considering three return periods: 72 years, 475 years, and 2475 years. The return period is defined as the average waiting time between event arrivals. If events are assumed to be described by a Poisson process with constant arrival intensity over time, then the return period T_R is simply the reciprocal of the mean annual frequency ν. This is obvious considering that ν is defined as "mean events per year" and T_R is defined as "mean years per event." As a result, the three MAFs for which the SAC ensemble is developed are (from most frequent to rarest): 0.0139 events/year, 0.00211 events/year, and 0.000404 events/year. Taking the median values of spectral acceleration, $\overline{s}$, at three frequencies for each of the three ensembles, three points can be plotted on the general hazard curve $\nu_S(\overline{s})$. These points are plotted below in Figure 7.2. Also included is the general hazard curve for each frequency considering the form $\nu_S(\overline{s}) = a\overline{s}^b$. The general form was found by taking the natural logarithm of both sides of the equation, then applying linear least-squares regression using three output observations and three factor levels. These seismic hazard curves are provided for reference, since generally these relationships can be estimated for a site. For the study presented here, the ground motions have been developed for three distinct hazard levels; hence the continuous hazard function is not used.

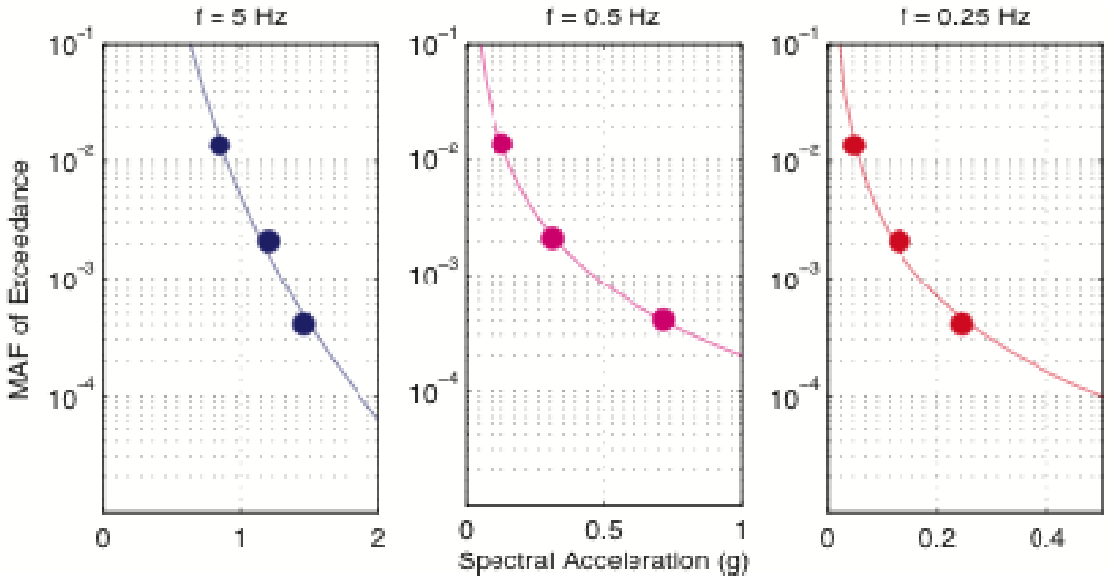

Figure 7.2: Median probabilistic ground-motion hazard curves based on SAC ensemble, for f= 5 Hz, f= 0.5 Hz, f= 0.25 Hz

7.4.2 Probabilistic Seismic Demand Analysis

With a probabilistic description of the seismic hazard at the site defined, it is possible to develop a probabilistic description of any number of demand parameters of interest. Previously, we described the collection of these demands as the random vector **X**, and assumed this vector is characterized by a joint lognormal distribution whose parameters can be estimated by observed data. The response data presented for three- and nine-story isolated buildings in Chapter 6 of this report is used for parameter estimation, which includes a mean vector $\hat{\Lambda}$ and covariance matrix $\hat{\Psi}$ for each of the three levels of seismic hazard considered.

In presenting median demand hazard, a general form is assumed and fitted to the observed data. A function to describe central tendency of structural response as a function of ground-motion intensity has been proposed by Miranda and Aslani [2003], and is of the form

$$\hat{x}_j = \alpha_1 \alpha_2^{\nu} \nu^{\alpha_3} \tag{7.32}$$

Where $\hat{x}_j$ is the median of the jth observed response parameter, ν is the intensity measure (which in this case has been extended to be the mean annual frequency of exceedance) and α_1 through α_3 are parameters to be estimated. Given the form of Equation (7.32), it is possible to estimate the parameters by taking the logarithm of both sides, giving

$$\ln \hat{x}_j = \ln \alpha_1 + \ln \alpha_2 \nu + \alpha_3 \ln \nu \tag{7.33}$$

By simple substitution of alternate parameters, this becomes

$$\hat{y} = \beta_1 + \beta_2 \nu + \beta_3 \ln \nu \tag{7.34}$$

The form of Equation (7.34) can be solved by linear least-squares regression where the basis functions are $\{1, \nu, \ln \nu\}$. Since these basis functions are linearly independent and span the space of dimension equal to the number of observations, the space is identifiable and the parameters β_1 through β_3 may be estimated. Finally, applying the relation $\alpha_{1,2} = e^{\beta_{1,2}}$ yields a complete expression for the median structural response described in Equation (7.32).

Figure 7.3 through Figure 7.8 present the median demand hazard curves for both three- and nine-story buildings on linear viscous (LV), bilinear hysteretic (BL), and triple pendulum (TP) isolation systems. Each plot is for a particular isolation system class. The solid squares indicate computed median EDPs from response history analysis using the SAC ensemble of ground motions, 20 records at each of the three MAF of exceedance. The solid line interpolating the data points are the regression lines fitting Equation (7.32) above. While the shape of this line does not always follow the expected shape (since it may not always be one-to-one), the curvature is interesting because it indicates the sensitivity of the response to the MAF. That is, a regression curve that is concave-left indicates a response that is insensitive to its MAF relative to a regression curve that is concave-right. As the regression curve becomes nearly vertical, the response approaches the characteristic response in which the peak observed over some time interval is independent of the duration of that interval (and so is intensity of seismic input). This is important only because the limit state vector does not display this type of behavior, an indication that eliciting response that is *sensitive* to its MAF is an efficient strategy to satisfy the limit state vector. This is discussed further with respect to individual cases.

Figure 7.3 presents median demand hazard curves for the three-story building on linear viscous isolation systems. These data are useful in that they form an estimate of EDPs for a linear system to which "equivalent" nonlinear systems may be easily compared. From these data, the isolator displacements and PFSA are sensitive to both period and damping. Interestingly, the PIDR shows little sensitivity to either period or damping for the cases considered. Additionally, the PFA appears to be sensitive only to period, but not damping.

These observations should be considered when evaluating the behavior of subsequent nonlinear isolation systems.

Figure 7.4 presents demand data for the three-story building on bilinear hysteretic isolation systems. The isolator displacement demands show similar trends to those for the LV system, in that isolator displacement decreases with decreased period and increased damping. However, all superstructural demand parameters show significant sensitivity to isolator period and damping characteristics. While drift demands under the 72- and 475-year seismic events show noticeable sensitivity to damping, they are relatively insensitive to the isolation period. However, under the 2475-year seismic event, drifts are sensitive to both period and damping. Floor accelerations, however, are sensitive to both period and damping at all levels of seismic hazard. Bilinear isolation systems with low damping display "concave-right" behavior, that is, the PFA tends to be sensitive to the level of seismic hazard. Systems with high damping, however, exhibit PFA demands that vary less significantly with seismic hazard, particularly for the lower period isolation system. However, for all BL isolation systems, PFSA demands appear to be approximately proportional to the MAF in linear-log space. One interesting observation is that, while the BL-3-10 and BL-4-25 systems exhibit nearly equivalent isolator displacements over all ranges of seismic hazard, PIDR demands are significantly lower and PFA demands are slightly lower for the BL-3-10 isolation system in the 72-year and 475-year seismic events compared to the BL-4-25 system.

Figure 7.5 presents demand data for the three-story building on triple pendulum isolation systems. The isolator displacement demands also show similar trends to those for the LV system, in that isolator displacement decreases with decreased period and increased damping. However, all superstructural demand parameters show similar shapes and sensitivities to isolator period and damping characteristics as the BL systems described above. However, while the BL-3-10 and BL-4-25 systems also exhibit nearly equivalent isolator displacements over all ranges of seismic hazard, PIDR demands are also similar for these two systems, and PFA demands are nearly equal for the 72- and 475-year events.

Figure 7.6 though Figure 7.8 present median demand hazard curves for the nine-story building on a linear viscous, bilinear hysteretic, and triple pendulum isolation systems, respectively. The general trends remain remarkably consistent between the three- and nine-story buildings for all cases. In general, the magnitude of all demand parameters is greater for the 9-story

To draw clear comparisons between isolation systems, it is useful to present median demand hazard curves at fixed damping parameters. Figure 7.9 through Figure 7.12 also present the median demand hazard curves for the three-story buildings on linear viscous, bilinear hysteretic, and triple pendulum isolation systems. However, each plot is for a particular isolation system effective stiffness and damping. In this way, conclusions may be drawn about the relative performance of equivalent classes of isolation systems.

Figure 7.9 presents median demand hazard curves for the three-story building on all short-period, low-damping isolation systems (T_{eff} = 3 sec, ζ_{eq} = 10%) considered in this study. Examination of these data reveals that the isolator displacement under the 2475-year event is approximately equal for all isolation systems, resulting is an equal isolation gap (or moat size). This is an expected result from targeting equivalent period and damping at the linear viscous isolator displacement. This criterion of "equal moat size" establishes equivalence of various isolation systems in these studies. Despite this equivalence there are clear differences in superstructural response for the systems investigated. Whereas the LV and TP systems show nearly equal median PIDR and PFA response for the 475- and 2475-year seismic events, the BL system shows significant amplification relative to LV and TP systems. For the 72-year event, the increase in PIDR and PFA is more significant relative to LV and TP systems. This is an indication that the BL isolation system is not activated under moderate levels of ground motion. This amplification is also clear from the PFSA demands, where the BL system clearly displays "concave right" behavior, or demand that is not sensitive to the intensity in seismic input.

Figure 7.10 presents median demand hazard curves for the three-story building on all short-period, high-damping isolation systems (T_{eff} = 3 sec, ζ_{eq} = 25%) considered in this study. As before, the isolator displacement under the 2475-year event is approximately equal for all isolation systems, establishing general equivalence. For the high-damping system, the LV and TP systems do not exhibit close agreement for PIDR and PFA except for the 2475-year event. For other cases, the TP system demands exceed the LV system demands. In all cases, the BL system demands exceed those of both the LV and TP systems.

Figure 7.11 presents median demand hazard curves for the three-story building on all long-period, low-damping isolation systems (T_{eff} = 4 sec, ζ_{eq} = 10%) considered in this study. Expectedly, the isolator displacement under the 2475-year event is approximately equal for all isolation systems. Contrary to data observed for the short-period systems, the TP system

shows lower PFA and PIDR demand compared to the LV system. However, the PFSA demand is approximately equal for all levels of seismic input for both LV and TP systems. As before, the observed BL system demands exceed all those of both the LV and TP systems for all superstructure demands considered.

Figure 7.12 presents median demand hazard curves for the three-story building on all long-period, high-damping isolation systems (T_{eff} = 4 sec, ζ_{eq} = 25%) considered in this study. As before, the isolator displacement under the 2475-year event is approximately equal for all isolation systems. There is a light increase in all TP system demands compared to the equivalent LV system. However, the BL system exhibits significant increase in all superstructure demands when compared with both the LV and TP systems.

Figure 7.13 through Figure 7.16 also present the median demand hazard curves for the nine-story buildings on linear viscous, bilinear hysteretic, and triple pendulum isolation systems for a particular isolation system's effective stiffness and damping. The conclusions regarding the comparative demands of LV, BL, and TP isolation system remain unchanged from those reached for the three-story isolated building described above. This reinforces the earlier observation that the flexibility of the superstructure does not appear to affect the general conclusions regarding comparative performance of the isolation systems investigated herein.

These data have compared median demand hazard curves across various types of isolation systems. However, the dispersion in these demand estimates has not yet been considered, nor has the joint probability of meeting a target complex performance objective been computed and compared. This analysis is the subject of the section that follows.

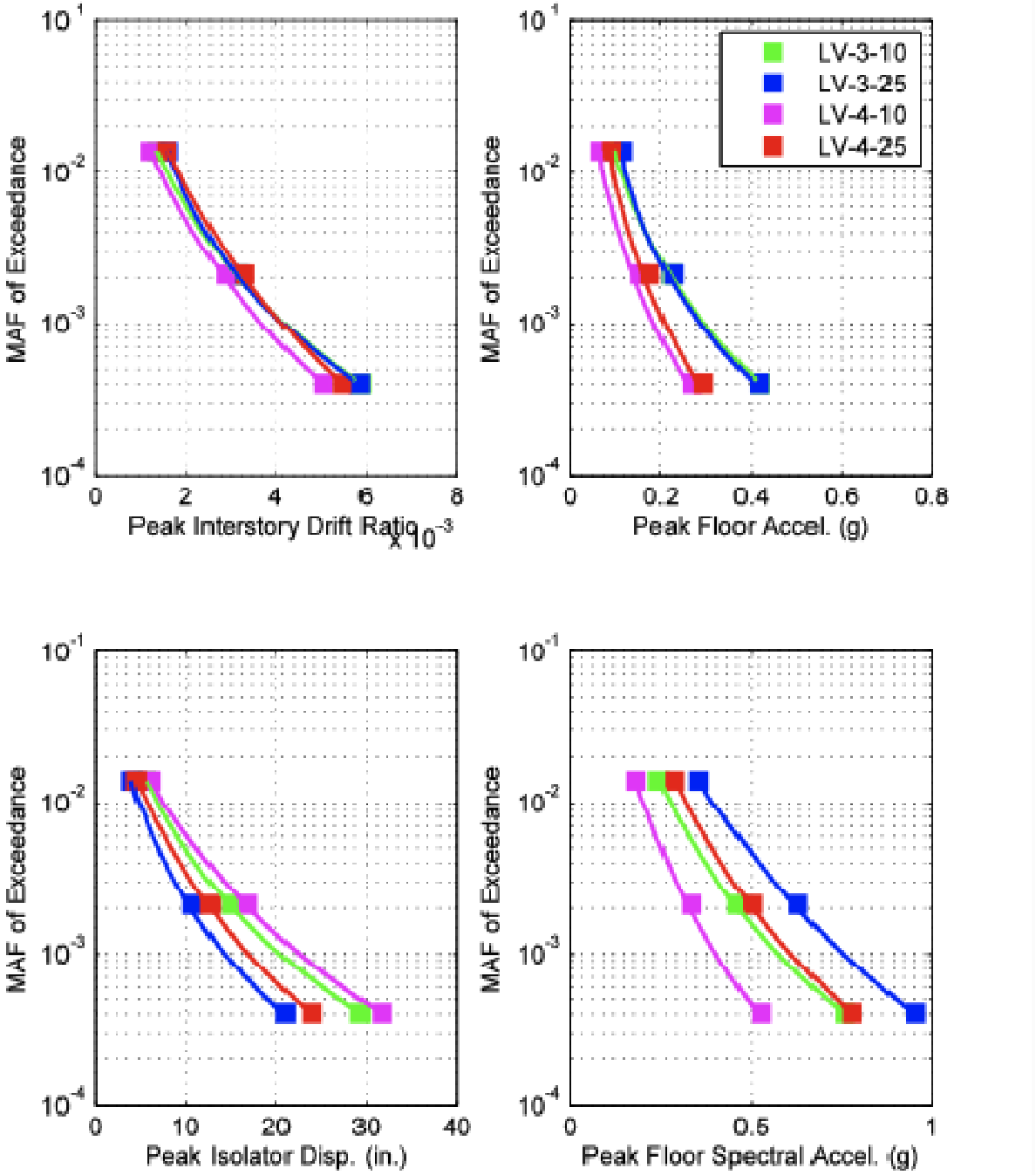

Figure 7.3: Comparison of median demand hazard curves for 3-story building on linear viscous isolation systems

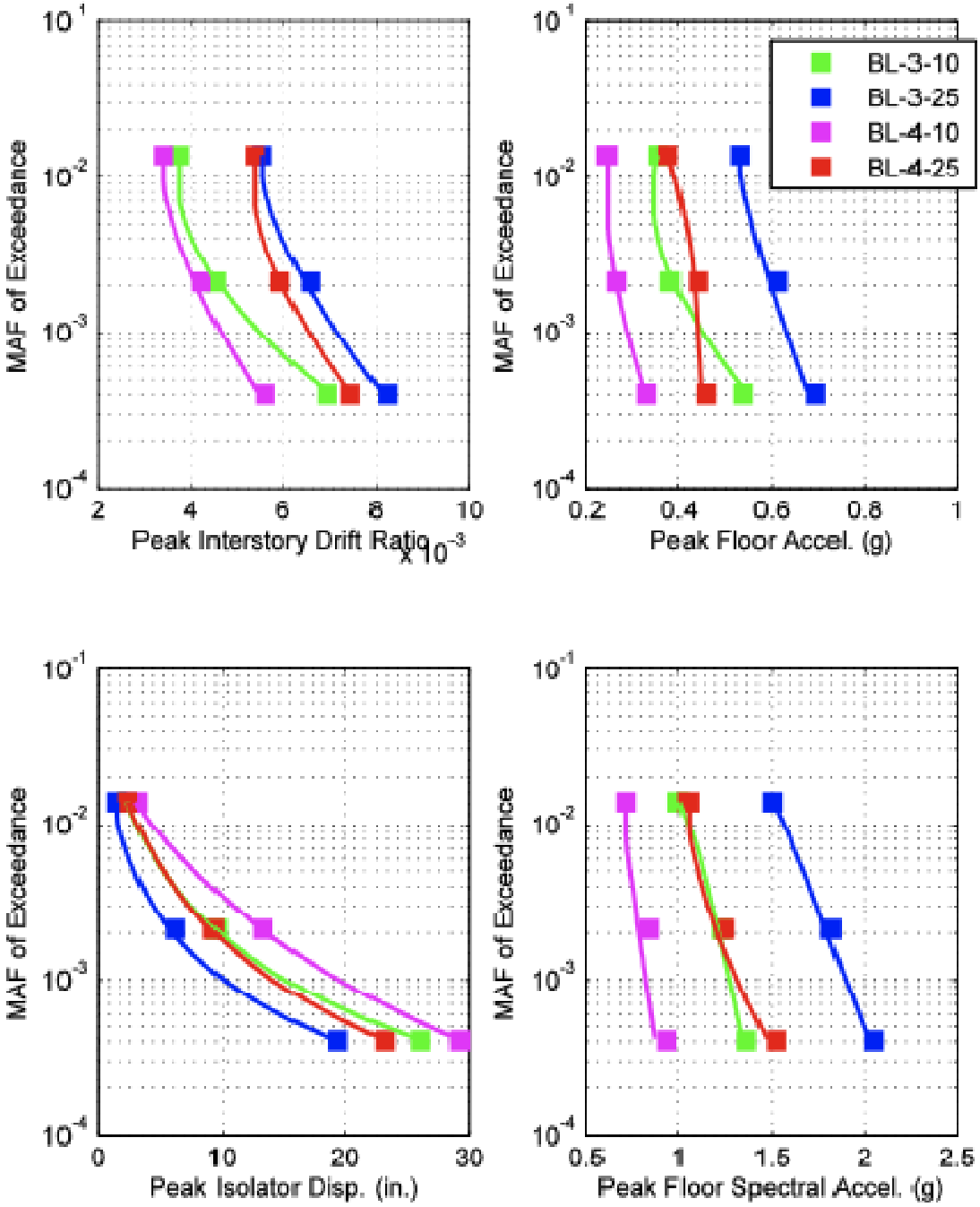

Figure 7.4: Comparison of median demand hazard curves for 3-story building on bilinear hysteretic isolation systems

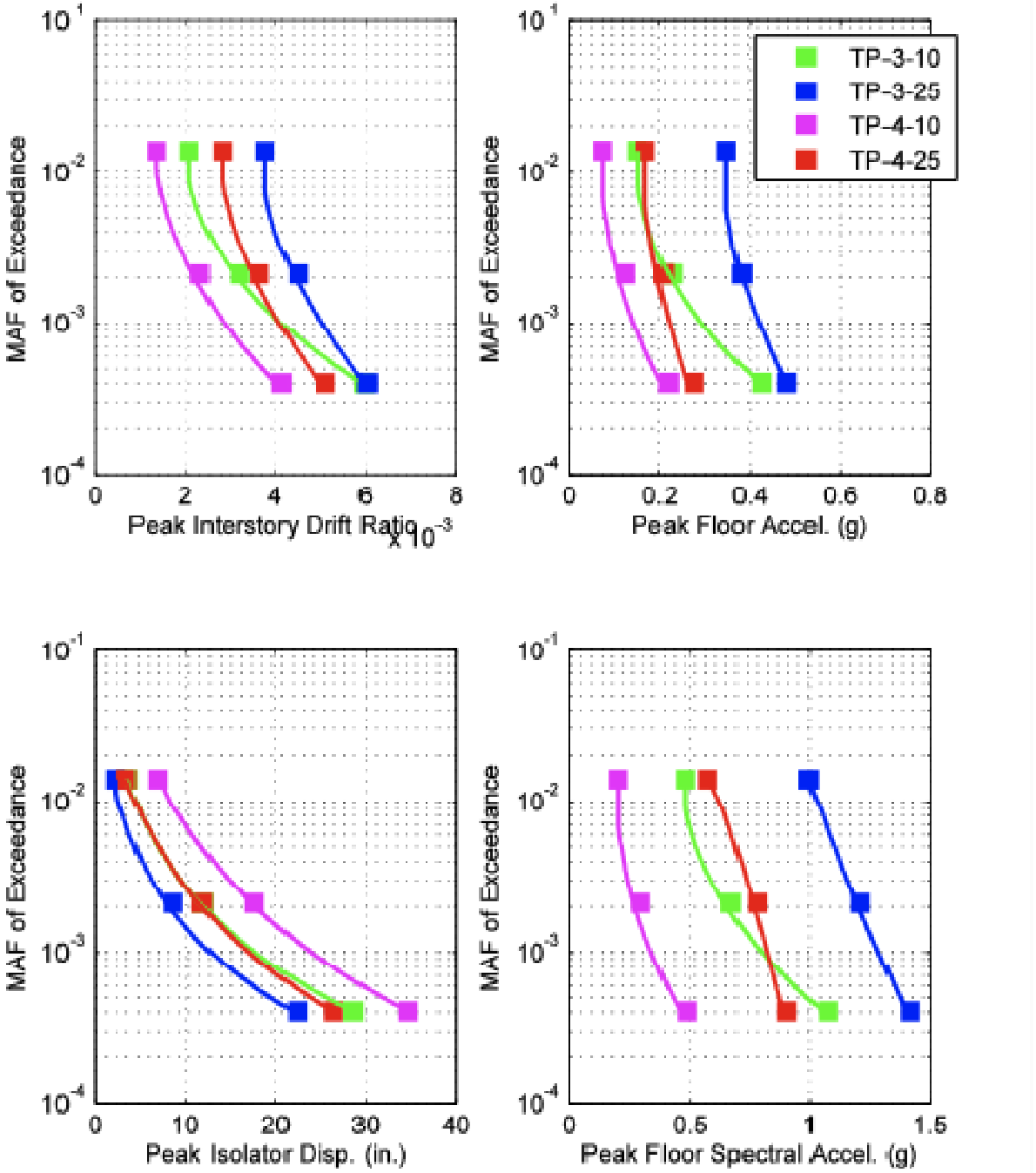

Figure 7.5: Comparison of median demand hazard curves for 3-story building on triple pendulum isolation systems

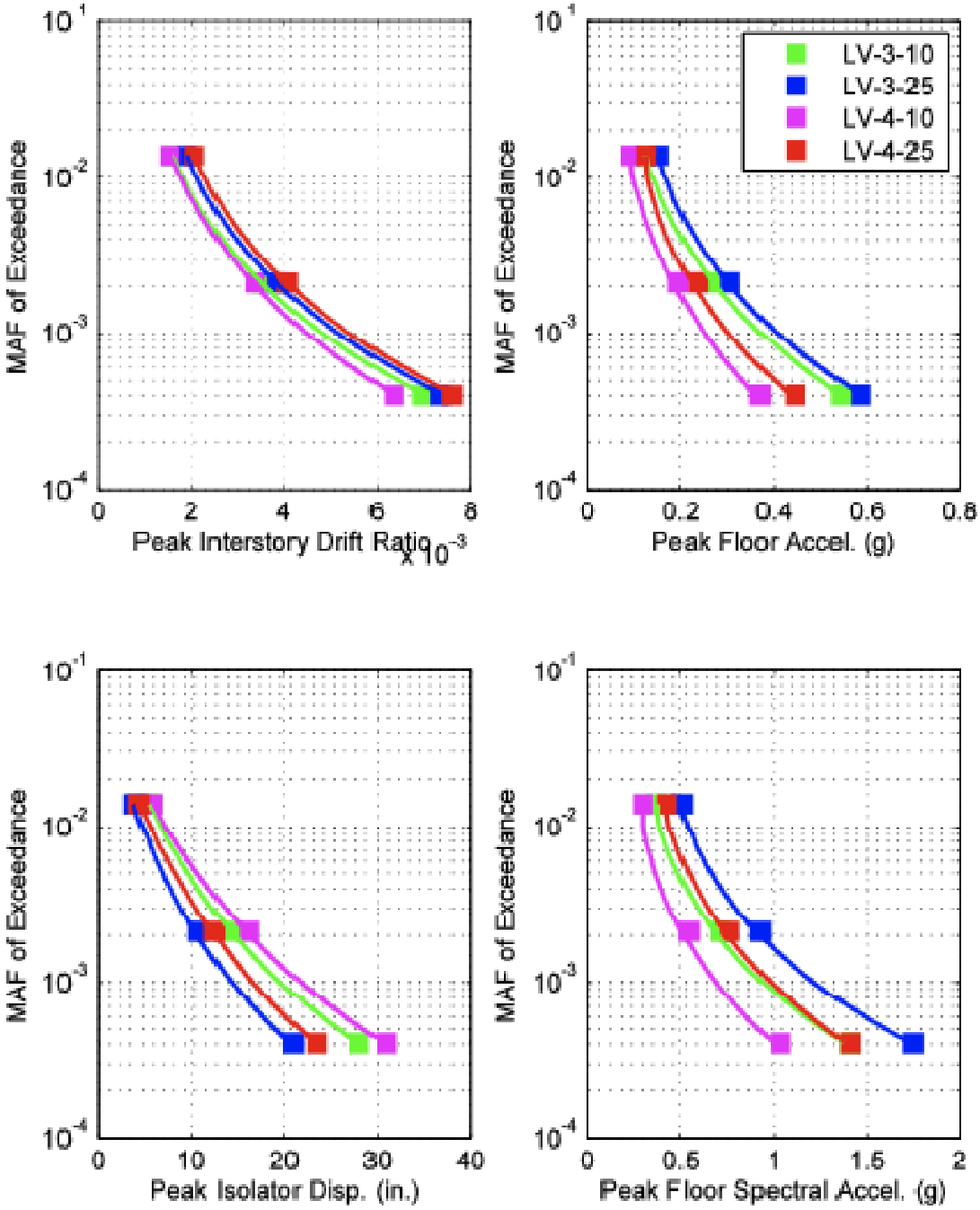

Figure 7.6: Comparison of median demand hazard curves for 9-story building on linear viscous isolation systems

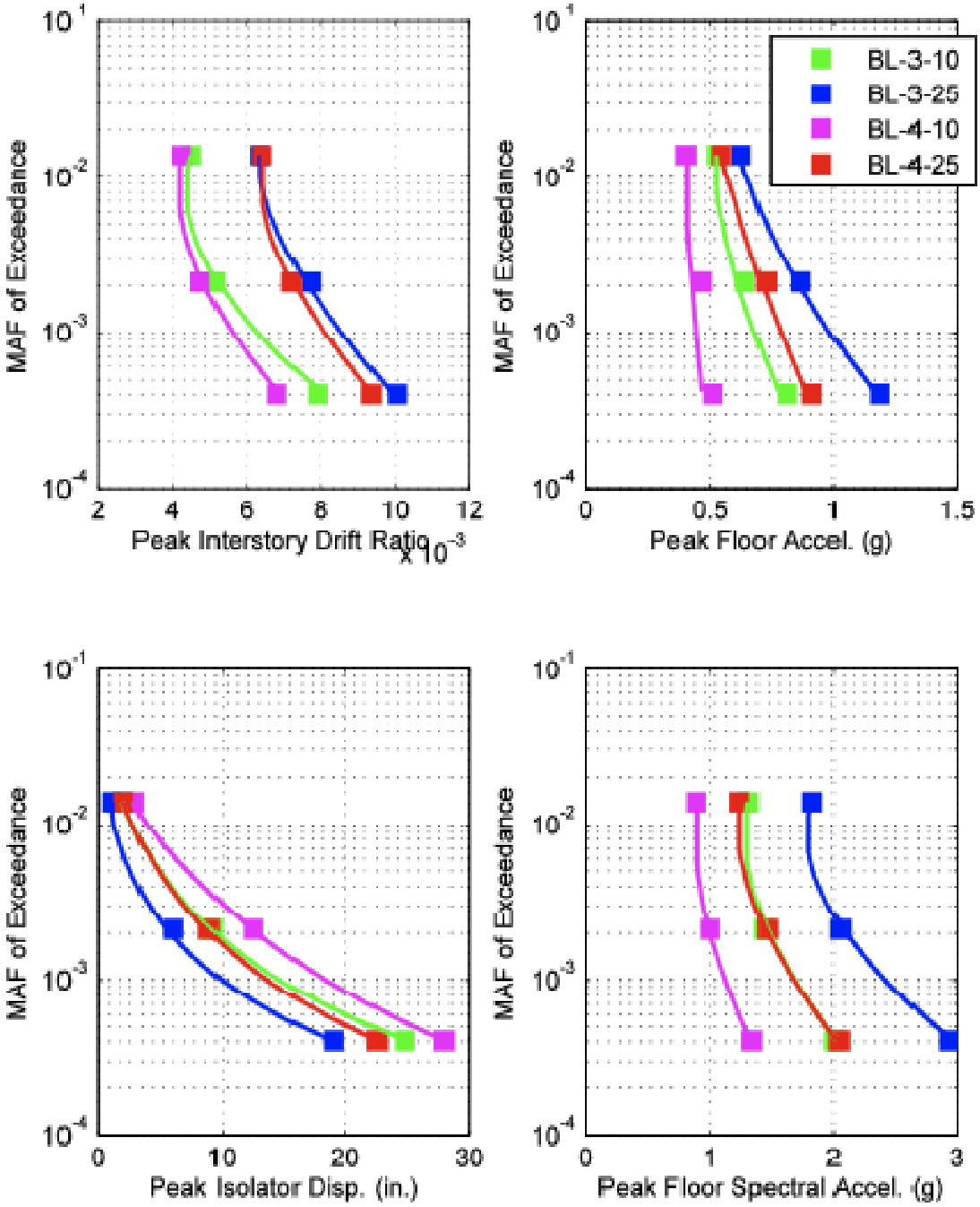

Figure 7.7: Comparison of median demand hazard curves for 9-story building on bilinear hysteretic isolation systems

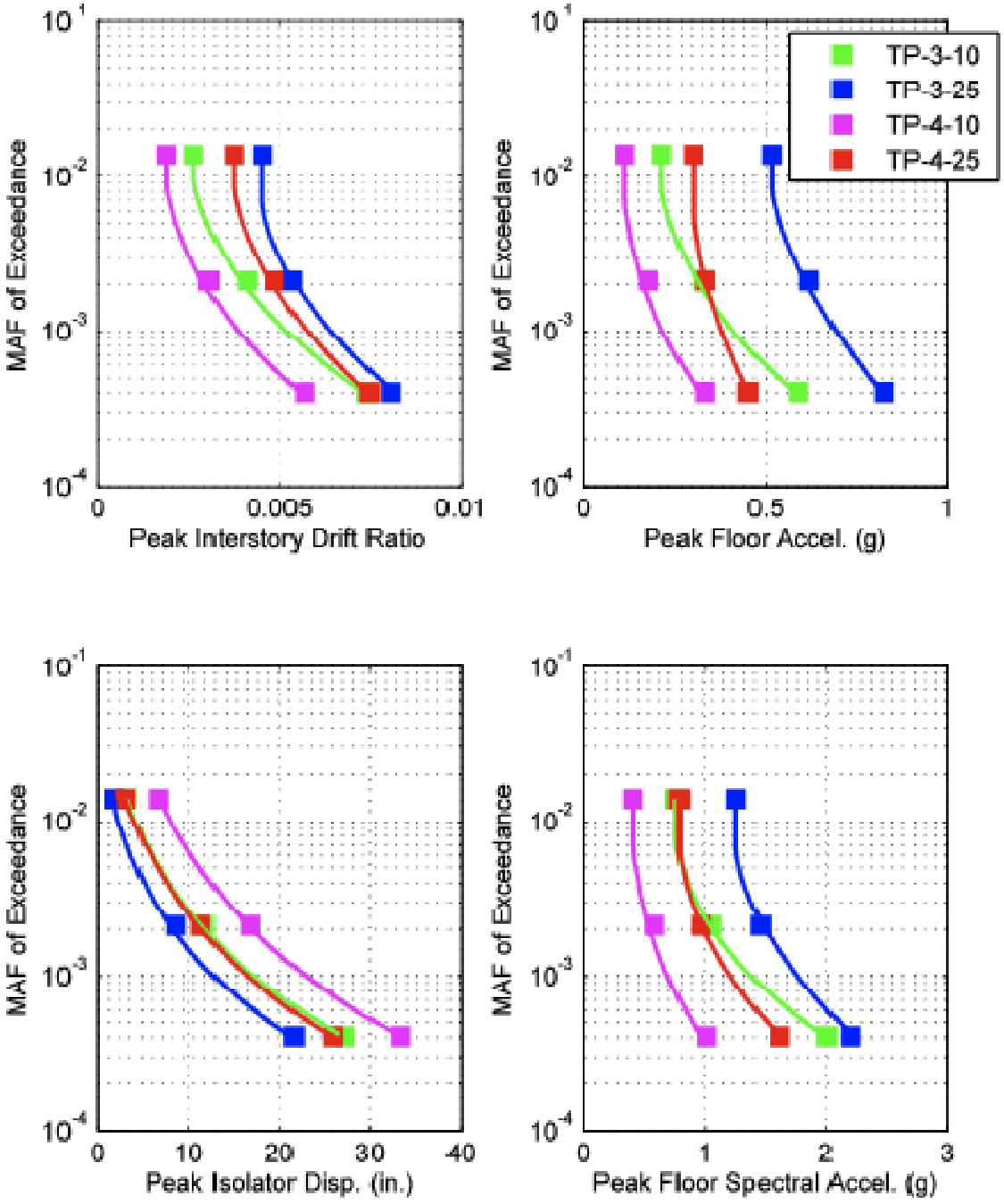

Figure 7.8: Comparison of median demand hazard curves for 3-story building on triple pendulum isolation systems

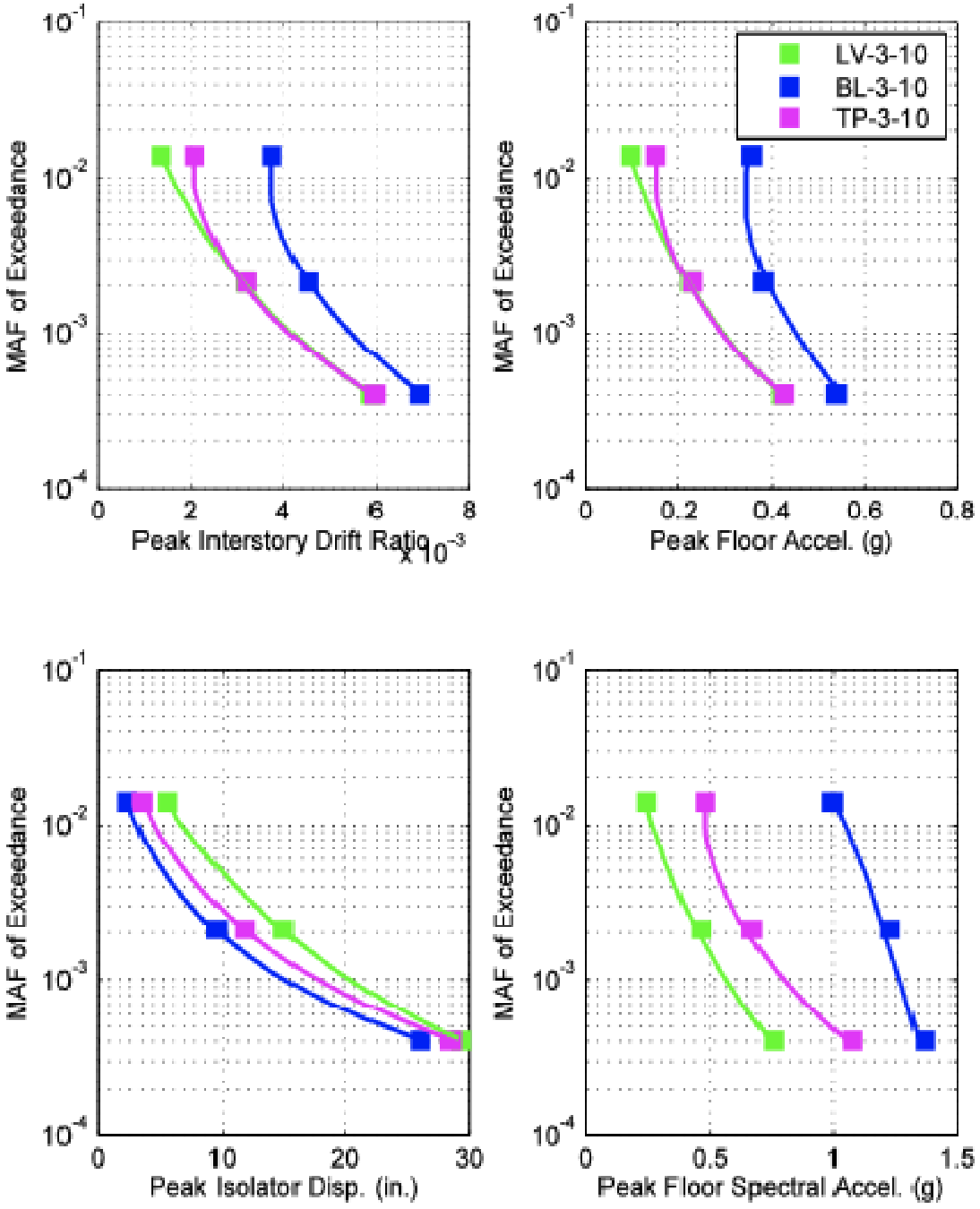

Figure 7.9: Comparison of median demand hazard curves for 3-story building on isolation systems with T_{eff} = 3 sec, ζ_{eq} = 10%

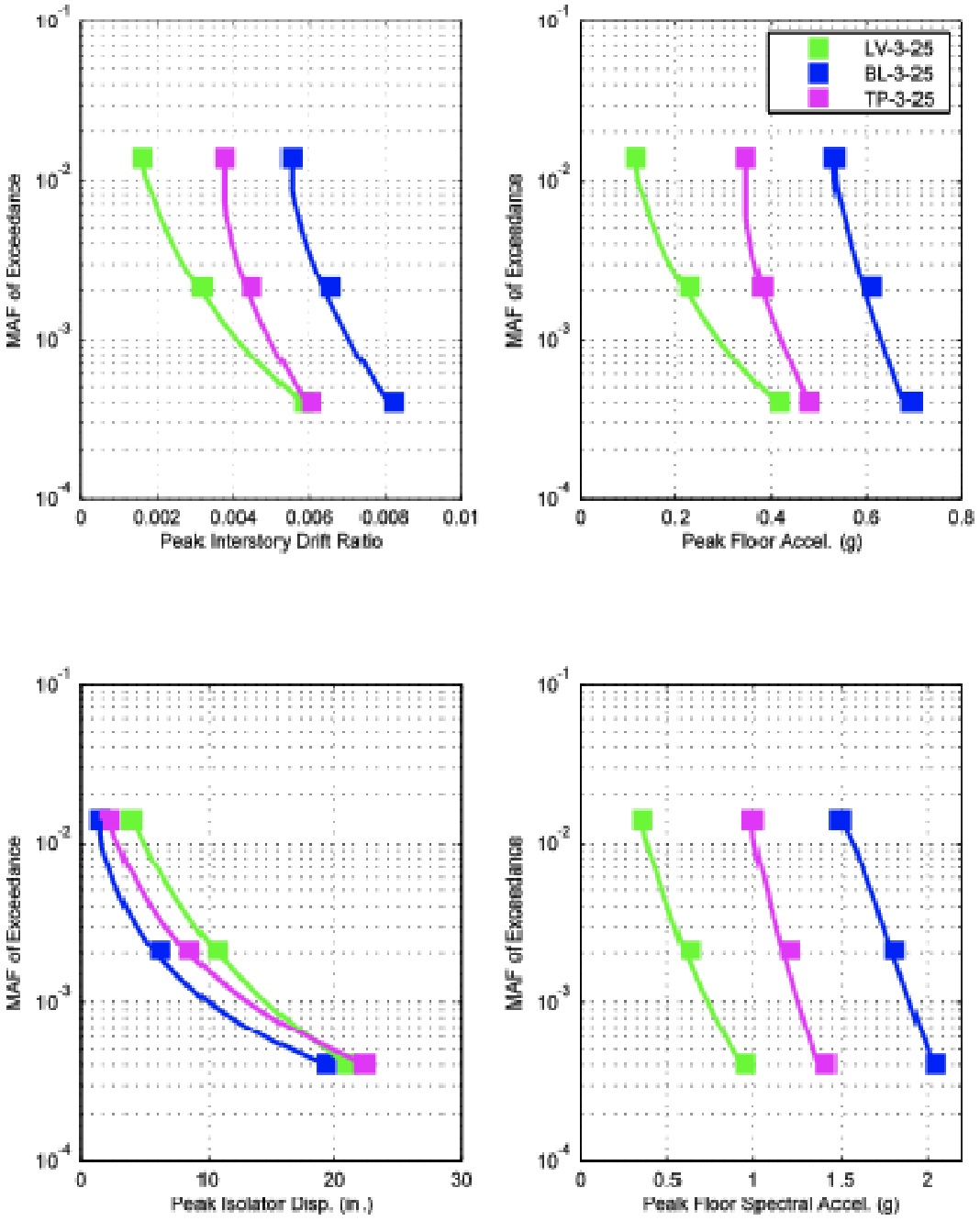

Figure 7.10: Comparison of median demand hazard curves for 3-story building on isolation systems with T_{eff} = 3 sec, ζ_{eq} = 25%

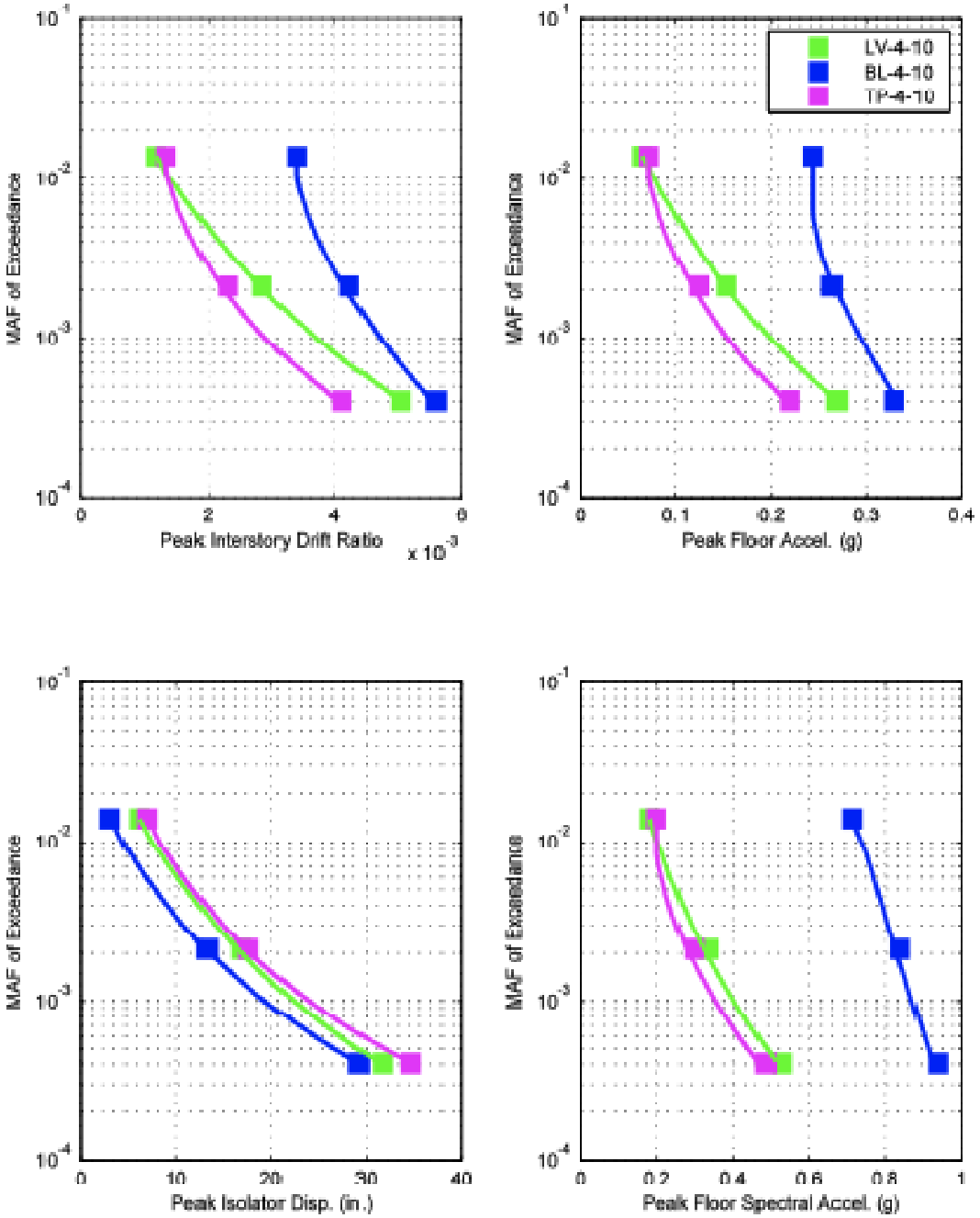

Figure 7.11: Comparison of median demand hazard curves for 3-story building on isolation systems with T_{eff} = 4 sec, ζ_{eq} = 10%

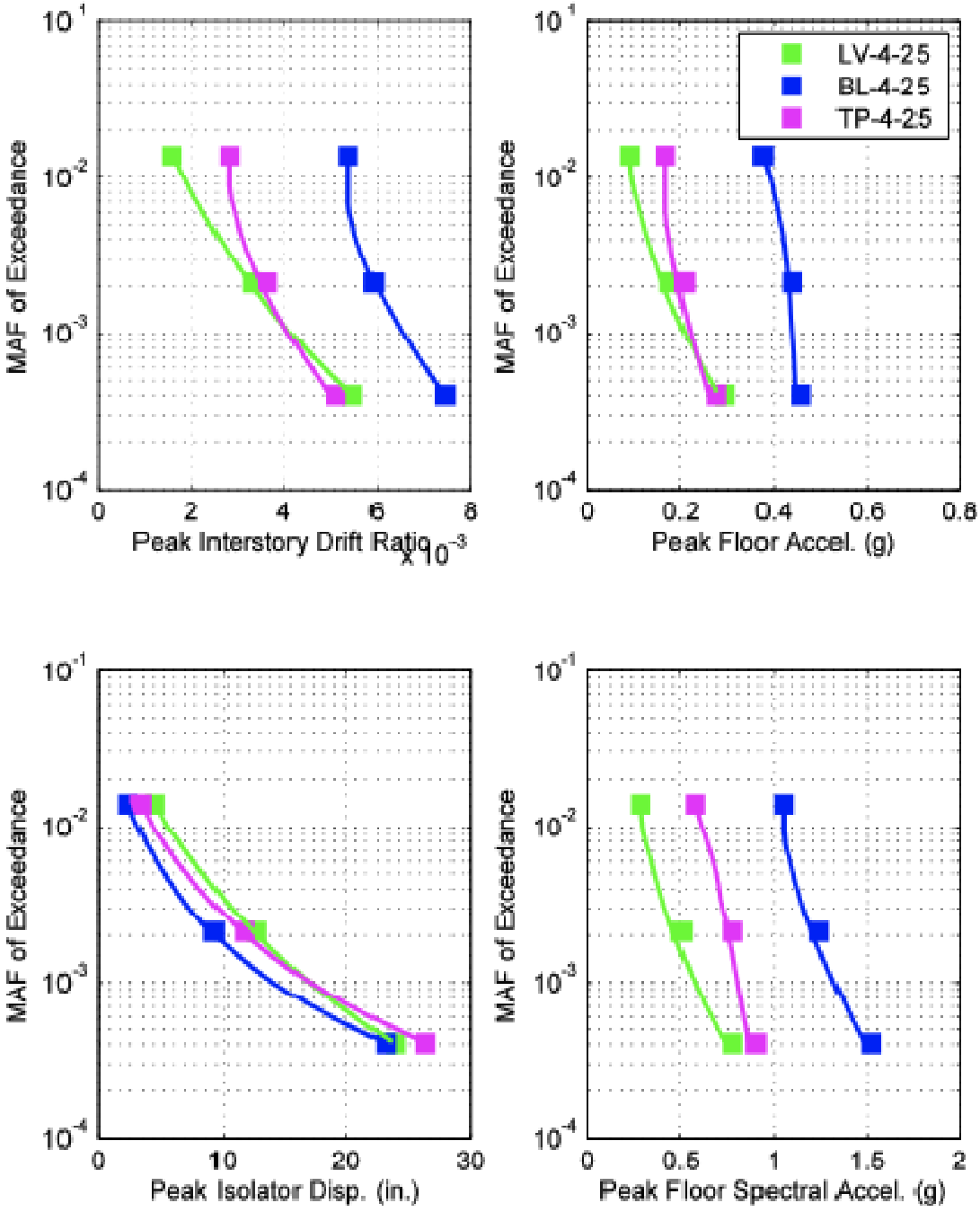

Figure 7.12: Comparison of median demand hazard curves for 3-story building on isolation systems with T_{eff} = 4 sec, ζ_{eq} = 25%

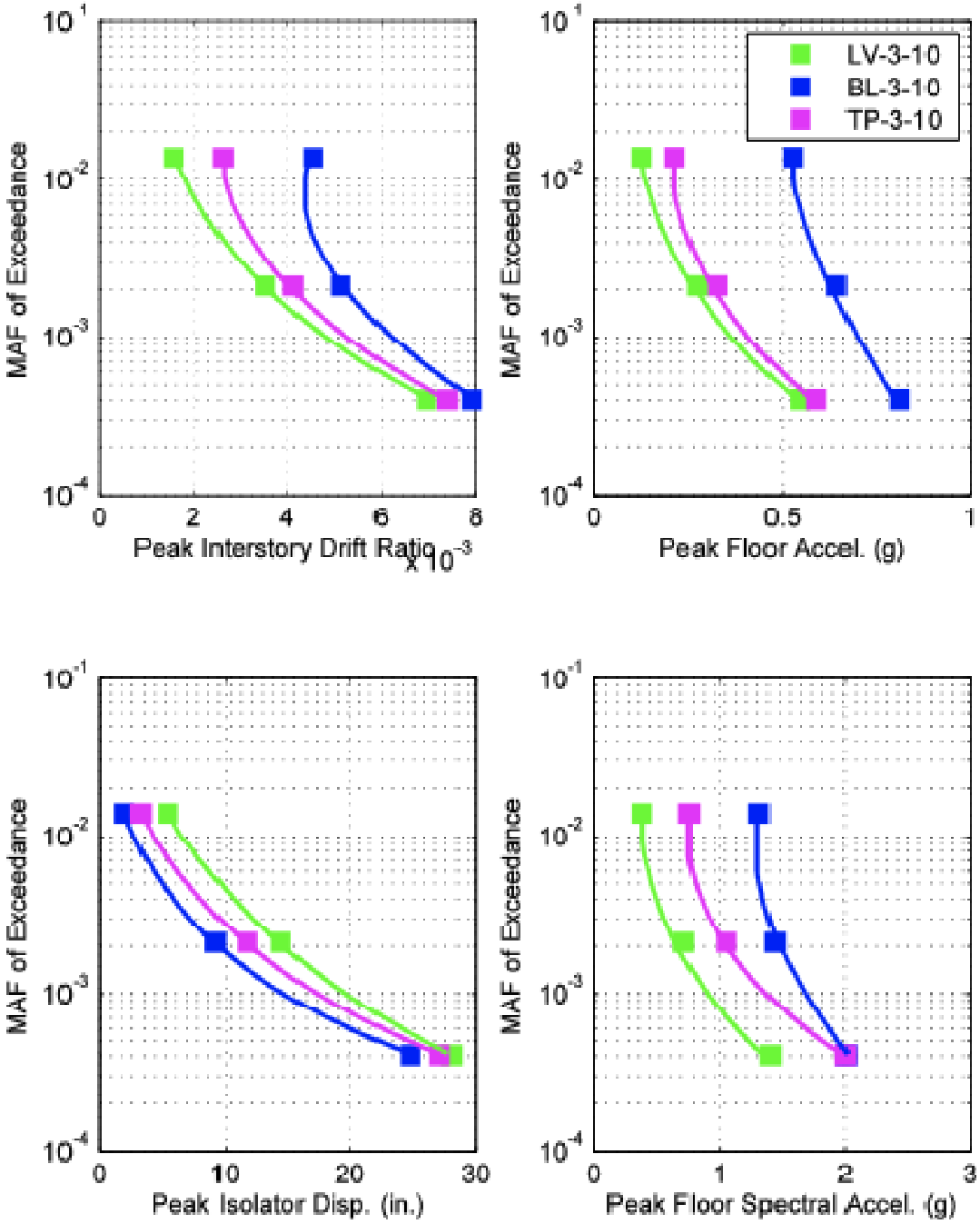

Figure 7.13: Comparison of median demand hazard curves for 9-story building on isolation systems with T_{eff} = 3 sec, ζ_{eq} = 10%

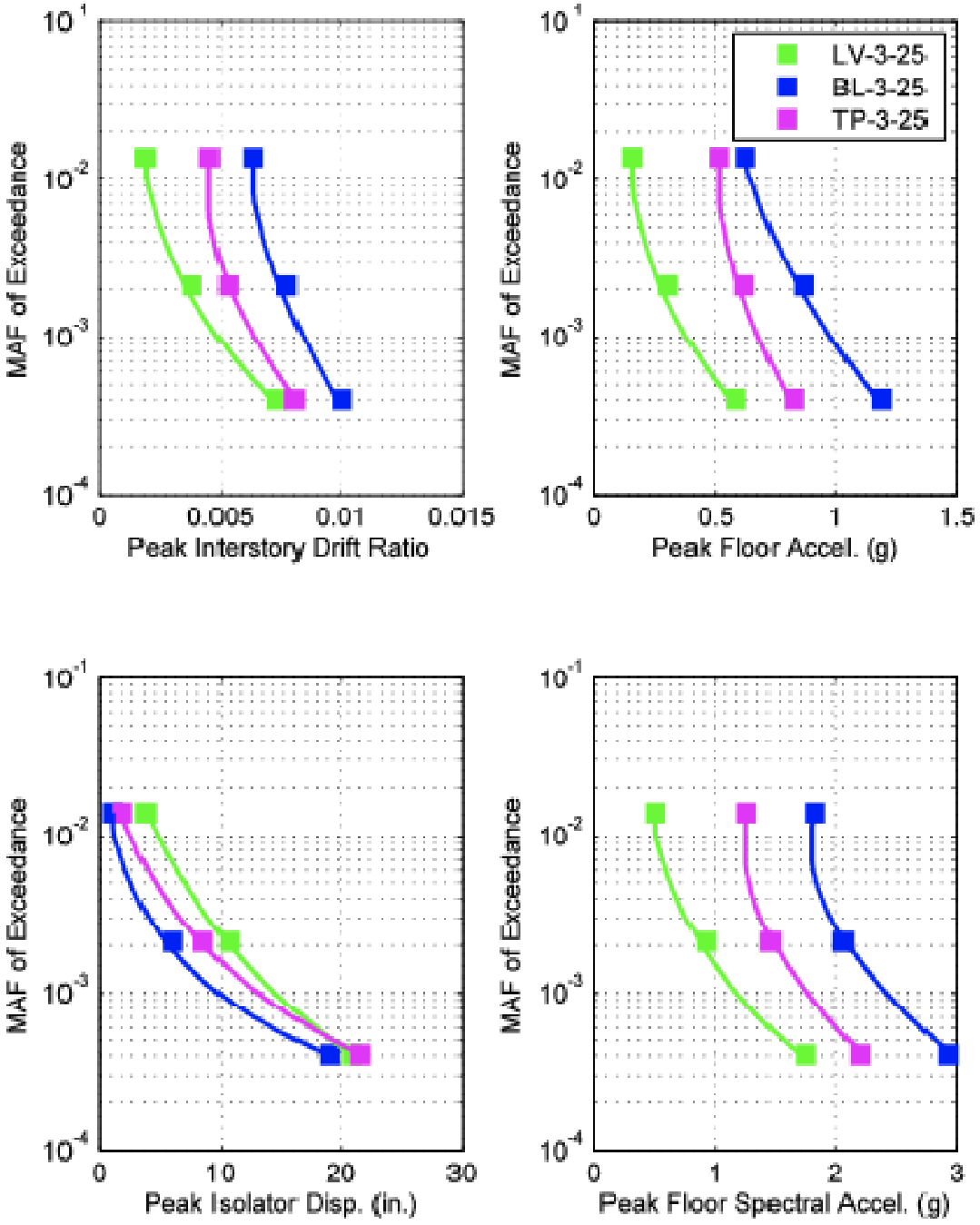

Figure 7.14: Comparison of median demand hazard curves for 9-story building on isolation systems with T_{eff} = 3 sec, ζ_{eq} = 25%

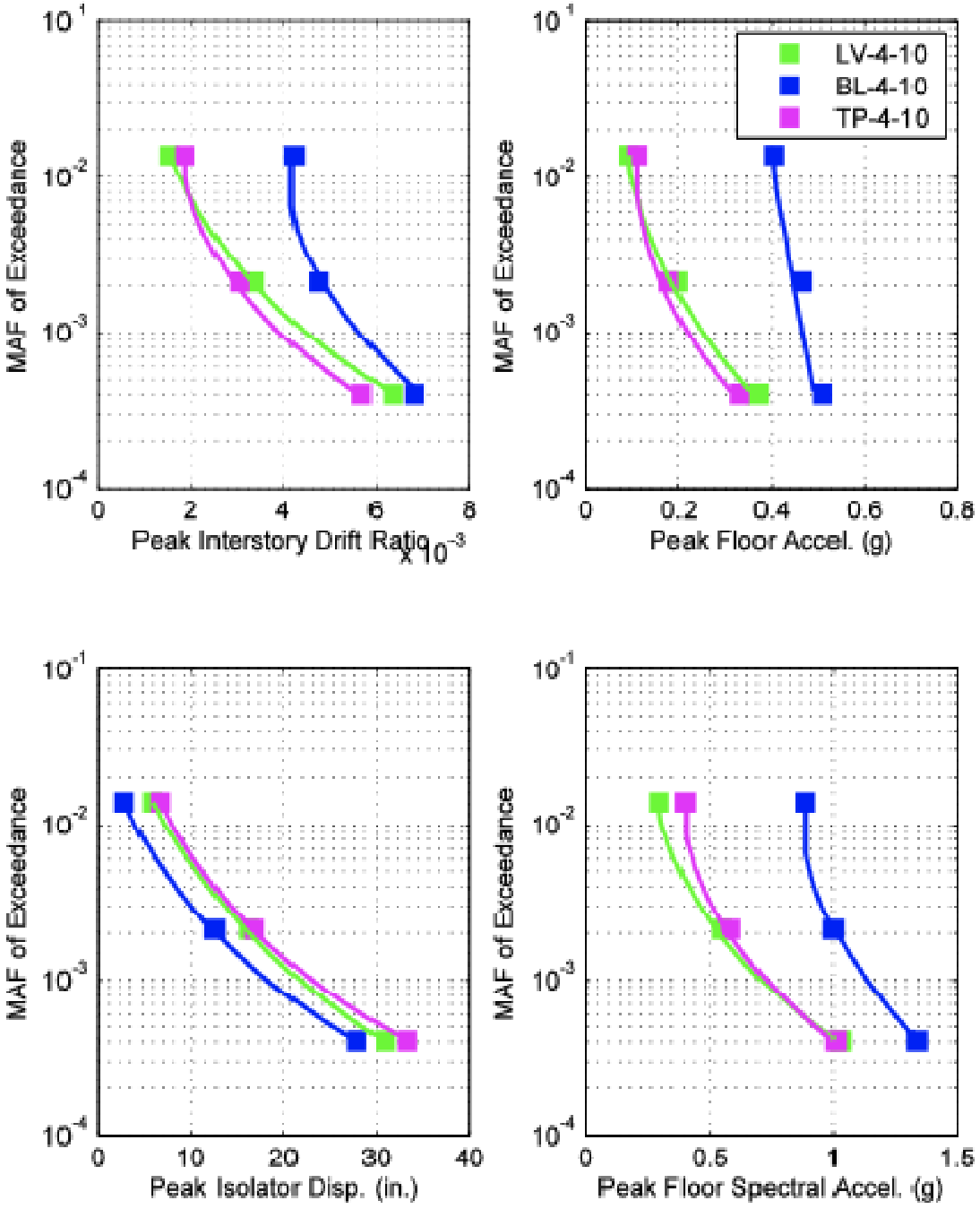

Figure 7.15: Comparison of median demand hazard curves for 9-story building on isolation systems with T_{eff} = 4 sec, ζ_{eq} = 10%

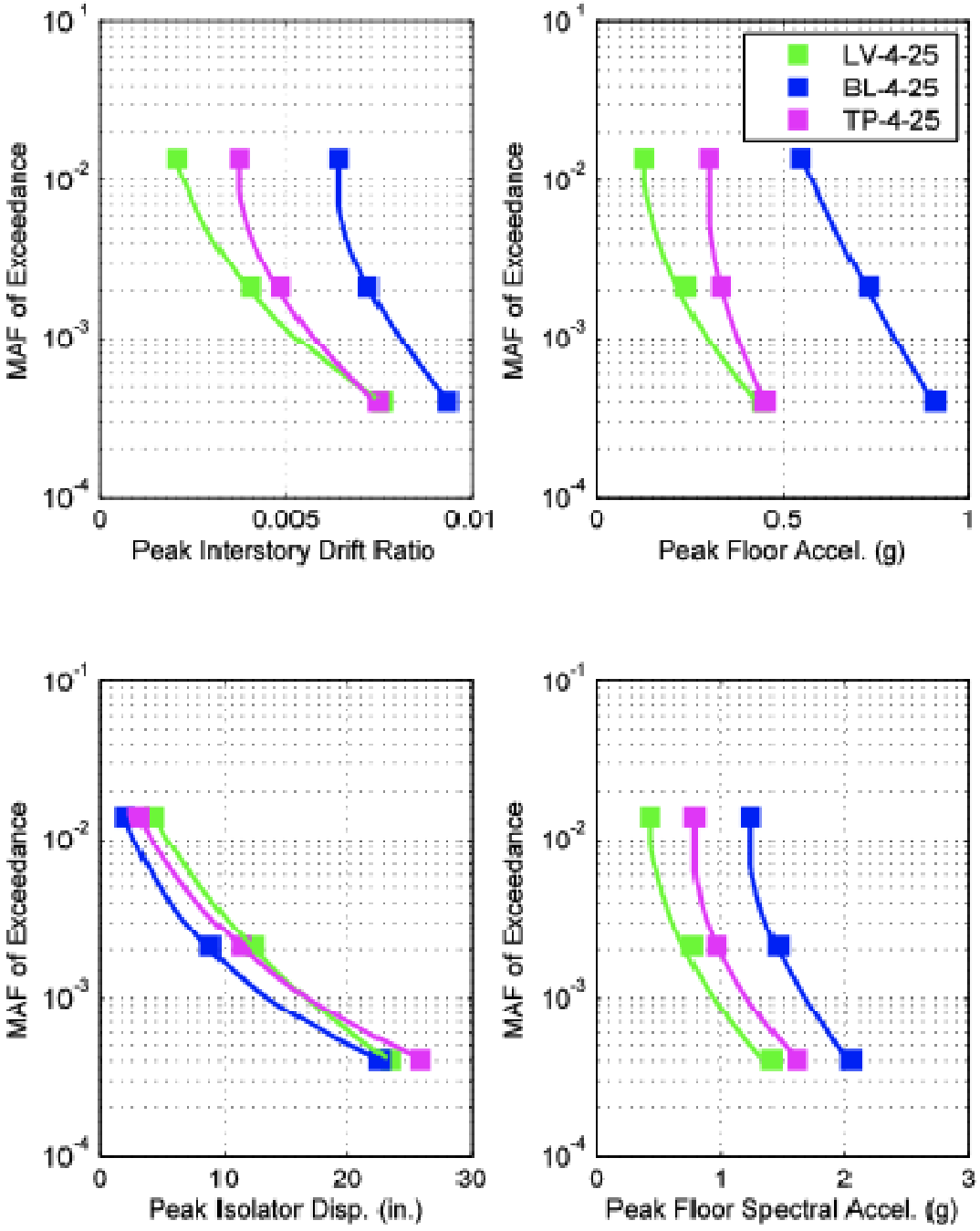

Figure 7.16: Comparison of median demand hazard curves for 9-story building on isolation systems with T_{eff} = 4 sec, ζ_{eq} = 25%

7.4.3 Reliability-Based Seismic Performance Classification

The median demand hazard curves presented in the previous section are useful in comparing the sensitivities of various isolation system parameters on the expected performance limit states considering multiple levels of seismic hazard. The main purpose of these studies is to identify sets of isolation system properties that most reliably meet some complex performance objective. Such a complex performance objective is defined here as a multiple-objective Seismic Performance Classification, a concept introduced in Section 7.3.1.

7.4.3.1 Effect of Damage State on Isolation Gap

To provide meaningful estimates of the probability of exceeding a near-collapse limit state, a revised limit state for peak isolator displacement is appropriate. It is unreasonable to assign a particular value to this limit irrespective of analysis results, since the designer is free to select an isolation gap (or moat size) that accommodates the expected displacement within some confidence bound. For example, current code provisions stipulate that the isolation gap must be larger than the computed isolator displacement (including torsion) for an earthquake having a return period of 2475 years. If the computation of this displacement is based on the mean of an ensemble of response history analysis (which is permitted by code), then the probability of exceeding the moat displacement given a 2475-year event is approximately 50%. Therefore, the probability of meeting a near collapse damage state for this level of seismic hazard can be no greater than 50% if moat collision is considered unacceptable for such a classification. However, without explicit consideration of impact in the analysis, it is not possible to assess the implications of moat collisions on the damage state of the structure. Indeed, such a consideration of moat collision of damage state is a subject of ongoing research, and no consensus has been reached.

To overcome the difficulty of assessing the damage state given a moat collision, the demand parameter is omitted from the random EDP vector **X**. Instead, the median isolator displacements for the 2475-year seismic event are reported for each isolation system. This approach has the advantage of illuminating the merits of each isolation system in achieving complex performance objectives while allowing these merits to be weighed against the likely moat size necessary to provide reliability of non-collision.

7.4.3.2 Superstructure Performance Classification

For all isolated structures considered in these studies, the same design approach was taken as is described in Chapter 6 of this report. The required stiffness of each story was determined based on assumed elastic behavior for the 475-year earthquake. Therefore, for each building, the superstructure is identical, and only the isolation system has properties that vary. Given the design approach taken, a vital question is: what is the probability that the building satisfies the requirements for some target Seismic Performance Classification? In the context of a complex performance objective, this probability is of the intersection of multiple events. Recall the definition of the event of simultaneous satisfaction (or nonexceedance) of k damage states at the corresponding k levels of seismic hazard:

$$\underbrace{\left\{\bigcap_{j=1}^{n} X_j^{R_1} \le \overline{x}_j^{\Upsilon_1}\right\}}_{DS-\Upsilon_1|R_1} \bigcap \cdots \bigcap \underbrace{\left\{\bigcap_{j=1}^{n} X_j^{R_k} \le \overline{x}_j^{\Upsilon_k}\right\}}_{DS-\Upsilon_k|R_k} \tag{7.35}$$

For the methodology outlined, there are four Seismic Performance Classifications, each of which is a function of three intersecting events. From the definition of each SPC given in Table 7.4, these events can be explicitly defined as follows:

SPC-I: $$\underbrace{\left\{\bigcap_{j=1}^{n} X_j^{72-yr} \le \overline{x}_j^{IO}\right\}}_{DS-IO|72-yr} \bigcap \underbrace{\left\{\bigcap_{j=1}^{n} X_j^{475-yr} \le \overline{x}_j^{LS}\right\}}_{DS-LS|475-yr} \bigcap \underbrace{\left\{\bigcap_{j=1}^{n} X_j^{2475-yr} \le \overline{x}_j^{NC}\right\}}_{DS-NC|2475-yr}$$

SPC-II: $$\underbrace{\left\{\bigcap_{j=1}^{n} X_j^{72-yr} \le \overline{x}_j^{F}\right\}}_{DS-F|72-yr} \bigcap \underbrace{\left\{\bigcap_{j=1}^{n} X_j^{475-yr} \le \overline{x}_j^{IO}\right\}}_{DS-IO|475-yr} \bigcap \underbrace{\left\{\bigcap_{j=1}^{n} X_j^{2475-yr} \le \overline{x}_j^{LS}\right\}}_{DS-LS|2475-yr}$$

SPC-III: $$\underbrace{\left\{\bigcap_{j=1}^{n} X_j^{72-yr} \le \overline{x}_j^{F}\right\}}_{DS-F|72-yr} \bigcap \underbrace{\left\{\bigcap_{j=1}^{n} X_j^{475-yr} \le \overline{x}_j^{F}\right\}}_{DS-F|475-yr} \bigcap \underbrace{\left\{\bigcap_{j=1}^{n} X_j^{2475-yr} \le \overline{x}_j^{IO}\right\}}_{DS-IO|2475-yr}$$

SPC-IV: $$\underbrace{\left\{\bigcap_{j=1}^{n} X_j^{72-yr} \le \overline{x}_j^{F}\right\}}_{DS-F|72-yr} \bigcap \underbrace{\left\{\bigcap_{j=1}^{n} X_j^{475-yr} \le \overline{x}_j^{F}\right\}}_{DS-F|475-yr} \bigcap \underbrace{\left\{\bigcap_{j=1}^{n} X_j^{2475-yr} \le \overline{x}_j^{F}\right\}}_{DS-F|2475-yr}$$

Recognizing that the demands resulting from seismic events having distinct frequencies of occurrence are largely independent, each of the three intersecting damage state events is

assumed to be statistically independent of the others. Therefore, to compute the probability of meeting some SPC designation, the fact can be used that

$$P\left[E_1 \cap E_2 \cap E_3\right] = P\left[E_1\right]P\left[E_2\right]P\left[E_3\right] \tag{7.36}$$

for mutually independent events E_1, E_2, and E_3. Moreover, the probability

$$P\left\{\bigcap_{j=1}^{n} X_j^R \le \overline{x}_j^{\Upsilon}\right\} = F_{\mathbf{Y}}\left(\ln \overline{\mathbf{x}}^{\Upsilon} \middle| \hat{\Lambda}^R, \hat{\Psi}^R\right) \tag{7.37}$$

for $\mathbf{X} \sim MLN\left(\mathbf{\Lambda}, \mathbf{\Psi}\right)$, where $F_{\mathbf{Y}}(\mathbf{y})$ is the multivariate Gaussian CDF. Taking the probability of each SPC event defined above and using the properties of assumed statistical independence and lognormality of $\mathbf{X}$, we obtain the following probabilities of achieving some Seismic Performance Classification:

$$P\left[SPC-I\right] = F_{\mathbf{Y}}\left(\ln \overline{\mathbf{x}}^{IO} \middle| \hat{\Lambda}^{72}, \hat{\Psi}^{72}\right) \cdot F_{\mathbf{Y}}\left(\ln \overline{\mathbf{x}}^{LS} \middle| \hat{\Lambda}^{475}, \hat{\Psi}^{475}\right) \cdot F_{\mathbf{Y}}\left(\ln \overline{\mathbf{x}}^{NC} \middle| \hat{\Lambda}^{2475}, \hat{\Psi}^{2475}\right)$$

$$P\left[SPC-II\right] = F_{\mathbf{Y}}\left(\ln \overline{\mathbf{x}}^{F} \middle| \hat{\Lambda}^{72}, \hat{\Psi}^{72}\right) \cdot F_{\mathbf{Y}}\left(\ln \overline{\mathbf{x}}^{IO} \middle| \hat{\Lambda}^{475}, \hat{\Psi}^{475}\right) \cdot F_{\mathbf{Y}}\left(\ln \overline{\mathbf{x}}^{LS} \middle| \hat{\Lambda}^{2475}, \hat{\Psi}^{2475}\right)$$

$$P\left[SPC-III\right] = F_{\mathbf{Y}}\left(\ln \overline{\mathbf{x}}^{F} \middle| \hat{\Lambda}^{72}, \hat{\Psi}^{72}\right) \cdot F_{\mathbf{Y}}\left(\ln \overline{\mathbf{x}}^{F} \middle| \hat{\Lambda}^{475}, \hat{\Psi}^{475}\right) \cdot F_{\mathbf{Y}}\left(\ln \overline{\mathbf{x}}^{IO} \middle| \hat{\Lambda}^{2475}, \hat{\Psi}^{2475}\right)$$

$$P\left[SPC-IV\right] = F_{\mathbf{Y}}\left(\ln \overline{\mathbf{x}}^{F} \middle| \hat{\Lambda}^{72}, \hat{\Psi}^{72}\right) \cdot F_{\mathbf{Y}}\left(\ln \overline{\mathbf{x}}^{F} \middle| \hat{\Lambda}^{475}, \hat{\Psi}^{475}\right) \cdot F_{\mathbf{Y}}\left(\ln \overline{\mathbf{x}}^{F} \middle| \hat{\Lambda}^{2475}, \hat{\Psi}^{2475}\right)$$

Given the estimation of all mean vectors $\mathbf{\Lambda}$ and covariance matrices $\mathbf{\Psi}$ in Section 7.2.2.3, and limit state vectors $\overline{\mathbf{x}}$ in Section 7.3.3 (omitting isolator displacement limits), these probabilities may be computed numerically following the procedure of Section 7.2.3. These results are presented in the tables that follow. Table 7.5 and Table 7.6 describe the probability of the three- and nine-story buildings meeting some complex performance objective given the type of isolation system and its period and damping parameters. Also shown, for reference, is the required moat size based on the median 2475-year peak isolator displacement. These data are useful because they answer the question posed at the beginning of this section: what is the probability that a facility satisfies the requirements for some target Seismic Performance Classification?

Considering the three-story building data, it is clear that nearly all isolation systems satisfy the most basic performance classification, SPC-I, with a high degree of certainty. The

only system that is unlikely to meet SPC-I is the bilinear hysteretic isolation system BL-3-25. Since seismic isolation is well known to provide superior seismic performance relative to that of conventional buildings (for which SPC-I is a common performance objective), it would be expected that all isolation systems would meet this basic performance objective. In meeting the more stringent performance classification of SPC-II, it appears that all triple pendulum systems *except* TP-3-25 have a greater than 90% probability of meeting this performance classification without modification of design. All linear viscous systems have a greater than 90% probability of meeting SPC-II.

Satisfying the SPC-III objective appears highly dependent on the target effective period of the isolation system. None of the bilinear hysteretic systems exhibit a likelihood of meeting the SPC-III objective. Among linear viscous and triple pendulum systems, the long-period systems show an increased probability of meeting SPC-III compared to short period systems. For the short period LV systems, an increase in damping from 10% to 25% only decreases the probability of meeting SPC-III from 0.44 to 0.43. However, for the long period LV systems, the same increase in damping decreases the probability from 0.83 to 0.72. A similar trend is observed for triple pendulum systems. For the short period TP systems, an increase in damping from 10% to 25% decreases the probability of meeting SPC-III from 0.38 to 0.25 and, for the long-period TP systems, the same increase in damping decreases the probability from 0.91 to 0.57.

It can be seen that none of the isolated buildings studies exhibits likelihood of meeting the SPC-IV objective. Of course, they were not specifically designed for this performance objective, so this is an expected result. However, for the design approach taken, the triple pendulum system TP-4-10 exhibits the highest reliability in achieving SPC-IV, with a probability of 0.47, whereas the equivalent linear viscous system LV-4-10 has a probability of 0.25. It is evident from the median demand hazard curves presented in the previous section that the induced peak drift demands and peak acceleration demands well exceed the functional damage state for the very rare event. However, the data of Table 7.5 suggests that, for the three-story structure under investigation, long-period, low-damping isolation systems provide the most reliable means of meeting this extremely stringent performance classification unless purely bilinear hysteretic damping is employed.

From the probabilistic data for the 9-story building in Table 7.6, many isolation systems clearly provide reliable means of achieving SPC-I performance. It is apparent,

however, that the bilinear hysteretic systems are the least reliable, with only BL-4-10 having a greater than 50% probability of meeting this basic performance objective. From Figure 7.4, this is clearly due to high floor acceleration demands for the frequent and rare events and, to a lesser extent, drift demands in the frequent event. For the SPC-II classification, only the low-power-law viscous damping, and low damping, high yield point hysteretic damping provide greater than 80% probability of achieving this performance objective. Among currently available isolation systems, only the low-friction TP system provides a non-negligible probability of meeting the SPC-II objective for the flexible structure considered. For the SPC-III objective, only low-damping, low-power-law viscous and high-yield-point hysteretic systems show a greater than 30% probability of meeting this performance objective. None of the isolation systems considered show appreciable reliability of meeting the SPC-IV performance objective.

7.5 CONCLUSIONS

A multi-objective Seismic Performance Classification (SPC) was introduced to describe aggregate damage state limitation over multiple levels of seismic hazard. From the analytical data presented in Chapter 6 of this report, a probabilistic seismic demand analysis was performed to estimate the joint density functions of a vector of EDPs. Based on a series of limit state vectors assumed to describe discrete damage states, the probability of satisfying specific SPCs was computed for three- and nine-story buildings on nonlinear viscous, hysteretic, and triple pendulum isolation systems. The results demonstrate the importance of limiting interstory drift and floor acceleration to satisfy enhanced SPCs, and the sensitivity of these responses to the level and type of energy dissipation present.

Table 7.5: Probability of the 3-story building meeting each defined Seismic Performance Classification for all isolation systems considered

		Seismic Performance Class				
		SPC-I	SPC-II	SPC-III	SPC-IV	Moat
LV	3-10	1.00	0.99	0.44	0.05	29.2 in.
	3-25	1.00	0.97	0.43	0.04	23.1 in.
	4-10	1.00	1.00	0.83	0.25	31.3 in.
	4-25	1.00	0.99	0.72	0.12	21.6 in.
BL	3-10	0.94	0.04	0.00	0.00	28.6 in.
	3-25	0.40	0.00	0.00	0.00	20.4 in.
	4-10	1.00	0.51	0.10	0.01	27.2 in.
	4-25	0.90	0.01	0.00	0.00	24.0 in.
TP	3-10	1.00	0.93	0.38	0.07	30.2 in.
	3-25	0.96	0.40	0.25	0.00	25.9 in.
	4-10	1.00	1.00	0.91	0.47	31.8 in.
	4-25	1.00	0.91	0.57	0.10	24.5 in.

Table 7.6: Probability of the 9-story building meeting each defined Seismic Performance Classification for all isolation systems considered

		Seismic Performance Class				
		SPC-I	SPC-II	SPC-III	SPC-IV	Moat
LV	3-10	1.00	0.92	0.12	0.00	29.2 in.
	3-25	0.99	0.80	0.04	0.00	23.1 in.
	4-10	1.00	0.98	0.60	0.05	31.3 in.
	4-25	1.00	0.91	0.23	0.00	21.6 in.
BL	3-10	0.44	0.01	0.00	0.00	28.6 in.
	3-25	0.19	0.00	0.00	0.00	20.4 in.
	4-10	0.74	0.04	0.00	0.00	27.2 in.
	4-25	0.35	0.00	0.00	0.00	24.0 in.
TP	3-10	0.98	0.55	0.01	0.00	30.2 in.
	3-25	0.86	0.40	0.00	0.00	25.9 in.
	4-10	1.00	0.96	0.68	0.14	31.8 in.
	4-25	0.94	0.26	0.01	0.00	24.5 in.

8 Conclusions and Recommendations

8.1 SUMMARY AND CONCLUSIONS OF RESEARCH PROGRAM

This report describes a research program that was conducted to investigate the ability of innovative isolation systems to reliably satisfy multi-objective seismic performance classifications. Phases of this research included analytical and experimental investigations on the cyclic behavior and seismic performance of multi-stage friction pendulum bearings, parametric studies on the seismic response of isolated multi-story buildings, and comparative performance assessment of isolated buildings in a probabilistic framework. A summary of each phase is provided in this section.

8.1.1 Multi-Stage Friction Pendulum Bearings

Initial studies focused on the characterization of a new class of friction pendulum bearings capable of progressively exhibiting different hysteretic properties at different stages of response. Based on basic mechanical principles of equilibrium, compatibility, and constitutive relations, force-deformation behaviors for single-, double-, and triple pendulum bearings were derived. It was shown that, for all friction pendulum bearings studied, the behavior is a function of the geometric properties of the spherical sliding surfaces and the coefficients of friction of each sliding interface. The newly developed model for the triple pendulum (TP) bearing demonstrates five unique stages of sliding behavior, the transitions of which can be explicitly computed given the bearing geometry and assumed friction coefficients of each slider. The nonlinear monotonic behavior of the TP bearing was extended to predict cyclic behavior under generalized displacement input, a necessary formulation for implementation in a response history analysis. This cyclic model was developed as a series formulation of three bilinear-gap elements in series, whose stiffness,

strength, and gap dimension parameters were computed to reproduce the derived sliding stages.

To validate the analytically derived behavior of the TP bearing and to motivate further studies, a series of shake table experiments was conducted on an isolated three-story steel braced frame specimen. Bearings investigated included a DP bearing with equal friction on each slider, and a TP bearing with three unique friction coefficients on each slider. Harmonic characterization tests identified cyclic behavior at various levels of displacement, velocity, and axial load. For each bearing specimen, earthquake simulation tests were conducted in a single horizontal direction at three levels of hazard, each with and without the inclusion of vertical acceleration. Acceleration records from three different historical earthquakes were applied to the model for each hazard level. For the moderate level of shaking, three components of excitation were applied such that bidirectional interaction with vertical acceleration could be observed. In all tests, displacement and acceleration data was collected at each level of the specimen, as well as shear and axial force reactions at each bearing.

The results of the cyclic characterization experiments provided validation of both the assumed model for the DP bearing and the newly developed model for the TP bearing. Tests were conducted such that lateral deformation of the TP bearing occurred in all five stages of sliding identified previously. Additionally, a procedure was described to estimate the friction coefficient for each sliding interface. The transitions between sliding stages observed from experimentation correspond well with those derived considering the estimated friction coefficients. A comparison of hysteretic behavior from the developed model and the observed behavior from collected data indicates excellent correlation between analysis and experiment for the stiffness of each sliding mechanism and the energy dissipation history. For all characterization tests, both DP and TP specimens show stable, repeatable performance with no degradation in properties over numerous cycles of deformation. Moreover, large deformation tests with substantial induced global overturning in the TP specimen shows stable performance following bearing uplift with no dislodgement of any sliding mechanism. This is an important limit state since uplift is often expected for a limited number of friction pendulum bearings under very rare levels of ground shaking.

The results of the earthquake simulation tests validated much of the behavior observed in the characterization tests. Under moderate levels of ground shaking, an increase

in force output for initial sliding on the second pendulum mechanism was observed. However, the causes of this were judged to be a result of the experimental specimens having used a new resin under development, and subsequent testing of TP bearings are expected to reveal very little increase in first cycle friction on any single-pendulum mechanism. Otherwise, cyclic behavior for both DP and TP bearings was as predicted from the developed analytical models for all levels of earthquake hazard investigated. For DP and TP specimens, the effect of vertical ground motion on both the hysteretic response of the isolation systems and the frequency content of superstructural accelerations was found to be negligible. Additionally, the experimental results considering two components of horizontal excitation validated the assumed coupling of the force output for both DP and TP specimens; however, the TP model has not yet been extended to capture the effects of bidirectional motion.

The observed response of the superstructure for earthquake testing revealed several key issues. For the specimen considered, there was negligible observed drift demand at any floor level, for all ground motions and levels of hazard. As expected, there was no slippage of the brace slotted bolted connections. Spectral analysis of recorded acceleration response at each floor level revealed that high-frequency acceleration content was reduced in the TP specimen relative to the DP specimen, particularly for low levels of excitation. The differences between DP and TP acceleration response became less pronounced as the level of shaking increased.

8.1.2 Analytical Simulations

To investigate the response of isolated buildings to earthquake excitation, an extensive parametric study was undertaken. These studies considered the height and flexibility of the isolated structure, and three classes of isolation systems: linear isolators with bilinear hysteretic damping, linear isolators with linear viscous damping, and triple pendulum isolators. Within each class of isolation system, parameters of stiffness and energy dissipation were varied to study the sensitivity or response parameters. Additionally, a method of selecting isolation system parameters to target a displacement limit for a level of seismic hazard was presented.

The first series of parametric studies was on a canonical two-degree-of-freedom (2-DOF) isolated structure. The superstructure is considered linear, and the fixed-based

period was varied between 0.5 sec and 1.5 sec. The linear isolation systems considered had an elastic period of 3 and 4 sec. The linear viscous damping parameters were varied to consider target equivalent damping of 0.10 and 0.25 critical. The hysteretic damping parameters were varied to consider the same target damping as above for the viscous damping. Triple pendulum bearings considered had variations in pendulum radii, friction coefficient, and dish displacement capacity to achieve target stiffness and damping properties that were equivalent to those for the linear viscous system. To avoid the complication of multiple ground motions, a single acceleration record was chosen and varied in amplitude to simulated earthquake intensity.

A remarkable result is that the triple pendulum bearing is generally effective at limiting isolator displacements in very rare earthquakes while controlling drifts and accelerations for low- and moderate-level excitations. While an increase in friction on all sliding surfaces results in an increased drift and acceleration, the increases are modest relative to those observed for the equivalent bilinear hysteretic systems.

8.1.3 Performance Assessment

A methodology is introduced to estimate the probability of achieving a target Seismic Performance Classification (SPC). An SPC is defined as simultaneously satisfying a series of prescribed damage states at their corresponding target levels of seismic hazard. The reliability of each isolation system in terms of meeting a target SPC is evaluated based on the analytical results for three- and nine-story buildings. To define each SPC, a series of limit state vectors are assumed to describe damage state levels for conventional braced frames. These damage states consider structural damage, nonstructural damage, and content damage. The observed analytical data was fitted to joint lognormal multivariate distributions for each level of seismic hazard. Based on the fitted distributions, the probability of meeting a target SPC is computed for each isolated system and comparisons are drawn.

Based on the results of this study, it is evident that low-damping isolation systems show enhanced reliability in achieving multiple-objective performance goals relative to high-damping systems for a fixed set of parameters. This improved reliability generally comes at a cost of higher peak isolator displacements. The triple pendulum bearing shows improved

performance reliability compared to bilinear hysteretic systems, combined with a moderate isolator displacement demand in the very rare seismic event.

8.2 RECOMMENDATIONS FOR FURTHER RESEARCH

While the analytical and experimental investigations described in this report constitute a valuable contribution to the study of performance-based earthquake engineering and seismic isolation, many issues identified could benefit from further study.

8.2.1 Triple Pendulum Model

The cyclic model developed for the triple pendulum bearing has several simplifications which, while appropriate for the studies described in this report, may be insufficiently detailed for certain applications. Potential improvements include the following:

1. Rotation in the formulation of the cyclic behavior could be considered. For some isolation applications, particularly flexible bridge piers where rotations at the top of the bent cap may be non-negligible, the imposed rotations may have a substantial effect on the deformation of each pendulum mechanism. Experimentation with such rotationally flexible specimens is crucial toward calibration of a coupled rotational-translational model.

2. Bidirectional interaction through a circular plasticity surface could be addressed. In fact, virtually all isolated structured are expected to undergo horizontal bidirectional motion during a seismic event, and prediction of peak isolator displacement is only possible with a model that captures this behavior. Data acquired as part of the experimental studies described in this report are appropriate to validate such a model.

3. While ultimate limit state behavior of bearing uplift was captured experimentally, the other important limit state of loss of bearing travel was not captured. In evaluating the performance of isolated buildings under very rare levels of seismic hazard, there is always a probability that the isolator displacement capacity will be less than the imposed demand. In estimating the likely performance of the building given such an event, it is important to have a reliable isolator model that captures the loss of travel and resulting impact. While this condition is widely considered detrimental to

performance, few studies exist to quantify the consequence, particularly for the triple pendulum bearing. Such studied would further the performance-based design of isolated buildings.

4. These studies are limited to reduced-scale devices, and validation of behavior at prototype scale, including rate dependency, is desired.

8.2.2 Analytical Simulations

A number of key simplifications were introduced in the analytical work described in this report. Those issues requiring further consideration include the following:

1. The investigation of superstructure yielding is an important consideration in estimating the probabilistic distribution of interstory drift and floor accelerations. While isolated buildings are traditionally designed to remain elastic in all but the rarest seismic events, this is generally only targeted in some average sense. For even moderate levels of shaking, there is a chance of yielding, and this may affect the estimated central tendencies, dispersions, and correlations of drift and acceleration. Additionally, the effect of hysteretic behavior in the superstructure on the behavior of isolated buildings is largely unknown. Studies conducted to date have considered simple structural systems with elastoplastic hysteresis, while isolated building routinely incorporate steel braces, moment frames, and concrete elements, all of which can exhibit degradation in strength and stiffness, and asymmetrical force-deformation behavior.
2. A consideration of residual drift as a demand parameter is important in the assessment of structural performance. Future studies, in combination with the consideration of superstructure yielding, should identify isolation system parameters that affect the residual drifts in the structure.

8.2.3 Performance Assessment

In the probabilistic assessment of Seismic Performance Class, the following issues deserve further treatment:

1. Given the lack of information on fragilities for steel braced frames, the dispersion in the estimation of damage state given a level of peak response should be considered. There is significant research being devoted to braced frame performance, and a reformulation of the described performance methodology accounting for the uncertainty in damage state is appropriate. This should be extended to other structural systems to elucidate their relative benefits on the performance of isolated buildings.
2. Given the attention to loss modeling in the research and practicing communities, an inclusion of an appropriate loss model given some damage state, incorporating both direct and indirect losses, would be a significant improvement to the methodology described in this report.
3. The two-degree-of-freedom studies would benefit significantly from consideration of an ensemble of ground motions.
4. The parametric studies of multi-story isolated buildings should be extended beyond shear buildings, to capture a greater variety of types of structural behavior.

REFERENCES

Almazán, J.L. and De la Llera, J.C. [2002] "Analytical model of structures with friction pendulum isolators," *Earthquake Engineering and Structural Dynamics*, **31**(3):305–322

Anderson, E. [2003] Performance-Based Design of Seismically Isolated Bridges, Doctoral Dissertation, University of California, Berkeley.

Deierlein, G.G. [2004] "Overview of a Comprehensive Framework for Earthquake Performance Assessment," *Proceedings*, International Workshop on Performance-Based Seismic Design Concepts and Implementation, Bled, Slovenia

Almazán, J.L., De la Llera, J.C., and Inaudi, J.A. [1998] "Modeling aspects of structures isolated with the friction pendulum system," *Earthquake Engineering and Structural Dynamics*, **27**(3):845–867

ASCE 7 [2002] *Minimum Design Loads for Buildings and Other Structures*, American Society of Civil Engineers, Reston, VA

Aslani, H. and Miranda, E. [2005] "Probabilistic Earthquake Loss Estimation and Loss Disaggregation in Buildings," *Report No. 157*, John A. Blume Earthquake Engineering Center, Dept. of Civil & Environ. Engineering, Stanford University, Palo Alto, CA

Astrella, M.J. and Whittaker, A.S. [2005] "The Performance-Based Design Paradigm," *Technical Report MCEER-05-0011*, Multidisciplinary Center for Earthquake Engineering Research, Buffalo, NY

Barroso, L.R., Breneman, S.E., and Smith, H.A. [2002] "Performance evaluation of controlled steel frames under multilevel seismic loads," *Journal of Structural Engineering*, ASCE, **128**(11):1368–1378

Becker, T.C. and Mahin, S.A. [2010] "Three Dimensional Modeling of Triple Friction Pendulum Isolators." *Proceedings*, 9th US National and 10th Canadian Conference on Earthquake Engineering, Toronto, Canada

Bertero, R.D. and Bertero, V.V. [2002] "Performance-based seismic engineering: the need for a reliable conceptual comprehensive approach," *Earthquake Engineering and Structural Dynamics*, **31**(3):627–652

Bertero, V.V. and Bozorgnia, Eds. [2005] *Earthquake Engineering: From Engineering Seismology to Performance-Based Engineering*, CRC Press, New York, NY

Bouc, R. [1967] "Forced vibration of mechanical systems with hysteresis," *Proceedings*, 4th Conference on Non-linear Oscillations, Prague, Czechoslovakia

Bouwkamp, J.G. and Meehan, J.F. [1960] "Drift limitations imposed by glass," *Proceedings*, Second World Conference on Earthquake Engineering, San Francisco, CA

Brookshire, D.S., Chang, S.E., Cochrane, H., Olson, R.A., Rose, A., and Steenson, J. [1997] "Direct and Indirect Economic Losses from Earthquake Damage," *Earthquake Spectra*, **14**(4):683-701

BSSC [2000] *FEMA 356: Prestandard and Commentary for the Seismic Rehabilitation of Buildings*, Building Seismic Safety Council, Washington D.C.

BSSC [2003] *FEMA 440: NEHRP Recommended Provisions for Seismic Regulations for New Buildings and Other Structures*, Building Seismic Safety Council, Washington D.C.

Chang, S.-P., Makris, N., Whittaker, A.S., and Thompson, A.C.T. [2002] "Experimental and analytical studies on the performance of hybrid isolation systems," *Earthquake Engineering and Structural Dynamics*, **31**(3):421-443

Chopra, A.K. [2007] *Dynamics of Structures: Theory and Application to Earthquake Engineering, 3rd Ed.*, Pearson Prentice Hall, Upper Saddle River, NJ

Christopoulos, C. and Filiatrault, A. [2006] *Principles of Passive Supplemental Damping and Seismic Isolation*, IUSS Press, Pavia, Italy

Cimellaro, G.P., Reinhorn, A.M., Bruneau, M., and Rutenberg, A. [2006] "Multi-Dimensional Fragility of Structures: Formulation and Evaluation," *Technical Report MCEER-06-0002*, Multidisciplinary Center for Earthquake Engineering Research, Buffalo, NY

Clark P.W., Aiken I.D., Nakashima, M., Miyazaki, M., and Midorikawa, M. [2000] "The 1995 Kobe (Hyoko-Ken Nanbu) earthquake as a trigger for implementing new seismic design technologies in Japan," Lessons Learned Over Time, Learning from Earthquakes Series: III. Earthquake Engineering Research Institute, Oakland, CA

Clark, P.W., Aiken, I.D., and Kelly J.M. [1997] "Experimental studies of the ultimate behavior of seismically isolated structures," *Report No. UCB/EERC-97/18*, Earthquake Engineering Research Center, Berkeley, CA

Clark, P.W., Higashino, M., and Kelly, J.M. [1994] "Performance of seismically isolated structures in the January 17, 1994 Northridge earthquake," *Proceedings*, 6th U.S.-Japan Workshop on Improvement of Design and Construction Practices, Applied Technology Council, ATC-15-5, Victoria, B.C.

Clough, R.W. and Penzien, J. [1993] *Dynamics of Structures*, McGraw-Hill, New York, NY

Clough, R.W. and Tang, D.T. [1975] "Earthquake simulator study of a steel frame structure, vol. I: Analytical Results," *Report No. UCB/EERC-75/6*, Earthquake Engineering Research Center, Berkeley, CA

Constantinou, M.C. and Tadjbakhsh, I.G. [1984] "The optimum design of a base isolation system with frictional elements," *Earthquake Engineering and Structural Dynamics*, **12**(2):203-214

Constantinou, M.C., Mokha, A., and Reinhorn, A.M. [1990] "Teflon bearings in base isolation II: Modeling," *Journal of Structural Engineering*, ASCE, **116**(2):455–474

Cooley, J.W. and Tukey, O.W. [1965] "An Algorithm for the Machine Calculation of Complex Fourier Series," *Journal of Mathematical Computation,* **19**:297-301

Den Hartog, J.P. [1947] *Mechanical Vibrations*, 3rd Ed., McGraw-Hill, New York, NY

Der Kiureghian, A. [2005] "First- and second-order reliability methods," Chapter 14 in *Engineering Design Reliability Handbook*, E. Nikolaidis, D. M. Ghiocel and S. Singhal, Eds., CRC Press, Boca Raton, FL

Dolce, M. and Cardone, D. [2003] "Seismic protection of light secondary systems through different base isolation systems," *Journal of Earthquake Engineering*, **7**(2):223-250

Fan, F.G. and Ahmadi, G., [1990] "Floor response spectra for base-isolated multistory structures", *Earthquake Engineering and Structural Dynamics*, **19**(3):377-388

Fenz, D.M. and Constantinou, M.C. [2008] "Spherical sliding isolation bearings with adaptive behavior: Theory," *Earthquake Engineering and Structural Dynamics*, **37**(2): 163-183

Fenz, D.M. and Constantinou, M.C. [2008] "Spherical sliding isolation bearings with adaptive behavior: Experimental verification," *Earthquake Engineering and Structural Dynamics 2008*, **37**(2): 185-205

Fenz, D.M. and Constantinou, M.C. [2006] "Behaviour of the double concave Friction Pendulum bearing," *Earthquake Engineering and Structural Dynamics*, **35**(11):1403-1422

Filiatrault, A., Christopoulos, C., Stearns, C. [2002] "Guidelines, Specifications, and Seismic Performance Characterization of Nonstructural Building Components and Equipment," *PEER Report 2002/05*, Pacific Earthquake Engineering Research Center, Berkeley, CA

Genz, A. [1992] "Numerical Computation of Multivariate Normal Probabilities," *Journal of Computational Graphical Statistics*, **1**(2):141-149

Grigorian, C.E. and Popov, E.P. [1994] "Energy dissipation with slotted bolted connections," *Report No. UCB/EERC-94/02*, Earthquake Engineering Research Center, Berkeley, CA

Hernried, A.G. and Lei, K.M. [1993] "Parametric studies on the response of equipment in resilient-friction base isolated structures subjected to ground motion," *Engineering Structures,* **15**(5):349-357

Higashino, M. and Okamoto, S., Eds. [2006] *Response Control and Seismic Isolation of Buildings*, Taylor & Francis, New York, NY

ICC [2003] International Building Code, International Code Council, Falls Church, VA

International Conference of Building Officials, [1997] *Uniform Building Code*, Volume 2, Whittier, CA

International Conference of Building Officials, [2006] *International Building Code*, Whittier, CA

Jacobsen, L.S. [1959] "Frictional Effects in Composite Structures Subjected to Earthquake Vibrations," *Technical Report*, Department of Mechanical Engineering, Stanford University, Stanford, CA

Jacobsen, L.S. and Ayre, R.S. [1958] *Engineering Vibrations*, McGraw-Hill, New York, NY

Juhn, G., Manolis, G., Constantinou, M.C. and Reinhorn, A.M. [1992] "Experimental Investigation of Secondary Systems in a Base-Isolated Structure," *Journal of Structural Engineering*, ASCE, **118**(8):2204-2221

Kelly, J.M. [1981] "The influence of base isolation on the seismic response of light secondary equipment," *Report No. UCB/EERC-81/17*, Earthquake Engineering Research Center, Berkeley, CA

Kelly, J.M. [1996] *Earthquake Resistant Design with Rubber*, 2nd Ed., Springer, New York, NY

Kelly, J.M. and Beucke, K.E. [1983] "A friction damped base isolation system with fail-safe characteristics," *Earthquake Engineering and Structural Dynamics*, **11**(1):33-56

Kelly, J.M., and Tsai, H.C., [1985] "Seismic response of light internal equipment in base-isolated structures," *Earthquake Engineering and Structural Dynamics*, **13**(6):711-732

Kinali, K. [2007] "Seismic Fragility Assessment of Steel Frames in the Central and Eastern United States," Ph.D. Dissertation, Department of Civil and Environmental Engineering, Georgia Institute of Technology, Atlanta, GA

Kramer, S.L. [1996] *Geotechnical Earthquake Engineering*, Prentice-Hall: Civil Engineering and Engineering Mechanics, Upper Saddle River, NJ

Lin, W.-H. and A.K. Chopra [2003] "Earthquake Response of Elastic Single-Degree-of-Freedom Systems with Nonlinear Viscoelastic Dampers," *Journal of Structural Engineering*, ASCE, **129**(6):597-606

Lin, Y-Y, Miranda, E., and Chang, K.C. [2005] "Evaluation of damping reduction factors for estimating elastic response of structures with high damping," *Earthquake Engineering and Structural Dynamics*, **34**(11):1427-1443

Lutes, L.D. and Sarkani, S. [2004] *Random Vibrations: Analysis of Structural and Mechanical Systems*, Elsevier Butterworth-Heinemann, New York, NY

Makris, N. and Black, C.J. [2004a] "Dimensional Analysis of Rigid-Plastic and Elastoplastic Structures under Pulse-Type Excitations," *Journal of Engineering Mechanics*, **130**(9): 1006-1018

Makris, N. and Black, C.J. [2004b] "Dimensional Analysis of Bilinear Oscillators under Pulse-Type Excitations," *Journal of Engineering Mechanics*, **130**(9):1019-1031

Makris, N. and Chang, S.-P. [2000] "Effect of viscous, viscoplastic and friction damping on the response of seismic isolated structures," *Earthquake Engineering and Structural Dynamics*, **29**(1):85-107

Mathworks, Inc. [2006] Matlab® R2006a, http://www.mathworks.com, Natick, MA

Mayes, R.L. [2002] "Impediments to the Implementation of Seismic Isolation," *Proceedings*, ATC 17-2 of a Seminar on Response Modification Technologies for Performance-based Seismic Design, Applied Technology Council, May 2002, Redwood City, CA

McGuire, R.K. [2004] *Seismic Hazard and Risk Analysis*, EERI Monograph, Earthquake Engineering Research Institute, Oakland, CA

Mokha, A., Amin, N., Constantinou, M.C., and Zayas, V. [1991] "Experimental study of friction pendulum isolation system," *Journal of Structural Engineering*, ASCE, **117**(4):1201–1217

Mokha, A., Constantinou, M.C., and Reinhorn, A.M. [1990] "Teflon bearings in base isolation I: Testing," *Journal of Structural Engineering*, **116**(2):438–454

Mokha, A., Constantinou, M.C., and Reinhorn, A.M. [1993] "Verification of friction model of Teflon bearings under triaxial load," *Journal of Structural Engineering*, ASCE, **119**(1):240–261

Mokha, A., Constantinou, M.C., Reinhorn, A.M., and Zayas, V. [1996] "Seismic Isolation Retrofit of a Large Historic Building," *Journal of Structural Engineering*, ASCE, **122**(3):298-308

Mosqueda, G., Whittaker, A.S., and Fenves, G.L. [2004] "Characterization and modeling of Friction Pendulum bearings subjected to multiple components of excitation," *Journal of Structural Engineering*, ASCE, **130**(3):433-442

Mostaghel, N. [1986] "Resilient-friction base isolator," *Proceedings*, ATC-17 Seminar on Base Isolation and Passive Energy Dissipation, 1986, San Francisco, CA

Naaseh, S., Morgan, T.A., and Walters, M.T. [2001] "A Critical Evaluation of Current U.S. Building Code Provisions for the Design of Seismically Isolated Structures", *Proceedings*, Seventh International Seminar on Seismic Isolation, Passive Energy Dissipation and Active Control of Vibrations of Structures, Assisi, Italy

Naeim, F. and Kelly, J.M. [1999] *Design of Seismic Isolated Structures*, John Wiley & Sons Ltd., New York, NY

Nagarajaiah, S. and Sun, X. [2000] "Response of base-isolated USC hospital building in Northridge earthquake," *Journal of Structural Engineering*, ASCE, **126**(10):1177-1186

Nagarajaiah, S., Reinhorn, A.M. and Constantinou, M.C. [1992] "Experimental study of sliding isolated structures with uplift restraint," *Journal of Structural Engineering*, ASCE, **118**(6):1666-1683

Newmark, N.M. and Hall, W.J. [1982] *Earthquake Spectra and Design*, EERI Monograph, Oakland, CA

Pan, P., Zamfirescu, D., Nakashima, M., Nakayasu, N., and Kashiwa, H., (2005), "Base-Isolation Design Practice in Japan: Introduction to the Post-Kobe Approach," *Journal of Earthquake Engineering*, **9**(1):147–171

Pavlou, E.A. [2005] "Performance of Primary and Secondary Systems in Buildings with Seismic Protective Systems," Ph.D. Dissertation, State University of New York at Buffalo, NY

Pinto, P.E., Giannini, R., and Franchin, P. [2004] *Seismic Reliability Analysis of Structures*, IUSS Press, Pavia, Italy

Retamales, R., Mosqueda, G., Filiatrault, A., and Reinhorn, A.M. [2006] "Experimental Study on the Seismic Behavior of Nonstructural Components Subjected to Full-Scale Floor Motions," *Proceedings*, Eighth US National Conference on Earthquake Engineering, April 18-22, San Francisco, CA

Rinawi, A.M. and Clough, R.W. [1991] "Shaking table-structure interaction," *Report No. UCB/EERC-91/13*, Earthquake Engineering Research Center, Berkeley, CA

Riven, E.I. [2003] *Passive Vibration Isolation*, ASME Press, New York, NY

Roussis, P.C. and Constantinou, M.C. [2006] "Experimental and analytical studies of structures seismically isolated with an uplift-restraining friction pendulum bearing system," *Earthquake Engineering and Structural Dynamics*, **35**(5):595-611

Ryan, K.L. and Chopra, A.K. [2004] "Estimating the seismic displacement of friction pendulum isolators based on nonlinear response history analysis," *Earthquake Engineering and Structural Dynamics*, **33**(3):359-373

Sakamoto, I. [1978] "Seismic performance of nonstructural and secondary structural elements," *Report No. UCB/EERC-78/10*, Earthquake Engineering Research Center, Berkeley, CA

SEAOC [1995] *Vision 2000: Performance-based Seismic Engineering of Buildings*, Report to California Office of Emergency Services, Sacramento, CA

SEAOC [1999] *Recommended Lateral Force Requirements and Commentary*, Sacramento, CA

SEAONC [1986] *Tentative Seismic Isolation Design Requirements*, San Francisco, CA

Shenton III, H.W. and Lin, A.N. [1993] "Relative Performance of Fixed-base and Base-isolated Concrete Frames," *Journal of Structural Engineering,* ASCE, **119**(10):2952-2968

Skinner, R.I., Beck, J.L. and Bycroft, G.N. [1975] "A practical system for isolating structures from earthquake attack," *Earthquake Engineering and Structural Dynamics*, **3**(3):297-309

Skinner, R.I., Kelly, J.M. and Heine, A.J. [1975] "Hysteretic dampers for earthquake-resistant structures," *Earthquake Engineering and Structural Dynamics*, **3**(3):287-296

Skinner, R.I., Robinson W.H., and McVerry G.H. [1993] *An Introduction to Seismic Isolation,* John Wiley & Sons Ltd., New York, NY

Somerville, P., Anderson, D., Sun, J., Punyamurthula, S., and Smith, N. [1998] "Generation of Ground Motion Time histories for Performance-Based Seismic Engineering," *Proceedings*, 6th National Earthquake Engineering Conference, Seattle, WA

Stone, C.J. [1996] *A Course in Probability and Statistics*, Duxbury Press, Belmont, CA

Symans, M.D. and Constantinou, M.C. [1998] "Passive fluid viscous damping systems for seismic energy dissipation," *ISET Journal of Earthquake Technology,* **35**(4):185-206

Taghavi, S. and Miranda, E. [2003] "Response Assessment of Nonstructural Building Elements," *PEER Report 2003/05*, Pacific Earthquake Engineering Research Center, Berkeley, CA

Tsai, H.C. and Kelly, J.M. [1984] "Seismic response of light internal equipment in base-isolated structures," *Report No. UCB/SESM-84/17*, Dept. of Civil Engineering, University of California, Berkeley, CA

Tsai, H.C. and Kelly, J.M. [1993] "Seismic response of heavily damped base isolation systems," *Earthquake Engineering and Structural Dynamics*, **22**(5), 633–645

Tsai, C.S., Lu, P.C., Chen. W.S., Chiang, T.C., Yang, T.C., Lin, Y.C. [2008] "Finite element formulations and shaking table tests of direction-optimized friction pendulum system," *Engineering Structures*, **30**(9), 2321-2329

USGS [2007] *Earthquake Ground Motion Parameter Java Application*, v. 5.0.7, http://earthquake.usgs.gov/research/hazmaps/design, United States Geological Survey, Menlo Park, CA

Vamvatsikos, D. and Cornell, C.A. [2006] "Direct estimation of the seismic demand and capacity of oscillators with multi-linear static pushovers through IDA," *Earthquake Engineering and Structural Dynamics*, **35**(9):1097-1117

Weisstein, E.W. [2006] "Correlation Coefficient." From MathWorld - A Wolfram Web Resource. http://mathworld.wolfram.com/CorrelationCoefficient.html

Wen, Y.K. [1976] "Method of random vibration of hysteretic systems," *Journal of Engineering Mechanics*, ASCE, **102**(2):249-263

Whittaker, A.S., Bertero, V.V., Alonso, J., and Thompson, C. [1989] "Earthquake simulator testing of steel plate added damping and stiffness elements," *Report No. UCB/EERC-89/02*, Earthquake Engineering Research Center, Berkeley, CA

Wolff, E.D. and Constantinou, M.C. [2004] "Experimental Study of Seismic Isolation Systems with Emphasis on Secondary System Response and Verification of Accuracy of Dynamic Response History Analysis Methods," *Technical Report MCEER-04-0001*, Multidisciplinary Center for Earthquake Engineering Research, Buffalo, NY

Zayas, V., Low, S., and Mahin, S. [1987] "The FPS earthquake resisting system," *Report No. UCB/EERC-87/01*, Earthquake Engineering Research Center, Berkeley, CA

Zayas, V., Low, S., Bozzo, L and Mahin, S. [1989] "Feasibility and performance studies on improving the earthquake resistance of new and existing buildings using the friction pendulum system," *UCB/EERC-89/09*, Earthquake Engineering Research Center, Berkeley, CA

PEER REPORTS

PEER reports are available individually or by yearly subscription. PEER reports can be ordered at http://peer.berkeley.edu/publications/peer_reports.html or by contacting the Pacific Earthquake Engineering Research Center, 325 Davis Hall mail code 1792, Berkeley, CA 94720. Tel.: (510) 642-3437; Fax: (510) 665-1655; Email: peer_editor@berkeley.edu

PEER 2011/06 *The Use of Base Isolation Systems to Achieve Complex Seismic Performance Objectives.* Troy A. Morgan and Stephen A. Mahin. July 2011.

PEER 2011/05 *Case Studies of the Seismic Performance of Tall Buildings Designed by Alternative Means.* Task 12 Report for the Tall Buildings Initiative. Jack Moehle, Yousef Bozorgnia, Nirmal Jayaram, Pierson Jones, Mohsen Rahnama, Nilesh Shome, Zeynep Tuna, John Wallace, Tony Yang, and Farzin Zareian. July 2011.

PEER 2011/04 *Recommended Design Practice for Pile Foundations in Laterally Spreading Ground.* Scott A. Ashford, Ross W. Boulanger, and Scott J. Brandenberg. June 2011.

PEER 2011/03 *New Ground Motion Selection Procedures and Selected Motions for the PEER Transportation Research Program.* Jack W. Baker, Ting Lin, Shrey K. Shahi, and Nirmal Jayaram. March 2011.

PEER 2011/02 *A Bayesian Network Methodology for Infrastructure Seismic Risk Assessment and Decision Support.* Michelle T. Bensi, Armen Der Kiureghian, and Daniel Straub. March 2011.

PEER 2011/01 *Demand Fragility Surfaces for Bridges in Liquefied and Laterally Spreading Ground.* Scott J. Brandenberg, Jian Zhang, Pirooz Kashighandi, Yili Huo, and Minxing Zhao. March 2011.

PEER 2010/05 *Guidelines for Performance-Based Seismic Design of Tall Buildings.* Developed by the Tall Buildings Initiative. November 2010.

PEER 2010/04 *Application Guide for the Design of Flexible and Rigid Bus Connections between Substation Equipment Subjected to Earthquakes.* Jean-Bernard Dastous and Armen Der Kiureghian. September 2010.

PEER 2010/03 *Shear Wave Velocity as a Statistical Function of Standard Penetration Test Resistance and Vertical Effective Stress at Caltrans Bridge Sites.* Scott J. Brandenberg, Naresh Bellana, and Thomas Shantz. June 2010.

PEER 2010/02 *Stochastic Modeling and Simulation of Ground Motions for Performance-Based Earthquake Engineering.* Sanaz Rezaeian and Armen Der Kiureghian. June 2010.

PEER 2010/01 *Structural Response and Cost Characterization of Bridge Construction Using Seismic Performance Enhancement Strategies.* Ady Aviram, Božidar Stojadinović, Gustavo J. Parra-Montesinos, and Kevin R. Mackie. March 2010.

PEER 2009/03 *The Integration of Experimental and Simulation Data in the Study of Reinforced Concrete Bridge Systems Including Soil-Foundation-Structure Interaction.* Matthew Dryden and Gregory L. Fenves. November 2009.

PEER 2009/02 *Improving Earthquake Mitigation through Innovations and Applications in Seismic Science, Engineering, Communication, and Response. Proceedings of a U.S.-Iran Seismic Workshop.* October 2009.

PEER 2009/01 *Evaluation of Ground Motion Selection and Modification Methods: Predicting Median Interstory Drift Response of Buildings.* Curt B. Haselton, Ed. June 2009.

PEER 2008/10 *Technical Manual for Strata.* Albert R. Kottke and Ellen M. Rathje. February 2009.

PEER 2008/09 *NGA Model for Average Horizontal Component of Peak Ground Motion and Response Spectra.* Brian S.-J. Chiou and Robert R. Youngs. November 2008.

PEER 2008/08 *Toward Earthquake-Resistant Design of Concentrically Braced Steel Structures.* Patxi Uriz and Stephen A. Mahin. November 2008.

PEER 2008/07 *Using OpenSees for Performance-Based Evaluation of Bridges on Liquefiable Soils.* Stephen L. Kramer, Pedro Arduino, and HyungSuk Shin. November 2008.

PEER 2008/06 *Shaking Table Tests and Numerical Investigation of Self-Centering Reinforced Concrete Bridge Columns.* Hyung IL Jeong, Junichi Sakai, and Stephen A. Mahin. September 2008.

PEER 2008/05 *Performance-Based Earthquake Engineering Design Evaluation Procedure for Bridge Foundations Undergoing Liquefaction-Induced Lateral Ground Displacement.* Christian A. Ledezma and Jonathan D. Bray. August 2008.

PEER 2008/04 *Benchmarking of Nonlinear Geotechnical Ground Response Analysis Procedures.* Jonathan P. Stewart, Annie On-Lei Kwok, Yousseff M. A. Hashash, Neven Matasovic, Robert Pyke, Zhiliang Wang, and Zhaohui Yang. August 2008.

PEER 2008/03 *Guidelines for Nonlinear Analysis of Bridge Structures in California.* Ady Aviram, Kevin R. Mackie, and Božidar Stojadinović. August 2008.

PEER 2008/02 *Treatment of Uncertainties in Seismic-Risk Analysis of Transportation Systems.* Evangelos Stergiou and Anne S. Kiremidjian. July 2008.

PEER 2008/01 *Seismic Performance Objectives for Tall Buildings.* William T. Holmes, Charles Kircher, William Petak, and Nabih Youssef. August 2008.

PEER 2007/12 *An Assessment to Benchmark the Seismic Performance of a Code-Conforming Reinforced Concrete Moment-Frame Building.* Curt Haselton, Christine A. Goulet, Judith Mitrani-Reiser, James L. Beck, Gregory G. Deierlein, Keith A. Porter, Jonathan P. Stewart, and Ertugrul Taciroglu. August 2008.

PEER 2007/11 *Bar Buckling in Reinforced Concrete Bridge Columns.* Wayne A. Brown, Dawn E. Lehman, and John F. Stanton. February 2008.

PEER 2007/10 *Computational Modeling of Progressive Collapse in Reinforced Concrete Frame Structures.* Mohamed M. Talaat and Khalid M. Mosalam. May 2008.

PEER 2007/09 *Integrated Probabilistic Performance-Based Evaluation of Benchmark Reinforced Concrete Bridges.* Kevin R. Mackie, John-Michael Wong, and Božidar Stojadinović. January 2008.

PEER 2007/08 *Assessing Seismic Collapse Safety of Modern Reinforced Concrete Moment-Frame Buildings.* Curt B. Haselton and Gregory G. Deierlein. February 2008.

PEER 2007/07 *Performance Modeling Strategies for Modern Reinforced Concrete Bridge Columns.* Michael P. Berry and Marc O. Eberhard. April 2008.

PEER 2007/06 *Development of Improved Procedures for Seismic Design of Buried and Partially Buried Structures.* Linda Al Atik and Nicholas Sitar. June 2007.

PEER 2007/05 *Uncertainty and Correlation in Seismic Risk Assessment of Transportation Systems.* Renee G. Lee and Anne S. Kiremidjian. July 2007.

PEER 2007/04 *Numerical Models for Analysis and Performance-Based Design of Shallow Foundations Subjected to Seismic Loading.* Sivapalan Gajan, Tara C. Hutchinson, Bruce L. Kutter, Prishati Raychowdhury, José A. Ugalde, and Jonathan P. Stewart. May 2008.

PEER 2007/03 *Beam-Column Element Model Calibrated for Predicting Flexural Response Leading to Global Collapse of RC Frame Buildings.* Curt B. Haselton, Abbie B. Liel, Sarah Taylor Lange, and Gregory G. Deierlein. May 2008.

PEER 2007/02 *Campbell-Bozorgnia NGA Ground Motion Relations for the Geometric Mean Horizontal Component of Peak and Spectral Ground Motion Parameters.* Kenneth W. Campbell and Yousef Bozorgnia. May 2007.

PEER 2007/01 *Boore-Atkinson NGA Ground Motion Relations for the Geometric Mean Horizontal Component of Peak and Spectral Ground Motion Parameters.* David M. Boore and Gail M. Atkinson. May. May 2007.

PEER 2006/12 *Societal Implications of Performance-Based Earthquake Engineering.* Peter J. May. May 2007.

PEER 2006/11 *Probabilistic Seismic Demand Analysis Using Advanced Ground Motion Intensity Measures, Attenuation Relationships, and Near-Fault Effects.* Polsak Tothong and C. Allin Cornell. March 2007.

PEER 2006/10 *Application of the PEER PBEE Methodology to the I-880 Viaduct.* Sashi Kunnath. February 2007.

PEER 2006/09 *Quantifying Economic Losses from Travel Forgone Following a Large Metropolitan Earthquake.* James Moore, Sungbin Cho, Yue Yue Fan, and Stuart Werner. November 2006.

PEER 2006/08 *Vector-Valued Ground Motion Intensity Measures for Probabilistic Seismic Demand Analysis.* Jack W. Baker and C. Allin Cornell. October 2006.

PEER 2006/07 *Analytical Modeling of Reinforced Concrete Walls for Predicting Flexural and Coupled–Shear-Flexural Responses.* Kutay Orakcal, Leonardo M. Massone, and John W. Wallace. October 2006.

PEER 2006/06 *Nonlinear Analysis of a Soil-Drilled Pier System under Static and Dynamic Axial Loading.* Gang Wang and Nicholas Sitar. November 2006.

PEER 2006/05 *Advanced Seismic Assessment Guidelines.* Paolo Bazzurro, C. Allin Cornell, Charles Menun, Maziar Motahari, and Nicolas Luco. September 2006.

PEER 2006/04 *Probabilistic Seismic Evaluation of Reinforced Concrete Structural Components and Systems.* Tae Hyung Lee and Khalid M. Mosalam. August 2006.

PEER 2006/03 *Performance of Lifelines Subjected to Lateral Spreading.* Scott A. Ashford and Teerawut Juirnarongrit. July 2006.

PEER 2006/02 *Pacific Earthquake Engineering Research Center Highway Demonstration Project.* Anne Kiremidjian, James Moore, Yue Yue Fan, Nesrin Basoz, Ozgur Yazali, and Meredith Williams. April 2006.

PEER 2006/01 *Bracing Berkeley. A Guide to Seismic Safety on the UC Berkeley Campus.* Mary C. Comerio, Stephen Tobriner, and Ariane Fehrenkamp. January 2006.

PEER 2005/16 *Seismic Response and Reliability of Electrical Substation Equipment and Systems.* Junho Song, Armen Der Kiureghian, and Jerome L. Sackman. April 2006.

PEER 2005/15 *CPT-Based Probabilistic Assessment of Seismic Soil Liquefaction Initiation.* R. E. S. Moss, R. B. Seed, R. E. Kayen, J. P. Stewart, and A. Der Kiureghian. April 2006.

PEER 2005/14 *Workshop on Modeling of Nonlinear Cyclic Load-Deformation Behavior of Shallow Foundations.* Bruce L. Kutter, Geoffrey Martin, Tara Hutchinson, Chad Harden, Sivapalan Gajan, and Justin Phalen. March 2006.

PEER 2005/13 *Stochastic Characterization and Decision Bases under Time-Dependent Aftershock Risk in Performance-Based Earthquake Engineering.* Gee Liek Yeo and C. Allin Cornell. July 2005.

PEER 2005/12 *PEER Testbed Study on a Laboratory Building: Exercising Seismic Performance Assessment.* Mary C. Comerio, editor. November 2005.

PEER 2005/11 *Van Nuys Hotel Building Testbed Report: Exercising Seismic Performance Assessment.* Helmut Krawinkler, editor. October 2005.

PEER 2005/10 *First NEES/E-Defense Workshop on Collapse Simulation of Reinforced Concrete Building Structures.* September 2005.

PEER 2005/09 *Test Applications of Advanced Seismic Assessment Guidelines.* Joe Maffei, Karl Telleen, Danya Mohr, William Holmes, and Yuki Nakayama. August 2006.

PEER 2005/08 *Damage Accumulation in Lightly Confined Reinforced Concrete Bridge Columns.* R. Tyler Ranf, Jared M. Nelson, Zach Price, Marc O. Eberhard, and John F. Stanton. April 2006.

PEER 2005/07 *Experimental and Analytical Studies on the Seismic Response of Freestanding and Anchored Laboratory Equipment.* Dimitrios Konstantinidis and Nicos Makris. January 2005.

PEER 2005/06 *Global Collapse of Frame Structures under Seismic Excitations.* Luis F. Ibarra and Helmut Krawinkler. September 2005.

PEER 2005//05 *Performance Characterization of Bench- and Shelf-Mounted Equipment.* Samit Ray Chaudhuri and Tara C. Hutchinson. May 2006.

PEER 2005/04 *Numerical Modeling of the Nonlinear Cyclic Response of Shallow Foundations.* Chad Harden, Tara Hutchinson, Geoffrey R. Martin, and Bruce L. Kutter. August 2005.

PEER 2005/03 *A Taxonomy of Building Components for Performance-Based Earthquake Engineering.* Keith A. Porter. September 2005.

PEER 2005/02 *Fragility Basis for California Highway Overpass Bridge Seismic Decision Making.* Kevin R. Mackie and Božidar Stojadinović. June 2005.

PEER 2005/01 *Empirical Characterization of Site Conditions on Strong Ground Motion.* Jonathan P. Stewart, Yoojoong Choi, and Robert W. Graves. June 2005.

PEER 2004/09 *Electrical Substation Equipment Interaction: Experimental Rigid Conductor Studies.* Christopher Stearns and André Filiatrault. February 2005.

PEER 2004/08 *Seismic Qualification and Fragility Testing of Line Break 550-kV Disconnect Switches.* Shakhzod M. Takhirov, Gregory L. Fenves, and Eric Fujisaki. January 2005.

PEER 2004/07 *Ground Motions for Earthquake Simulator Qualification of Electrical Substation Equipment.* Shakhzod M. Takhirov, Gregory L. Fenves, Eric Fujisaki, and Don Clyde. January 2005.

PEER 2004/06 *Performance-Based Regulation and Regulatory Regimes.* Peter J. May and Chris Koski. September 2004.

PEER 2004/05 *Performance-Based Seismic Design Concepts and Implementation: Proceedings of an International Workshop.* Peter Fajfar and Helmut Krawinkler, editors. September 2004.

PEER 2004/04 *Seismic Performance of an Instrumented Tilt-up Wall Building.* James C. Anderson and Vitelmo V. Bertero. July 2004.

PEER 2004/03 *Evaluation and Application of Concrete Tilt-up Assessment Methodologies.* Timothy Graf and James O. Malley. October 2004.

PEER 2004/02 *Analytical Investigations of New Methods for Reducing Residual Displacements of Reinforced Concrete Bridge Columns.* Junichi Sakai and Stephen A. Mahin. August 2004.

PEER 2004/01 *Seismic Performance of Masonry Buildings and Design Implications.* Kerri Anne Taeko Tokoro, James C. Anderson, and Vitelmo V. Bertero. February 2004.

PEER 2003/18 *Performance Models for Flexural Damage in Reinforced Concrete Columns.* Michael Berry and Marc Eberhard. August 2003.

PEER 2003/17 *Predicting Earthquake Damage in Older Reinforced Concrete Beam-Column Joints.* Catherine Pagni and Laura Lowes. October 2004.

PEER 2003/16 *Seismic Demands for Performance-Based Design of Bridges.* Kevin Mackie and Božidar Stojadinović. August 2003.

PEER 2003/15 *Seismic Demands for Nondeteriorating Frame Structures and Their Dependence on Ground Motions.* Ricardo Antonio Medina and Helmut Krawinkler. May 2004.

PEER 2003/14 *Finite Element Reliability and Sensitivity Methods for Performance-Based Earthquake Engineering.* Terje Haukaas and Armen Der Kiureghian. April 2004.

PEER 2003/13 *Effects of Connection Hysteretic Degradation on the Seismic Behavior of Steel Moment-Resisting Frames.* Janise E. Rodgers and Stephen A. Mahin. March 2004.

PEER 2003/12 *Implementation Manual for the Seismic Protection of Laboratory Contents: Format and Case Studies.* William T. Holmes and Mary C. Comerio. October 2003.

PEER 2003/11 *Fifth U.S.-Japan Workshop on Performance-Based Earthquake Engineering Methodology for Reinforced Concrete Building Structures.* February 2004.

PEER 2003/10 *A Beam-Column Joint Model for Simulating the Earthquake Response of Reinforced Concrete Frames.* Laura N. Lowes, Nilanjan Mitra, and Arash Altoontash. February 2004.

PEER 2003/09 *Sequencing Repairs after an Earthquake: An Economic Approach.* Marco Casari and Simon J. Wilkie. April 2004.

PEER 2003/08 *A Technical Framework for Probability-Based Demand and Capacity Factor Design (DCFD) Seismic Formats.* Fatemeh Jalayer and C. Allin Cornell. November 2003.

PEER 2003/07 *Uncertainty Specification and Propagation for Loss Estimation Using FOSM Methods.* Jack W. Baker and C. Allin Cornell. September 2003.

PEER 2003/06 *Performance of Circular Reinforced Concrete Bridge Columns under Bidirectional Earthquake Loading.* Mahmoud M. Hachem, Stephen A. Mahin, and Jack P. Moehle. February 2003.

PEER 2003/05 *Response Assessment for Building-Specific Loss Estimation.* Eduardo Miranda and Shahram Taghavi. September 2003.

PEER 2003/04 *Experimental Assessment of Columns with Short Lap Splices Subjected to Cyclic Loads.* Murat Melek, John W. Wallace, and Joel Conte. April 2003.

PEER 2003/03 *Probabilistic Response Assessment for Building-Specific Loss Estimation.* Eduardo Miranda and Hesameddin Aslani. September 2003.

PEER 2003/02 *Software Framework for Collaborative Development of Nonlinear Dynamic Analysis Program.* Jun Peng and Kincho H. Law. September 2003.

PEER 2003/01 *Shake Table Tests and Analytical Studies on the Gravity Load Collapse of Reinforced Concrete Frames.* Kenneth John Elwood and Jack P. Moehle. November 2003.

PEER 2002/24 *Performance of Beam to Column Bridge Joints Subjected to a Large Velocity Pulse.* Natalie Gibson, André Filiatrault, and Scott A. Ashford. April 2002.

PEER 2002/23 *Effects of Large Velocity Pulses on Reinforced Concrete Bridge Columns.* Greg L. Orozco and Scott A. Ashford. April 2002.

PEER 2002/22 *Characterization of Large Velocity Pulses for Laboratory Testing.* Kenneth E. Cox and Scott A. Ashford. April 2002.

PEER 2002/21 *Fourth U.S.-Japan Workshop on Performance-Based Earthquake Engineering Methodology for Reinforced Concrete Building Structures.* December 2002.

PEER 2002/20 *Barriers to Adoption and Implementation of PBEE Innovations.* Peter J. May. August 2002.

PEER 2002/19 *Economic-Engineered Integrated Models for Earthquakes: Socioeconomic Impacts.* Peter Gordon, James E. Moore II, and Harry W. Richardson. July 2002.

PEER 2002/18 *Assessment of Reinforced Concrete Building Exterior Joints with Substandard Details.* Chris P. Pantelides, Jon Hansen, Justin Nadauld, and Lawrence D. Reaveley. May 2002.

PEER 2002/17 *Structural Characterization and Seismic Response Analysis of a Highway Overcrossing Equipped with Elastomeric Bearings and Fluid Dampers: A Case Study.* Nicos Makris and Jian Zhang. November 2002.

PEER 2002/16 *Estimation of Uncertainty in Geotechnical Properties for Performance-Based Earthquake Engineering.* Allen L. Jones, Steven L. Kramer, and Pedro Arduino. December 2002.

PEER 2002/15 *Seismic Behavior of Bridge Columns Subjected to Various Loading Patterns.* Asadollah Esmaeily-Gh. and Yan Xiao. December 2002.

PEER 2002/14 *Inelastic Seismic Response of Extended Pile Shaft Supported Bridge Structures.* T.C. Hutchinson, R.W. Boulanger, Y.H. Chai, and I.M. Idriss. December 2002.

PEER 2002/13 *Probabilistic Models and Fragility Estimates for Bridge Components and Systems.* Paolo Gardoni, Armen Der Kiureghian, and Khalid M. Mosalam. June 2002.

PEER 2002/12 *Effects of Fault Dip and Slip Rake on Near-Source Ground Motions: Why Chi-Chi Was a Relatively Mild M7.6 Earthquake.* Brad T. Aagaard, John F. Hall, and Thomas H. Heaton. December 2002.

PEER 2002/11 *Analytical and Experimental Study of Fiber-Reinforced Strip Isolators.* James M. Kelly and Shakhzod M. Takhirov. September 2002.

PEER 2002/10 *Centrifuge Modeling of Settlement and Lateral Spreading with Comparisons to Numerical Analyses.* Sivapalan Gajan and Bruce L. Kutter. January 2003.

PEER 2002/09 *Documentation and Analysis of Field Case Histories of Seismic Compression during the 1994 Northridge, California, Earthquake.* Jonathan P. Stewart, Patrick M. Smith, Daniel H. Whang, and Jonathan D. Bray. October 2002.

PEER 2002/08 *Component Testing, Stability Analysis and Characterization of Buckling-Restrained Unbonded Braces™.* Cameron Black, Nicos Makris, and Ian Aiken. September 2002.

PEER 2002/07 *Seismic Performance of Pile-Wharf Connections.* Charles W. Roeder, Robert Graff, Jennifer Soderstrom, and Jun Han Yoo. December 2001.

PEER 2002/06 *The Use of Benefit-Cost Analysis for Evaluation of Performance-Based Earthquake Engineering Decisions.* Richard O. Zerbe and Anthony Falit-Baiamonte. September 2001.

PEER 2002/05 *Guidelines, Specifications, and Seismic Performance Characterization of Nonstructural Building Components and Equipment.* André Filiatrault, Constantin Christopoulos, and Christopher Stearns. September 2001.

PEER 2002/04 *Consortium of Organizations for Strong-Motion Observation Systems and the Pacific Earthquake Engineering Research Center Lifelines Program: Invited Workshop on Archiving and Web Dissemination of Geotechnical Data, 4–5 October 2001.* September 2002.

PEER 2002/03 *Investigation of Sensitivity of Building Loss Estimates to Major Uncertain Variables for the Van Nuys Testbed.* Keith A. Porter, James L. Beck, and Rustem V. Shaikhutdinov. August 2002.

PEER 2002/02 *The Third U.S.-Japan Workshop on Performance-Based Earthquake Engineering Methodology for Reinforced Concrete Building Structures.* July 2002.

PEER 2002/01 *Nonstructural Loss Estimation: The UC Berkeley Case Study.* Mary C. Comerio and John C. Stallmeyer. December 2001.

PEER 2001/16 *Statistics of SDF-System Estimate of Roof Displacement for Pushover Analysis of Buildings.* Anil K. Chopra, Rakesh K. Goel, and Chatpan Chintanapakdee. December 2001.

PEER 2001/15 *Damage to Bridges during the 2001 Nisqually Earthquake.* R. Tyler Ranf, Marc O. Eberhard, and Michael P. Berry. November 2001.

PEER 2001/14 *Rocking Response of Equipment Anchored to a Base Foundation.* Nicos Makris and Cameron J. Black. September 2001.

PEER 2001/13 *Modeling Soil Liquefaction Hazards for Performance-Based Earthquake Engineering.* Steven L. Kramer and Ahmed-W. Elgamal. February 2001.

PEER 2001/12 *Development of Geotechnical Capabilities in OpenSees.* Boris Jeremić. September 2001.

PEER 2001/11 *Analytical and Experimental Study of Fiber-Reinforced Elastomeric Isolators.* James M. Kelly and Shakhzod M. Takhirov. September 2001.

PEER 2001/10 *Amplification Factors for Spectral Acceleration in Active Regions.* Jonathan P. Stewart, Andrew H. Liu, Yoojoong Choi, and Mehmet B. Baturay. December 2001.

PEER 2001/09 *Ground Motion Evaluation Procedures for Performance-Based Design.* Jonathan P. Stewart, Shyh-Jeng Chiou, Jonathan D. Bray, Robert W. Graves, Paul G. Somerville, and Norman A. Abrahamson. September 2001.

PEER 2001/08 *Experimental and Computational Evaluation of Reinforced Concrete Bridge Beam-Column Connections for Seismic Performance.* Clay J. Naito, Jack P. Moehle, and Khalid M. Mosalam. November 2001.

PEER 2001/07 *The Rocking Spectrum and the Shortcomings of Design Guidelines.* Nicos Makris and Dimitrios Konstantinidis. August 2001.

PEER 2001/06 *Development of an Electrical Substation Equipment Performance Database for Evaluation of Equipment Fragilities*. Thalia Agnanos. April 1999.

PEER 2001/05 *Stiffness Analysis of Fiber-Reinforced Elastomeric Isolators.* Hsiang-Chuan Tsai and James M. Kelly. May 2001.

PEER 2001/04 *Organizational and Societal Considerations for Performance-Based Earthquake Engineering.* Peter J. May. April 2001.

PEER 2001/03 *A Modal Pushover Analysis Procedure to Estimate Seismic Demands for Buildings: Theory and Preliminary Evaluation.* Anil K. Chopra and Rakesh K. Goel. January 2001.

PEER 2001/02 *Seismic Response Analysis of Highway Overcrossings Including Soil-Structure Interaction.* Jian Zhang and Nicos Makris. March 2001.

PEER 2001/01 *Experimental Study of Large Seismic Steel Beam-to-Column Connections*. Egor P. Popov and Shakhzod M. Takhirov. November 2000.

PEER 2000/10 *The Second U.S.-Japan Workshop on Performance-Based Earthquake Engineering Methodology for Reinforced Concrete Building Structures.* March 2000.

PEER 2000/09 *Structural Engineering Reconnaissance of the August 17, 1999 Earthquake: Kocaeli (Izmit), Turkey*. Halil Sezen, Kenneth J. Elwood, Andrew S. Whittaker, Khalid Mosalam, John J. Wallace, and John F. Stanton. December 2000.

PEER 2000/08 *Behavior of Reinforced Concrete Bridge Columns Having Varying Aspect Ratios and Varying Lengths of Confinement*. Anthony J. Calderone, Dawn E. Lehman, and Jack P. Moehle. January 2001.

PEER 2000/07 *Cover-Plate and Flange-Plate Reinforced Steel Moment-Resisting Connections.* Taejin Kim, Andrew S. Whittaker, Amir S. Gilani, Vitelmo V. Bertero, and Shakhzod M. Takhirov. September 2000.

PEER 2000/06 *Seismic Evaluation and Analysis of 230-kV Disconnect Switches.* Amir S. J. Gilani, Andrew S. Whittaker, Gregory L. Fenves, Chun-Hao Chen, Henry Ho, and Eric Fujisaki. July 2000.

PEER 2000/05 *Performance-Based Evaluation of Exterior Reinforced Concrete Building Joints for Seismic Excitation.* Chandra Clyde, Chris P. Pantelides, and Lawrence D. Reaveley. July 2000.

PEER 2000/04 *An Evaluation of Seismic Energy Demand: An Attenuation Approach.* Chung-Che Chou and Chia-Ming Uang. July 1999.

PEER 2000/03 *Framing Earthquake Retrofitting Decisions: The Case of Hillside Homes in Los Angeles.* Detlof von Winterfeldt, Nels Roselund, and Alicia Kitsuse. March 2000.

PEER 2000/02 *U.S.-Japan Workshop on the Effects of Near-Field Earthquake Shaking.* Andrew Whittaker, ed. July 2000.

PEER 2000/01 *Further Studies on Seismic Interaction in Interconnected Electrical Substation Equipment.* Armen Der Kiureghian, Kee-Jeung Hong, and Jerome L. Sackman. November 1999.

PEER 1999/14 *Seismic Evaluation and Retrofit of 230-kV Porcelain Transformer Bushings*. Amir S. Gilani, Andrew S. Whittaker, Gregory L. Fenves, and Eric Fujisaki. December 1999.

PEER 1999/13 *Building Vulnerability Studies: Modeling and Evaluation of Tilt-up and Steel Reinforced Concrete Buildings.* John W. Wallace, Jonathan P. Stewart, and Andrew S. Whittaker, editors. December 1999.

PEER 1999/12 *Rehabilitation of Nonductile RC Frame Building Using Encasement Plates and Energy-Dissipating Devices.* Mehrdad Sasani, Vitelmo V. Bertero, James C. Anderson. December 1999.

PEER 1999/11 *Performance Evaluation Database for Concrete Bridge Components and Systems under Simulated Seismic Loads.* Yael D. Hose and Frieder Seible. November 1999.

PEER 1999/10 *U.S.-Japan Workshop on Performance-Based Earthquake Engineering Methodology for Reinforced Concrete Building Structures.* December 1999.

PEER 1999/09 *Performance Improvement of Long Period Building Structures Subjected to Severe Pulse-Type Ground Motions*. James C. Anderson, Vitelmo V. Bertero, and Raul Bertero. October 1999.

PEER 1999/08 *Envelopes for Seismic Response Vectors.* Charles Menun and Armen Der Kiureghian. July 1999.

PEER 1999/07 *Documentation of Strengths and Weaknesses of Current Computer Analysis Methods for Seismic Performance of Reinforced Concrete Members.* William F. Cofer. November 1999.

PEER 1999/06 *Rocking Response and Overturning of Anchored Equipment under Seismic Excitations.* Nicos Makris and Jian Zhang. November 1999.

PEER 1999/05 *Seismic Evaluation of 550 kV Porcelain Transformer Bushings.* Amir S. Gilani, Andrew S. Whittaker, Gregory L. Fenves, and Eric Fujisaki. October 1999.

PEER 1999/04 *Adoption and Enforcement of Earthquake Risk-Reduction Measures.* Peter J. May, Raymond J. Burby, T. Jens Feeley, and Robert Wood.

PEER 1999/03 *Task 3 Characterization of Site Response General Site Categories.* Adrian Rodriguez-Marek, Jonathan D. Bray, and Norman Abrahamson. February 1999.

PEER 1999/02 *Capacity-Demand-Diagram Methods for Estimating Seismic Deformation of Inelastic Structures: SDF Systems*. Anil K. Chopra and Rakesh Goel. April 1999.

PEER 1999/01 *Interaction in Interconnected Electrical Substation Equipment Subjected to Earthquake Ground Motions.* Armen Der Kiureghian, Jerome L. Sackman, and Kee-Jeung Hong. February 1999.

PEER 1998/08 *Behavior and Failure Analysis of a Multiple-Frame Highway Bridge in the 1994 Northridge Earthquake.* Gregory L. Fenves and Michael Ellery. December 1998.

PEER 1998/07 *Empirical Evaluation of Inertial Soil-Structure Interaction Effects.* Jonathan P. Stewart, Raymond B. Seed, and Gregory L. Fenves. November 1998.

PEER 1998/06 *Effect of Damping Mechanisms on the Response of Seismic Isolated Structures.* Nicos Makris and Shih-Po Chang. November 1998.

PEER 1998/05 *Rocking Response and Overturning of Equipment under Horizontal Pulse-Type Motions.* Nicos Makris and Yiannis Roussos. October 1998.

PEER 1998/04 *Pacific Earthquake Engineering Research Invitational Workshop Proceedings, May 14–15, 1998: Defining the Links between Planning, Policy Analysis, Economics and Earthquake Engineering.* Mary Comerio and Peter Gordon. September 1998.

PEER 1998/03 *Repair/Upgrade Procedures for Welded Beam to Column Connections.* James C. Anderson and Xiaojing Duan. May 1998.

PEER 1998/02 *Seismic Evaluation of 196 kV Porcelain Transformer Bushings.* Amir S. Gilani, Juan W. Chavez, Gregory L. Fenves, and Andrew S. Whittaker. May 1998.

PEER 1998/01 *Seismic Performance of Well-Confined Concrete Bridge Columns.* Dawn E. Lehman and Jack P. Moehle. December 2000.

ONLINE REPORTS

The following PEER reports are available by Internet only at http://peer.berkeley.edu/publications/peer_reports.html

PEER 2011/104 *Design and Instrumentation of the 2010 E-Defense Four-Story Reinforced Concrete and Post-Tensioned Concrete Buildings.* Takuya Nagae, Kenichi Tahara, Taizo Matsumori, Hitoshi Shiohara, Toshimi Kabeyasawa, Susumu Kono, Minehiro Nishiyama (Japanese Research Team) and John Wallace, Wassim Ghannoum, Jack Moehle, Richard Sause, Wesley Keller, Zeynep Tuna (U.S. Research Team). June 2011.

PEER 2011/103 *In-Situ Monitoring of the Force Output of Fluid Dampers: Experimental Investigation.* Dimitrios Konstantinidis, James M. Kelly, and Nicos Makris. April 2011.

PEER 2011/102 *Ground-motion prediction equations 1964 - 2010.* John Douglas. April 2011.

PEER 2011/101 *Report of the Eighth Planning Meeting of NEES/E-Defense Collaborative Research on Earthquake Engineering.* Convened by the Hyogo Earthquake Engineering Research Center (NIED), NEES Consortium, Inc. February 2011.

PEER 2010/111 *Modeling and Acceptance Criteria for Seismic Design and Analysis of Tall Buildings.* Task 7 Report for the Tall Buildings Initiative - Published jointly by the Applied Technology Council. October 2010.

PEER 2010/110 *Seismic Performance Assessment and Probabilistic Repair Cost Analysis of Precast Concrete Cladding Systems for Multistory Buildlings.* Jeffrey P. Hunt and Božidar Stojadinovic. November 2010.

PEER 2010/109 *Report of the Seventh Joint Planning Meeting of NEES/E-Defense Collaboration on Earthquake Engineering. Held at the E-Defense, Miki, and Shin-Kobe, Japan, September 18–19, 2009.* August 2010.

PEER 2010/108 *Probabilistic Tsunami Hazard in California.* Hong Kie Thio, Paul Somerville, and Jascha Polet, preparers. October 2010.

PEER 2010/107 *Performance and Reliability of Exposed Column Base Plate Connections for Steel Moment-Resisting Frames.* Ady Aviram, Božidar Stojadinovic, and Armen Der Kiureghian. August 2010.

PEER 2010/106 *Verification of Probabilistic Seismic Hazard Analysis Computer Programs.* Patricia Thomas, Ivan Wong, and Norman Abrahamson. May 2010.

PEER 2010/105 *Structural Engineering Reconnaissance of the April 6, 2009, Abruzzo, Italy, Earthquake, and Lessons Learned.* M. Selim Günay and Khalid M. Mosalam. April 2010.

PEER 2010/104 *Simulating the Inelastic Seismic Behavior of Steel Braced Frames, Including the Effects of Low-Cycle Fatigue.* Yuli Huang and Stephen A. Mahin. April 2010.

PEER 2010/103 *Post-Earthquake Traffic Capacity of Modern Bridges in California.* Vesna Terzic and Božidar Stojadinović. March 2010.

PEER 2010/102 *Analysis of Cumulative Absolute Velocity (CAV) and JMA Instrumental Seismic Intensity (I_{JMA}) Using the PEER–NGA Strong Motion Database.* Kenneth W. Campbell and Yousef Bozorgnia. February 2010.

PEER 2010/101 *Rocking Response of Bridges on Shallow Foundations.* Jose A. Ugalde, Bruce L. Kutter, and Boris Jeremic. April 2010.

PEER 2009/109 *Simulation and Performance-Based Earthquake Engineering Assessment of Self-Centering Post-Tensioned Concrete Bridge Systems.* Won K. Lee and Sarah L. Billington. December 2009.

PEER 2009/108 *PEER Lifelines Geotechnical Virtual Data Center.* J. Carl Stepp, Daniel J. Ponti, Loren L. Turner, Jennifer N. Swift, Sean Devlin, Yang Zhu, Jean Benoit, and John Bobbitt. September 2009.

PEER 2009/107 *Experimental and Computational Evaluation of Current and Innovative In-Span Hinge Details in Reinforced Concrete Box-Girder Bridges: Part 2: Post-Test Analysis and Design Recommendations.* Matias A. Hube and Khalid M. Mosalam. December 2009.

PEER 2009/106 *Shear Strength Models of Exterior Beam-Column Joints without Transverse Reinforcement.* Sangjoon Park and Khalid M. Mosalam. November 2009.

PEER 2009/105 *Reduced Uncertainty of Ground Motion Prediction Equations through Bayesian Variance Analysis.* Robb Eric S. Moss. November 2009.

PEER 2009/104 *Advanced Implementation of Hybrid Simulation.* Andreas H. Schellenberg, Stephen A. Mahin, Gregory L. Fenves. November 2009.

PEER 2009/103 *Performance Evaluation of Innovative Steel Braced Frames.* T. Y. Yang, Jack P. Moehle, and Božidar Stojadinovic. August 2009.

PEER 2009/102 *Reinvestigation of Liquefaction and Nonliquefaction Case Histories from the 1976 Tangshan Earthquake.* Robb Eric Moss, Robert E. Kayen, Liyuan Tong, Songyu Liu, Guojun Cai, and Jiaer Wu. August 2009.

PEER 2009/101 *Report of the First Joint Planning Meeting for the Second Phase of NEES/E-Defense Collaborative Research on Earthquake Engineering.* Stephen A. Mahin et al. July 2009.

PEER 2008/104 *Experimental and Analytical Study of the Seismic Performance of Retaining Structures.* Linda Al Atik and Nicholas Sitar. January 2009.

PEER 2008/103 *Experimental and Computational Evaluation of Current and Innovative In-Span Hinge Details in Reinforced Concrete Box-Girder Bridges. Part 1: Experimental Findings and Pre-Test Analysis.* Matias A. Hube and Khalid M. Mosalam. January 2009.

PEER 2008/102 *Modeling of Unreinforced Masonry Infill Walls Considering In-Plane and Out-of-Plane Interaction.* Stephen Kadysiewski and Khalid M. Mosalam. January 2009.

PEER 2008/101 *Seismic Performance Objectives for Tall Buildings.* William T. Holmes, Charles Kircher, William Petak, and Nabih Youssef. August 2008.

PEER 2007/101 *Generalized Hybrid Simulation Framework for Structural Systems Subjected to Seismic Loading.* Tarek Elkhoraibi and Khalid M. Mosalam. July 2007.

PEER 2007/100 *Seismic Evaluation of Reinforced Concrete Buildings Including Effects of Masonry Infill Walls.* Alidad Hashemi and Khalid M. Mosalam. July 2007.

The Pacific Earthquake Engineering Research Center (PEER) is a multi-institutional research and education center with headquarters at the University of California, Berkeley. Investigators from over 20 universities, several consulting companies, and researchers at various state and federal government agencies contribute to research programs focused on performance-based earthquake engineering.

These research programs aim to identify and reduce the risks from major earthquakes to life safety and to the economy by including research in a wide variety of disciplines including structural and geotechnical engineering, geology/seismology, lifelines, transportation, architecture, economics, risk management, and public policy.

PEER is supported by federal, state, local, and regional agencies, together with industry partners.

PEER reports can be ordered at http://peer.berkeley.edu/publications/peer_reports.html or by contacting

Pacific Earthquake Engineering Research Center
University of California, Berkeley
325 Davis Hall, mail code 1792
Berkeley, CA 94720-1792
Tel: 510-642-3437
Fax: 510-642-1655
Email: peer_editor@berkeley.edu

ISSN 1547-0587X